PONTIFICIA UNIVERSIDAD CATÓLICA DE CHILE

ESCUELA DE INGENIERÍA

APPLICATIONS OF BOUNDARY INTEGRAL EQUATIONS AND HOMOGENIZATION FOR THE NUMERICAL SIMULATION OF LIVING TISSUES

ISABEL ALEJANDRA MARTÍNEZ ÁVILA

Thesis submitted to the Office of Graduate Studies in partial fulfillment of the requirements for the Degree of
Doctor in Engineering Sciences

Advisor:
CARLOS JEREZ-HANCKES
CARLOS SING-LONG

Santiago de Chile, May 2023

PONTIFICIA UNIVERSIDAD CATOLICA DE CHILE

ESCUELA DE INGENIERIA

APPLICATIONS OF BOUNDARY INTEGRAL EQUATIONS AND HOMOGENIZATION FOR THE NUMERICAL SIMULATION OF LIVING TISSUES

ISABEL ALEJANDRA MARTÍNEZ ÁVILA

Members of the Committee:

CARLOS SING-LONG
CARLOS JEREZ
ELWIN VAN´T WOUT
DANIEL HURTADO
CHRISTOPHER COOPER
IRINA PETTERSSON
JUAN DE DIOS ORTÚZAR

Thesis submitted to the Office of Graduate Studies in partial fulfillment of the requirements for the degree of Doctor in Engineering Sciences

Santiago de Chile, May 2023

A la familia

ACKNOWLEDGEMENTS

during these years. Thanks to Fernando, for his time and patience discussing with me time schemes and electrophysiological concepts.

I want to thank my family, my mother María Isabel, my grandmother María Aurelia, my aunts Apsara, María Cecilia, María Aurelia Valentina, my uncles José María, José Leonardo and José Rodrigo, my dear Blanquita, Victoria, Paloma and Edito. Thank you for all your love, for listening to me, for being with me and for praying for me. Special thanks to my mom, who is always with me, and to my uncle José María for his time and wisdom.

Thanks to all friends and people that gave me their support during this time.

TABLE OF CONTENTS

LIST OF FIGURES

ABSTRACT

During the last decades, enormous progress has been achieved in biomedical applications thanks to the ability to model and computationally simulate complex underlying phenomena. Indeed, the derivation and analysis of ever more realistic physiological models as well as suitable numerical methods to solve them has allowed the identification of relevant variables and behavior patterns with immediate use for clinical practitioners and biomedical specialists.

The present thesis proposes mathematical and computational models to study complex electrophysiological phenomena at the cellular scale using integral boundary equations and homogenization techniques. Specific applications considered are peripheral neural stimulation and cell electropermeabilization.

We employ multiscale analysis and homogenization methods to obtain two reduced-order models: (a) a non-linear cable equation for one myelinated axon that considers the microstructure of it in three dimensions; and, (b) a non-linear bidomain model in three dimensions, which describes the macroscopic behaviour of the electric potential in a bundle of myelinated axons.

For the cell electropermeabilization process, we apply and develop a mathematical theoretical framework for the resolution of the phenomena at the cell scale in three dimensions using the multiple traces boundary integral formulation with a semi-implicit time scheme. We also present a numerical algorithm to simulate the process.

Keywords: multiscale analysis, asymptotic homogenization, boundary integral formulations, myelinated axons, electropermeabilization, cell modeling, spectral methods, numerical simulations, non-linear partial differential equations.

RESUMEN

Durante las últimas décadas se ha logrado un enorme progreso en las aplicaciones biomédicas gracias a la capacidad de modelar y simular computacionalmente fenómenos complejos. De hecho, la derivación y análisis de modelos fisiológicos cada vez más realistas, así como métodos numéricos adecuados para resolverlos, ha permitido la identificación de variables relevantes y patrones de comportamiento con uso inmediato para médicos y especialistas biomédicos.

La presente tesis propone modelos matemáticos y computacionales para estudiar fenómenos electrofisiológicos complejos a escala celular utilizando técnicas de ecuaciones integrales de frontera y homogeneización. Las aplicaciones específicas consideradas son la estimulación neural periférica y la electropermeabilización celular.

Los métodos de homogeneización y análisis multi-escala se utilizarán para obtener dos modelos de orden reducido: (a) una ecuación de cable no lineal para un axón mielinizado que considera la microestructura del mismo en tres dimensiones; y, (b) un modelo de bidominio no lineal en tres dimensiones, que describe el comportamiento macroscópico del potencial eléctrico en un manojo de axones mielinados.

Para el proceso de electropermeabilización, aplicamos y desarrollamos un marco teórico para la resolución del fenómeno a escala celular en tres dimensiones usando la formulación integral de múltiples trazas junto a un esquema temporal semi-implícito. También presentamos un algoritmo numérico para simular el proceso.

Palabras Claves: análisis multiescala, homogenización asintótica, formulaciones integrales de frontera, axones mielinados, electropermeabilización, electorporación, modelamiento celular, métodos espectrales, simulaciones numéricas, ecuaciones diferenciales parciales no lineales.

1. INTRODUCTION

During the last decades, enormous progress has been achieved in biomedical applications thanks to the ability to model and computationally simulate complex underlying phenomena (Maini, 2002; Mackey & Maini, 2015; Winslow, Trayanova, Geman, & Miller, 2012). Indeed, the derivation and analysis of ever more realistic physiological models, as well as suitable numerical methods to solve them, has allowed the identification of relevant variables and behavior patterns with immediate use for clinical practitioners and biomedical specialists.

The present doctoral thesis aims to study such mathematical models and numerical methods for specific applications in electrophysiology. This branch of physiology studies the electrical properties of biological cells and tissues. It involves measurements of voltage changes or electric current or manipulations on a wide variety of scales from single ion channel proteins to whole organs, like the heart. In neuroscience, it includes measurements of the electrical activity of neurons, and, in particular, action potential activity. However, there are other complex processes, such as electropermeabilization, that are less obvious and showcase non-trivial cell reactions to electrical stimuli.

In particular, this work tackles two electrophysiological phenomena: (i) the transmission of electrical impulses along peripheral axons and the interaction in axon bundles; and, (ii) electropermeabilization and electroporation in cells. These processes follow nonlinear dynamics, the geometries are complex and involve several scales, which lead to a high computational costs when trying to model and simulate them numerically. Then, is it possible to derived simplified models? How to reduce the computational complexity? In both cases, rigorous mathematical models are derived along with the development of suitable numerical methods to solve the corresponding problems.

Multiple applications of these processes can be found in the literature, as it will be discussed below, but it helps to have in mind for (i) peripheral nerve stimulation used in regional anesthesia, while for (ii) drug absorption in cancer treatment.

The thesis is structured in the following way. First, basic electrophysiology elements as well as a discussion on the state-of-the-art of the phenomena under study are given. Then, key ideas of the homogenization theory and asymptotic analysis are introduced to be later employed in two of the three main contributions of this manuscript. These are presented as follows:

- Chapter 3, entitled *Multiscale analysis of myelinated axons*, published in Emerging Problems in the Homogenization of Partial Differential Equations, SEMA SIMAI Springer Series, **10** (2021). Here, a nonlinear cable equation for periodically myelinated and unmyelinated segments is derived by asymptotic homogenization takes into account the microstructure of the axon.

- Chapter 4, entitled *Derivation of a Bidomain model for bundles of myelinated axons*, published in Nonlinear Analysis: Real World Applications, **70** (2023), 4:103789. The main result consists of a bidomain model describing macroscopic behavior of the electric potential in a bundle of myelinated axons.

- Chapter 5, entitled *Cell Electropermeabilization Modeling via Multiple Traces Formulation and Time Semi-Implicit Coupling* (submitted to SISC). In this chapter, we apply and develop a mathematical theoretical framework for the resolution of cellular electro-permeabilization models in three dimensions using the formulation of multiple traces together with a temporal scheme. A numerical algorithm based on integral equations for a set of electrically stimulated cells is proposed.

Finally, concluding remarks as well as future research directions are provided, as well as bibliographic references for further reading.

1.1. Peripheral axon modeling

As stated, one of the main interests in electrophysiology is to better understand and describe the transmission of electrical stimuli through nerves and other biological cells making up tissues. This allows to more accurately model, for instance, nerve stimulation,

which is nowadays a commonly used method for localizing nerves for regional anesthesia, the treatment of chronic pain, and reducing symptoms in many neurological disorders, like eliminating involuntary muscle activity in multiple sclerosis.

Nerve impulses can be seen as the transmission of information along nerve fibers, which may trigger events to communicate with a different cell via chemical (synapse) or electrical (gap junction) signals. It is the way a nerve cell communicates with another cell and makes it act. For example, a signal from the nerve cell might make a muscle cell to contract. Any disorder in the nervous system can result in a range of symptoms, which include chronic pain, poor coordination, and loss of sensation. Electrical stimulation, applied using implanted or surface electrodes, sometimes can avoke neuron activity, which may restore the lost functions of the patients or relieve certain symptoms (Wahls, Reese, Kaplan, & Darling, 2010).

Neurological diseases might be caused by various factors, as genetic factors, nerve injuries, environmental issues, or even malnutrition, but many of them have common features—they are often difficult to identify and treat, and there is a clear need of new non-invasive diagnose techniques as well as alternative treatment methods. For example, in multiple sclerosis the immune system attacks the myelin sheath covering nerve fibers and causes communication problems between the brain and the rest of the body. Though there is no cure for multiple sclerosis and the cause is not known, it has been documented that electrical stimulation leads to the augmentation of myelin development (Li & Li, 2017), and helps also, for example, people with foot drop walk more normally (Wahls et al., 2010).

To be able to simulate nerve electrical stimulation, one needs a suitable model. The process of excitability of nerve fibers and a mathematical model for the electrical currents across the axon membrane was first properly studied in the famous work of Alan Lloyd Hodgkin and Andrew Fielding Huxley (Hodgkin & Huxley, 1952), later on to be rewarded the Nobel Prize in Physiology or Medicine jointly with Sir John Carew Eccles.
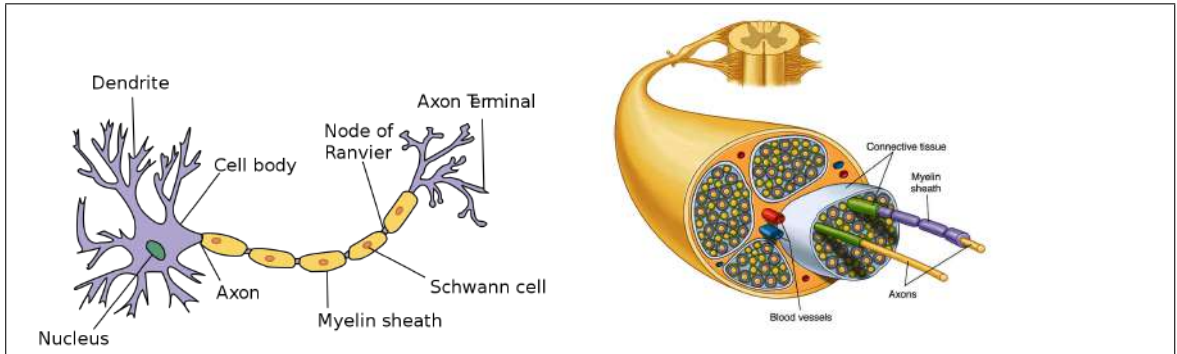
FIGURE 1-1. Typical structure of a single myelinated neuron and a nerve. Sources: "Anatomy and Physiology" by the US National Cancer Institute's Surveillance, Epidemiology and End Results (SEER) Program; www.tabers.com

1.1.1. Single axon modeling

A typical nerve contains several grouped fascicles, each of them containing many axons (see Figure 1-1). The jump of the potential across the membrane, i.e. the transmembrane potential or nerve impulse, of each individual axon can be modeled in the framework of the Hodgkin-Huxley model, but the complex microstructure of the tissue as a whole presents an obvious problem for those attempting to describe its macroscopic response to the electrical stimulation. In order to model and simulate the nerve fiber response to electrical stimulation, one needs to know both how signals propagate along single neurons and how they influence each other in a bundle of axons.

When it comes to individual axons, a commonly adopted model for signal propagation is the so-called *cable equation*:

$$\frac{\partial V}{\partial t} = D\frac{\partial^2 V}{\partial x^2} + f(t, V), \tag{1.1}$$

where $V(t, x)$ is the membrane potential, D is the diffusion coefficient, and f is a continuous function representing the reaction term, depending on both membrane potential and time. Note that it is a one-dimensional—in space variable—partial differential equation, which is much easier to solve and analyze than a corresponding 3D model.

A classical cable equation is derived by modeling dendrites and axons as cylinders composed of segments with capacitances and resistances combined in parallel (Rattay, 1990; P. Basser, 1993; Meffin et al., 2014). The resistances of the cable equation can be modeled as nonlinear resistors using the Hodgkin-Huxley mathematical formulation, and the coefficients in equation (1.1) depend on the membrane resistances and capacitance of Ranvier nodes and internodes—myelinated parts—, as well as on the length of nodes and internodes. In (McIntyre, Richardson, & Grill, 2002), the authors present a computer-based model for myelinated axons reproducing a wide range of experimental data. The models developed in this study use an explicit representation of the Ranvier nodes, paranodal, and internodal sections of the axon—21 nodes of Ranvier separated by 20 internodes— as well as a finite impedance myelin sheath. The result is the accurate adjustment of the Hodgkin-Huxley model to the experimental data.

Since classical continuum cable models are derived modeling neurons as electrical circuits, the one-dimensional cable equation does not contain any information about the geometry of the myelin sheath, of the axon itself, and, consequently is not able to predict the effect of myelin defects on the impulse propagation. In the recent work (Jerez-Hanckes, Pettersson, & Rybalko, 2020), the authors derived a one-dimensional nonlinear cable equation describing one single axon in the absence of external stimulation. In order to trace the dependence of the time and space constants on the microstructure of neurons, a finite resistivity of the myelin was assumed. In contrast to the case when myelin is assumed to be a perfect insulator, the non-zero conductivity of the myelin sheath leads to the appearance of an additional potential in the effective cable equation. This potential depends on the geometry of the myelin sheath and on the conductivities of intra- and extracellular space.

The main contribution of Chapter 3 is the derivation of a one-dimensional nonlinear cable equation for a single myelinated axon in the case of a varying cross-section and infinite resistivity of the myelin. Assuming the homogeneous Neumann boundary conditions on the myelin surface, we show that the geometrical assumptions on the myelin sheath such as radial symmetry assumption and specific geometry near the points where myelin meets

the intracellular domain, can be suppressed. We perform also numerical computations illustrating the solution of the auxiliary cell problems, as well as analysing how the effective coefficients vary with respect to the area of the Ranvier nodes.

1.1.2. Axon bundles modeling

Modeling a bundle of axons is more complicated. Traditionally, it was assumed that interactions between neurons (ephaptic interactions) are negligible and neighboring axons do not affect each other by current spread through the extracellular space (Barr & Plonsey, 1992). However, it is now commonly accepted that ephaptic interactions play an important role, for example, in the electrical conductance of the heart (Lin & Keener, 2010) and in the mammalian olfactory system (Bokil, Laaris, Blinder, Ennis, & Keller, 2001). Recently, there has been a revival of interest in ephaptic interactions as they appear to impact brain function at different scales from the synapse to cell networks (Anastassiou, Perin, Markram, & Koch, 2011; Anastassiou & Koch, 2015). Although axon-to-axon effects in myelinated fibers have not been clearly demonstrated, conduction velocity and perhaps other physiological functions may be affected by axon-to-axon impulse coupling, despite the insulating properties of myelin (Binczak, Eilbeck, & Scott, 2001; Henríquez & Jerez-Hanckes, 2018). Further, in tightly packed bundles of unmyelinated fibers, an action potential from one axon may evoke an action potential in a different axon by means of ephaptic coupling, which can play a role in, for example, the olfactory code as the mammalian olfactory nerve presents such anatomical structure (Bokil et al., 2001).

Ephaptic interactions might be modelled by coupling systems of large numbers of cable equations (Bokil et al., 2001; Binczak et al., 2001), but a continuous mathematical model would facilitate the numerical simulations.

The main contribution of Chapter 4 is a rigorous derivation of a continuum model for signal propagation in bundles of myelinated neurons. Namely, we present a rigorous derivation of a macroscopic bidomain model describing the behavior of the electric potential in the fascicle based on the FitzHugh–Nagumo membrane dynamics. The technique used combines the two-scale convergence machinery and the method of monotone operators.

In order to derive continuous models for signal propagation in individual axons and axon bundles, the homogenization methods is used. Let us shortly explain the homogenization method in the situation when we have just one single axon. A more detailed introduction to the homogenization theory is presented in Chapter 3.

Modeling of a myelinated neuron as a thin cylinder with alternating nodes and internodes of small length leads us to an asymptotic analysis problem. Indeed, the thickness of an axon and the distance between two neighboring nodes are of the same order and is very small compared with the length of the axon. That is why it is natural to introduce a small parameter $\varepsilon > 0$, the characteristic size of the microstructure (for example, the relation between the thickness and the length of the axon). The unknown potential solving a coupled system of nonlinear partial differential equations will then depend on ε, and to derive a simplified equation, one asks what happens with the domain and with the equations when the domain shrinks into a segment and, at the same time, the microstructure (alternating nodes and internodes) becomes finer and finer. Since the distance between the Ranvier nodes is approximately the same, one can assume that the microstructure is periodic, and try to look for the unknown functions (extra- and intracellular potentials, the potential in the myelin, and the transmembrane potential) in the form of the ansatz

$$u_\varepsilon = u_0(x_1) + \varepsilon u_1\big(x_1, \frac{x}{\varepsilon}\big) + \varepsilon^2 u_2\big(x_1, \frac{x}{\varepsilon}\big) + \dots,$$

where the functions u_k depend periodically on the second variable (much "easier" dependence on ε). The fact that the domain is thin and shrinks to a segment yields the dependence on x_1 only in the first (slow) variable. Substituting this ansatz into the three-dimensional problem describing the potential distribution for an axon placed in an extracellular space, and equating coefficients in front of different powers of ε one gets a cascade of equations for the unknown functions u_k. The equation satisfied by the leading term of the asymptotics u_0 is called the effective (homogenized) equation. The form of the effective equation as well as the domain where it is stated is different from the original ones. What is, however, important is that a certain (finite) number of terms in the ansatz is close in some norm to the original solution. To make the whole procedure rigorous, one should prove the

well-posedness of both original and effective problems, as well as the convergence of the solutions of the original problem to the solution of the effective problem. This constitutes the asymptotic analysis (or homogenization) of the problem; see, e.g. (V. Marchenko & Khruslov, 2006; Bensoussan, Lions, & Papanicolaou, 2011; Allaire, 1992).

1.2. Cell electropermeabilization modeling

Electropermeabilization designates the use of short high-voltage or electric field pulses to overcome the barrier of the cell membrane to increase its permeability (Kotnik, Rems, Tarek, & Miklavčič, 2019; Rols, 2006). This process is used to deliver therapeutic molecules, such as drugs and genes, into cells to treat cancer, perform genetic engineering, screen drugs, among others applications; see (Kim & Lee, 2017) or (Choi, Khoo, & Hur, 2022, Section 4), among other references.

Theoretically, several models having proposed to explain the reversible membrane electropermeabilization mechanism and its potentiality to allow the access of non-permeant molecules into the cell. However, no model has yet been rigorously proven to explain the phenomenon. For instance, during electropermeabilization it is thought that aqueous pores are formed along the membrane cell—a process known as electroporation—thereby increasing the permeability of the membrane. Yet, this has not been experimentally observed to occur for the voltage values commonly employed. The pores are too small to be observed by optical microscopy and too fragile for electron microscopy. Only molecular dynamics simulations have been able to provide a corroboration of the pore formation (Kotnik et al., 2019, Section 3), (Choi et al., 2022, Section 2.1). Moreover, the application of external electric pulses triggers other physical and chemical cell mechanisms, many of them not fully understood, with complex interactions at multiple length scales, from nanometers at the cell membrane to centimeters in tissues (Kotnik et al., 2019). "Therefore, while the term electroporation is commonly used among biologists, the term electropermeabilization should be preferred in order to prevent any molecular description of the phenomenon" (Rols, 2006).

Still, mathematical models and numerical methods have been used to gain a better understanding of the different underlying phenomena. For instance, Neu and Krassowska (J. C. Neu & Krassowska, 1999) consider a electroporation process by modeling the nanoscale phenomena involved in the creation and resealing of the cell membrane pores, and applying homogenization theory leading to nonlinear time dynamics occurring at the membrane. Well-posedness of the Neu-Krassowska model and a new model including anisotropies are derived in (Ammari, Widlak, & Zhang, 2016). Alternatively, in (Kavian et al., 2014) the authors propose a phenomenological model that forgoes the ab initio understanding of the mechanisms involved, leading to a dynamical model with parameters inferred experimentally. A more complete phenomenological model considers two different stages in the electroporation process, conducting and permeable (Leguèbe, Silve, Mir, & Poignard, 2014). This model also takes into account the diffusion and electric transport of non-permeable molecules. In (Guittet, Poignard, & Gibou, 2017; Mistani et al., 2019), the authors discard particle diffusion and transport in (Leguèbe et al., 2014) to then apply the Voronoi Interface Method (Guittet, Lepilliez, Tanguy, & Gibou, 2015) for its computational approximation. Specifically, they construct a Voronoi mesh of the volume which when coupled to a ghost fluid method (Liu, Fedkiw, & Kang, 2000) is able to capture discontinuous boundary conditions. Further enhancements via parallelization are given in (Mistani et al., 2019).

In Chapter 5, we apply the local Multiple Traces Formulation (MTF) (Hiptmair & Jerez-Hanckes, 2012) to reduce the problem to boundary integral equations on cell membranes. We simulate the electric potential response of a fixed number of disjoint cells in three dimensions when they are subject to electric pulses. Spatially, the boundary unknowns are approximated by spherical harmonics, thereby allowing for spectral convergence rates. The nonlinear dynamics of the cell membrane follow (Kavian et al., 2014).

2. THEORY AND METHODS

2.1. Homogenization theory

In this section, we describe briefly the history and the main concepts of the homogenization theory, which is used in Papers A and B for multiscale modeling of myelinated axons.

The mathematical theory of homogenization is a rigorous version of what is known in mechanics as averaging. The main goal is to describe macroscopic (or effective) properties of heterogeneous media. In a classical setting, one deals with some physical processes in media with periodic microstructure. If the period of the microstructure is much smaller than the size of a sample of the heterogeneous material, one can introduce a small parameter $\varepsilon > 0$ as the ratio of these two scales. After that, the asymptotic analysis, as $\varepsilon \to 0$, is used in order to derive the limit problem. The last, so-called homogenized problem, is stated in a domain without microstructure, and, thus, is often easier to analyze numerically. In other words, instead of analyzing one problem with a fixed ratio between the microstructure period and the sample size, one considers a sequence of problems, parametrized by ε, and pass to the limit as $\varepsilon \to 0$ to derive a suitable approximation for the solutions in the heterogeneous medium. One should ensure that a solution of the original problem is close in some sense to a solution of the effective problem.

Interesting enough, in 1826, Poisson (Poisson, 1821) derived the effective conductivity for a non-conductive matrix with conductive spherical inclusions. Also Maxwell (Maxwell, 1873) studied the effective conductivity of an array of spherical inclusions with different conductivity i a matrix. The homogenization theory in the form it exists now started in the 60s. Marchenko and Khruslov (V. A. Marchenko & Khruslov, 1964) studied a Dirichlet problem in domains with fine grained boundary. Their technique is based on the notion of capacity and convergence of functionals. The effective conductivity of the checkerboard was proved to be the geometric mean of the two conductivities by Keller in (Keller, 1964). Time dependent problems were first considered by Freidlin in (Freidlin, 1964), where the

author used probabilistic techniques. After these works the homogenization theory developed very rapidly, and it was applied to both stationary and time-dependent problems, systems of equations, higher-order differential operators, in periodic, non-periodic, and stochastic setting. We refer to (Bakhvalov & Panasenko, 1989), (Bensoussan et al., 2011), (Jikov, Kozlov, & Oleinik, 2012). The Γ-convergence technique efficiently used to treat nonlinear problems was introduced by De Giorgi (De Giorgi & Spagnolo, 1979). In Papers A and B we use the two-scale convergence technique introduced by Nguetseng (Nguetseng, 1989) and developed by Allaire (Allaire, 1992).

One important contribution of the homogenization theory is a rigorous derivation of the effective coefficients reflecting the macroscopic properties of the heterogeneous media. Let us consider a one-dimensional example where the effective coefficients can be computed explicitly as the geometric average of the original coefficient.

Given $f \in L^2(\Omega)$, let u_ε be a unique solution of

$$\frac{d}{dx}\Big(a\big(\frac{x}{\varepsilon}\big)\frac{du_\varepsilon}{dx}\Big) = f(x) \text{ in } (0,1), \tag{2.1}$$

$$u_\varepsilon(0) = u_\varepsilon(1) = 0,$$

where $0 < \alpha \leq a(y) \leq C$ is 1-periodic. Next proposition provides the homogenization result for this problem. The proof is classical, and can be found, for example, in (Jikov et al., 2012).

PROPOSITION 2.1. *Let u_ε be a unique solution of (2.1). Then u_ε converges weakly to u_0 in $H_0^1(0,1)$ where u_0 is a unique solution to the following homogenized (effective) problem:*

$$\frac{d}{dx}\Big(a_0\frac{du_0}{dx}\Big) = f(x) \text{ in } (0,1), \tag{2.2}$$

$$u_0(0) = u_0(1) = 0,$$

with $a_0 = \langle a^{-1}\rangle^{-1} = \big(\int_0^1 a(y)^{-1}\,dy\big)^{-1}$.

PROOF. The first step is to derive a priori estimates. To this end, we multiply (2.1) by u_ε and integrate by parts. By the positivity of the coefficient $a(y) \geq \alpha > 0$ and the Schwartz inequality, we have

$$\alpha \| \frac{du_\varepsilon}{dx} \|^2_{L^2(0,1)} \leq \int_0^1 a\left(\frac{x}{\varepsilon}\right) \left| \frac{du_\varepsilon}{dx} \right|^2 dx \leq \|f\|_{L^2(0,1)} \|u_\varepsilon\|_{L^2(0,1)} \leq C \| \frac{du_\varepsilon}{dx} \|_{L^2(0,1)},$$

$$\| \frac{du_\varepsilon}{dx} \|_{L^2(0,1)} \leq C.$$

Note that, since u_ε satisfies the homogeneous Dirichlet condition on the boundary of Ω, by the Friedrichs inequality $\|u_\varepsilon\|_{L^2(0,1)} \leq \| \frac{du_\varepsilon}{dx} \|$, u_ε is uniformly bounded in $H^1_0(0,1)$ and thus, up to a subsequence, has a weak limit $u_0 \in H^1_0(0,1)$.

In the next step we identify the limit u_0. Integrate (2.1) from 0 to x:

$$a\left(\frac{x}{\varepsilon}\right) \frac{du_\varepsilon}{dx} = \int_0^x f(\xi)d\xi + c_\varepsilon = F(x) + c_\varepsilon,$$

$$\frac{du_\varepsilon}{dx} = a\left(\frac{x}{\varepsilon}\right)^{-1} (F(x) + c_\varepsilon).$$

Both $a(y)$ and $a(y)^{-1}$ are periodic, so $a(x/\varepsilon)^{-1}$ converges to its mean value $\int_0^1 a(y)^{-1}\,dy$, as $\varepsilon \to 0$. Since $u_\varepsilon(0) = u_\varepsilon(1) = 0$, we have

$$0 = \int_0^1 \frac{du_\varepsilon}{dx} dx = \int_0^1 a\left(\frac{x}{\varepsilon}\right)^{-1} (F(x) + c_\varepsilon)dx \xrightarrow[\varepsilon \to 0]{} \langle a^{-1} \rangle \int_0^1 F(x)dx + \langle a^{-1} \rangle \lim_{\varepsilon \to 0} c_\varepsilon.$$

Therefore

$$\lim_{\varepsilon \to 0} c_\varepsilon = -\int_0^1 F(x)dx.$$

In this way, we have the following weak limits in $L^2(\Omega)$:

$$\lim_{\varepsilon \to 0} a\left(\frac{x}{\varepsilon}\right) \frac{du_\varepsilon}{dx} = F(x) - \int_0^1 F(x)dx,$$

$$\lim_{\varepsilon \to 0} \frac{du_\varepsilon}{dx} = \langle a^{-1} \rangle \left(F(x) - \int_0^1 F(x)dx \right) \equiv \frac{du_0}{dx}.$$

Multiplying by $\langle a^{-1} \rangle^{-1}$ and differentiating both sides of the equality, we obtain

$$\langle a^{-1} \rangle^{-1} \frac{du_0}{dx} = F(x) - \int_0^1 F(x)dx \quad \Rightarrow \quad \frac{d}{dx}\left(\langle a^{-1} \rangle^{-1} \frac{du_0}{dx}\right) = f(x).$$

Proposition 2.1 is proved.

$\square$

The formula $a_0 = \langle a^{-1} \rangle^{-1}$ for the effective conductivity can be understood intuitively in terms of electrostatics. Indeed, given two resistors connected in series, the effective conductance is known to be the geometric average $C^{\text{eff}} = (C_1^{-1} + C_2^{-1})^{-1}$ (see Figure 2-1). At the same time, the formula for the effective conductivity in a one-dimensional heterogeneous material with a piecewise constant conductivity $a(x/\varepsilon)$, as illustrated in Figure 2-2, gives $a_0 = 2(a_1^{-1} + a_2^{-1})^{-1}$.
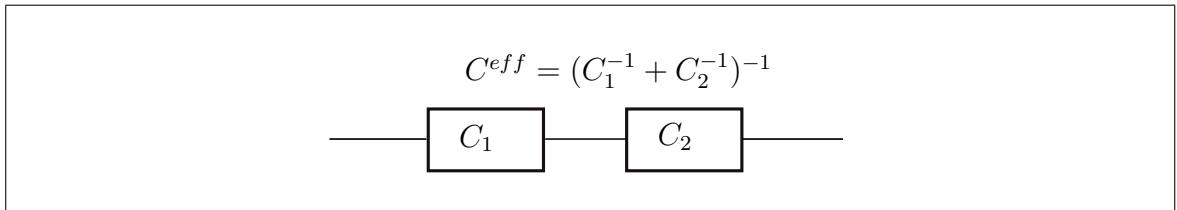
FIGURE 2-1. Resistors in series and effective conductance
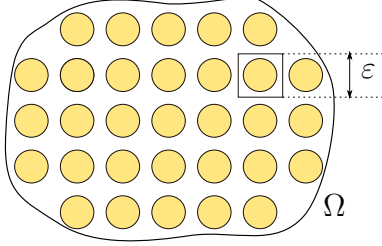
FIGURE 2-2. 1D-heterogeneous material with periodic conductivity $a(x/\varepsilon)$

The next step is to formulate a similar problem in higher dimensions, to derive the effective coefficients and the macroscopic problem.

Let us consider a model problem of finding the effective conductivity of a composite material consisting of two different homogeneous materials, where the matrix (background material) has a large number of periodically distributed inclusions.

Given a bounded domain $\Omega \subset \mathbb{R}^n$ with a smooth boundary $\partial\Omega$, consider the following Dirichlet problem for a stationary heat equation in the domain with inclusions:

$$-\text{div}\big(\sigma\big(\tfrac{x}{\varepsilon}\big)\nabla u_\varepsilon\big) = f(x) \qquad \text{in } \Omega, \quad (2.3)$$

$$u_\varepsilon = 0 \qquad \text{on } \partial\Omega.$$

We assume that the conductivity $\sigma(y) > \sigma_0 > 0$ is a $\square$-periodic function, where $\square = [0,1)^n$ is the periodicity cell. The positive parameter ε represents the size of the microstructure, that is the scale on which the properties of the medium change. One can think about a perforated domain or a domain with inclusions.

We want to understand how u_ε behaves for small ε, i.e. for ε much smaller than the size of the domain.

The first method used for such kind of problems, used long before the rigorous homogenization techniques had been designed, is the method of formal asymptotic expansions. We postulate the following two-scale asymptotic ansatz:

$$u_\varepsilon(x) \sim u_0\big(x, \tfrac{x}{\varepsilon}\big) + \varepsilon u_1\big(x, \tfrac{x}{\varepsilon}\big) + \varepsilon u_2\big(x, \tfrac{x}{\varepsilon}\big) + \ldots . \qquad (2.4)$$

Each term $u_i(x, y)$ is assumed to be $\square$-periodic function in y. The chain rule yields

$$\nabla u_i\big(x, \tfrac{x}{\varepsilon}\big) = \big(\nabla_x u_i(x, y) + +\varepsilon^{-1}\nabla_y u(x, y)\big)\Big|_{y=\frac{x}{\varepsilon}}$$

Now we substitute (2.4) into (2.3) and equate the coefficients in front of different powers of ε:

$$\varepsilon^{-2}: \qquad\qquad\qquad\qquad\qquad\qquad\qquad -\text{div}_y(\sigma\nabla_y u_0) = 0$$

$$\varepsilon^{-1}: \qquad\qquad\qquad -\text{div}_y(\sigma\nabla_y u_1) = \text{div}_y(\sigma\nabla_x u_0) + \text{div}_x(\sigma\nabla_y u_0)$$

$$\varepsilon^{0}: \qquad -\text{div}_y(\sigma\nabla_y u_2) = \text{div}_y(\sigma\nabla_x u_1) + \text{div}_x(\sigma\nabla_y u_1) + \text{div}_x(\sigma\nabla_x u_0) + f(x)$$

. . .

All the problems are stated on the periodicity cell, and the Fredholm alternative holds. The first problem is well-posed, and it has a unique, up to an additive constant, solution which is constant in y, so $u_0(x, y) = u_0(x)$. The second problem is obviously solvable since the right-hand side is orthogonal to the kernel of the formally adjoint operator (consisting of constants):

$$\int_\Omega \mathrm{div}_y(\sigma(y)\nabla_x u_0)\, dy = 0.$$

Applying the Fredholm alternative to the last problem for u_2, we conclude that there exists a periodic in y, defined up to an additive constant, function $u_2 \in H^1_{per}(\square)$ if and only if

$$-\mathrm{div}\Big(\int_\square \sigma(y)(\nabla_y u_1 + \nabla_x u_0)dy\Big) = f(x), \quad x \in \Omega.$$

In this way, we get a coupled system

$$-\mathrm{div}_y(\sigma\nabla_y u_1) = \mathrm{div}_y(\sigma\nabla_x u_0), \quad y \in \square,\ x \in \Omega, \tag{2.5}$$

$$-\mathrm{div}\Big(\int_\square \sigma(y)(\nabla_y u_1 + \nabla_x u_0)dy\Big) = f(x), \quad x \in \Omega. \tag{2.6}$$

Looking for a solution of (2.5) in the form of the right-hand side, we set

$$u_1(x, y) = N(y) \cdot \nabla u_0(x) + v_1(x),$$

where $N(y)$ is $\square$-periodic vector valued function. The problems for N_i are called cell problems:

$$-\mathrm{div}\,\sigma(y)(e_i + \nabla_y N_i(y)) = 0 \quad \text{in } \square, \tag{2.7}$$

$$N_i \text{ is } \square\text{-periodic}.$$

From (2.6) we obtain the homogenized equation:

$$-\operatorname{div}(\sigma^{\text{eff}}\nabla u_0) = f(x) \quad \text{in } \Omega, \tag{2.8}$$

$$u_0 = 0 \quad \text{on } \partial\Omega,$$

where, due to (2.7), the effective conductivity σ^{eff} is defined by

$$\sigma_{ij}^{\text{eff}} = \int_{\square} \sigma(y)(e_j + \nabla N_j) \cdot (e_i + \nabla N_i)dy. \tag{2.9}$$

In this way, we have reduced a problem stated in a complex heterogeneous media to two simpler ones: one problem with constant coefficients σ^{eff} stated in Ω, and a cell problem on the periodicity cell $\square$. The solution u_ε is then approximated by $U_\varepsilon(x) = u_0(x) + \varepsilon N\left(\frac{x}{\varepsilon}\right) \cdot \nabla u_0(x)$.

These computations are, however, formal, and one needs to prove the convergence of the solutions u_ε to u_0. One way is to insert the difference $u_\varepsilon - U_\varepsilon$ into the original problem, estimate the right-hand side (will be small, as $\varepsilon \to 0$), and finally use the a priori estimates to obtain an estimate for the norm of the difference $u_\varepsilon - U_\varepsilon$. This method requires, however, high regularity of the data, and is therefore not appropriate for problems with discontinuous data.

Let us illustrate how the two-scale convergence technique (Nguetseng, 1989), (Allaire, 1992) works in our example (2.3). The weak formulation for problem (2.3) reads: Find $u(x) \in H_0^1(\Omega)$ such that

$$\int_{\Omega} \sigma\left(\frac{x}{\varepsilon}\right)\nabla u_\varepsilon \cdot \nabla \varphi(x)\, dx = \int_{\Omega} f(x)\varphi(x)\, dx, \quad \forall \varphi \in H_0^1(\Omega).$$

To approximate u_ε for small ε, we pass to the limit, as $\varepsilon \to 0$.

The first step, as in the one-dimensional case, is to obtain a priori estimates. We multiply (2.3) by u_ε, integrate by parts, and use the positiveness of σ:

$$\alpha\|\nabla u_\varepsilon\|_{L^2(\Omega)}^2 \leq \int_{\Omega} \sigma\left(\frac{x}{\varepsilon}\right)|\nabla u_\varepsilon|^2 dx = \int_{\Omega} f(x)u_\varepsilon(x)\, dx$$

$$\leq \|f\|_{L^2(\Omega)}\|u_\varepsilon\|_{L^2(\Omega)} \quad \text{(Cauchy-Schwartz inequality)}$$

$$\leq C\|f\|_{L^2(\Omega)}\|\nabla u_\varepsilon\|_{L^2(\Omega)} \quad \text{(Poincaré inequality)}.$$

Now we divide both sides by $\alpha\|\nabla u_\varepsilon\|$ and obtain a uniform in ε estimate $\|\nabla u_\varepsilon\|_{L^2(\Omega)} \leq C$. Due to the Poincaré inequality, u_ε is uniformly bounded in $H_0^1(\Omega)$, and thus, u_ε, up to a subsequence, has a weak limit $u_0 \in H_0^1(\Omega)$.

Next step is to pass to the limit in the weak formulation. To this end, we prove the so-called averaging lemma, that gives the convergence of a periodically oscillating function to its average.

Lemma 2.1 (Averaging Lemma). *Let $\Omega \subset \mathbf{R}^d$ be bounded, and $g \in L^2_{loc}(\mathbf{R}^d)$ be $\Box$-periodic, then*

$$g\left(\frac{x}{\varepsilon}\right) \rightharpoonup \langle g \rangle = \frac{1}{|\Box|} \int_\Box g(y)dy \quad \text{weakly in } L^2(\Omega) \text{ as } \varepsilon \to 0. \tag{2.10}$$

Proof.

We start by proving that $g(x/\varepsilon)$ is uniformly bounded in $L^2(\Omega)$. Let us divide Ω into (small) cells $\Box_i^\varepsilon = \varepsilon\Box + x_i^\varepsilon$, translations of the rescaled cells $\varepsilon\Box$ to points $x_i^\varepsilon \in \varepsilon\mathbf{Z}^d \cap \Omega$. Then,

$$\int_\Omega \left|g\left(\frac{x}{\varepsilon}\right)\right|^2 dx = \sum_i \int_{\Box_i^\varepsilon \cap \Omega} \left|g\left(\frac{x}{\varepsilon}\right)\right|^2 dx \leq \frac{C}{\varepsilon^d} \int_\Box |g(y)|^2 dy = C\|g\|_{L^2(\Box)}^2.$$

Thus, $g(x/\varepsilon)$ converges weakly in $L^2(\Omega)$ to some limit, as $\varepsilon \to 0$.

The next step is to identify the limit of $g(x/\varepsilon)$. For $\varphi \in C_0^\infty(\Omega)$, consider piecewise constant interpolation $\varphi_\varepsilon(x) = \varphi(x_i^\varepsilon)$, $x \in \Box_i^\varepsilon$. One can show that $\|\varphi - \varphi_\varepsilon\|_{L^2(\Omega)} \to 0$, $\varepsilon \to 0$. For piecewise constant functions we have

$$\int_\Omega g\left(\frac{x}{\varepsilon}\right)\varphi_\varepsilon(x)dx = \sum_i \int_{\Box_i^\varepsilon} g\left(\frac{x}{\varepsilon}\right)\varphi_i^\varepsilon(x)dx = \langle g \rangle \int_\Omega \varphi_\varepsilon(x)dx.$$

For arbitrary $\varphi \in C_0^\infty(\Omega)$ we add and subtract its piecewise constant approximation and obtain

$$\int_\Omega g\left(\frac{x}{\varepsilon}\right)\varphi(x)dx = \int_\Omega g\left(\frac{x}{\varepsilon}\right)(\varphi - \varphi_\varepsilon)dx + \int_\Omega g\left(\frac{x}{\varepsilon}\right)\varphi_\varepsilon(x)dx$$

$$\to \langle g \rangle \int_\Omega \varphi(x)dx, \quad \varepsilon \to 0.$$

since

$$\int_\Omega |g\left(\frac{x}{\varepsilon}\right)(\varphi - \varphi_\varepsilon)|dx \le C\|g\|_{L^2(\square)}\|\varphi - \varphi_\varepsilon\|_{L^2(\Omega)} \to 0$$

$$\langle g \rangle \int_\Omega \varphi_\varepsilon(x)dx \to \langle g \rangle \int_\Omega \varphi(x)dx, \quad \varepsilon \to 0.$$

The proof of the averaging lemma is complete.

We turn back to the weak formulation of (2.3):

$$\int_\Omega \sigma\left(\frac{x}{\varepsilon}\right)\nabla u_\varepsilon \cdot \nabla\varphi(x)\,dx = \int_\Omega f(x)\varphi(x)\,dx, \quad \varphi \in H_0^1(\Omega).$$

Thanks to the averaging lemma, $\sigma\left(\frac{x}{\varepsilon}\right) \rightharpoonup \langle \sigma \rangle$ in $L^2(\Omega)$. Due to the a priori estimates, $\nabla u_\varepsilon \rightharpoonup \nabla u_0$ in $L^2(\Omega)$. However, we will see

$$\sigma\left(\frac{x}{\varepsilon}\right)\nabla u_\varepsilon \quad \text{does not converge to} \quad \langle \sigma \rangle \nabla u_0 \quad \text{in } L^2(\Omega)^d.$$

The main obstacle in passage to the limit is the lack of strong convergence for oscillating functions. Two-scale convergence, in contrast to weak convergence, takes into account oscillations of the function. The definition is given below.

Definition 2.1. $u_\varepsilon \in L^2(\Omega)$ *is said to two-scale converge* $u_0(x,y) \in L^2(\Omega \times \square)$ *if* $\|u_\varepsilon\|_{L^2(\Omega)} < C$, *and, for any* $\varphi(x,y) \in C_0^\infty(\Omega; C_{per}^\infty(\square))$, *it satisfies*

$$\lim_{\varepsilon \to 0} \int_\Omega u_\varepsilon(x)\varphi\left(x, \frac{x}{\varepsilon}\right)dx = \frac{1}{|\square|}\int_\Omega \int_\square u_0(x,y)\varphi(x,y)\,dy\,dx. \tag{2.11}$$

The proof of the next lemma can be found in (Allaire, 1992).

Lemma 2.2. *Compactness theorem If* $\|u_\varepsilon\|_{L^2(\Omega)} < C$, *then it contains a subsequence that two-scale converges to some* $u_0(x, y) \in L^2(\Omega \times \square)$, *as* $\varepsilon \to 0$.

Moreover, it can be proved (see (Allaire, 1992)) that

(i) For any smooth $u(x, y)$ periodic in y we have $u(x, \frac{x}{\varepsilon}) \xrightarrow{2} u(x, y)$.

(ii) If $u_\varepsilon \to u(x)$ strongly in $L^2(\Omega)$, then $u_\varepsilon(x) \xrightarrow{2} u(x)$.

(iii) If $u_\varepsilon(x) \xrightarrow{2} u_0(x, y)$, then $u_\varepsilon \rightharpoonup \dfrac{1}{|\square|} \displaystyle\int_\square u_0(x, y) dy$.

The above formulated properties are used when passing to the limit in integral equalities.

The example below illustrates the relations between the strong, weak, and two-scale convergence.

Example 2.1. *Consider a rapidly oscillating function* $\sin(x/\varepsilon)$. *It is* $2\pi\varepsilon$-periodic and *converges weakly to its average* $\sin\left(\frac{x}{\varepsilon}\right) \rightharpoonup \langle\sin(y)\rangle = 0$. *On the other hand, by the properties of the two-scale convergence,* $\sin\left(\frac{x}{\varepsilon}\right) \xrightarrow{2} \sin(y)$. *Thus, the two-scale convergence captures the oscillations which are averaged out when passing to the weak limit.*

Consider now another sequence $(-1)^n \sin(nx)$ *with* $n = 1/\varepsilon$. *It converges weakly to* $\langle\sin(y)\rangle = 0$, *but* $u_{2k} \xrightarrow{2} \sin(y)$ *and* $u_{2k+1} \xrightarrow{2} -\sin(y)$, *so the two-scale limit does not exist.*

Applying the two-scale convergence technique to problem (2.3), we obtain the effective problem (2.8). The passage to the limit relies on a clever choice of test functions. In Chapter 4 and (5) we will apply this technique to a time-dependent nonlinear problem. The method of formal asymptotic expansions serves often as a practical tool to make a right choice of test functions, which is illustrated in the appendix in Chapter 4.

2.2. Monotonicity method

The passage to the limit in the nonlinear microscopic problem requires us to adapt the method of monotone operators due to G. Minty (Minty, 1962). The monotonicity method is applied for passing to the limit in the microscopic problem in Chapter 4. The construction of test functions and the proof itself is quite technical, and in order to extract the main idea of the method we provide its brief description for a model case when the monotone operator is independent of ε. In (Allaire, 1992), it is shown how to combine the method of monotone operators and the two-scale convergence for a toy stationary problem.

Let A be a nonlinear continuous monotone operator in a Hilbert space H. The scalar product in H will be denoted by (u, v). We consider a parabolic problem

$$\partial_t u_\varepsilon + A(u_\varepsilon) = f_\varepsilon, \tag{2.12}$$

$$u_\varepsilon\big|_{t=0} = V_\varepsilon^0.$$

Assume that we know that u_ε converges weakly to u_0, $\partial_t u_\varepsilon$ converges weakly to $\partial_t u_0$, and $f_\varepsilon, V_\varepsilon^0$ converge strongly in H to f and V^0, respectively, as $\varepsilon \to 0$. We aim to show that u_0 satisfies the limit equation $\partial_t u_0 + A(u_0) = f$. Note that, because of the weak convergence, we cannot pass to the limit in the nonlinear term $A(u_\varepsilon)$ directly.

By monotonicity, for any $w_1, w_2 \in D(A)$, one has

$$(A(w_1) - A(w_2), w_1 - w_2) \geq 0.$$

Taking $w_1 = u_\varepsilon$, $w_2 = u_0 + \delta\varphi$, with $\delta \in \mathbb{R}$ and $\varphi \in C^1([0, T]; D(A))$, and using (2.12), we get

$$0 \leq \int_0^t (A(u_\varepsilon) - A(u_0 + \delta\varphi), u_\varepsilon - (u_0 + \delta\varphi))d\tau.$$

$$= \int_0^t (f_\varepsilon, u_\varepsilon - (u_0 + \delta\varphi))d\tau - \int_0^t (\partial_\tau u_\varepsilon, u_\varepsilon)d\tau + \int_0^t (\partial_\tau u_\varepsilon, (u_0 + \delta\varphi))d\tau. \tag{2.13}$$

$$- \int_0^t (A(u_0 + \delta\varphi), u_\varepsilon - (u_0 + \delta\varphi))d\tau.$$

Integrating by parts, we get

$$\int_0^t (\partial_\tau u_\varepsilon, u_\varepsilon)d\tau = \frac{1}{2}\int_0^t \frac{d}{d\tau}\|u_\varepsilon\|_H^2 d\tau = \frac{1}{2}\|u_\varepsilon(t,\cdot)\|_H^2 - \frac{1}{2}\|V_\varepsilon^0\|_H^2.$$

Then inequality (2.13) transforms into

$$\begin{aligned}
&\frac{1}{2}\|u_\varepsilon(t,\cdot)\|_H^2 - \frac{1}{2}\|u_0(t,\cdot)\|_H^2 - \frac{1}{2}\|V_\varepsilon^0\|_H^2 + \frac{1}{2}\|V^0\|_H^2 \\
&\leq \int_0^t (f_\varepsilon, u_\varepsilon - (u_0 + \delta\varphi))d\tau - \int_0^t (\partial_\tau u_0, u_0)d\tau \\
&+ \int_0^t (\partial_\tau u_\varepsilon, (u_0 + \delta\varphi))d\tau - \int_0^t (A(u_0 + \delta\varphi), u_\varepsilon - (u_0 + \delta\varphi))d\tau.
\end{aligned} \tag{2.14}$$

Passage to the limit, as $\varepsilon \to 0$, in (2.14) yields

$$\begin{aligned}
0 &\leq \frac{1}{2}\limsup_{\varepsilon\to 0}\left(\|u_\varepsilon(t,\cdot)\|_H^2 - \|u_0(t,\cdot)\|_H^2\right) \\
&\leq \delta \int_0^t (-f + \partial_\tau u_0 + A(u_0 + \delta\varphi), \varphi)d\tau.
\end{aligned}$$

Since the left-hand side is positive and δ is arbitrary, that delivers the strong convergence of u_ε

$$\limsup_{\varepsilon\to 0}\left(\|u_\varepsilon(t,\cdot)\|_H^2 - \|u_0(t,\cdot)\|_H^2\right) = 0.$$

Furthermore,

$$\int_0^t (\partial_\tau u_0 + A(u_0 + \delta\varphi) - f, \delta\varphi)d\tau \geq 0. \tag{2.15}$$

Dividing (2.15) first by $\delta > 0$ and passing to the limit, as $\delta \to 0$, we obtain

$$\int_0^t (\partial_\tau u_0 + A(u_0) - f, \varphi)d\tau \geq 0.$$

Then, dividing (2.15) by $\delta < 0$ and passing to the limit, as $\delta \to 0$, we have the opposite inequality

$$\int_0^t (\partial_\tau u_0 + A(u_0) - f, \varphi) d\tau \leq 0.$$

Thus,

$$\int_0^t (\partial_\tau u_0 + A(u_0) - f, \varphi) d\tau = 0.$$

The last equality holds for an arbitrary $\varphi \in C^1(0, T; D(A))$, so $\partial_t u_0 + A(u_0) = f$.

This method is used for passing to the limit in the microscopic problem in Chapter 4, where both the domain and the operator A depend on ε, and the test functions have a more complicated two-scale structure.

3. MULTISCALE MODELING OF MYELINATED AXONS

We start from a three-dimensional model for a myelinated neuron suspended in an extracellular medium which includes Hodgkin-Huxley ordinary differential equations to represent the membrane at the Ranvier nodes. Assuming periodic microstructure with alternating myelinated parts and Ranvier nodes, we use homogenization methods to derive a one-dimensional nonlinear cable equation describing the potential propagation along the neuron. Since the resistivity of the intracellular and extracellular domains is much smaller than the resistivity of the myelin, we assume that the myelin is a perfect insulator and impose homogeneous Neumann boundary conditions on the boundary of the myelin. In contrast to the case when the conductivity of the myelin is non-zero, no additional terms appear in the one-dimensional limit equation, and the geometry of the model affects the limit solution implicitly through an auxiliary cell problem used to compute the effective coefficient.

The chapter is based on the paper: Jerez-Hanckes, C., Martínez, I. A., Pettersson, I., & Rybalko, V. (2021). Multiscale analysis of myelinated axons. In *Emerging Problems in the Homogenization of Partial Differential Equations* (pp. 17-35). Springer, Cham.

3.1. Introduction

A nerve impulse is the movement of the so-called action potential along a nerve fiber in response to a stimulus such as touch, pain, heat or cold. It is the way nerve cells communicates with another cell so as to generate an adequate response. In their work (Hodgkin & Huxley, 1952), Hodgkin and Huxley gave a plausible explanation of the physiological process behind the excitability of nerve fibers, and provided a phenomenological mathematical model describing electric currents across axon membranes in terms of ions fluxes. The model describes how ionic currents nonlinear dynamic behavior depends on the potential difference across neurons' membranes and so-called *gating variables*, i.e. the probability for different ionic channels to be open or closed. The jump of the potential across the membrane of each individual axon can be modeled in the framework of the

Hodgkin-Huxley (HH) model, but the alternating myelinated and unmyelinated parts of the membrane present an obvious problem for those attempting to describe its macroscopic response to the electrical stimulation. In order to model and simulate the response of biological tissues to electrical stimulation, one needs to know how signals propagate along single neurons and, as the next step, how they influence each other in a bundle of axons.

Signal propagation along a neuron is portrayed by a cable equation usually derived by modeling axons as cylinders composed of segments with capacitances and resistances combined in parallel (Hodgkin & Huxley, 1952; Rall, 1969; Rattay, 1990; P. Basser, 1993; Meffin et al., 2014). The coefficients in such equation depend on the resistances and capacitances of Ranvier nodes and myelinated parts, as well as some geometric parameters of the neuron such as the diameter, nodal and inter-nodal lengths. In (P. Basser, 1993; Meunier & d'Incamps, 2008), the authors apply a formal two-scale expansion to a one-dimensional model in order to show that a myelinated neuron can be approximated by a homogeneous cable equation. However, these works do not consider the derivation of the one-dimensional equation nor they provide any justification of the formal approximations.

We derive a nonlinear cable equation for signal propagation along a myelinated axon under the classical assumption that the conductivity of the myelin is zero, i.e. the myelin is a perfect insulator. This assumption is justified by the fact that the resistivity of the myelin is much larger than the resistivity of intracellular and extracellular domains. This assumption does not lead to the appearance of a potential in the limit equation as in (Jerez-Hanckes et al., 2020). Consequently, in this classical case, we can suppress the geometrical assumptions on the myelin sheath such as radial symmetry assumption and specific features at the points where myelin meets intracellular domain. Our proof is in some sense simpler than the one in (Jerez-Hanckes et al., 2020), but since the intracellular domain is not a straight cylinder any more, an additional cell problem appears (3.13). When the intracellular domain is a straight cylinder –the first component of the normal vector is zero–, the cell problem (3.13) has a trivial constant solution and the effective coefficient coincides with one in (Jerez-Hanckes et al., 2020).

The paper is organized as follows. In Section 3.2, we formulate our model problem and present the main result in Theorem 3.1, with the rest of the paper devoted to its proof. Section 3.3 presents a priori estimates for the potential u_ε and its jump across Ranvier nodes, to then finally derive the one-dimensional effective problem in Section 3.4. Numerical solutions of the auxiliary cell problem and effective coefficient a^{eff} (see (3.11)) are provided in Section 3.5. We also present computational results showing the dependence of the effective coefficient on the length of the Ranvier node and on the angle at which the myelin is attached to the intracellular domain.

3.2. Problem setup

Let us consider a myelinated axon sparsely suspended in an extracellular medium. We assume that the axon has a periodic structure, containing myelinated and unmyelinated parts (nodes of Ranvier) as illustrated on Figure 3-3.

3.2.1. Geometry

Given a bounded Lipschitz domain $\omega \subset \mathbb{R}^2$, we denote by Y (see Figure 3-3) a periodicity cell:

$$Y := \left\{ y = (y_1, y') \in \mathbb{R}^3 : \quad y_1 \in \mathbf{T}^1, \ y' \in \phi(y_1)\omega \right\}.$$

Here, $\mathbf{T}^1$ is the one-dimensional torus and $\phi \in C(\mathbf{T}^1)$. Let also ω_0 be a compact subset of ω in $\mathbb{R}^2$. The intracellular medium is defined as

$$Y_i := \left\{ y = (y_1, y') \in \mathbb{R}^3 : \quad y_1 \in \mathbf{T}^1, \ y' \in \phi_0(y_1)\omega_0 \right\},$$

where $\phi_0 \in C(\mathbf{T}^1)$. We assume that the cell Y is decomposed into two disjoint nonempty subdomains: an intracellular part Y_i and an extracellular medium Y_e as shown in the left-hand side of Figure 3-3. The myelin sheath Y_m – depicted as white areas – is supposed to be perfectly insulating and modelled as voids. The extracellular part of the periodicity cell $Y_e := Y \setminus (Y_i \cup Y_m)$. The functions ϕ_0 and ϕ are supposed to be such that the boundary of Y_i does not touch the boundary of Y.

In case when $\phi(y_1)$ and $\phi_0(y_1)$ are constant, both the intracellular medium Y_i and the periodicity cell have constant cross-sections, while the factors $\phi(y_1), \phi_0(y_1)$ allow the cross-sections to vary.
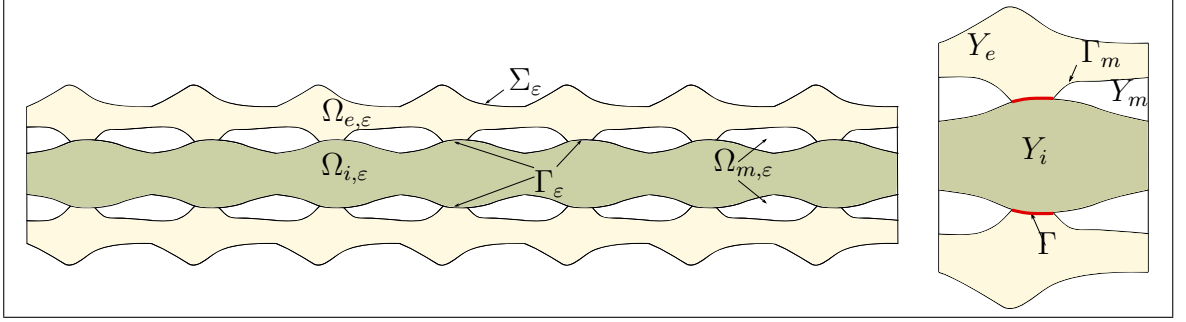
FIGURE 3-1. Simplified geometry of the cross-section of a myelinated axon and the periodicity cell Y.

We denote by Γ_m the boundary of the myelin sheath, and by Γ the Ranvier node – the unmyelinated part of the interface between Y_i and Y_e. The lateral boundary of Y is denoted by Σ. We assume that the boundary of the myelin part Γ_m is Lipschitz continuous.

We rescale the periodicity cell by a small parameter $\varepsilon > 0$ and translate it along the x_1-axis to form a thin periodic cylinder of thickness of order ε suspended in the thin extracellular medium with alternating myelinated and unmyelinated parts on the lateral boundary (*cf*. Figure 3-3).

For simplicity, let us denote by $L \in \mathbb{N}$ an integer number of periods. The whole domain

$$\Omega_\varepsilon := \left\{ (x_1, x') : \ x_1 \in (0, L), \ x' \in \varepsilon\phi\left(\frac{x_1}{\varepsilon}\right)\omega, \ \varepsilon > 0 \right\}$$

is the union of the disjoint extracellular, intracellular domains, and Ranvier nodes: $\Omega_\varepsilon = \Omega_{i,\varepsilon} \cup \Omega_{e,\varepsilon} \cup \Gamma_\varepsilon$, wherein

$$\Omega_{i,\varepsilon} = \left\{ (x_1, x') : \ x_1 \in (0, L), \ x' \in \varepsilon\phi_0\left(\frac{x_1}{\varepsilon}\right)\omega_0 \right\}.$$

The lateral part of Ω_ε is denoted by Σ_ε. Let Γ_ε and $\Gamma_{m,\varepsilon}$ denote the Ranvier nodes and the boundary of the myelin respectively. Note that we plot a cross section of the domain

Ω_ε. In $\mathbb{R}^3$, $\Omega_{e,\varepsilon}$ is connected, while Γ_ε and $\Omega_{m,\varepsilon}$ consist of a finite number of connected components.

Since the resistivity of intracellular and extracellular domains (e.g. 5.47×10^{-2} kOhm·cm) is much smaller than the resistivity of the myelin sheath (e.g. 7.4×10^5 kOhm·cm), a classical simplification is to assume that myelin is a perfect insulator. This implies that the areas Y_m constitute voids in our domain Y.

3.2.2. Governing equations

Let u_ε^i, u_ε^e denote the electric potential in the intracellular and extracellular domains, respectively. We assume that the electric potential satisfies homogeneous Neumann boundary conditions on the lateral boundary Σ_ε and homogeneous Dirichlet ones at the bases $\Gamma_0^\varepsilon = \{x \in \Omega_\varepsilon : \ x_1 = 0\}$ and $\Gamma_L^\varepsilon = \{x \in \Omega_\varepsilon : \ x_1 = L\}$. Since we assume that the myelin acts as a perfect insulator, we impose homogeneous Neumann boundary conditions on its boundary.

The transmembrane potential is the potential jump across the axon membrane and will be denoted by $[u_\varepsilon] = u_\varepsilon^i - u_\varepsilon^e$, and u_ε denotes the potential $u_\varepsilon = u_\varepsilon^l$ in $\Omega_{i,\varepsilon}$, $l = i, e$. We assume conductivity to be a piecewise constant function $\sigma_\varepsilon = \sigma_l$ in $\Omega_{l,\varepsilon}$, $l = e, i$.

On Ranvier nodes, we assume continuity of currents (3.2) and HH dynamics for the transmembrane potential (3.3). Thus, the current through the membrane is a sum of the capacitive current $c_m \partial_t [u_\varepsilon]$, where c_m is the membrane capacitance per unit area, and the ionic current $I_{ion}([u_\varepsilon], g_\varepsilon)$ through the ion channels. The vector-function g_ε is a vector of the so-called gating variables describing the probability of each particular ionic channel to be open or closed. Due to this, the gating variables have nonegative components $0 \leq (g_\varepsilon)_j \leq 1$. The vector of gating variables satisfies an ordinary differential equation (ODE) $\partial_t g_\varepsilon = HH([u_\varepsilon], g_\varepsilon)$. In the classical HH model (Hodgkin & Huxley, 1952) there are three types of channels: a sodium (Na), a potassium (K), and a leakage channels, and, consequently, three gating variables (see Section 3.5 for explicit expressions). We assume that

(H1) The function $I_{ion}(v, g)$ is linear w.r.t v and has the following form:

$$I_{ion}(v, g) = \sum_{j=1}^{m} H_j(g_j)(v - v_{r,j}),$$

where $g_{,j}$ is the jth component of g, $v_{r,j}$ is the $j$the component of the resting potential v_r, and H_j is positive, bounded, and Lipschitz continuous, i.e.

$$|H_j(g_1) - H_j(g_2)| \leq L_1|g_1 - g_2|.$$

The constant v_r is the reference constant voltage, and g_ε is a gate variable vector with nonnegative components $0 \leq (g_\varepsilon)_j \leq 1$, $j = \overline{1, m}$.

(H2) The vector function $HH(g, v) = F(v) - \alpha g$, where F is a vector function with positive Lipschitz continuous components, and α is a diagonal $m \times m$ matrix with positive Lipschitz continuous entries.

(H3) $G_0 \in C(0, L)^m$ with components taking values between zero and one (as the corresponding g_ε).

We assume the homogeneous Dirichlet boundary condition for u_ε^e and for u_ε^i on the bases of the domain, i.e. when $x_1 = 0$ and $x_1 = L$. On the lateral boundary of Ω_ε we assume the homogeneous Neumann boundary condition, with ν the unit normal exterior to $\Omega_{e,\varepsilon}$ on Σ and exterior to $\Omega_{i,\varepsilon}$ on Γ_ε.

The dynamics of the electric potential and the gating variables is then described by the following system of equations:

$$-\text{div}\big(\sigma_\varepsilon \Delta u_\varepsilon\big) = 0, \qquad\qquad (t, x) \in (0, T) \times \Omega_\varepsilon \setminus \Gamma_\varepsilon, \qquad (3.1)$$

$$\sigma_e \nabla u_\varepsilon^e \cdot \nu = \sigma_i \nabla u_\varepsilon^i \cdot \nu, \qquad\qquad (t, x) \in (0, T) \times \Gamma_\varepsilon, \qquad (3.2)$$

$$\varepsilon(c_m \partial_t[u_\varepsilon] + I_{ion}([u_\varepsilon], g_\varepsilon)) = -\sigma_i \nabla u_\varepsilon^i \cdot \nu, \quad (t, x) \in (0, T) \times \Gamma_\varepsilon, \qquad (3.3)$$

$$\partial_t g_\varepsilon = HH([u_\varepsilon], g_\varepsilon), \qquad\qquad (t, x) \in (0, T) \times \Gamma_\varepsilon, \qquad (3.4)$$

$$[u_\varepsilon](x, 0) = 0, \ g_\varepsilon(x, 0) = G_0(x_1), \qquad\qquad x \in \Gamma_\varepsilon, \qquad (3.5)$$

$$\nabla u_\varepsilon^e \cdot \nu = 0, \qquad\qquad (t, x) \in (0, T) \times (\Gamma_{m,\varepsilon} \cup \Sigma_\varepsilon), \qquad (3.6)$$

$$u_\varepsilon = 0, \qquad\qquad\qquad (t, x) \in (0, T) \times (\Gamma_0^\varepsilon \cup \Gamma_L^\varepsilon). \qquad (3.7)$$

We will study the asymptotic behavior of u_ε, as $\varepsilon \to 0$, and derive a one-dimensional nonlinear cable equation describing the potential propagation along the axon.

To define a weak solution of (3.1)–(3.7), we will use test function $\phi \in L^\infty(0, T; H^1(\Omega_\varepsilon \setminus \Gamma_\varepsilon))$, $\partial_t[\phi] \in L^2(0, T; L^2(\Gamma_\varepsilon))$ such that $\phi = 0$ for $x_1 = 0$ and $x_1 = L$. The jump of ϕ across the Ranvier nodes is denoted by $[\phi]$, $[\phi] = (\phi^i - \phi^e)\big|_{\Gamma_\varepsilon}$. Then, the weak formulation corresponding to (3.1)–(3.7) reads: find

$$u_\varepsilon \in L^\infty(0, T; H^1(\Omega_\varepsilon \setminus \Gamma_\varepsilon)), \quad \partial_t[u_\varepsilon] \in L^2(0, T; L^2(\Gamma_\varepsilon)),$$

satisfying $u_\varepsilon = 0$ for $x_1 = 0$ and $x_1 = L$ and the initial condition $[u_\varepsilon](0, x) = 0$, such that, for any test functions $\phi \in L^\infty(0, T; H^1(\Omega_\varepsilon \setminus \Gamma_\varepsilon))$, $\phi = 0$ for $x_1 = 0$ and $x_1 = L$, and for almost all $t \in (0, T)$, it holds

$$\varepsilon \int_{\Gamma_\varepsilon} c_m \partial_t[u_\varepsilon][\phi]\, ds + \int_{\Omega_\varepsilon \setminus \Gamma_\varepsilon} \sigma_\varepsilon \nabla u_\varepsilon \cdot \nabla \phi\, dx + \varepsilon \int_{\Gamma_\varepsilon} I_{ion}([u_\varepsilon], g_\varepsilon)[\phi]\, ds = 0. \qquad (3.8)$$

The vector of gating variables g_ε solves the following ODE:

$$\partial_t g_\varepsilon = HH([u_\varepsilon], g_\varepsilon), \ g_\varepsilon(0, x) = G_0(x_1).$$

Since HH is linear with respect to g_ε, we can solve the last ODE and obtain g_ε as a function – integral functional – of the jump $[u_\varepsilon]$:

$$\langle g_\varepsilon, v_\varepsilon \rangle = e^{-\int_0^t \alpha(v_\varepsilon(\zeta, x))d\zeta} \left(G_0(x) + \int_0^t F(v_\varepsilon(\tau, x)) e^{\int_0^\tau \alpha(v_\varepsilon(\zeta, x))d\zeta}\, d\tau \right).$$

Substituting this expression into (3.8) we obtain the weak formulation of (3.1)–(3.7) in terms of the potential u_ε and its jump $v_\varepsilon = [u_\varepsilon]$ across Γ_ε:

$$\varepsilon \int_{\Gamma_\varepsilon} c_m \partial_t v_\varepsilon[\phi]\, ds + \int_{\Omega_\varepsilon \setminus \Gamma_\varepsilon} \sigma_\varepsilon \nabla u_\varepsilon \cdot \nabla \phi\, dx + \varepsilon \int_{\Gamma_\varepsilon} I_{ion}(v_\varepsilon, \langle g_\varepsilon, v_\varepsilon \rangle)[\phi]\, ds = 0. \qquad (3.9)$$

3.2.3. Main result

The main result of the paper is given by Theorem 3.1 describing the convergence of the transmembrane potential $[u_\varepsilon]$ and the gating variables g_ε to the unique solution of the following one-dimensional effective problem:

$$
\begin{aligned}
c_m \partial_t v_0 + I_{ion}(v_0, g_0) &= a^{\text{eff}} \partial^2_{x_1 x_1} v_0, & (t, x_1) &\in (0, T) \times (0, L), \\
\partial_t g_0 &= HH(v_0, g_0), & (t, x_1) &\in (0, T) \times (0, L), \\
v_0(t, 0) &= v_0(t, L) = 0, & t &\in (0, T), \\
v_0(0, x_1) &= 0, \ g_0(0, x_1) = G_0(x_1), & x_1 &\in (0, L).
\end{aligned}
\tag{3.10}
$$

The effective coefficient a^{eff} is given by

$$
a^{\text{eff}} = \frac{1}{|\Gamma|} \left(\left(\sigma_e \int_{Y_e} (\partial_{y_1} N_e + 1) \, dy \right)^{-1} + \left(\sigma_i \int_{Y_i} (\partial_{y_1} N_i + 1) \, dy \right)^{-1} \right)^{-1},
\tag{3.11}
$$

where the 1-periodic in y_1 functions, N_e and N_i solve the auxiliary cell problems:

$$
\begin{aligned}
-\Delta N_e(y) &= 0, & y &\in Y_e, \\
\nabla N_e \cdot \nu &= -\nu_1, & y &\in \Gamma \cup \Gamma_m \cup \Sigma, \\
N_e(y_1, y') \text{ is periodic in } y_1;
\end{aligned}
\tag{3.12}
$$

and

$$
\begin{aligned}
-\Delta N_i(y) &= 0, & y &\in Y_i, \\
\nabla N_i \cdot \nu &= -\nu_1, & y &\in \Gamma \cup \Gamma_m, \\
N_i(y_1, y') \text{ is periodic in } y_1.
\end{aligned}
\tag{3.13}
$$

Theorem 3.1. *The solutions $[u_\varepsilon]$ and g_ε of problem (3.1)–(3.7) converge to the solutions v_0 and g_0 of (3.10) in the following sense:*

$$
\sup_{t \in (0,T)} \varepsilon^{-1} \int_{\Gamma_\varepsilon} |[u_\varepsilon] - v_0|^2 ds \to 0, \quad \text{as } \varepsilon \to 0,
$$

$$\sup_{t \in (0,T)} \varepsilon^{-1} \int_{\Gamma_\varepsilon} |g_\varepsilon - g_0|^2 ds \to 0, \quad as \ \varepsilon \to 0.$$

To prove Theorem 3.1 we first derive a priori estimates in Section 3.3 (Lemma 3.2), then we prove the two-scale convergence of u_ε and its gradient (Lemma 3.3) and the convergence of $[u_\varepsilon]$ in appropriate spaces (Lemma 3.4). Finally, in Section 3.4 we pass to the limit in the weak formulation and derive the limit problem (3.10).

3.3. A priori estimates

The existence and uniqueness of a solution of (3.1)–(3.7) follows from the classical semigroup theory (see, for example, (Pazy, 2012)). Its regularity is addressed in (Matano & Mori, 2011; Henríquez et al., 2017; Henríquez & Jerez-Hanckes, 2018). The proof of Lemma 3.1 follows the lines of that in (Jerez-Hanckes et al., 2020) (see Lemma 3.1).

Lemma 3.1 (Existence result)**.** *There exists a unique*

$$u_\varepsilon \in L^\infty(0,T; H^1(\Omega_\varepsilon \setminus \Gamma_\varepsilon)), \quad \partial_t v_\varepsilon = \partial_t [u_\varepsilon] \in L^2(0,T; L^2(\Gamma_\varepsilon))$$

such that $u_\varepsilon = 0$ for $x_1 = 0$ and $x_1 = L$, for any test functions $\phi \in L^\infty(0,T; H^1(\Omega_\varepsilon \setminus \Gamma_\varepsilon))$, $\phi = 0$ for $x_1 = 0$ and $x_1 = L$, and for almost all $t \in (0,T)$

$$\varepsilon \int_{\Gamma_\varepsilon} c_m \partial_t v_\varepsilon [\phi] \, ds + \int_{\Omega_\varepsilon \setminus \Gamma_\varepsilon} \sigma_\varepsilon \nabla u_\varepsilon \cdot \nabla \phi \, dx + \varepsilon \int_{\Gamma_\varepsilon} I_{ion}(v_\varepsilon, \langle g_\varepsilon, v_\varepsilon \rangle)[\phi] \, ds = 0. \quad (3.14)$$

In order to pass to the limit in the weak formulation, we need first to obtain a priori estimates which will guarantee the compactness of the solution in appropriate spaces.

Lemma 3.2 (A priori estimates)**.** *Let $(u_\varepsilon, g_\varepsilon)$ be a solution of (3.1)–(3.7). Denote $v_\varepsilon = [u_\varepsilon]$. Then, the following estimates hold:*

(i) $\varepsilon^{-1} \int_{\Gamma_\varepsilon} |v_\varepsilon|^2 \, ds \leq C, \quad t \in (0,T).$

(ii) $\varepsilon^{-1} \int_0^t \int_{\Gamma_\varepsilon} |\partial_\tau v_\varepsilon|^2 \, ds \, d\tau \leq C, \quad t \in (0,T).$

(iii) $\varepsilon^{-2} \int_{\Omega_{i,\varepsilon}\cup\Omega_{e,\varepsilon}} (|u_\varepsilon|^2 + |\nabla u_\varepsilon|^2)\, dx \le C, \quad t \in (0,T).$

PROOF. We multiply (3.1) by u_ε and integrate by parts over $\Omega_\varepsilon \setminus \Gamma_\varepsilon$:

$$\frac{\varepsilon}{2}\frac{d}{dt}\int_{\Gamma_\varepsilon} c_m v_\varepsilon^2 ds + \varepsilon \int_{\Gamma_\varepsilon} I_{ion}(v_\varepsilon, \langle g_\varepsilon, v_\varepsilon\rangle)v_\varepsilon\, ds + \int_{\Omega_\varepsilon\setminus\Gamma_\varepsilon} \sigma_\varepsilon |\nabla u_\varepsilon|^2\, dx = 0.$$

Integrating the last equality with respect to t and using (3.5) we get

$$\frac{\varepsilon}{2}\int_{\Gamma_\varepsilon} c_m v_\varepsilon^2 ds + \varepsilon \int_0^t \int_{\Gamma_\varepsilon} I_{ion}(v_\varepsilon, \langle g_\varepsilon, v_\varepsilon\rangle)v_\varepsilon\, dsd\tau + \int_0^t \int_{\Omega_\varepsilon\setminus\Gamma_\varepsilon} \sigma_\varepsilon |\nabla u_\varepsilon|^2\, dxd\tau = 0.$$

$$(3.15)$$

Dividing the resulting identity by ε^2 (the scaling factor of the order $|\Omega_\varepsilon|$) and recalling the the positivity of H we get

$$\frac{\varepsilon^{-1}}{2}\int_{\Gamma_\varepsilon} c_m v_\varepsilon^2 ds + \varepsilon^{-1}\int_0^t \int_{\Gamma_\varepsilon} \sum_j H(\langle g_\varepsilon, v_\varepsilon\rangle_j)(v_\varepsilon - v_{r,j})v_\varepsilon\, ds\, d\tau \le 0,$$

$$\frac{\varepsilon^{-1}}{2}\int_{\Gamma_\varepsilon} c_m v_\varepsilon^2 ds \le \frac{\varepsilon^{-1}}{2}\int_0^t \int_{\Gamma_\varepsilon} \sum_j H(\langle g_\varepsilon, v_\varepsilon\rangle_j)(v_{r,j})^2\, ds\, d\tau \le C.$$

In this way estimate (i) is proved. Next, we derive an integral estimate for ∇u_ε from (3.15) and (i):

$$\varepsilon^{-2}\int_0^t \int_{\Omega_\varepsilon\setminus\Gamma_\varepsilon} \sigma_\varepsilon |\nabla u_\varepsilon|^2\, dxd\tau \le C.$$

Let us now multiply (3.1) by $\partial_t u_\varepsilon$ and integrate by parts over $\Omega_\varepsilon \setminus \Gamma_\varepsilon$:

$$\varepsilon^{-1}\int_{\Gamma_\varepsilon} c_m |\partial_t v_\varepsilon|^2 ds + \varepsilon^{-1}\int_{\Gamma_\varepsilon} I_{ion}(v_\varepsilon, \langle g_\varepsilon, v_\varepsilon\rangle)\partial_t v_\varepsilon\, ds$$
$$+ \frac{\varepsilon^{-2}}{2}\frac{d}{dt}\int_{\Omega_\varepsilon\setminus\Gamma_\varepsilon} \sigma_\varepsilon |\nabla u_\varepsilon|^2\, dx = 0.$$

Integrating with respect to t gives

$$\varepsilon^{-1}\int_0^t \int_{\Gamma_\varepsilon} c_m |\partial_\tau v_\varepsilon|^2 dsd\tau + \varepsilon^{-1}\int_0^t \int_{\Gamma_\varepsilon} I_{ion}(v_\varepsilon, \langle g_\varepsilon, v_\varepsilon\rangle)\partial_\tau v_\varepsilon\, dsd\tau$$

$$+\frac{\varepsilon^{-2}}{2}\int_{\Omega_\varepsilon}\sigma_\varepsilon|\nabla u_\varepsilon|^2\,dx = \frac{\varepsilon^{-2}}{2}\int_{\Omega_\varepsilon\backslash\Gamma_\varepsilon}\sigma_\varepsilon|\nabla u_\varepsilon|^2\Big|_{t=0}\,dx. \tag{3.16}$$

Since v_ε is a strict solution, we can choose $\phi = u_\varepsilon$ and set $t = 0$ in (3.8). Then, $\nabla u_\varepsilon\big|_{t=0} = 0$. By (H1), the boundedness of H and the estimate (i), we derive

$$\varepsilon^{-1}\int_0^t\int_{\Gamma_\varepsilon}c_m|\partial_\tau v_\varepsilon|^2 ds d\tau + \varepsilon^{-1}\int_0^t\int_{\Gamma_\varepsilon}\sum_j H(\langle g_\varepsilon, v_\varepsilon\rangle_j)(v_\varepsilon - v_{r,j})\partial_\tau v_\varepsilon\,ds d\tau \le 0,$$

$$\varepsilon^{-1}\int_0^t\int_{\Gamma_\varepsilon}c_m|\partial_\tau v_\varepsilon|^2 ds d\tau \le C\varepsilon^{-1}\int_0^t\int_{\Gamma_\varepsilon}(v_\varepsilon - v_{r,j})\partial_\tau v_\varepsilon\,ds d\tau,$$

$$\varepsilon^{-1}\int_0^t\int_{\Gamma_\varepsilon}|\partial_\tau v_\varepsilon|^2 ds d\tau \le C\varepsilon^{-1}\int_0^t\int_{\Gamma_\varepsilon}(v_\varepsilon - v_{r,j})^2\,ds d\tau \le C.$$

Estimate (ii) is proved. Estimates (3.16) and (ii) imply that

$$\varepsilon^{-2}\int_{\Omega_\varepsilon\backslash\Gamma_\varepsilon}\sigma_\varepsilon|\nabla u_\varepsilon|^2\,dx \le C, \quad t \in (0, T). \tag{3.17}$$

Since u_ε satisfies the homogeneous Dirichlet boundary condition for $x_1 = 0$, the Friedrichs inequality is valid for u_ε in Ω_ε^i and Ω_ε^e leading to (iii).

$$\square$$

When passing to the limit, as $\varepsilon \to 0$, we will use the notion of the two-scale convergence. Let us recall the definition.

Definition 3.1. *We say that $u_\varepsilon(t, x)$ converges two-scale to $u_0(t, x_1, y)$ in $L^2(0, T; L^2(\Omega_{l,\varepsilon}))$, $l = i, e$, if*

(i) $\varepsilon^{-2}\displaystyle\int_0^T\int_{\Omega_{l,\varepsilon}}|u_\varepsilon|^2 dx\,dt < \infty.$

(ii) *For any $\phi(t, x_1) \in C(0, T; L^2(0, L))$, $\psi(y) \in L^2(Y_l)$ we have*

$$\lim_{\varepsilon\to 0}\varepsilon^{-2}\int_0^T\int_{\Omega_{l,\varepsilon}}u_\varepsilon(x)\phi(t, x_1)\psi\Big(\frac{x}{\varepsilon}\Big)\,dx\,dt$$

$$= \int_0^T\int_0^L\int_{Y_l}u_0(t, x_1, y)\phi(t, x_1)\psi(y)\,dy\,dx_1\,dt,$$

for some function $u_0 \in L^2(0, T; L^2((0, L) \times Y))$.

Definition 3.2. *We say that $v_\varepsilon(t, x)$ converges two-scale to $v_0(t, x_1, y)$ in $L^2(0, T; L^2(\Gamma_\varepsilon))$ if it holds that*

(i) $\varepsilon^{-1} \displaystyle\int_0^T \int_{\Gamma_\varepsilon} v_\varepsilon^2 \, ds \, dt < \infty$.

(ii) *For any $\phi(t, x_1) \in L^\infty(0, T; L^2(0, L))$, $\psi(y) \in L^2(\Gamma)$ we have*

$$\lim_{\varepsilon \to 0} \varepsilon^{-1} \int_0^T \int_{\Gamma_\varepsilon} v_\varepsilon(x) \phi(t, x_1) \psi\left(\frac{x}{\varepsilon}\right) ds_x \, dt$$

$$= \int_0^T \int_0^L \int_\Gamma v_0(t, x_1, y) \phi(t, x_1) \psi(y) \, ds_y \, dx_1 \, dt$$

for some function $v_0 \in L^2(0, T; L^2((0, L) \times \Gamma))$.

Lemma 3.3. *Let u_ε be a solution of (3.1)–(3.7). Denote by $\mathbf{I}_{\Omega_{l,\varepsilon}}$ the characteristic functions of $\Omega_{l,\varepsilon}$, $l = i, e$. Then, up to a subsequence,*

(i) *$[u_\varepsilon]$ converges two-scale to $v_0(t, x_1, y)$ in $L^2(0, T; L^2(\Gamma_\varepsilon))$.*

(ii) *$\partial_t[u_\varepsilon]$ converges two-scale to $\partial_t v_0(t, x_1, y)$ in $L^2(0, T; L^2(\Gamma_\varepsilon))$.*

(iii) *$\mathbf{I}_{\Omega_{l,\varepsilon}} u_\varepsilon$ converges two-scale to $|Y_l| \, u_0^l(t, x_1)$ in $L^2(0, T; L^2(\Omega_{l,\varepsilon}))$.*

(iv) *$\mathbf{I}_{\Omega_{l,\varepsilon}} \nabla u_\varepsilon$ converges two-scale to $(\partial_{x_1} u_0^l(t, x_1)\mathbf{e_1} + \nabla_y w^l(t, x_1, y)$*
in $(L^2(0, T; L^2(\Omega_{l,\varepsilon})))$. Here $\mathbf{e_1} = (1, 0, 0) \in \mathbf{R}^3$,
$w^l \in L^2(0, T; L^2(0, L) \times H^1(Y))$.

For the proof, we refer to (Allaire & Damlamian, 1995) for two-scale convergence on periodic surfaces (on Γ_ε), to (Zhikov, 2000) and (Pettersson, 2017) for two-scale convergence in thin structures and dimension reduction.

One of the technical difficulties in the present paper is the passage to the limit in the integral over Γ_ε containing a nonlinear function since we need to ensure a strong convergence of v_ε in an appropriate sense. In the next lemma, we show that v_ε can be approximated by a piecewise constant function $\tilde{v}_\varepsilon(t, x_1)$ which in its turn converges, up to a subsequence, to a function $v_0(t, x_1) \in L^\infty(0, T; H^1(0, L))$ uniformly on $[0, T]$, as $\varepsilon \to 0$.

Lemma 3.4. *Let u_ε be a solution of (3.1)–(3.7). Then, there exists a function*

$$\tilde{v}_\varepsilon(t, x_1) \in L^\infty(0, T; H^1(0, L)) \cap H^1(0, T; L^2(0, L))$$

such that, it holds

    (i) *For $t \in (0, T)$, the function $\tilde{v}_\varepsilon$ approximates $[u_\varepsilon]$:*

$$\int_{\Gamma_\varepsilon} |\tilde{v}_\varepsilon - [u_\varepsilon]|^2 ds \leq C\varepsilon \int_{\Omega_{i,\varepsilon} \cup \Omega_{e,\varepsilon}} |\nabla u_\varepsilon|^2 dx.$$

    (ii) *There exists $v_0(t, x_1) \in L^\infty(0, T; L^2(0, L))$ such that along a subsequence $\tilde{v}_\varepsilon$ converges to $v_0(t, x_1)$ uniformly on $[0, T]$, as $\varepsilon \to 0$.*

PROOF. Let us cover Ω_ε by a union of overlapping cells $\varepsilon\tilde{Y}_k$ as shown in Figure 3-2 so that each cell contains two Ranvier nodes. The Ranvier node which belongs to the intersection $\varepsilon\tilde{Y}_k \cap \varepsilon\tilde{Y}_{k+1}$ is denoted by $\varepsilon\Gamma_k$. The intra- and extracellular parts of $\tilde{Y}_k$ are referred to as $\tilde{Y}_{i,k}$ and $\tilde{Y}_{e,k}$, respectively.
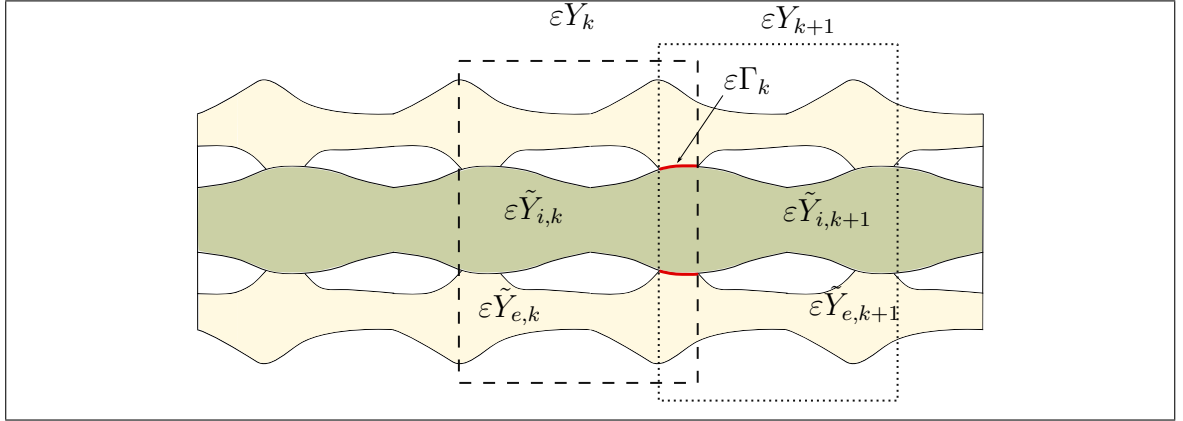
FIGURE 3-2. Overlapping cells $\varepsilon\tilde{Y}_k$ and $\varepsilon\tilde{Y}_{k+1}$.

Let us show that the difference between the mean values of $[u_\varepsilon]$ over $\varepsilon\Gamma_k$ and $\varepsilon\Gamma_{k+1}$ is small. Let

$$\bar{u}_{\varepsilon,k}^l = \frac{1}{|\varepsilon\Gamma|} \int_{\varepsilon\Gamma_k} u_\varepsilon^l ds, \quad l = i, e.$$

For each $\varepsilon\tilde{Y}_{l,k}$, $l = i, e$, due to the Poincaré inequality, we have

$$\int_{\varepsilon\tilde{Y}_{l,k}} |u_\varepsilon^l - \bar{u}_{\varepsilon,k}^l|^2 dx \leq C\varepsilon^2 \int_{\varepsilon\tilde{Y}_{l,k}} |\nabla u_\varepsilon^l|^2 dx,$$

with C independent of ε. Considering traces on Γ_k, by a simple scaling argument one has

$$\int_{\varepsilon\Gamma_k} |u_\varepsilon^l - \bar{u}_{\varepsilon,k}^l|^2 ds \leq C\varepsilon^{-1} \left(\int_{\varepsilon\tilde{Y}_{l,k}} |u_\varepsilon^l - \bar{u}_{\varepsilon,k}^l|^2 dx + \varepsilon^2 \int_{\varepsilon\tilde{Y}_{l,k}} |\nabla u_\varepsilon^l|^2 dx \right)$$
$$\leq C\varepsilon \int_{\varepsilon\tilde{Y}_{l,k}} |\nabla u_\varepsilon^l|^2 dx, \quad l = i, e. \tag{3.18}$$

Then, the difference between $\bar{u}_{\varepsilon,k}$ and $\bar{u}_{\varepsilon,k+1}$ is estimated as follows

$$\left|\bar{u}_{\varepsilon,k}^l - \bar{u}_{\varepsilon,k+1}^l\right|^2 \leq \frac{2}{|\varepsilon\tilde{Y}_{l,k} \cap \varepsilon\tilde{Y}_{l,k+1}|} \int_{\varepsilon\tilde{Y}_{l,k}\cap\varepsilon\tilde{Y}_{l,k+1}} \left(|u_\varepsilon^l - \bar{u}_{\varepsilon,k}^l|^2 + |u_\varepsilon^l - \bar{u}_{\varepsilon,k+1}^l|^2 \right) dx$$
$$\leq C\varepsilon^{-1} \int_{\varepsilon\tilde{Y}_{l,k}\cup\varepsilon\tilde{Y}_{l,k+1}} |\nabla u_\varepsilon^l|^2 dx.$$

Adding up in k the above estimates, we obtain an estimate in Ω_ε^l:

$$\sum_k |\bar{u}_{\varepsilon,k}^l - \bar{u}_{\varepsilon,k+1}^l|^2 \leq C\varepsilon^{-1} \int_{\Omega_\varepsilon^l} |\nabla u_\varepsilon^l|^2 dx. \tag{3.19}$$

Let us denote by

$$\bar{v}_{\varepsilon,k} = \bar{u}_{\varepsilon,k}^i - \bar{u}_{\varepsilon,k}^e = \frac{1}{|\varepsilon\Gamma|} \int_{\varepsilon\Gamma_k} [u_\varepsilon] ds$$

the jump of the average across the membrane. Then, using (3.18) and (3.19) yields

$$\int_{\varepsilon\Gamma_k} |[u_\varepsilon] - \bar{v}_{\varepsilon,k}|^2 ds \leq C\varepsilon \int_{\varepsilon\tilde{Y}_{i,k}\cup\varepsilon\tilde{Y}_{e,k}} |\nabla u_\varepsilon|^2 dx,$$
$$\sum_k |\bar{v}_{\varepsilon,k} - \bar{v}_{\varepsilon,k+1}|^2 \leq C\varepsilon^{-1} \int_{\Omega_\varepsilon^i\cup\Omega_\varepsilon^e} |\nabla u_\varepsilon|^2 dx. \tag{3.20}$$

Bounds (3.20) show that $[u_\varepsilon]$ in each cell $\varepsilon\tilde{Y}_k$ is close to a constant $\bar{v}_{\varepsilon,k}$, and the difference between $\bar{v}_{\varepsilon,k}$ and $\bar{v}_{\varepsilon,k+1}$ is small due to (iii) in Lemma 3.2.

Next, we construct a piecewise linear function $\tilde{v}_\varepsilon(t, x_1)$ interpolating values $\bar{v}_{\varepsilon,k}$ linearly and show that

$$\int_0^L |\tilde{v}_\varepsilon|^2 dx_1 \le C, \qquad t \in (0, T), \tag{3.21}$$

$$\int_0^L |\partial_{x_1} \tilde{v}_\varepsilon|^2 dx_1 \le C, \quad t \in (0, T), \tag{3.22}$$

$$\int_0^T \int_0^L |\partial_t \tilde{v}_\varepsilon|^2 \, dx_1 dt \le C. \tag{3.23}$$

Indeed, (3.21) and (3.22) follow directly from (3.20) and $(i), (ii)$ in Lemma 3.2:

$$\int_0^L |\tilde{v}_\varepsilon|^2 dx_1 = \sum_k \int_{-\varepsilon/2}^{\varepsilon/2} \left| \frac{\bar{v}_{\varepsilon,k} + \bar{v}_{\varepsilon,k+1}}{2} + x_1 \frac{\bar{v}_{\varepsilon,k+1} - \bar{v}_{\varepsilon,k}}{\varepsilon} \right|^2 dx_1$$

$$\le C \sum_k \varepsilon(|\bar{v}_{\varepsilon,k}|^2 + |\bar{v}_{\varepsilon,k+1}|^2) \le C \frac{1}{|\varepsilon\Gamma|} \int_{\Gamma_\varepsilon} [u_\varepsilon]^2 ds \le C. \tag{3.24}$$

Estimate (3.22) is proved in a similar way using (3.20):

$$\int_0^L |\partial_{x_1} \tilde{v}_\varepsilon|^2 dx_1 \le C \sum_k \int_{-\varepsilon/2}^{\varepsilon/2} \left| \frac{\bar{v}_{\varepsilon,k} - \bar{v}_{\varepsilon,k+1}}{\varepsilon} \right|^2 dx_1$$

$$\le C\varepsilon^{-1} \sum_k |\bar{v}_{\varepsilon,k} - \bar{v}_{\varepsilon,k+1}|^2$$

$$\le C\varepsilon^{-2} \int_{\Omega_\varepsilon^i \cup \Omega_\varepsilon^e} |\nabla u_\varepsilon|^2 dx \le C.$$

Let us prove (3.23). Differentiating $\bar{v}_{\varepsilon,k}$ with respect to t, using the Cauchy-Schwarz inequality yields

$$|\partial_t \bar{v}_{\varepsilon,k}|^2 = \left| \frac{1}{|\varepsilon\Gamma_k|} \int_{\varepsilon\Gamma_k} \partial_t [u_\varepsilon] \, ds \right|^2 \le \frac{1}{|\varepsilon\Gamma_k|} \int_{\varepsilon\Gamma_k} (\partial_t [u_\varepsilon])^2 \, ds.$$

Similarly to (3.24), estimate (3.23) follows from the last bound and (ii) in Lemma 3.2. Estimate (i) in the current lemma follows from (3.20).

The uniform convergence on $(0, T)$ of the constructed piecewise linear approximation is given by the Arzelà-Ascoli theorem. Indeed, the precompactness is guaranteed for $\tilde{v}_\varepsilon$ by

(3.21) and (3.22), while the equicontinuity property follows from (3.23):

$$\tilde{v}_\varepsilon(t + \Delta t) - \tilde{v}_\varepsilon(t) = \int_t^{t+\Delta t} \partial_\tau \tilde{v}_\varepsilon(\tau) d\tau,$$

$$\varepsilon^{-1} \int_0^L |\tilde{v}_\varepsilon(t + \Delta t) - \tilde{v}_\varepsilon(t)|^2 dx \leq \int_0^L \left(\int_t^{t+\Delta t} \partial_\tau \tilde{v}_\varepsilon(\tau) d\tau \right)^2 dx_1$$

$$\leq \Delta t \int_0^L \int_t^{t+\Delta t} |\partial_\tau \tilde{v}_\varepsilon(\tau)|^2 d\tau dx_1 \leq \Delta t.$$

The proof is complete. $\qquad\qquad\qquad\qquad\qquad\qquad\qquad\qquad\qquad\qquad\qquad$ $\square$

3.4. Justification of macroscopic model

Let us denote $v_\varepsilon = [u_\varepsilon]$. Using Lemmata 3.3 and 3.4, we will pass to the limit in the weak formulation of (3.1)–(3.7):

$$\varepsilon^{-1} \int_0^T \int_{\Gamma_\varepsilon} (c_m \partial_t v_\varepsilon + I_{ion}(v_\varepsilon, \langle g_\varepsilon, v_\varepsilon \rangle))[\phi] \, dx dt$$

$$+\varepsilon^{-2} \int_0^T \int_{\Omega_\varepsilon \backslash \Gamma_\varepsilon} \sigma_\varepsilon \nabla u_\varepsilon \cdot \nabla \phi \, dx dt = 0, \qquad (3.25)$$

where $\phi(t, x) \in L^\infty(0, T; H^1(\Omega_\varepsilon \backslash \Gamma_\varepsilon))$ such that $\phi = 0$ for $x_1 = 0$ and $x_1 = L$.

For the functions $U_i(t, x_1), U_e(t, x_1) \in C(0, T; C_0^\infty(0, L))$ and $V_i, V_e(t, x_1, y) \in C(0, T; C_0^\infty(0, L) \times H^1(Y))$ we construct the following test function:

$$\phi_\varepsilon(t, x) = (U_i(t, x_1) + \varepsilon V_i(t, x_1, y))\chi_{\Omega_{i,\varepsilon}} + \chi_{\Omega_{e,\varepsilon}}(U_e(t, x_1) + \varepsilon V_e\left(t, x_1, \frac{x}{\varepsilon}\right)),$$

where $\chi_{\Omega_{l,\varepsilon}}$ is the characteristic function of $\Omega_{l,\varepsilon}$, $l = i, e$.

Note that the jump of ϕ_ε on Γ_ε converges strongly in $L^2(\Gamma_\varepsilon)$ to $U_i(t, x_1) - U_e(t, x_1)$. Substituting ϕ_ε into (3.25) we get

$$\varepsilon^{-1} \int_0^T \int_{\Gamma_\varepsilon} (c_m \partial_t v_\varepsilon + I_{ion}(v_\varepsilon, \langle g_\varepsilon, v_\varepsilon \rangle))[\phi_\varepsilon] \, ds dt \qquad (3.26)$$

$$+\varepsilon^{-2} \int_0^T \int_{\Omega_{i,\varepsilon}} \sigma_i \nabla u_\varepsilon^i \cdot (\mathbf{e_1} \partial_{x_1} U_i + \varepsilon \nabla V_i\left(x_1, \frac{x}{\varepsilon}\right)) dx dt \qquad (3.27)$$

$$+\varepsilon^{-2}\int_0^T\int_{\Omega_{e,\varepsilon}}\sigma_e\nabla u_\varepsilon^e\cdot(\mathbf{e_1}\partial_{x_1}U_e+\varepsilon\nabla V_e\big(x_1,\frac{x}{\varepsilon}\big))dxdt \tag{3.28}$$

$$= I_{1\varepsilon}+I_{2\varepsilon}+I_{3\varepsilon}=0.$$

We will pass to the limit, as $\varepsilon\to 0$, in each integral $I_{k\varepsilon}$, $k=1,2,3$ given by (3.26)-(3.28).

Since $[\phi_\varepsilon]$ on Γ_ε converges strongly in $L^2(\Gamma_\varepsilon)$ to $U_i(t,x_1)-U_e(t,x_1)$ and $\partial_t v_\varepsilon$ converges two-scale (weakly) in $L^2(0,T;L^2(\Gamma_\varepsilon))$ and uniformly on $(0,T)$ to $v_0(t,x_1)$, we can pass to the limit in (3.26) and obtain

$$I_{1\varepsilon}=\varepsilon^{-1}\int_0^T\int_{\Gamma_\varepsilon}(c_m\partial_t v_\varepsilon+I_{ion}(v_\varepsilon,\langle g_\varepsilon,v_\varepsilon\rangle))[\phi_\varepsilon]\,dsdt$$

$$\xrightarrow[\varepsilon\to 0]{}\quad |\Gamma|\int_0^T\int_0^L(c_m\partial_t v_0+I_{ion}(v_0,\langle g_0,v_0\rangle))(U_i-U_e)\,dx_1dt.$$

To pass to the two-scale limit in (3.27)–(3.28), we use (iv) in Lemma 3.3 and get

$$I_{2\varepsilon}=\varepsilon^{-2}\int_0^T\int_{\Omega_{i,\varepsilon}}\sigma_i\nabla u_\varepsilon^i\cdot(\mathbf{e_1}\partial_{x_1}U_i+\nabla_y V_i\big(x_1,\frac{x}{\varepsilon}\big)+\varepsilon\partial_{x_1}V_i\big(x_1,\frac{x}{\varepsilon}\big))dxdt$$

$$\xrightarrow[\varepsilon\to 0]{}\quad \int_0^T\int_0^L\int_{Y_i}\sigma_i(\mathbf{e_1}\partial_{x_1}u_0^i+\nabla_y w^i)\cdot(\mathbf{e_1}\partial_{x_1}V_i(t,x_1)+\nabla_y V_i(t,x_1,y))\,dy\,dx_1dt.$$

$$I_{3\varepsilon}=\varepsilon^{-2}\int_0^T\int_{\Omega_{e,\varepsilon}}\sigma_e\nabla u_\varepsilon^e\cdot(\mathbf{e_1}\partial_{x_1}U_e+\nabla_y V_e\big(x_1,\frac{x}{\varepsilon}\big)+\varepsilon\partial_{x_1}V_e\big(x_1,\frac{x}{\varepsilon}\big))dxdt$$

$$\xrightarrow[\varepsilon\to 0]{}\quad \int_0^T\int_0^L\int_{Y_e}\sigma_e(\mathbf{e_1}\partial_{x_1}u_0^e+\nabla_y w^e)\cdot(\mathbf{e_1}\partial_{x_1}V_e(t,x_1)+\nabla_y V_e(t,x_1,y))\,dy\,dx_1dt.$$

Thus, we obtain a weak formulation of the effective problem:

$$|\Gamma|\int_0^T\int_0^L(c_m\partial_t v_0+I_{ion}(v_0,\langle g_0,v_0\rangle))(U_i-U_e)\,dx_1dt$$

$$+\int_0^T\int_0^L\int_{Y_i}\sigma_i(\mathbf{e_1}\partial_{x_1}u_0^i+\nabla_y w^i)\cdot(\mathbf{e_1}\partial_{x_1}U_i(t,x_1)+\nabla_y V_i(t,x_1,y))\,dy\,dx_1dt$$

$$+\int_0^T\int_0^L\int_{Y_e}\sigma_e(\mathbf{e_1}\partial_{x_1}u_0^e+\nabla_y w^e)\cdot(\mathbf{e_1}\partial_{x_1}U_e(t,x_1)+\nabla_y V_e(t,x_1,y))\,dy\,dx_1dt=0.$$
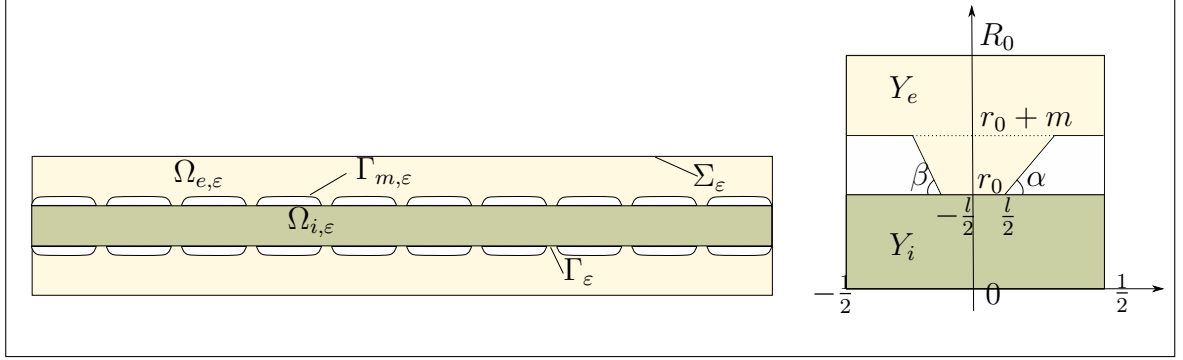
FIGURE 3-3. The cross section of half of the periodic cell, where $Y = \left(-\frac{1}{2}, \frac{1}{2}\right) \times D_{R_0}$ and $Y_i = \left(-\frac{1}{2}, \frac{1}{2}\right) \times D_{r_0}$, with D_{R_0} and D_{r_0} being the open disks in $\mathbb{R}^2$ of radius R_0 and r_0, respectively.

Consequently, computing the variation of the left-hand side of the last equality with respect to V_i, V_e, U_i and U_e gives the representations $V_i(t, x_1, y) = N_i(y)\partial_{x_1} U_i(t, x_1)$, $V_e(t, x_1, y) = N_e(y)\partial_{x_1} U_e(t, x_1)$, the cell problems (3.12) and (3.13), and the two one-dimensional equations

$$|\Gamma|(c_m \partial_t v_0 + I_{ion}(v_0, \langle g_0, v_0 \rangle)) = \int_{Y_i} \sigma_e |\mathbf{e_1} + \nabla_y N_i|^2 \, \partial^2_{x_1 x_1} u_0^i \, dy, \qquad (3.29)$$

$$|\Gamma|(c_m \partial_t v_0 + I_{ion}(v_0, \langle g_0, v_0 \rangle)) = -\int_{Y_e} \sigma_e |\mathbf{e_1} + \nabla_y N_e|^2 \, \partial^2_{x_1 x_1} u_0^e \, dy. \qquad (3.30)$$

Introducing (3.11) and adding up (3.30) and (3.29) yield (3.10). The proof of Theorem 3.1 is complete.

3.5. Numerical example

The goal of this numerical example is to see how the effective coefficient defined by (3.11) varies with respect to the area of Γ. We consider a rotationally symmetric geometry as illustrated in Fig. 3-3. Since the first component of the normal to Y_i is zero in this case, the problem reduces to solving the auxiliary cell problem (3.12) in the extracellular domain Y_e. For this, we use a finite element approximation. Having N_e, we compute the effective

coefficient a^{eff}, whose formula in this cylindrical geometry becomes

$$a^{\text{eff}} = \frac{1}{|\Gamma|} \left(\left(\sigma_e \int_{Y_e} (\partial_{y_1} N_e + 1) \, dy \right)^{-1} + \left(\sigma_i |Y_i| \right)^{-1} \right)^{-1}, \qquad (3.31)$$

as the cell problem (3.13) has a constant solution in this case and $\partial_{y_1} N_i = 0$. The effective coefficient has units $S \cdot cm^2$, that is the units of the conductivity S/cm multiplied by cm^3. The conductivity of the extra- and intracellular domains are assumed to be $\sigma_e = 20$ mS/cm and $\sigma_i = 5$ mS/cm. The node-node separation might vary between $500\,\mu$m and $1500\,\mu$m (see (McIntyre et al., 2002)), and we will take the period $L = 1250\,\mu$m. To make the period equal to one, we need to rescale the domain by L. For example, the radius of the node is 1.8μm, so $r_0 = 1.8/1250$.

Table 3.1 contains the geometric parameters of the domain.

TABLE 3.1. Geometric parameters in μm.

$R_0 L$	$(r_0 + m)L$	$r_0 L$	$l \cdot L$
9	5.75	1.8	1

The values for the effective coefficient a^{eff} computed for angles $\alpha = \beta = \pi/2$ (angles of the myelin attachment) and for different values of the length of the Ranvier node $l \cdot L$ are shown in Table 3.2 and Fig. 3-4. It can be observed that a^{eff} decreases when l increases.

TABLE 3.2. Results of the effective coefficient a^{eff} for different values of l, the length of the Ranvier node. l is in μm.

$l \cdot L$	0.5	1	2	4	8	16
a^{eff}	1.1	$5.5 \cdot 10^{-1}$	$2.8 \cdot 10^{-1}$	$1.4 \cdot 10^{-1}$	$6.9 \cdot 10^{-2}$	$3.5 \cdot 10^{-2}$
$l \cdot L$	32	64	128	256	512	1024
a^{eff}	$1.7 \cdot 10^{-2}$	$8.6 \cdot 10^{-3}$	$4.3 \cdot 10^{-3}$	$2.2 \cdot 10^{-3}$	$1.1 \cdot 10^{-3}$	$5.4 \cdot 10^{-4}$

We also analyze how the effective coefficient depends on the angles of the myelin attachment. The results of the computations are presented in Table 3.3 and on Fig. 3-5.
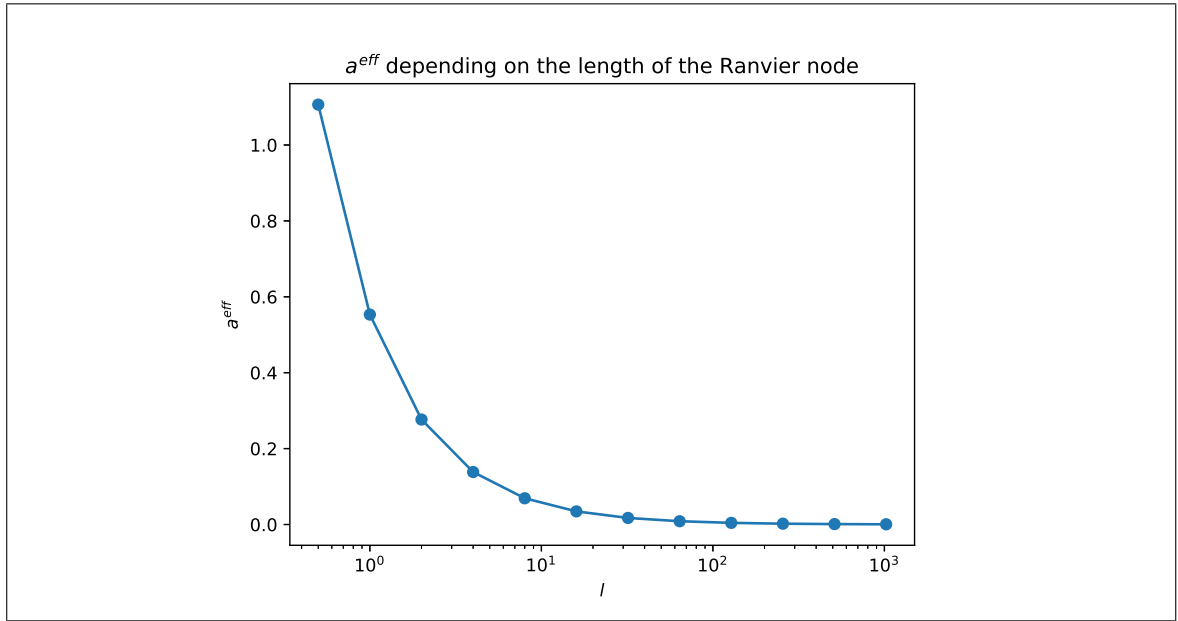
FIGURE 3-4. Effective coefficient a^{eff} for different values of l, the length of the Ranvier node. l is in μm.

One can see that the variation of a^{eff} is not significant, but the effective coefficient cleary decreases when the angles go to zero.

TABLE 3.3. Results of the effective coefficient a^{eff} for different values of the angle. The angles are in degrees and the results presented with six significant digits.

α°	0.4	0.5	1	2	5
a^{eff}	0.555167	0.554720	0.553897	0.553516	0.553297

α°	10	20	46	95	
a^{eff}	0.553223	0.553187	0.553165	0.553153	

Acknowledgements
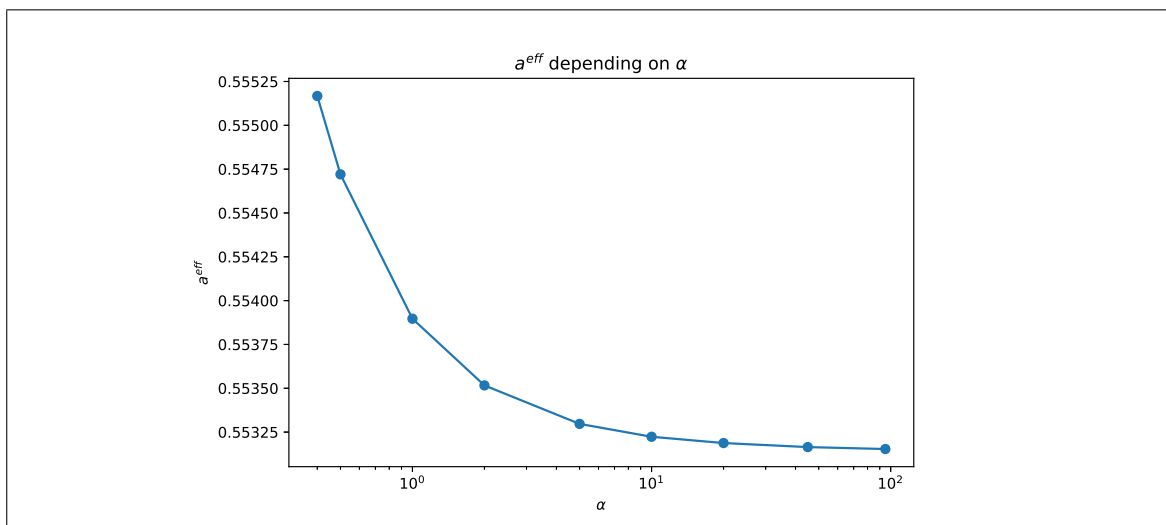
FIGURE 3-5. Effective coefficient a^{eff} for different values of the angle. The angles are in °.

4. DERIVATION OF BIDOMAIN MODEL FOR BUNDLES OF AXONS

The chapter concerns the multiscale modeling of a nerve fascicle of myelinated axons. We present a rigorous derivation of a macroscopic bidomain model describing the behavior of the electric potential in the fascicle based on the FitzHugh-Nagumo membrane dynamics. The approach is based on the two-scale convergence machinery combined with the method of monotone operators.

The chapter is based on the paper: Jerez-Hanckes, C., Martínez, I. A., Pettersson, I., & Rybalko, V.. Derivation of a bidomain model for bundles of myelinated axons (Nonlinear Analysis: Real World Applications, in press).

4.1. Introduction

Modeling the electrical stimulation of nerves requires biophysically consistent descriptions amenable also for computational purposes. A typical nerve in the peripheral nervous system contains several grouped fascicles, each of them comprising hundreds of axons (Standring, 2021). This complex microstructure of neural tissue presents an obvious problem for those attempting to desribe its macroscopic response to electrical excitation. Specifically, one needs to know both how signals propagate along a single axon and how axons influence each other in a bundle.

Electric currents along individual axons are usually modeled via cable theory, which dates back to works of W. Thomson (Lord Kelvin). Fundamental insights into nerve cell excitability were made by A. Hodgkin and A. Huxley, who proposed a model that describes ionic mechanisms underlying the initiation and propagation of action potentials in axons (Hodgkin & Huxley, 1952). Later a more simple model for nonlinear dynamics in axons was introduced in (FitzHugh, 1955), known as the FitzHugh–Nagumo model.

Multiscale homogenization techniques were used in recent works (Jerez-Hanckes et al., 2020; Jerez-Hanckes, Martínez, Pettersson, & Rybalko, 2021) to derive an effective

cable equation describing propagation of signals in myelinated axons. Ideas of homogenization theory can also be naturally applied to account for ephaptic coupling in bundles of axons, where neighboring axons can communicate via current flow through the extracellular space. In 1978, experiments on giant squid axons were conducted (Ramon & Moore, 1978) revealing evidence of ephaptic events and their physiological importance. Ephaptic interactions might be modelled by coupled systems of a large number of cable equations (as, e.g., in (Bokil et al., 2001), (Binczak et al., 2001)), but a continuous mathematical model for a fascicle of myelinated axons, to our best knowledge, has not been rigorously derived. An analogous phenomenon of coupling is observed in the electrical conductance of cardiac tissues (Lin & Keener, 2010), leading to the celebrated *bidomain model*. It was first derived by J. Neu and W. Krassowska (J. Neu & Krassowska, 1993). In (Franzone & Savaré, 2002) the authors study the well-posedness of the reaction-diffusion systems modeling cardiac electric activity at the micro- and macroscopic level. They focus on the FitzHugh-Nagumo model (with recovery variable), and present a formal derivation of the effective bidomain model. The homogenization procedure is justified in (Pennacchio, Savaré, & Franzone, 2005) where Γ-convergence is used for asymptotic analysis. Homogenization techniques based on two-scale convergence and unfolding are applied in, e.g., (Collin & Imperiale, 2018), (Bendahmane, Mroue, Saad, & Talhouk, 2019), (Grandelius & Karlsen, 2019), (Amar, Andreucci, & Timofte, 2021) for modeling of syncytial tissues.

The multiscale analysis of syncytial tissues includes the well-posedness of the microscopic problem, the homogenization procedure, and the well-posedness of the effective bidomain model. The latter question is interesting by itself, with solvability proven using different approaches depending on the nonlinearity. The solvability for a bidomain model in (Franzone & Savaré, 2002) is based on a reformulation as a Cauchy problem for a variational evolution inequality in a properly chosen Sobolev space. This approach applies to the case of the FitzHugh-Nagumo equations. In (Veneroni, 2006) existence and uniqueness are given for solutions of a wide class of models, including the classical Hodgkin-Huxley model, the first membrane model for ionic currents in an axon, and the Phase-I Luo-Rudy (LR1) model. In (Bourgault, Coudiere, & Pierre, 2009) the authors reformulate the coupled

parabolic and elliptic PDEs into a single parabolic PDE by the introduction of a bidomain operator, which is a non-differential and non-local operator. This approach applies to fairly general ionic models, such as the Aliev-Panfilov and MacCulloch models.

The asymptotic analysis of a nerve fascicle with a large number of axons also leads to a bidomain model. It was suggested in (P. J. Basser & Roth, 2000) that bidomain models provides a unified framework for modeling electrical stimulation of both peripheral nerves, cortical neurons, and syncytical tissues. In (Mandonnet & Pantz, 2011) a linear model is considered without recovery variables. Therein, it is hypothesized that the homogenization procedure in (Pennacchio et al., 2005) leading to a macroscopic bidomain model for syncytical tissues can also be carried out for a fascicle of unmyelinated axons. We extend this result to a nonlinear case and rigorously derive a bidomain model for a fascicle of myelinated axons. In particular, we consider the propagation of signals in a fascicle formed by a large number of axons. The microstructure of the fascicle is depicted as a set of closely packed thin cylinders (axons) with myelin sheaths arranged periodically in the surrounding extracellular matrix. The characteristic microscale of the structure is given by a small parameter $\varepsilon > 0$. Distances between neighboring axons, their diameters and the spacing of unmyelinated parts of the axon's membrane—Ranvier nodes—are assumed to be of order ε. By means of two-scale analysis we derive a bidomain model that describes the asymptotic behavior of the transmembrane potential on Ranvier nodes when ε is sufficiently small. We adopt the FitzHugh-Nagumo dynamics on the unmyelinated membrane. Main technical difficulties come from the nonlinear dynamics and the lack of a priori estimates ensuring strong convergence of the membrane potential on the Ranvier nodes. This lack of compactness is caused by the fact that the axons form a disconnected microstructure inside the fascicle, which stands in the contrast with connected microstructure of syncytial tissues. In order to derive the homogenized problem we transform problem to a form allowing us to combine two-scale convergence machinery with the method of monotone operators. Well-posedness of the micro- and macroscopic problems are also shown via reduction to parabolic equations with monotone operators.

4.2. Microscopic model

4.3. Problem setup

A nerve fascicle is modeled by the cylinder $\Omega := (0, L) \times \omega \subset \mathbb{R}^3$ with length $L > 0$ and cross section $\omega \subset \mathbb{R}^2$, being a bounded domain in $\mathbb{R}^2$ with a Lipschitz boundary $\partial\omega$ (see Figure 4-1). The lateral boundary of the cylinder is denoted by $\Sigma := [0, L] \times \partial\omega$, with bases $S_0 := \{0\} \times \omega$, $S_L := \{L\} \times \omega$. The bulk of the cylinder consists of an intracellular part formed by thin cylinders (axons), an extracellular part, and myelin sheaths. To describe the microstructure of the fascicle, we introduce a periodicity cell $Y := [-\frac{1}{2}, \frac{1}{2}) \times [-R_0, R_0)^2$, consisting of three disjoint Lipschitz domains: (i) an intracellular part $Y_i := [-\frac{1}{2}, \frac{1}{2}) \times D_{r_0}$, where D_{r_0} is the disk with radius $0 < r_0 < \frac{1}{2}$; (ii) a myelin sheath Y_m; (iii) an extracellular domain Y_e. The real positive radii satisfy $r_0 < R_0$. We denote by $\Gamma_{mi} := \overline{Y_i} \cap \overline{Y_m}$ the interface between Y_i and Y_m. The interface between the extracellular domain Y_e and a myelin sheath Y_m is $\Gamma_{me} := \overline{Y_e} \cap \overline{Y_m}$. The unmyelinated part of the boundary of Y_i (the Ranvier node) will be denoted by $\Gamma = \overline{Y_i} \cap \overline{Y_e}$ (see Figure 4-1). We will assume that Γ does not degenerate, and, for simplicity, that Γ is connected.

The periodicity cell is translated by vertices of the lattice $\mathbb{Z} \times (2R_0\mathbb{Z})^2$ to form a Y-periodic structure, and then scaled by a small parameter $\varepsilon > 0$. We take only those axons that are entirely contained in Ω. As a result, the domain is the union of three disjoint parts $\Omega_\varepsilon^i, \Omega_\varepsilon^e, \Omega_\varepsilon^m$, and their boundaries (see Figure 4-1). The unmyelinated part of the boundary of Ω_ε^i is denoted by Γ_ε. The boundary of the myelin is denoted by Γ_ε^m. Let
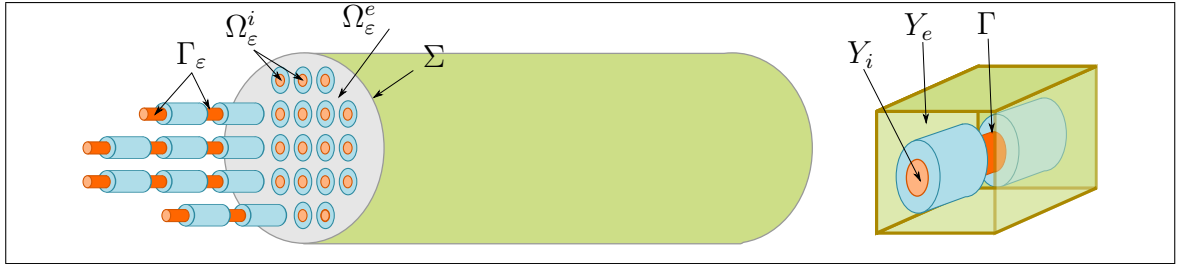
FIGURE 4-1. A fascicle of myelinated axons and the periodicity cell Y.

u_ε denotes the electric potential $u_\varepsilon = u_\varepsilon^l$ in Ω_ε^l, $l = i, e$. We assume that u_ε satisfies homogeneous Neumann boundary conditions on the boundary of the myelin sheath Γ_ε^m, i.e the myelin sheath is assumed to be a perfect insulator (see (Jerez-Hanckes et al., 2020) for other insulation assumptions). The transmembrane potential $v_\varepsilon = [u_\varepsilon] = u_\varepsilon^i - u_\varepsilon^e$ is the potential jump across the Ranvier nodes Γ_ε. We assume that the conductivity is a piecewise constant function:

$$a_\varepsilon = \begin{cases} a_e & \text{in } \Omega_\varepsilon^e, \\ a_i & \text{in } \Omega_\varepsilon^i. \end{cases}$$

On Γ_ε we further assume current continuity, and FitzHugh-Nagumo (FitzHugh, 1955; Nagumo, Arimoto, & Yoshizawa, 1962) dynamics for the transmembrane potential. Namely, the ionic current is described as

$$I_{ion}(v_\varepsilon, g_\varepsilon) = \frac{v_\varepsilon^3}{3} - v_\varepsilon - g_\varepsilon,$$

where g_ε is the recovery variable whose evolution is governed by the ordinary differential equation

$$\partial_t g_\varepsilon = \theta v_\varepsilon + a - b g_\varepsilon$$

with constant coefficients $\theta, a, b > 0$. The recovery variable is introduced to eliminate the excitability of the model after excitation has occurred (see (FitzHugh, 1955)).

We consider an arbitrary time interval $(0, T)$, $T > 0$. The electric activity in the bundle Ω is described by the following system of equations for the unknowns v_ε and g_ε:

$$
\begin{aligned}
&- \operatorname{div}(a_\varepsilon \nabla u_\varepsilon) = 0, && (t, x) \in (0, T) \times (\Omega_\varepsilon^i \cup \Omega_\varepsilon^e), \\
&a_e \nabla u_\varepsilon^e \cdot \nu = a_i \nabla u_\varepsilon^i \cdot \nu, && (t, x) \in (0, T) \times \Gamma_\varepsilon, \\
&\varepsilon(c_m \partial_t [u_\varepsilon] + I_{ion}([u_\varepsilon], g_\varepsilon)) = -a_i \nabla u_\varepsilon^i \cdot \nu, && (t, x) \in (0, T) \times \Gamma_\varepsilon, \\
&\partial_t g_\varepsilon = \theta [u_\varepsilon] + a - b g_\varepsilon, && (t, x) \in (0, T) \times \Gamma_\varepsilon, \\
&u_\varepsilon = 0, && (t, x) \in (0, T) \times (S_0 \cup S_L), \quad (4.1)
\end{aligned}
$$

$$a_e \nabla u_\varepsilon^e \cdot \nu = J_\varepsilon^e(t,x), \qquad\qquad (t,x) \in (0,T) \times \Sigma,$$

$$\nabla u_\varepsilon^e \cdot \nu = 0, \qquad\qquad (t,x) \in (0,T) \times \Gamma_\varepsilon^m,$$

$$[u_\varepsilon](0,x) = V_\varepsilon^0(x), \ \ g_\varepsilon(0,x) = G_\varepsilon^0(x), \qquad x \in \Gamma_\varepsilon,$$

where ν denotes the unit normal on Γ_ε, Γ_ε^m, and Σ, exterior to Ω_ε^i, Ω_ε^m, and Ω, respectively. The function $J_\varepsilon^e(t,x)$ models an external boundary excitation of the nerve fascicle. The membrane capacity per unit area c_m is assumed to be a positive constant. The myelin sheath is assumed to be a perfect insulator implying that the electrical field does not penetrate it, this leads to the homogeneous Neumann boundary condition on Γ_ε^m. That is why the equation in the bulk is posed for $x \in \Omega_\varepsilon^i \cup \Omega_\varepsilon^e$.

System (4.1), modeling the electrical conduction in nerves, arises from the Maxwell equations in the quasi-stationary approximation. A derivation of (4.1) from the first principles is presented in (Jæger & Tveito, 2021). See also (Tveito et al., 2017) for a numerical comparison of different models. On the membrane Γ_ε we assume the continuity of fluxes condition and the nonlinear FitzHugh dynamics for the potential jump (action potential) $[u_\varepsilon]$. A similar model has been used for modeling the electric conduction in the cardiac tissue (see e.g. (Franzone & Savaré, 2002), (Pennacchio et al., 2005), (Amar et al., 2021), (Grandelius & Karlsen, 2019)). While the cardiac tissue models assume that both intracellular and extracellular domains are connected, in the present model the intracellular domain is formed by non-intersecting individual axons.

We study the asymptotic behavior of u_ε, as $\varepsilon \to 0$, and derive a macroscopic model describing the potential u_ε in the fascicle, under the following conditions:

(H1) The initial data is such that[1] $\|V_\varepsilon^0\|_{L^4(\Gamma_\varepsilon)} \le C$. Moreover, we assume that V_ε^0 can be extended to the whole Ω such that, keeping the same notation for the extension, $\|V_\varepsilon^0\|_{H^1(\Omega)} \le C$ and $V_\varepsilon^0 = 0$ on $S_0 \cup S_L$. We also assume that there exists a weak limit $V_\varepsilon^0 \rightharpoonup V^0$ in $H^1(\Omega)$.

---

[1]Throughout, C denotes a generic constant independent of ε, whose value may be different from line to line.

(H2) There exists $G^0 \in L^2(\Omega)$, such that

- for any $\phi \in C(\overline{\Omega})$, it holds that

$$\lim_{\varepsilon \to 0} \varepsilon \int_{\Gamma_\varepsilon} G_\varepsilon^0(x)\phi(x)\, d\sigma = \frac{|\Gamma|}{|Y|} \int_\Omega G^0(x)\phi(x)\, dx;$$

- $\varepsilon \int_{\Gamma_\varepsilon} |G_\varepsilon^0|^2\, d\sigma \to \frac{|\Gamma|}{|Y|} \int_\Omega |G^0|^2\, dx, \quad \varepsilon \to 0.$

(H3) The external excitation $J_\varepsilon^e \in L^2((0,T) \times \Sigma)$ converges weakly to $J^e(t,x)$, as $\varepsilon \to 0$, and

$$\int_0^T \int_\Sigma |\partial_t J_\varepsilon^e|^2\, d\sigma d\tau \leq C.$$

REMARK 4.1. *Hypothesis (H2) actually assumes strong two-scale convergence (cf. Proposition 2.5 in (Allaire & Damlamian, 1995)). Hypothesis (H2) is satisfied if G_ε^0 is sufficiently regular, e.g. continuous, and independent of ε. Note that hypotheses (H1), (H2) are not satisfied for rapidly oscillating initial data.*

REMARK 4.2. *The scaling factor ε in the nonlinear equation for $[u_\varepsilon]$ on Γ_ε leads to a limit bidomain model and a nontrivial coupling of the potentials in the individual axons in the bundle through the extracellular currents. Different scaling factors in the equation on the Ranvier nodes Γ_ε might be considered. In (Amar, Andreucci, Bisegna, & Gianni, 2006) and (Amar, Andreucci, Bisegna, & Gianni, 2013), the authors address an hierarchy of models for the electrical conduction of biological tissue in linear and nonlinear cases. Namely, for ε^k, $k = -1, 0, 1$, the homogenization procedure yields different limit problems.*

4.3.1. Main result

The main result of the paper (Theorem 4.1 below) shows that the asymptotic behavior of solutions of the boundary value problem (4.1) is described by the following effective bidomain model in Ω:

$$c_m \partial_t v_0 + I_{ion}(v_0, g_0) = a_i^{\text{eff}} \partial_{x_1 x_1}^2 u_0^i, \qquad (t,x) \in (0,T) \times \Omega,$$

$$c_m \partial_t v_0 + I_{ion}(v_0, g_0) = -\text{div}(a_e^{\text{eff}} \nabla u_0^e), \qquad (t,x) \in (0,T) \times \Omega,$$

$$\partial_t g_0 = \theta v_0 + a - b\, g_0, \qquad\qquad (t,x) \in (0,T) \times \Omega, \qquad\qquad (4.2)$$

$$u_0^{i,e}(t,x) = 0, \qquad\qquad (t,x) \in (0,T) \times (S_0 \cup S_L),$$

$$a_e^{\text{eff}} \nabla u_0^e \cdot \nu = J^e, \qquad\qquad (t,x) \in (0,T) \times \Sigma,$$

$$v_0(0,x) = V^0(x), \;\; g_0(0,x) = G^0(x), \qquad\qquad x \in \Omega,$$

where $v_0 = u_0^i - u_0^e$. The effective scalar coefficient a_i^{eff} is

$$a_i^{\text{eff}} := \frac{|Y_i|}{|\Gamma|} a_i. \qquad\qquad (4.3)$$

The effective matrix $a_e^{\text{eff}} \in \mathbb{R}^{3\times 3}$ is given by

$$(a_e^{\text{eff}})_{kl} := \frac{1}{|\Gamma|} \int_{Y_e} a_e(\partial_l N_k^e(y) + \delta_{kl})\, dy, \quad k,l = 1,2,3, \qquad\qquad (4.4)$$

with the functions N_k^e, $k = 1,2,3$, solving the following auxiliary cell problems in Y_e

$$-\Delta N_k^e = 0, \qquad\qquad y \in Y_e,$$

$$\nabla N_k^e \cdot \nu = -\nu_k, \qquad\qquad y \in \Gamma \cup \Gamma_m,$$

$$N_k^e(y) \text{ is } Y - \text{periodic}.$$

Theorem 4.1. *Under the hypothesis (H1)–(H3), the solutions $v_\varepsilon = [u_\varepsilon]$, g_ε of the microscopic problem* (4.1) *converge to the solutions $v_0 = u_0^i - u_0^e$, g_0 of the macroscopic one* (4.2) *in the following sense:*

(i) *For any $\phi(t,x) \in C([0,T] \times \overline{\Omega})$, it holds that*

$$\lim_{\varepsilon \to 0} \varepsilon \int_0^T \int_{\Gamma_\varepsilon} v_\varepsilon(t,x)\phi(t,x)\, d\sigma_x dt = \frac{|\Gamma|}{|Y|} \int_0^T \int_\Omega v_0(t,x)\phi(t,x)\, dxdt,$$

and for any $t \in [0,T]$ $\displaystyle \lim_{\varepsilon \to 0} \varepsilon \int_{\Gamma_\varepsilon} |v_\varepsilon|^2\, d\sigma = \frac{|\Gamma|}{|Y|} \int_\Omega |v_0|^2\, dx.$

(ii) *For any $\phi(t,x) \in C([0,T] \times \overline{\Omega})$,*

$$\lim_{\varepsilon \to 0} \varepsilon \int_0^T \int_{\Gamma_\varepsilon} g_\varepsilon(t,x)\phi(t,x)\, d\sigma_x dt = \frac{|\Gamma|}{|Y|} \int_0^T \int_\Omega g_0(t,x)\phi(t,x)\, dxdt,$$

and for any $t \in [0, T]$ $\lim\limits_{\varepsilon \to 0} \varepsilon \int_{\Gamma_\varepsilon} |g_\varepsilon|^2 \, d\sigma = \dfrac{|\Gamma|}{|Y|} \int_\Omega |g_0|^2 \, dx.$

(iii) $\lim\limits_{\varepsilon \to 0} \int_0^T \int_{\Omega_\varepsilon^{i,e}} |u_\varepsilon^{i,e} - u_0^{i,e}|^2 \, dx dt = 0.$

REMARK 4.3. *If v_0 is continuous, the convergences (i), (ii) imply strong convergence of v_ε. Namely, for any $t \in [0, T]$, one obtains*

$$\lim_{\varepsilon \to 0} \varepsilon \int_{\Gamma_\varepsilon} |v_\varepsilon - v_0|^2 \, d\sigma = 0.$$

In general, approximating v_0 in $L^2(\Omega)$ by $v_{0\delta} \in C(\Omega)$, we have

$$\limsup_{\delta \to 0} \limsup_{\varepsilon \to 0} \varepsilon \int_{\Gamma_\varepsilon} |v_\varepsilon - v_{0\delta}|^2 \, d\sigma = 0.$$

REMARK 4.4. *The result can be generalized to the case of a varying cross section, as in (Jerez-Hanckes et al., 2021). In such case, the solution N_1^i of the cell problem (4.40) is no longer constant, and the corresponding effective coefficient is given by*

$$a_i^{\mathrm{eff}} = \frac{1}{|\Gamma|} \int_{Y_i} a_i (\partial_1 N_1^i + 1) dy.$$

REMARK 4.5. *Hypothesis (H2) can be generalized to the case of an oscillating initial function G_ε^0. Namely, assume that there exists $G^0(x, y) \in L^2(\Omega \times \Gamma)$, Y-periodic in y such that*

- *for any $\phi(x, y) \in C(\overline{\Omega} \times Y)$, Y-periodic in y,*

$$\lim_{\varepsilon \to 0} \varepsilon \int_{\Gamma_\varepsilon} G_\varepsilon^0(x) \phi\left(x, \frac{x}{\varepsilon}\right) d\sigma_x = \frac{1}{|Y|} \int_\Omega \int_\Gamma G^0(x, y) \phi(x, y) \, d\sigma_y dx;$$

- $\varepsilon \int_{\Gamma_\varepsilon} |G_\varepsilon^0|^2 \, d\sigma \to \dfrac{1}{|Y|} \int_\Omega \int_\Gamma |G^0(x, y)|^2 \, d\sigma_y dx, \quad \varepsilon \to 0.$

Then, the two-scale limit $\widetilde{g}_0(t, x, y)$ of g_ε does depend on the fast variable y, and denoting $g_0(t, x) = \dfrac{1}{|\Gamma|} \int_\Gamma \widetilde{g}_0(t, x, y) \, d\sigma_y$, the effective problem reads

$$c_m \partial_t v_0 + I_{ion}(v_0, g_0) = a_i^{\mathrm{eff}} \partial_{x_1 x_1}^2 u_0^i, \qquad (t, x) \in (0, T) \times \Omega,$$

$$c_m \partial_t v_0 + I_{ion}(v_0, g_0) = -\mathrm{div}(a_e^{\mathrm{eff}} \nabla u_0^e), \qquad (t, x) \in (0, T) \times \Omega,$$

$$\partial_t \widetilde{g}_0 = \theta v_0 + a - b \widetilde{g}_0, \qquad\qquad (t, x, y) \in (0, T) \times \Omega \times Y,$$

$$u_0^{i,e}(t, x) = 0, \qquad\qquad (t, x) \in (0, T) \times (S_0 \cup S_L),$$

$$a_e^{\mathrm{eff}} \nabla u_0^e \cdot \nu = J^e, \qquad\qquad (t, x) \in (0, T) \times \Sigma,$$

$$v_0(0, x) = V^0(x), \ \widetilde{g}_0(0, x) = G^0(x, y) \qquad\qquad x \in \Omega, \ y \in Y.$$

Thanks to the linearity of the equation $\partial_t \widetilde{g}_0 = \theta v_0 + a - b \widetilde{g}_0$, averaging in y, yields (4.2) *with the initial condition* $g_0(0, x) = \dfrac{1}{|\Gamma|} \displaystyle\int_\Gamma G^0(x, y) \, d\sigma_y.$

4.3.2. Well-posedness

In order to show the well-posedness of the microscopic problem (4.1), we write it as a Cauchy problem for an abstract parabolic equation.

We multiply (4.1) by a smooth function $\phi = \begin{cases} \phi^i \text{ in } \Omega_\varepsilon^i \\ \phi^e \text{ in } \Omega_\varepsilon^e \end{cases}$, $\phi^{i,e} = 0$ on $S_0 \cup S_L$, and integrate by parts:

$$\varepsilon \int_{\Gamma_\varepsilon} c_m \partial_t v_\varepsilon [\phi] \, d\sigma + \int_{\Omega_\varepsilon^i \cup \Omega_\varepsilon^e} a_\varepsilon \nabla u_\varepsilon \cdot \nabla \phi \, dx + \varepsilon \int_{\Gamma_\varepsilon} I_{ion}(v_\varepsilon, g_\varepsilon)[\phi] \, d\sigma = \int_\Sigma J_\varepsilon^e \phi \, d\sigma.$$

Let us introduce an auxiliary function q_ε solving the following problem:

$$-\mathrm{div}(a_\varepsilon \nabla q_\varepsilon) = 0, \qquad\qquad x \in \Omega_\varepsilon^i \cup \Omega_\varepsilon^e \cup \Gamma_\varepsilon,$$

$$\nabla q_\varepsilon \cdot \nu = 0, \qquad\qquad x \in \Gamma_{m,\varepsilon}, \qquad\qquad (4.5)$$

$$a_e \nabla q_\varepsilon \cdot \nu = J_\varepsilon^e(t, x), \qquad\qquad x \in \Sigma,$$

$$q_\varepsilon = 0, \qquad\qquad x \in (S_0 \cup S_L).$$

Since the jump of q_ε through the Ranvier nodes Γ_ε is zero, the change of unknown

$$\widetilde{u}_\varepsilon = u_\varepsilon - q_\varepsilon$$

allows us to transfer the external excitation J_ε^e from the lateral boundary Σ to the membrane Γ_ε. Namely, we get the following weak formulation for the new unknown function $\widetilde{u}_\varepsilon$:

$$\varepsilon \int_{\Gamma_\varepsilon} c_m \partial_t v_\varepsilon [\phi] \, d\sigma + \int_{\Omega_\varepsilon^i \cup \Omega_\varepsilon^e} a_\varepsilon \nabla \widetilde{u}_\varepsilon \cdot \nabla \phi \, dx + \varepsilon \int_{\Gamma_\varepsilon} I_{ion}(v_\varepsilon, g_\varepsilon)[\phi] \, d\sigma$$

$$+ \int_{\Gamma_\varepsilon} (a_i \nabla q_\varepsilon \cdot \nu)[\phi] \, d\sigma = 0.$$

Let us define the subspace

$$H^1_{S_0 \cup S_L}(\Omega_\varepsilon^i \cup \Omega_\varepsilon^e) := \left\{ \phi \in H^1(\Omega_\varepsilon^i \cup \Omega_\varepsilon^e) \ : \ \phi\big|_{S_0 \cap S_L} = 0 \right\},$$

and introduce the operator $A_\varepsilon : D(A_\varepsilon) \subset H^{1/2}(\Gamma_\varepsilon) \to H^{-1/2}(\Gamma_\varepsilon)$ as follows

$$(A_\varepsilon v_\varepsilon, [\phi])_{L^2(\Gamma_\varepsilon)} := \int_{\Omega_\varepsilon^i \cup \Omega_\varepsilon^e} a_\varepsilon \nabla \widetilde{u}_\varepsilon \cdot \nabla \phi \, dx, \quad \forall \, \phi \in H^1_{S_0 \cup S_L}(\Omega_\varepsilon^i \cup \Omega_\varepsilon^e), \qquad (4.6)$$

where $\widetilde{u}_\varepsilon \in H^1(\Omega_\varepsilon^i \cup \Omega_\varepsilon^e)$, for a given jump $[\widetilde{u}_\varepsilon] = v_\varepsilon$, solves the following problem:

$$\begin{aligned}
-\operatorname{div}(a_\varepsilon \nabla \widetilde{u}_\varepsilon) &= 0, & x &\in \Omega_\varepsilon^i \cup \Omega_\varepsilon^e, \\
a_e \nabla \widetilde{u}_\varepsilon^e \cdot \nu &= a_i \nabla \widetilde{u}_\varepsilon^i \cdot \nu, & x &\in \Gamma_\varepsilon, \\
\widetilde{u}_\varepsilon^i - \widetilde{u}_\varepsilon^e &= v_\varepsilon, & x &\in \Gamma_\varepsilon, \qquad (4.7) \\
a_\varepsilon \nabla \widetilde{u}_\varepsilon \cdot \nu &= 0, & x &\in \Gamma_{m,\varepsilon}, \\
a_e \nabla \widetilde{u}_\varepsilon \cdot \nu &= 0, & x &\in \Sigma, \\
\widetilde{u}_\varepsilon &= 0, & x &\in (S_0 \cup S_L).
\end{aligned}$$

Thus, problem (4.1) can be rewritten in the following compact form:

$$\varepsilon c_m \partial_t v_\varepsilon + A_\varepsilon v_\varepsilon + \varepsilon I_{ion}(v_\varepsilon, g_\varepsilon) = -a_i \nabla q_\varepsilon \cdot \nu, \qquad (4.8)$$

$$\partial_t g_\varepsilon + b g_\varepsilon - \theta v_\varepsilon = a$$

on Γ_ε. In order to reduce the problem to a monotone one, we perform the following change of unknowns:

$$W_\varepsilon = \begin{pmatrix} w_\varepsilon \\ h_\varepsilon \end{pmatrix} = e^{-\lambda t} \begin{pmatrix} v_\varepsilon \\ g_\varepsilon \end{pmatrix}, \quad W_\varepsilon^0 = \begin{pmatrix} V_\varepsilon^0 \\ G_\varepsilon^0 \end{pmatrix}. \tag{4.9}$$

with λ real positive. Substituting (4.9) into (4.8) yields

$$\varepsilon \partial_t \begin{pmatrix} w_\varepsilon \\ h_\varepsilon \end{pmatrix} + \begin{pmatrix} \dfrac{1}{c_m} A_\varepsilon w_\varepsilon + \dfrac{\varepsilon}{c_m} \left(\dfrac{e^{2\lambda t}}{3} w_\varepsilon^3 - w_\varepsilon - h_\varepsilon \right) + \varepsilon \lambda w_\varepsilon \\ \varepsilon (b + \lambda) h_\varepsilon - \varepsilon \theta w_\varepsilon \end{pmatrix}$$

$$= e^{-\lambda t} \begin{pmatrix} -\dfrac{a_i}{c_m} \nabla q_\varepsilon \cdot \nu \\ \varepsilon a \end{pmatrix},$$

which can be further rewritten as follows:

$$\varepsilon \partial_t W_\varepsilon + \mathbb{A}_\varepsilon(t, W_\varepsilon) = F_\varepsilon(t), \quad (t, x) \in (0, T) \times \Gamma_\varepsilon, \tag{4.10}$$

$$W_\varepsilon(0, x) = W_\varepsilon^0(x), \quad x \in \Gamma_\varepsilon.$$

$$\mathbb{A}_\varepsilon(t, W_\varepsilon) := B_\varepsilon^{(1)}(t, W_\varepsilon) + B_\varepsilon^{(2)}(t, W_\varepsilon), \tag{4.11}$$

$$B_\varepsilon^{(1)}(t, W_\varepsilon) := \begin{pmatrix} \dfrac{1}{c_m} A_\varepsilon w_\varepsilon + \varepsilon \left(\lambda - \dfrac{1}{c_m} \right) w_\varepsilon - \dfrac{\varepsilon}{c_m} h_\varepsilon \\ \varepsilon (b + \lambda) h_\varepsilon - \varepsilon \theta w_\varepsilon \end{pmatrix}, \tag{4.12}$$

$$B_\varepsilon^{(2)}(t, W_\varepsilon) := \begin{pmatrix} \varepsilon \dfrac{e^{2\lambda t}}{3c_m} w_\varepsilon^3 \\ 0 \end{pmatrix}, \quad F_\varepsilon(t) := e^{-\lambda t} \begin{pmatrix} -\dfrac{a_i}{c_m} \nabla q_\varepsilon \cdot \nu \\ \varepsilon a \end{pmatrix}. \tag{4.13}$$

Here the operator A_ε is defined in (4.6).

The existence of a unique solution to problem (4.10) follows from Theorem 1.4 in (Lions, 1969) and Remark 1.8 in Chapter 2 (see also Theorem 4.1 in (Showalter, 2013)). For the reader's convenience, we formulate the corresponding result below.

Lemma 4.1. *Let V_i, $i = 1, \ldots, m$, be reflexive Banach spaces, and H be a real Hilbert space such that $V_i \subset H \subset V_i'$. Let $A(t) = \sum_{i=1}^{m} A_i(t)$, and let $\{A_i(t); \ t \in [0, T]\}$, $i = 1, \ldots, m$, be a family of nonlinear, monotone, and demi-continuous operators from V_i to V_i' that satisfy the following conditions:*

(i) *The function $t \mapsto A_i(t)u(t) \in V_i'$ is measurable for every measurable function $u : [0, T] \to V$.*

(ii) *There exists a seminorm $[u]$ on V_i such that, for some constants $\alpha_1 > 0$ and $\alpha_2 > 0$, we have that*

$$[u] + \alpha_1 \|u\|_H \geq \alpha_2 \|u\|_{V_i},$$

and for some $\bar{c} > 0$ and $p_i > 1$,

$$(A_i(t)u, u) \geq \bar{c}[u]^{p_i}, \quad u \in V_i, \ t \in [0, T].$$

(iii) *For some $\underline{C}$ and the same $p_i > 1$ as in (ii),*

$$\|A_i(t)u\|_{V_i'} \leq \underline{C}(1 + \|u\|_{V_i}^{p_i - 1}), \quad u \in V_i, \ t \in [0, T].$$

Then, for every $u_0 \in H$ and $f \in \sum_{i=1}^{m} L^{q_i}(0, T; V_i')$, $1/p_i + 1/q_i = 1$, there is a unique absolutely continuous function $u \in \cap_{i=1}^{m} W^{1,q_i}([0, T]; V_i')$ that satisfies

$$u \in L^\infty([0, T]; H), \ u \in \cap_{i=1}^{m} L^{p_i}([0, T]; V_i),$$

$$\frac{du}{dt}(t) + A(t)u(t) = f(t), \quad a.e. \ t \in (0, T),$$

$$u(0) = u_0.$$

In order to apply Lemma 4.1, we introduce the necessary functional spaces:

$$H = L^2(\Gamma_\varepsilon) \times L^2(\Gamma_\varepsilon),$$

$$\widetilde{H}^{1/2}(\Gamma_\varepsilon) = \left\{ v = (u^i - u^e)\big|_{\Gamma_\varepsilon} : \ u^l \in H^1(\Omega_\varepsilon^l), \ u^l = 0 \text{ on } S_0 \cap S_L, l = i, e \right\},$$

$$V_1 = \widetilde{H}^{1/2}(\Gamma_\varepsilon) \times L^2(\Gamma_\varepsilon), \quad V_1' = H^{-1/2}(\Gamma_\varepsilon) \times L^2(\Gamma_\varepsilon),$$

$$V_2 = L^4(\Gamma_\varepsilon) \times L^2(\Gamma_\varepsilon), \quad V_2' = L^{4/3}(\Gamma_\varepsilon) \times L^2(\Gamma_\varepsilon).$$

As the operator $A_1(t, \cdot) : V_1 \to V_1'$ we take $B_\varepsilon^{(1)}(t, \cdot)$ given by (4.12); as the operator $A_2(t, \cdot) : V_2 \to V_2'$ we take $B_\varepsilon^{(2)}(t, \cdot)$ given by (4.13). Let us check that the operator $\mathbb{A}_\varepsilon(t, \cdot) = B_\varepsilon^{(1)} + B_\varepsilon^{(2)}$ satisfies the assumptions of Lemma 4.1 with $p_1 = 2$ and $p_2 = 4$. The right-hand side F_ε satisfies clearly the assumptions of Lemma 4.1.

Lemma 4.2. *For every $t \in [0, T]$, the linear operator $B_\varepsilon^{(1)}(t, \cdot) : V_1 \to V_1'$ has the following properties:*

(i) *Monotonicity:*

$$(B_\varepsilon^{(1)}(t, W_1) - B_\varepsilon^{(1)}(t, W_2), W_1 - W_2) \geq 0, \quad \forall\, W_1, W_2 \in V_1.$$

(ii) *Coercivity:*

$$(B_\varepsilon^{(1)}(t, W), W) \geq C_1 \|W\|_{V_1}^2, \quad \forall\, W \in V_1.$$

(iii) *Boundedness:*

$$\|B_\varepsilon^{(1)}(t, W)\|_{V_1'} \leq C_2 \|W\|_{V_1}, \quad \forall\, W \in V_1.$$

PROOF. (i) The monotonicity of the operator $B_\varepsilon^{(1)}$ follows from its linearity and coercivity properties (as shown below).

(ii) By (4.12), for any $W_\varepsilon \in \widetilde{H}^{1/2}(\Gamma_\varepsilon) \times L^2(\Gamma_\varepsilon)$, we have

$$(B_\varepsilon^{(1)}(t, W_\varepsilon), W_\varepsilon) = \frac{1}{c_m} \int_{\Omega_\varepsilon^i \cup \Omega_\varepsilon^e} a_\varepsilon |\nabla \widetilde{w}_\varepsilon|^2 \, dx + \varepsilon \left(\lambda - \frac{1}{c_m} \right) \int_{\Gamma_\varepsilon} |w_\varepsilon|^2 \, d\sigma$$
$$- \varepsilon \left(\theta + \frac{1}{c_m} \right) \int_{\Gamma_\varepsilon} h_\varepsilon w_\varepsilon \, d\sigma + \varepsilon(b + \lambda) \int_{\Gamma_\varepsilon} |h_\varepsilon|^2 \, d\sigma.$$

Here $\widetilde{w}_\varepsilon = e^{-\lambda t} u_\varepsilon$ solves (4.7) with the jump on Γ_ε that equals to $e^{-\lambda t} v_\varepsilon$. Using the trace inequality and choosing λ sufficiently large and independent of ε, we obtain

$$(B_\varepsilon^{(1)}(t, W_\varepsilon), W_\varepsilon) \geq C_1^\varepsilon \|w_\varepsilon\|_{\widetilde{H}^{1/2}(\Gamma_\varepsilon)}^2 + C_2^\varepsilon \|h_\varepsilon\|_{L^2(\Gamma_\varepsilon)}^2 = C^\varepsilon \|W_\varepsilon\|_{V_1}^2.$$

Here $C_1^\varepsilon, C_2^\varepsilon$, and C^ε are positive constants.

(iii) Let us estimate the norm of $B_\varepsilon^{(1)}(t, W)$. For any $W_\varepsilon \in V_1$ and a test function $\Phi = ([\varphi], \psi)^T \in V_1$, by (4.11) we have

$$(B_\varepsilon^{(1)}(t, W_\varepsilon), \Phi)_{L^2(\Gamma_\varepsilon)^2} = \frac{1}{c_m} \int_{\Omega_\varepsilon^i \cup \Omega_\varepsilon^e} a_\varepsilon \nabla \widetilde{w}_\varepsilon \cdot \nabla \varphi \, dx + \varepsilon \left(\lambda - \frac{1}{c_m} \right) \int_{\Gamma_\varepsilon} w_\varepsilon [\varphi] d\sigma$$
$$- \frac{\varepsilon}{c_m} \int_{\Gamma_\varepsilon} h_\varepsilon [\varphi] d\sigma + \varepsilon (b + \lambda) \int_{\Gamma_\varepsilon} h_\varepsilon \psi d\sigma - \varepsilon \theta \int_{\Gamma_\varepsilon} w_\varepsilon \psi d\sigma.$$

Here φ solves a stationary problem (4.7) with a given jump $[\varphi]$ on Γ_ε.

Clearly, $\|\nabla \widetilde{w}_\varepsilon\|_{L^2(\Omega_\varepsilon^i \cup \Omega_\varepsilon^e)} \leq C \|w_\varepsilon\|_{\widetilde{H}^{1/2}(\Gamma_\varepsilon)}$. The test function φ is estimated in a standard way in terms of $\|[\varphi]\|_{\widetilde{H}^{1/2}(\Gamma_\varepsilon)}$. Then, by the Cauchy-Schwartz inequality, one retrieves

$$(B_\varepsilon^{(1)}(t, W_\varepsilon), \Phi)_{L^2(\Gamma_\varepsilon)^2} \leq C_1 \|w_\varepsilon\|_{\widetilde{H}^{1/2}(\Gamma_\varepsilon)} \|[\varphi]\|_{\widetilde{H}^{1/2}(\Gamma_\varepsilon)}$$
$$+ C_2 (\|w_\varepsilon\|_{\widetilde{H}^{1/2}(\Gamma_\varepsilon)} + \|h_\varepsilon\|_{\widetilde{H}^{1/2}(\Gamma_\varepsilon)}) \|[\Phi]\|_{V_1},$$

which proves the estimate from above for $\|B_\varepsilon^{(1)}(t, W)\|_{V_1'}$. $\qquad \square$

Lemma 4.3. *For every $t \in [0, T]$, the operator $B_\varepsilon^{(2)}(t, \cdot) : V_2 \to V_2'$ has the following properties:*

(i) *Monotonicity:*

$$(B_\varepsilon^{(2)}(t, W_1) - B_\varepsilon^{(2)}(t, W_2), W_1 - W_2) \geq 0, \quad \forall W_1, W_2 \in V_2.$$

(ii) *Coercivity:* $\| \cdot \|_{L^4(\Gamma_\varepsilon)}$ *defines a seminorm on V_2 such that, for some constants $\alpha_1 > 0$ and $\alpha_2 > 0$, we have*

$$\|W\|_{L^4(\Gamma_\varepsilon)} + \alpha_1 \|W\|_H \geq \alpha_2 \|W\|_{V_2},$$

and

$$(B_\varepsilon^{(2)}(t, W), W) \geq C_1 \|W\|_{V_2}^4, \quad \forall W \in V_1.$$

(iii) *Boundedness:*

$$\|B_\varepsilon^{(2)}(t,W)\|_{V_2'} \le C_2\|W\|_{L^4(\Gamma_\varepsilon)}^3, \quad \forall\, W \in V_2.$$

PROOF. (i) The monotonicity of $B_\varepsilon^{(2)}$ follows from the monotonicity of the cubic function $f(u) = u^3$.

(ii) By definition (4.13), it holds that

$$(B_\varepsilon^{(2)}(t,W_\varepsilon), W_\varepsilon) = \frac{\varepsilon e^{2\lambda t}}{3c_m} \int_{\Gamma_\varepsilon} |w_\varepsilon|^4 \, d\sigma,$$

which proves (ii).

(iii) The boundedness follows from (4.13):

$$\|B_\varepsilon^{(2)}(t,W_\varepsilon)\|_{V_2'} = \varepsilon \left[\int_{\Gamma_\varepsilon} \left(\frac{e^{2\lambda t}}{3c_m}(w_\varepsilon)^3\right)^{\frac{4}{3}} d\sigma\right]^{\frac{3}{4}} = \frac{\varepsilon e^{2\lambda t}}{3c_m}\|w_\varepsilon\|_{L^4(\Gamma_\varepsilon)}^3 \le C^\varepsilon \|W_\varepsilon\|_{V_2}^3,$$

where C^ε is a positive constant. $\qquad\square$

Obviously, the function $t \mapsto \mathbb{A}_\varepsilon(t,W)$ satisfies the measurability assumption of Lemma 4.1, and the demi-continuity property follows from the estimates in Lemmas 4.2 and 4.3.

4.4. Proof of Theorem 4.1

4.4.1. A priori estimates

The next lemma provides the estimates for $(z_\varepsilon, h_\varepsilon) = e^{-\lambda t}(u_\varepsilon, g_\varepsilon)$, where $[z_\varepsilon] = w_\varepsilon$, at time $t = 0$.

Lemma 4.4. *Under hypotheses (H1)–(H3), at time $t = 0$ the following estimates hold*

$$\int_{\Omega_\varepsilon^i \cup \Omega_\varepsilon^e} a_\varepsilon |\nabla z_\varepsilon|^2 \, dx \bigg|_{t=0} + \int_\Sigma |z_\varepsilon|^2 \, d\sigma \bigg|_{t=0} \le C. \tag{4.14}$$

PROOF. One can see that the operator A_ε given by (4.6) can be defined by means of the minimization problem

$$(A_\varepsilon w_\varepsilon, w_\varepsilon) = \min_{[\phi_\varepsilon]=w_\varepsilon} \int_{\Omega_\varepsilon^i \cup \Omega_\varepsilon^e} a_\varepsilon |\nabla \phi_\varepsilon|^2 \, dx,$$

where the minimum is taken over the functions $\phi_\varepsilon \in H^1(\Omega_\varepsilon^i \cup \Omega_\varepsilon^e)$ with the given jump $[\phi_\varepsilon] = w_\varepsilon$ on Γ_ε. Consider the test function $\phi_\varepsilon = \begin{cases} V_\varepsilon^0 \text{ in } \Omega_\varepsilon^i \\ 0 \text{ in } \Omega_\varepsilon^e \end{cases}$, then thanks to the assumption (H1) we have

$$\int_{\Omega_\varepsilon^i \cup \Omega_\varepsilon^e} a_\varepsilon |\nabla z_\varepsilon|^2 \, dx \Big|_{t=0} = (A_\varepsilon w_\varepsilon, w_\varepsilon) \Big|_{t=0} = \int_{\Omega_\varepsilon^i} a_i |\nabla V_\varepsilon^0|^2 \, dx \leq C.$$

The proof of the lemma is completed by using an extension operator from Ω_ε^e to Ω (see (4.17) below) together with the trace inequality. □

Now we prove the a priori estimates for the solutions of (4.10).

Lemma 4.5 (A priori estimates). *Let $W_\varepsilon = (w_\varepsilon, h_\varepsilon)$ be a solution of* (4.10). *Then, for $t \in [0, T]$, the following estimates hold:*

(i) $\varepsilon \displaystyle\int_{\Gamma_\varepsilon} |w_\varepsilon|^4 \, d\sigma + \varepsilon \int_0^t \int_{\Gamma_\varepsilon} |\partial_\tau w_\varepsilon|^2 \, d\sigma \, d\tau \leq C.$

(ii) $\varepsilon \displaystyle\int_{\Gamma_\varepsilon} |h_\varepsilon|^2 \, d\sigma + \varepsilon \int_0^t \int_{\Gamma_\varepsilon} |\partial_\tau h_\varepsilon|^2 \, d\sigma \, d\tau \leq C.$

(iii) *Let $z_\varepsilon = e^{-\lambda t} u_\varepsilon$ with the jump $[z_\varepsilon] = w_\varepsilon$ on Γ_ε. Then, one has that*

$$\int_{\Omega_\varepsilon^i \cup \Omega_\varepsilon^e} (|z_\varepsilon|^2 + |\nabla z_\varepsilon|^2) \, dx \leq C,$$

for a constant C independent of ε and t, but depending on T and the norms of initial functions $\|G_\varepsilon^0\|_{L^2(\Gamma_\varepsilon)}, \|V_\varepsilon^0\|_{L^4(\Gamma_\varepsilon)}, \|V_\varepsilon^l\|_{H^1(\Omega)}$.

PROOF. We will work with the equation in vector form (4.10) and derive the a priori estimates for the pair $(w_\varepsilon, h_\varepsilon)$. Let z_ε be the solution of the stationary problem with the jump w_ε:

$$- \operatorname{div}(a_\varepsilon \nabla z_\varepsilon) = 0, \qquad\qquad x \in \Omega_\varepsilon^i \cup \Omega_\varepsilon^e,$$

$$a_e \nabla z_\varepsilon^e \cdot \nu = a_i \nabla z_\varepsilon^i \cdot \nu, \qquad\qquad x \in \Gamma_\varepsilon,$$

$$z_\varepsilon^i - z_\varepsilon^e = w_\varepsilon, \qquad\qquad x \in \Gamma_\varepsilon, \qquad (4.15)$$

$$a_\varepsilon \nabla z_\varepsilon \cdot \nu = 0, \qquad\qquad x \in \Gamma_{m,\varepsilon},$$

$$a_e \nabla z_\varepsilon \cdot \nu = \frac{e^{-\lambda t}}{c_m} J_\varepsilon^e, \qquad\qquad x \in \Sigma,$$

$$z_\varepsilon = 0, \qquad\qquad x \in (S_0 \cup S_L).$$

We multiply (4.10) by W_ε and integrate over Γ_ε:

$$\frac{\varepsilon}{2} \partial_t \int_{\Gamma_\varepsilon} |w_\varepsilon|^2 \, d\sigma + \frac{1}{c_m} \int_{\Omega_\varepsilon^i \cup \Omega_\varepsilon^e} a_\varepsilon \nabla z_\varepsilon \cdot \nabla z_\varepsilon \, dx + \frac{\varepsilon}{c_m} \int_{\Gamma_\varepsilon} \frac{e^{2\lambda t}}{3} w_\varepsilon^4 \, d\sigma$$

$$+ \varepsilon \left(\lambda - \frac{1}{c_m} \right) \int_{\Gamma_\varepsilon} |w_\varepsilon|^2 \, d\sigma - \varepsilon \left(\theta + \frac{1}{c_m} \right) \int_{\Gamma_\varepsilon} h_\varepsilon w_\varepsilon \, d\sigma + \frac{\varepsilon}{2} \partial_t \int_{\Gamma_\varepsilon} |h_\varepsilon|^2 \, d\sigma \qquad (4.16)$$

$$+ \varepsilon(\lambda + b) \int_{\Gamma_\varepsilon} |h_\varepsilon|^2 \, d\sigma = \frac{e^{-\lambda t}}{c_m} \int_\Sigma J_\varepsilon^e z_\varepsilon \, d\sigma + \varepsilon a e^{-\lambda t} \int_{\Gamma_\varepsilon} h_\varepsilon d\sigma.$$

It is known (Acerbi, ChiadoPiat, Dal Maso, & Percivale, 1992) that there exists an extension operator P_ε from Ω_ε^e to Ω such that $\|\nabla P_\varepsilon z_\varepsilon^e\|_{L^2(\Omega)} \le C \|\nabla z_\varepsilon^e\|_{L^2(\Omega_\varepsilon^e)}$ with a constant C independent of ε. This result combined with the Friedrichs inequality ($z_\varepsilon = 0$ on $S_0 \cup S_L$) implies that

$$\|P_\varepsilon z_\varepsilon^e\|_{H^1(\Omega)} \le C \|\nabla z_\varepsilon^e\|_{L^2(\Omega_\varepsilon^e)}. \qquad (4.17)$$

By the trace inequality, the $L^2(\Sigma)$-norm of z_ε is then bounded by $\|\nabla z_\varepsilon^e\|_{L^2(\Omega_\varepsilon^e)}$. Using the Young inequality with a parameter in (4.16) and (4.17), yields

$$\partial_t \left(\varepsilon \int_{\Gamma_\varepsilon} |w_\varepsilon|^2 d\sigma + \varepsilon \int_{\Gamma_\varepsilon} |h_\varepsilon|^2 d\sigma \right) + \int_{\Omega_\varepsilon^i \cup \Omega_\varepsilon^e} |\nabla z_\varepsilon|^2 \, dx + \varepsilon \int_{\Gamma_\varepsilon} |w_\varepsilon|^4 d\sigma$$

$$+ \left(\varepsilon \int_{\Gamma_\varepsilon} |w_\varepsilon|^2 d\sigma + \varepsilon \int_{\Gamma_\varepsilon} |h_\varepsilon|^2 d\sigma \right) \le C \int_\Sigma |J_\varepsilon^e|^2 \, d\sigma. \qquad (4.18)$$

Applying the Grönwall inequality in (4.18), we obtain the following estimate:

$$\varepsilon \int_{\Gamma_\varepsilon} |w_\varepsilon|^2 d\sigma + \varepsilon \int_{\Gamma_\varepsilon} |h_\varepsilon|^2 d\sigma \le C. \qquad (4.19)$$

Integrating (4.18) with respect to t gives

$$\int_0^t \int_{\Omega_\varepsilon^i \cup \Omega_\varepsilon^e} |\nabla z_\varepsilon|^2 \, dx + \varepsilon \int_0^t \int_{\Gamma_\varepsilon} |w_\varepsilon|^4 d\sigma \qquad (4.20)$$

$$\leq C \left(\int_0^t \int_\Sigma |J_\varepsilon^e|^2 d\sigma d\tau + \varepsilon \int_{\Gamma_\varepsilon} |V_\varepsilon^0|^2 \, d\sigma + \varepsilon \int_{\Gamma_\varepsilon} |G_\varepsilon^0|^2 \, d\sigma \right).$$

Next, we derive the estimates for $\partial_t W_\varepsilon$. To this end, we multiply (4.10) by $\partial_t W_\varepsilon$ and integrate over $(0, t) \times \Gamma_\varepsilon$:

$$\frac{\varepsilon}{2} \int_0^t \int_{\Gamma_\varepsilon} |\partial_\tau w_\varepsilon|^2 \, d\sigma d\tau + \frac{\varepsilon}{2} \int_0^t \int_{\Gamma_\varepsilon} |\partial_\tau h_\varepsilon|^2 \, d\sigma d\tau$$

$$+ \frac{1}{2c_m} \int_{\Omega_\varepsilon^i \cup \Omega_\varepsilon^e} a_\varepsilon |\nabla z_\varepsilon|^2 \, dx - \frac{1}{2c_m} \int_{\Omega_\varepsilon^i \cup \Omega_\varepsilon^e} a_\varepsilon |\nabla z_\varepsilon|^2 \, dx \Big|_{t=0}$$

$$+ \frac{\varepsilon}{12c_m} e^{2\lambda t} \int_{\Gamma_\varepsilon} |w_\varepsilon|^4 \, d\sigma - \frac{\varepsilon}{12c_m} \int_{\Gamma_\varepsilon} |V_\varepsilon^0|^4 \, d\sigma$$

$$+ \frac{\varepsilon}{2}(\lambda - \frac{1}{c_m}) \int_{\Gamma_\varepsilon} |w_\varepsilon|^2 \, d\sigma - \frac{\varepsilon}{2}(\lambda - \frac{1}{c_m}) \int_{\Gamma_\varepsilon} |V_\varepsilon^0|^2 \, d\sigma$$

$$+ \frac{\varepsilon}{2}(\lambda + b) \int_{\Gamma_\varepsilon} |h_\varepsilon|^2 \, d\sigma - \frac{\varepsilon}{2}(\lambda + b) \int_{\Gamma_\varepsilon} |G_\varepsilon^0|^2 \, d\sigma \qquad (4.21)$$

$$\leq 2\lambda \varepsilon \int_0^t e^{2\lambda \tau} \int_{\Gamma_\varepsilon} |w_\varepsilon|^4 \, d\sigma d\tau$$

$$+ 2\theta^2 \varepsilon \int_0^t \int_{\Gamma_\varepsilon} |w_\varepsilon|^2 \, d\sigma d\tau + \frac{2\varepsilon}{c_m^2} \int_0^t \int_{\Gamma_\varepsilon} |h_\varepsilon|^2 \, d\sigma d\tau$$

$$+ \frac{e^{-\lambda t}}{c_m} \int_\Sigma J_\varepsilon^e z_\varepsilon \, d\sigma - \frac{1}{c_m} \int_\Sigma J_\varepsilon^e z_\varepsilon \, d\sigma \Big|_{t=0}$$

$$+ \frac{\lambda}{c_m} \int_0^t e^{-\lambda \tau} \int_\Sigma J_\varepsilon^e z_\varepsilon \, d\sigma d\tau - \int_0^t \frac{e^{-\lambda \tau}}{c_m} \int_\Sigma \partial_\tau J_\varepsilon^e z_\varepsilon \, d\sigma d\tau$$

$$+ \varepsilon a e^{-\lambda t} \int_{\Gamma_\varepsilon} h_\varepsilon \, d\sigma - \varepsilon a \int_{\Gamma_\varepsilon} G_\varepsilon^0 \, d\sigma + \varepsilon a \lambda \int_0^t e^{-\lambda \tau} \int_{\Gamma_\varepsilon} h_\varepsilon \, d\sigma d\tau.$$

Combining (4.19), (4.20), and (4.14) we get

$$\varepsilon \int_0^t \int_{\Gamma_\varepsilon} |\partial_\tau w_\varepsilon|^2 \, d\sigma d\tau + \int_{\Omega_\varepsilon^i \cup \Omega_\varepsilon^e} |\nabla z_\varepsilon|^2 \, dx + \varepsilon \int_{\Gamma_\varepsilon} |w_\varepsilon|^4 \, d\sigma \leq C.$$

Thanks to the homogeneous Dirichlet boundary condition on the bases $S_0 \cup S_L$, the L^2-norm of z_ε is estimated in terms on the ∇z_ε. Namely,

$$\int_{\Omega_\varepsilon^i} |z_\varepsilon^i|^2 \, dx \leq C \int_{\Omega_\varepsilon^i} |\partial_{x_1} z_\varepsilon^i|^2 \, dx,$$

$$\int_{\Omega_\varepsilon^e} |z_\varepsilon^e|^2 \, dx \leq C \int_{\Omega_\varepsilon^e} |\nabla z_\varepsilon^e|^2 \, dx.$$

The proof of Lemma 4.5 is finally complete. $\qquad\qquad\qquad\qquad\qquad\square$

4.4.2. Derivation of the macroscopic model

Since the axons inside the bundle are disconnected, a priori estimates provided by Lemma 4.5 do not imply the strong convergence of the transmembrane potential v_ε on Γ_ε. In turn, this makes passing to the limit in the nonlinear term I_{ion} problematic. We choose to combine the two-scale convergence machinery with the method of monotone operators due to G. Minty (Minty, 1962). For reader's convenience we provide a brief description of the method for a simple case in Appendix A, while its adaptation for problem (4.1) is presented below. For passage to the limit, as $\varepsilon \to 0$, we will use the two-scale convergence (Allaire, 1992). We refer to (Allaire & Damlamian, 1995) for two-scale convergence on periodic surfaces (namely, on Γ_ε).

Definition 4.1. *We say that a sequence $\{u_\varepsilon^l(t,x)\}$ two-scale converges to the function $u_0^l(t,x,y)$ in $L^2(0,T;L^2(\Omega_\varepsilon^l))$, $l = i, e$, as $\varepsilon \to 0$, and write*

$$u_\varepsilon^l(t,x) \xrightarrow{2} u_0^l(t,x,y),$$

if

(i) $\int_0^T \int_{\Omega_\varepsilon^l} |u_\varepsilon|^2 dx \, dt < C.$

(ii) *For any $\phi(t,x) \in C(0,T;L^2(\Omega))$, $\psi(y) \in L^2(Y_l)$ we have*

$$\lim_{\varepsilon \to 0} \int_0^T \int_{\Omega_\varepsilon^l} u_\varepsilon^l(t,x)\phi(t,x)\psi\left(\frac{x}{\varepsilon}\right) \, dx \, dt$$

$$= \frac{1}{|Y|} \int_0^T \int_\Omega \int_{Y^l} u_0^l(t,x,y)\phi(t,x)\psi(y)\,dy\,dx\,dt,$$

for some function $u_0^l \in L^2(0,T;L^2(\Omega \times Y))$.

Definition 4.2. *A sequence $\{v_\varepsilon(t,x)\}$ converges two-scale to the function $v_0(t,x,y)$ in $L^2(0,T;L^2(\Gamma_\varepsilon))$, as $\varepsilon \to 0$, if*

(i) $\varepsilon \int_0^T \int_{\Gamma_\varepsilon} v_\varepsilon^2 \, d\sigma \, dt < C.$

(ii) *For any $\phi(t,x) \in C([0,T];C(\overline{\Omega}))$, $\psi(y) \in C(\Gamma)$ we have that*

$$\lim_{\varepsilon \to 0} \varepsilon \int_0^T \int_{\Gamma_\varepsilon} v_\varepsilon(t,x)\phi(t,x)\psi\left(\frac{x}{\varepsilon}\right) d\sigma_x \, dt$$

$$= [(i)]\frac{1}{|Y|} \int_0^T \int_\Omega \int_\Gamma v_0(t,x,y)\phi(t,x)\psi(y)\,d\sigma_y\,dx\,dt$$

for some function $v_0 \in L^2(0,T;L^2(\Omega \times \Gamma))$.

(iii) *We say that $\{v_\varepsilon\}$ converges t-pointwise two-scale in $L^2(\Gamma_\varepsilon)$ if, for any $t \in [0,T]$, and for any $\phi(x) \in C(\overline{\Omega})$, $\psi(y) \in C(\Gamma)$ we have*

$$\lim_{\varepsilon \to 0} \varepsilon \int_{\Gamma_\varepsilon} v_\varepsilon(t,x)\phi(x)\psi\left(\frac{x}{\varepsilon}\right) d\sigma_x = \frac{1}{|Y|} \int_\Omega \int_\Gamma v_0(t,x,y)\phi(x)\psi(y)\,d\sigma_y\,dx$$

for some function $v_0 \in L^2(0,T;L^2(\Omega \times \Gamma))$.

Lemma 4.6. *Let W_ε be a solution of (4.10), and let z_ε be a solution of problem (4.15). Then there exist functions $z_0^l \in L^2(0,T;L^2(\Omega))$, $l = i,e$, such that $\partial_{x_1} z_0^i, \partial_{x_j} z_0^e \in L^2(0,T;L^2(\Omega))$ ($j=1,2,3$), $w_0 = z_0^i - z_0^e \in L^4(0,T;L^4(\Omega))$, and up to a subsequence, as $\varepsilon \to 0$, the following two-scale convergence holds:*

(i) $\chi^l\left(\frac{x}{\varepsilon}\right) z_\varepsilon^l(t,x) \xrightarrow{2} \chi^l(y)z_0^l(t,x)$ in $L^2(0,T;L^2(\Omega_\varepsilon^l))$, $l = i,e$.

(ii) $\chi^i\left(\frac{x}{\varepsilon}\right) \nabla z_\varepsilon^i(t,x) \xrightarrow{2} \chi^i(y)\left[\mathbf{e}_1\partial_{x_1}z_0^i(t,x)+\nabla_y z_1^i(t,x,y)\right]$, where $z_1^i(t,x,y) \in L^2((0,T)\times\Omega;H^1(Y_i))$ is 1-periodic in y_1.

(iii) $\chi^e\left(\frac{x}{\varepsilon}\right)\nabla z_\varepsilon^e(t,x) \xrightarrow{\;2\;} \chi^e(y)\left[\nabla z_0^e(t,x) + \nabla_y z_1^e(t,x,y)\right]$, *where* $z_1^e(t,x,y) \in$ $L^2((0,T)\times\Omega; H^1(Y_e))$ *is Y-periodic in y.*

(iv) $w_\varepsilon \xrightarrow{\;2\;} w_0(t,x)$ *t–pointwise in $L^2(\Gamma_\varepsilon)$, and $w_0 = (z_0^i - z_0^e)$.*
Moreover, $\partial_t w_\varepsilon \xrightarrow{\;2\;} \partial_t w_0$ in $L^2(0,T;L^2(\Gamma_\varepsilon))$.

(v) $h_\varepsilon \xrightarrow{\;2\;} \widetilde{h}_0(t,x,y)$ *t–pointwise in $L^2(\Gamma_\varepsilon)$, and $\partial_t h_\varepsilon \xrightarrow{\;2\;} \partial_t \widetilde{h}_0$*
in $L^2(0,T;L^2(\Gamma_\varepsilon))$.

PROOF. From a priori estimates the two-scale convergence of z_ε^e and ∇z_ε^e is proved applying standard arguments (see (Allaire, 1992)). When it comes to z_ε^i and its gradient, the main difficulty stems from the fact that Ω_ε^i consists of many disconnected components.

Since z_ε^i is bounded uniformly in ε (cf. Lemma 4.5) in $L^2((0,T)\times\Omega_\varepsilon^i)$, there exists a subsequence—still denoted by $\{z_\varepsilon^i\}$—such that $\chi^i(\frac{x}{\varepsilon})z_\varepsilon^i(t,x)$ converging two-scale to some $\chi^i(y)z_0^i(t,x,y)$ in $L^2(0,T;L^2(\Omega\times Y))$. Similarly, due to (4.20), up to a subsequence, $\chi^i\left(\frac{x}{\varepsilon}\right)\nabla z_\varepsilon^i(t,x)$ converges two-scale to $\chi^i(y)p^i(t,x,y)$. Let us show that $z_0^i = z_0^i(t,x)$. Take a smooth test function $\Phi\left(t,x,\frac{x}{\varepsilon}\right) = \varphi(t,x)\psi\left(\frac{x}{\varepsilon}\right)$, where $\varphi \in C([0,T];C_0^\infty(\Omega))$, and $\psi \in (C^\infty(Y_i))^3$ is 1-periodic in y_1 and such that $\psi = 0$ on $\Gamma_{mi}\cup\Gamma$.

$$\varepsilon\int_0^T\int_{\Omega_\varepsilon^i}\nabla z_\varepsilon^i(t,x)\cdot\varphi(t,x)\psi\left(\frac{x}{\varepsilon}\right)\,dxdt$$

$$= -\varepsilon\int_0^T\int_{\Omega_\varepsilon^i}z_\varepsilon^i(t,x)\nabla\varphi(t,x)\cdot\psi\left(\frac{x}{\varepsilon}\right)\,dxdt$$

$$-\int_0^T\int_{\Omega_\varepsilon^i}z_\varepsilon^i(t,x)\varphi(t,x)\mathrm{div}_y\psi\left(\frac{x}{\varepsilon}\right)\,dxdt.$$

Passing to the limit, we derive

$$\frac{1}{|Y|}\int_0^T\int_\Omega\int_{Y_i}z_0^i(t,x,y)\varphi(t,x)\mathrm{div}_y\psi(y)\,dydxdt = 0,$$

which implies that $\partial_{y_i}z_0^i(t,x,y) = 0$, $i = 1,2,3$. Thus, $z_0^i = z_0^i(t,x)$.

Next we prove that $\partial_{x_1} z_0^i \in L^2((0,T) \times \Omega)$. Let us take a test function $\Phi\left(t, x, \frac{x}{\varepsilon}\right) = \varphi(t,x)\mathbf{e}_1 + \varphi(t,x)\nabla_y N_1^i\left(\frac{x}{\varepsilon}\right)$ such that

$$\Delta_y N_1^i = 0, \quad Y_i,$$

$$\nabla N_1^i \cdot \nu = -\nu_1, \quad \Gamma \cup \Gamma_{mi}, \tag{4.22}$$

$$N_1^i \text{ is 1-periodic in } y_1.$$

Integrating by parts yields

$$\int_0^T \int_{\Omega_\varepsilon^i} \nabla z_\varepsilon^i(t,x) \cdot \Phi\left(t, x, \frac{x}{\varepsilon}\right) \, dx dt$$

$$= -\int_0^T \int_{\Omega_\varepsilon^i} z_\varepsilon^i(t,x) \left(\mathbf{e}_1 + \nabla_y N_1^i\left(\frac{x}{\varepsilon}\right)\right) \cdot \nabla\varphi(t,x) \, dx dt,$$

and passing to the limit, as $\varepsilon \to 0$, we obtain

$$\frac{1}{|Y|} \int_0^T \int_\Omega \int_{Y_i} p^i(t,x,y) \cdot \varphi(t,x) \left(\mathbf{e}_1 + \nabla_y N_1^i(y)\right) \, dy dx dt \tag{4.23}$$

$$= -\frac{1}{|Y|} \int_0^T \int_\Omega \int_{Y_i} z_0^i(t,x) \nabla\varphi(t,x) \cdot \left(\mathbf{e}_1 + \nabla_y N_1^i(y)\right) \, dy dx dt.$$

Let us observe that $\int_{Y_i} \partial_{y_k} N_1^i(y) \, dy = 0$ for $k \neq 1$. Indeed, for $k \neq 1$, y_k can be taken as a test function in (4.22):

$$0 = -\int_{Y_i} \Delta N_1^i(y) y_k \, dy = \int_{Y_i} \partial_{y_k} N_1^i(y) \, dy.$$

Furthermore, it holds that

$$\int_{Y_i} \left(\delta_{1k} + \partial_{y_k} N_1^i(y)\right) \, dy = \delta_{1k} |\Gamma| \frac{a_i^{\text{eff}}}{a_i}.$$

Consequently, it is straightforward to check that

$$a_i^{\text{eff}} = \frac{1}{|\Gamma|} \int_{Y_i} a_i \left(1 + \partial_{y_1} N_1^i(y)\right) \, dy = \frac{1}{|\Gamma|} \int_{Y_i} a_i \left(1 + \partial_{y_1} N_1^i(y)\right)^2 \, dy > 0. \tag{4.24}$$

We turn back to (4.23). Due to (4.24), we have the estimate

$$\left| \int_0^T \int_\Omega z_0^i(t,x) \partial_{x_1} \varphi(t,x) \, dx dt \right|$$

$$= \left| \frac{a_i}{(a_i^{\text{eff}})_{11}} \int_0^T \int_\Omega \int_{Y_i} p^i(t,x,y) \cdot \varphi(t,x) \left(\mathbf{e}_1 + \nabla_y N_1^i(y) \right) \, dy dx dt \right|$$

$$\leq C \|\varphi\|_{L^2((0,T)\times\Omega)}.$$

Next, we show that $p^i(t,x,y) = \mathbf{e}_1 \partial_{x_1} z_0^i(t,x) + \nabla_y z_1^i(t,x,y)$ for some z_1^i periodic in y_1. Take a smooth test function $\varphi(t,x)\psi(y)$ such that $\text{div}_y \psi = 0$ in Y_i, $\psi \cdot \nu = 0$ on $\Gamma_{mi} \cup \Gamma$, and periodic in y_1.

$$\int_0^T \int_{\Omega_\varepsilon^i} \nabla z_\varepsilon^i \cdot \varphi(t,x)\psi\left(\frac{x}{\varepsilon}\right) \, dx dt = - \int_0^T \int_{\Omega_\varepsilon^i} z_\varepsilon^i \nabla\varphi(t,x) \cdot \psi\left(\frac{x}{\varepsilon}\right) \, dx dt.$$

Passing to the limit, as $\varepsilon \to 0$ we obtain

$$\frac{1}{|Y|} \int_0^T \int_\Omega \int_{Y_i} p^i \cdot \varphi(t,x)\psi(y) \, dy dx dt = -\frac{1}{|Y|} \int_0^T \int_\Omega \int_{Y_i} z_0^i \nabla\varphi(t,x) \cdot \psi(y) \, dy dx dt.$$

Since $\int_{Y_i} \psi_k(y) \, dy = 0$ for $k \neq 1$,

$$\int_0^T \int_\Omega \int_{Y_i} p^i(t,x,y) \cdot \varphi(t,x)\psi(y) \, dy dx dt = \int_0^T \int_\Omega \int_{Y_i} \partial_{x_1} z_0^i(t,x)\varphi(t,x)\psi_1(y) \, dy dx dt,$$

and thus

$$\int_0^T \int_\Omega \int_{Y_i} \left(p^i(x,y) - \mathbf{e}_1 \partial_{x_1} z_0^i(t,x) \right) \varphi(t,x) \cdot \psi(y) \, dy dx dt = 0.$$

Since ψ is solenoidal, there exists $z_1^i(t,x,y) \in L^2((0,T) \times \Omega; H^1(Y_i))$, 1-periodic in y_1, such that

$$p^i(t,x,y) = \mathbf{e}_1 \partial_{x_1} z_0^i(t,x) + \nabla_y z_1^i(t,x,y).$$

Next we prove that the jump w_ε converges two-scale in $L^2(0, T; L^2(\Gamma_\varepsilon))$ to $z_0^i - z_0^e$. To this end, for $\psi \in H^{1/2}(\Gamma)$, we consider test functions $\widetilde{\psi}^l$, $l = i, e$, solving

$$\Delta \widetilde{\psi}^l = \frac{1}{|Y_l|} \int_\Gamma \psi \, d\sigma, \quad y \in Y_l,$$

$$\nabla \widetilde{\psi}^l \cdot \nu^l = \psi, \quad y \in \Gamma; \quad \nabla \widetilde{\psi}^l \cdot \nu^l = 0, \quad y \in \Gamma_{ml},$$

$$\widetilde{\psi}^l \text{ is } Y - \text{periodic}.$$

Integration by parts yields

$$\varepsilon \int_0^T \int_{\Gamma_\varepsilon} w_\varepsilon \, \varphi(t, x) \psi \left(\frac{x}{\varepsilon} \right) dx dt$$

$$= \varepsilon \int_0^T \int_{\Omega_\varepsilon^i} \nabla z_\varepsilon^i \cdot \varphi(t, x) \nabla_y \widetilde{\psi}^i \left(\frac{x}{\varepsilon} \right) dx dt + \varepsilon \int_0^T \int_{\Omega_\varepsilon^i} z_\varepsilon^i \, \nabla \varphi(t, x) \cdot \nabla_y \widetilde{\psi}^i \left(\frac{x}{\varepsilon} \right) dx dt$$

$$+ \frac{1}{|Y_i|} \int_0^T \int_{\Omega_\varepsilon^i} z_\varepsilon^i \varphi(t, x) \int_\Gamma \psi(y) \, d\sigma dx dt$$

$$- \varepsilon \int_0^T \int_{\Omega_\varepsilon^e} \nabla z_\varepsilon^e \cdot \varphi(t, x) \nabla_y \widetilde{\psi}^e \left(\frac{x}{\varepsilon} \right) dx dt - \varepsilon \int_0^T \int_{\Omega_\varepsilon^e} z_\varepsilon^e \nabla \varphi(t, x) \cdot \nabla_y \widetilde{\psi}^e \left(\frac{x}{\varepsilon} \right) dx dt$$

$$- \frac{1}{|Y_e|} \int_0^T \int_{\Omega_\varepsilon^e} z_\varepsilon^e \varphi(t, x) \int_\Gamma \psi(y) \, d\sigma dx dt.$$

Passing to the limit, as $\varepsilon \to 0$, we get

$$\frac{1}{|Y|} \int_0^T \int_\Omega \int_\Gamma w_0(t, x, y) \varphi(t, x) \psi(y) \, d\sigma dx dt$$

$$= \frac{1}{|Y|} \int_0^T \int_\Omega \int_\Gamma (z_0^i - z_0^e) \varphi(t, x) \psi(y) \, d\sigma dx dt,$$

that proves the two-scale convergence of w_ε to the difference $w_0 = z_0^i - z_0^e$.

Note that the uniform bound of w_ε in $L^4((0, T) \times \Gamma_\varepsilon)$—by Lemma 4.5(i)—implies $w_0 \in L^4((0, T) \times \Omega)$. Indeed, for smooth $\varphi(t, x)$, we have that

$$|\Gamma| \int_0^T \int_\Omega w_0(t, x) \varphi(t, x) \, dx dt = \lim_{\varepsilon \to 0} \varepsilon |Y| \int_0^T \int_{\Gamma_\varepsilon} w_\varepsilon(t, x) \varphi(t, x) \, d\sigma dt$$

$$\leq |Y| \lim_{\varepsilon \to 0} \left(\varepsilon \int_0^T \int_{\Gamma_\varepsilon} |w_\varepsilon|^4 \, d\sigma dt \right)^{\frac{1}{4}} \left(\varepsilon \int_0^T \int_{\Gamma_\varepsilon} |\varphi(t,x)|^{4/3} \, d\sigma dt \right)^{\frac{3}{4}}$$

$$\leq C \lim_{\varepsilon \to 0} \left(\varepsilon \int_0^T \int_{\Gamma_\varepsilon} |\varphi(t,x)|^{\frac{4}{3}} \, d\sigma_x dt \right)^{\frac{3}{4}}$$

$$= C \left(\frac{|\Gamma|}{|Y|} \int_0^T \int_\Omega \int_\Gamma |\varphi(t,x)|^{\frac{4}{3}} \, dx dt \right)^{\frac{3}{4}}.$$

By density of smooth functions in $L^{\frac{4}{3}}((0,T) \times \Omega)$, $\|w_0\|_{L^4((0,T) \times \Omega)} \leq C$.

Thanks to the uniform in ε estimates (i), (ii) in Lemma 4.5, (iv) and (v) hold. Indeed, for any $t \in [0,T]$ and any $\varphi(t,x) \in C^1([0,T] \times \overline{\Omega})$, $\psi(y) \in C(\Gamma)$, such that $\varphi(0,x) = 0$

$$\varepsilon \int_{\Gamma_\varepsilon} w_\varepsilon(t,x) \varphi(t,x) \psi\left(\frac{x}{\varepsilon}\right) d\sigma$$

$$= \varepsilon \int_0^t \int_{\Gamma_\varepsilon} (w_\varepsilon(\tau,x) \partial_\tau \varphi(\tau,x) + \partial_\tau w_\varepsilon(\tau,x) \varphi(\tau,x)) \psi\left(\frac{x}{\varepsilon}\right) d\sigma$$

$$\to \frac{1}{|Y|} \int_0^t \int_\Omega \int_\Gamma (w_0(\tau,x) \partial_\tau \varphi(\tau,x) + \partial_\tau w_0(\tau,x) \varphi(\tau,x)) \psi(y) d\sigma_y dx d\tau$$

$$= \frac{1}{|Y|} \int_\Omega \int_\Gamma w_0(t,x) \varphi(t,x) \psi(y) d\sigma_y dx, \quad \varepsilon \to 0.$$

$\square$

Lemma 4.7. *Let the initial functions V_ε^0 satisfy hypothesis (H1). Then $V_\varepsilon^0 \overset{2}{\rightharpoonup} V^0$ in $L^2(\Gamma_\varepsilon)$, and*

$$\limsup_{\varepsilon \to 0} \varepsilon \int_{\Gamma_\varepsilon} |V_\varepsilon^0|^2 \, d\sigma = \frac{|\Gamma|}{|Y|} \int_\Omega |V^0|^2 \, dx.$$

PROOF. The weak two-scale convergence follows from Proposition 2.6 in (Allaire & Damlamian, 1995). Approximating V^0 by smooth functions V_δ^0 in $H^1(\Omega)$, we find

$$\varepsilon \int_{\Gamma_\varepsilon} |V_\varepsilon^0|^2 \, d\sigma = \varepsilon \int_{\Gamma_\varepsilon} |V_\varepsilon^0 - V_\delta^0|^2 \, d\sigma + 2\varepsilon \int_{\Gamma_\varepsilon} (V_\varepsilon^0 - V_\delta^0) V_\delta^0 \, d\sigma + \varepsilon \int_{\Gamma_\varepsilon} |V_\delta^0|^2 \, d\sigma. \quad (4.25)$$

Applying the trace inequality in the rescaled periodicity cell εY, adding up over all the cells in Ω, and using assumption (H1) leads to

$$\varepsilon \int_{\Gamma_\varepsilon} |V_\varepsilon^0 - V_\delta^0|^2 \, d\sigma \le C\varepsilon^2 \int_\Omega |\nabla(V_\varepsilon^0 - V_\delta^0)|^2 \, dx + C \int_\Omega |V_\varepsilon^0 - V_\delta^0|^2 \, dx$$

$$\le C\varepsilon^2 \int_\Omega |\nabla(V_\varepsilon^0 - V_\delta^0)|^2 \, dx + C \int_\Omega |V_\varepsilon^0 - V^0|^2 \, dx$$

$$+ C \int_\Omega |V_\delta^0 - V^0|^2 \, dx \quad \to \quad 0, \quad \varepsilon, \delta \to 0.$$

Then, since V_δ^0 is smooth, it converges strongly two-scale, and passing to the limit as $\varepsilon \to 0$ in (4.25) we obtain

$$\lim_{\delta \to 0} \limsup_{\varepsilon \to 0} \varepsilon \int_{\Gamma_\varepsilon} |V_\varepsilon^0|^2 \, d\sigma = \frac{|\Gamma|}{|Y|} \int_\Omega |V^0|^2 \, dx,$$

as stated. $\qquad\qquad\qquad\qquad\qquad\qquad\qquad\qquad\qquad\qquad\qquad\qquad\qquad\qquad$ □

We proceed with the Minty method for passing to the limit in the microscopic problem. Consider arbitrary functions $\mu_0^l(t,x) \in C^\infty([0,T] \times \overline{\Omega})$ and $\mu_1^l(t,x,y) \in C^\infty([0,T] \times \overline{\Omega} \times Y)$, Y-periodic in y, and such that $\mu_0^l = \mu_1^l = 0$ when $x \in S_0 \cap S_L$. Take the test function

$$M_\varepsilon := \begin{pmatrix} [\mu_\varepsilon] \\ \rho \end{pmatrix}, \quad \text{where } \rho = \rho(t,x), \text{ and}$$

$$\mu_\varepsilon(x) := \begin{cases} \mu_0^e(t,x) + \varepsilon\mu_1^e\left(t,x,\dfrac{x}{\varepsilon}\right), & x \in \Omega_\varepsilon^e \\[2mm] \mu_0^i(t,x) + \varepsilon\mu_1^i\left(t,x,\dfrac{x}{\varepsilon}\right), & x \in \Omega_\varepsilon^i. \end{cases}$$

The monotonicity property of the operator $\mathbb{A}_\varepsilon(t,\cdot)$ entails

$$\int_0^t \int_{\Gamma_\varepsilon} (\mathbb{A}_\varepsilon(\tau, W_\varepsilon) - \mathbb{A}_\varepsilon(\tau, M_\varepsilon)) \cdot (W_\varepsilon - M_\varepsilon) \, d\sigma d\tau \ge 0. \qquad (4.26)$$

By the definition of A_ε (4.6),

$$(A_\varepsilon([\mu_\varepsilon] - w_\varepsilon), ([\mu_\varepsilon] - w_\varepsilon))_{L^2(\Gamma_\varepsilon)} \le \int_{\Omega_\varepsilon^i \cup \Omega_\varepsilon^e} a_\varepsilon \nabla(\mu_\varepsilon - z_\varepsilon) \cdot \nabla(\mu_\varepsilon - z_\varepsilon) \, dx,$$

where z_ε solves (4.15). It follows then from (4.26), (4.10), and the definition of the operator $\mathbb{A}_\varepsilon(t, \cdot)$ that

$$
\varepsilon \int_0^t \int_{\Gamma_\varepsilon} \partial_\tau w_\varepsilon ([\mu_\varepsilon] - w_\varepsilon) \, d\sigma d\tau + \varepsilon \int_0^t \int_{\Gamma_\varepsilon} \partial_\tau h_\varepsilon (\rho - h_\varepsilon) \, d\sigma d\tau
$$

$$
+ \frac{1}{c_m} \int_0^t \int_{\Omega_\varepsilon^e \cup \Omega_\varepsilon^i} a_\varepsilon \nabla \mu_\varepsilon \cdot \nabla(\mu_\varepsilon - z_\varepsilon) \, dx d\tau + \varepsilon(\lambda - \frac{1}{c_m}) \int_0^t \int_{\Gamma_\varepsilon} [\mu_\varepsilon]([\mu_\varepsilon] - w_\varepsilon) \, d\sigma d\tau
$$

$$
- \frac{\varepsilon}{c_m} \int_0^t \int_{\Gamma_\varepsilon} \rho([\mu_\varepsilon] - w_\varepsilon) \, d\sigma d\tau + \varepsilon(b + \lambda) \int_0^t \int_{\Gamma_\varepsilon} \rho(\rho - h_\varepsilon) \, d\sigma d\tau \qquad (4.27)
$$

$$
- \varepsilon\theta \int_0^t \int_{\Gamma_\varepsilon} [\mu_\varepsilon](\rho - h_\varepsilon) \, d\sigma d\tau + \varepsilon\frac{1}{3c_m} \int_0^t e^{2\lambda\tau} \int_{\Gamma_\varepsilon} [\mu_\varepsilon]^3([\mu_\varepsilon] - w_\varepsilon) \, d\sigma d\tau
$$

$$
+ \int_0^t \int_{\Gamma_\varepsilon} \frac{e^{-\lambda\tau}}{c_m}(a_i \nabla q_\varepsilon \cdot \nu)([\mu_\varepsilon] - w_\varepsilon) \, d\sigma d\tau - \varepsilon a \int_0^t \int_{\Gamma_\varepsilon} e^{-\lambda\tau}(\rho - h_\varepsilon) \, d\sigma d\tau \geq 0.
$$

Consider the first two terms in (4.27), specifically integrals $\varepsilon \int_0^t \int_{\Gamma_\varepsilon} w_\varepsilon \partial_\tau w_\varepsilon \, d\sigma d\tau$ and $\varepsilon \int_0^t \int_{\Gamma_\varepsilon} h_\varepsilon \partial_\tau h_\varepsilon \, d\sigma d\tau$. Integrating by parts with respect to time, passing to the limit as $\varepsilon \to 0$, and using the lower semi-continuity of L^2-norm with respect to two-scale convergence (Proposition 2.5, (Allaire & Damlamian, 1995)) and Lemma 4.7 renders

$$
\limsup_{\varepsilon \to 0} \left[\varepsilon \int_0^t \int_{\Gamma_\varepsilon} w_\varepsilon \partial_\tau w_\varepsilon \, d\sigma d\tau - \frac{|\Gamma|}{|Y|} \int_0^t \int_\Omega w_0 \partial_\tau w_0 \, dx d\tau \right]
$$

$$
= \limsup_{\varepsilon \to 0} \left[\frac{\varepsilon}{2} \int_{\Gamma_\varepsilon} w_\varepsilon^2 \, d\sigma \Big|_{\tau=t} - \frac{|\Gamma|}{2|Y|} \int_\Omega w_0^2 \, dx \right]
$$

$$
+ \lim_{\varepsilon \to 0} \left[-\frac{\varepsilon}{2} \int_{\Gamma_\varepsilon} (V_\varepsilon^0)^2 \, d\sigma + \frac{|\Gamma|}{2|Y|} \int_\Omega (V^0)^2 \, dx \right] \geq 0.
$$

Similarly, for the integral of $h_\varepsilon \partial_\tau h_\varepsilon$, denoting the mean value of the two-scale limit $\widetilde{h}_0(t, x, y)$ in y by $h_0(t, x) = \frac{1}{|\Gamma|} \int_\Gamma \widetilde{h}_0(t, x, y) \, dy$, we get

$$
\limsup_{\varepsilon \to 0} \left[\varepsilon \int_0^t \int_{\Gamma_\varepsilon} h_\varepsilon \partial_\tau h_\varepsilon \, d\sigma d\tau - \frac{|\Gamma|}{|Y|} \int_0^t \int_\Omega h_0 \partial_\tau h_0 \, dx d\tau \right]
$$

$$
= \limsup_{\varepsilon \to 0} \left[\frac{\varepsilon}{2} \int_{\Gamma_\varepsilon} h_\varepsilon^2 \, d\sigma \Big|_{\tau=t} - \frac{|\Gamma|}{2|Y|} \int_\Omega h_0^2 \, dx \Big|_{\tau=t} \right]
$$

$$
+ \lim_{\varepsilon \to 0} \left[-\frac{\varepsilon}{2} \int_{\Gamma_\varepsilon} (G_\varepsilon^0)^2 \, d\sigma + \frac{|\Gamma|}{2|Y|} \int_\Omega (G^0)^2 \, dx \right] \geq 0.
$$

For smooth $\mu_0^l(t,x)$ and $\mu_1^l(t,x,y)$, $l = i, e$, we use Lemma 4.6 to pass to the limit in the third term:

$$\frac{1}{c_m} \int_0^t \int_{\Omega_\varepsilon^e \cup \Omega_\varepsilon^i} a_\varepsilon \nabla \mu_\varepsilon \cdot \nabla(\mu_\varepsilon - z_\varepsilon) \, dx d\tau$$

$$\to \frac{1}{c_m |Y|} \int_0^t \int_\Omega \int_{Y_i} a_i (\nabla \mu_0^i + \nabla_y \mu_1^i) \cdot (\nabla \mu_0^i + \nabla_y \mu_1^i - \partial_1 z_0^i \mathbf{e}_1 - \nabla_y z_1^i) dx dy d\tau$$

$$+ \frac{1}{c_m |Y|} \int_0^t \int_\Omega \int_{Y_e} a_e (\nabla \mu_0^e + \nabla_y \mu_1^e) \cdot (\nabla \mu_0^e + \nabla_y \mu_1^e - \nabla z_0^e - \nabla_y z_1^e) dx dy d\tau.$$

Taking the limit in (4.27) as $\varepsilon \to 0$ (along a subsequence) we obtain

$$\limsup_{\varepsilon \to 0} \left[\varepsilon \int_0^t \int_{\Gamma_\varepsilon} w_\varepsilon \partial_\tau w_\varepsilon \, d\sigma d\tau - \frac{|\Gamma|}{|Y|} \int_0^t \int_\Omega w_0 \partial_\tau w_0 \, dx d\tau \right]$$

$$+ \limsup_{\varepsilon \to 0} \left[\varepsilon \int_0^t \int_{\Gamma_\varepsilon} h_\varepsilon \partial_\tau h_\varepsilon \, d\sigma d\tau - \frac{|\Gamma|}{|Y|} \int_0^t \int_\Omega h_0 \partial_\tau h_0 \, dx d\tau \right]$$

$$\leq \frac{|\Gamma|}{|Y|} \int_0^t \int_\Omega \partial_\tau w_0 ([\mu_0] - w_0) \, dx d\tau + \frac{|\Gamma|}{|Y|} \int_0^t \int_\Omega \partial_\tau h_0 (\rho - h_0) \, dx d\tau$$

$$+ \frac{1}{c_m |Y|} \int_0^t \int_\Omega \int_{Y_i} a_i (\nabla \mu_0^i + \nabla_y \mu_1^i) \cdot (\nabla \mu_0^i + \nabla_y \mu_1^i - \partial_1 z_0^i \mathbf{e}_1 - \nabla_y z_1^i) dx dy d\tau$$

$$+ \frac{1}{c_m |Y|} \int_0^t \int_\Omega \int_{Y_e} a_e (\nabla \mu_0^e + \nabla_y \mu_1^e) \cdot (\nabla \mu_0^e + \nabla_y \mu_1^e - \nabla z_0^e - \nabla_y z_1^e) dx dy d\tau$$

$$+ (\lambda - \frac{1}{c_m}) \frac{|\Gamma|}{|Y|} \int_0^t \int_\Omega [\mu_0]([\mu_0] - w_0) \, dx d\tau \qquad (4.28)$$

$$- \frac{|\Gamma|}{|Y| c_m} \int_0^t \int_\Omega \rho([\mu_0] - w_0) \, dx d\tau + (b + \lambda) \frac{|\Gamma|}{|Y|} \int_0^t \int_\Omega \rho(\rho - h_0) \, dx d\tau$$

$$- \theta \frac{|\Gamma|}{|Y|} \int_0^t \int_\Omega [\mu_0](\rho - h_0) \, dx d\tau + \frac{1|\Gamma|}{3c_m |Y|} \int_0^t \int_\Omega e^{2\lambda \tau} [\mu_0]^3 ([\mu_0] - w_0) \, dx d\tau$$

$$- \int_0^t \int_\Sigma \frac{e^{-\lambda \tau}}{c_m} J^e (\mu_0^e - z_0^e) \, d\sigma d\tau - a \frac{|\Gamma|}{|Y|} \int_0^t \int_\Omega e^{-\lambda \tau} (\rho - h_0) \, d\sigma d\tau,$$

where $[\mu_0] = \mu_0^i - \mu_0^e$. Consider the spaces

$$H_i = \{ z^i \in L^2(\Omega) : \ \partial_{x_1} z^i \in L^2(\Omega), \ z^i = 0 \text{ on } S_0 \cup S_L \},$$

$$H_e = \{ z^e \in L^2(\Omega) : \ \nabla z^e \in L^2(\Omega)^3, \ z^e = 0 \text{ on } S_0 \cup S_L \},$$

with the standard H^1-norm in H_e, and

$$\|z\|_{H_i} = \left(\int_\Omega |z|^4 \, dx \right)^{\frac{1}{4}} + \left(\int_\Omega |\partial_{x_1} z|^2 \, dx \right)^{\frac{1}{2}}.$$

By density of smooth functions, inequality (4.28) still holds for test functions $\mu_1^l \in L^2((0,T) \times \Omega; H^1(Y_l))$, and $\mu_0^l \in L^2(0,T; H_l)$ such that $[\mu_0] \in L^4((0,T) \times \Omega)$.

Modifying the test function μ_1^i by setting $\mu_1^i(x,y) = \widetilde{\mu}_1^i(x,y) - \nabla_{x'}\mu_0^i \cdot y'$ we transform the integrand in the fourth line of (4.28) to the form

$$a_i(\partial_{x_1}\mu_0^i \mathbf{e}_1 + \nabla_y \widetilde{\mu}_1^i) \cdot (\partial_{x_1}\mu_0^i \mathbf{e}_1 + \nabla_y \widetilde{\mu}_1^i - \partial_{x_1} z_0^i \mathbf{e}_1 - \nabla_y z_1^i).$$

Then, for smooth test functions $\psi^l(t,x)$, $\varphi(t,x)$ vanishing at $x = 0, L$, and $\Psi^l(t,x,y)$ periodic in y and equal to zero when $x = 0, L$, $l = i, e$, we can set

$$\mu_0^l(t,x) = z_0^l(t,x) + \delta\psi^l(t,x), \quad l = i, e,$$

$$\mu_1^e(t,x,y) = z_1^e(t,x,y) + \delta\Psi^e(t,x,y),$$

$$\widetilde{\mu}_1^i(t,x,y) = z_1^i(t,x,y) + \delta\Psi^i(t,x,y),$$

$$\rho(t,x) = h_0(t,x) + \delta\varphi(t,x),$$

where δ is a small auxiliary parameter. Setting $[\psi] = \psi^i - \psi^e$, we have that

$$\limsup_{\varepsilon \to 0} \left[\varepsilon \int_0^t \int_{\Gamma_\varepsilon} w_\varepsilon \partial_\tau w_\varepsilon \, d\sigma d\tau - \frac{|\Gamma|}{|Y|} \int_0^t \int_\Omega w_0 \partial_\tau w_0 \, dxd\tau \right]$$

$$+ \limsup_{\varepsilon \to 0} \left[\varepsilon \int_0^t \int_{\Gamma_\varepsilon} h_\varepsilon \partial_\tau h_\varepsilon \, d\sigma d\tau - \frac{|\Gamma|}{|Y|} \int_0^t \int_\Omega h_0 \partial_\tau h_0 \, dxd\tau \right]$$

$$\leq \frac{\delta|\Gamma|}{|Y|} \int_0^t \int_\Omega \partial_\tau w_0 [\psi] \, dxd\tau + \frac{\delta|\Gamma|}{|Y|} \int_0^t \int_\Omega \partial_\tau h_0 \, \varphi \, dxd\tau$$

$$+ \frac{\delta}{c_m|Y|} \int_0^t \int_\Omega \int_{Y_i} a_i(\partial_{x_1}(z_0^i + \delta\psi^i)\mathbf{e}_1 + \nabla_y(z_1^i + \delta\Psi^i)) \cdot (\partial_{x_1}\psi^i \mathbf{e}_1 + \nabla_y\Psi^i) dxdyd\tau$$

$$+ \frac{\delta}{c_m|Y|} \int_0^t \int_\Omega \int_{Y_e} a_e(\nabla(z_0^e + \delta\psi^e) + \nabla_y(z_1^e + \delta\Psi^e)) \cdot (\nabla\psi^e + \nabla_y\Psi^e) dxdyd\tau$$

$$+ (\lambda - \frac{1}{c_m})\frac{\delta|\Gamma|}{|Y|} \int_0^t \int_\Omega (w_0 + \delta[\psi])[\psi] \, dxd\tau \tag{4.29}$$

$$-\frac{\delta|\Gamma|}{|Y|c_m}\int_0^t\int_\Omega (h_0+\delta\varphi)[\psi]\,dxd\tau + (b+\lambda)\frac{\delta|\Gamma|}{|Y|}\int_0^t\int_\Omega (h_0+\delta\varphi)\varphi\,dxd\tau$$

$$-\theta\frac{\delta|\Gamma|}{|Y|}\int_0^t\int_\Omega (w_0+\delta[\psi])\varphi\,dxd\tau + \frac{|\Gamma|}{3c_m|Y|}\delta\int_0^t\int_\Omega e^{2\lambda\tau}(w_0+\delta[\psi])^3[\psi]\,dxd\tau$$

$$-\frac{\delta}{c_m}\int_0^t\int_\Sigma e^{-\lambda\tau}J^e\psi^e\,d\sigma d\tau - a\frac{\delta|\Gamma|}{|Y|}\int_0^t\int_\Omega e^{-\lambda\tau}\varphi\,d\sigma d\tau.$$

Since the left-hand side of (4.29) is non-negative and δ is arbitrary, we obtain

$$\limsup_{\varepsilon\to 0}\left[\varepsilon\int_{\Gamma_\varepsilon}|w_\varepsilon|^2\,d\sigma - \frac{|\Gamma|}{|Y|}\int_\Omega |w_0|^2\,dx\right]=0,$$

$$\limsup_{\varepsilon\to 0}\left[\varepsilon\int_{\Gamma_\varepsilon}|h_\varepsilon|^2\,d\sigma - \frac{|\Gamma|}{|Y|}\int_\Omega |h_0|^2\,dx\right]=0.$$

Note that the last convergence implies that the two-scale limit $\widetilde{h}_0$ does not depend on y. Indeed, by Proposition 2.5 in (Allaire & Damlamian, 1995), one has the estimate

$$\limsup_{\varepsilon\to 0}\varepsilon\int_{\Gamma_\varepsilon}|h_\varepsilon|^2\,d\sigma \geq \frac{1}{|Y|}\int_\Omega\int_\Gamma |\widetilde{h}_0|^2\,d\sigma_y dx \geq \frac{|\Gamma|}{|Y|}\int_\Omega |h_0|^2\,dx.$$

Thus, one can see that

$$\frac{1}{|\Gamma|}\int_\Omega\int_\Gamma |\widetilde{h}_0|^2\,d\sigma_y dx = \int_\Omega\left(\frac{1}{|\Gamma|}\int_\Gamma \widetilde{h}_0\,d\sigma_y\right)^2\,dx.$$

Moreover, it is clear that

$$\frac{1}{|\Gamma|}\int_\Omega\int_\Gamma |\widetilde{h}_0|^2\,d\sigma_y dx = \frac{1}{|\Gamma|}\int_\Omega\int_\Gamma |\widetilde{h}_0-h_0|^2\,d\sigma_y dx$$

$$+\frac{2}{|\Gamma|}\int_\Omega\int_\Gamma (\widetilde{h}_0-h_0)h_0\,d\sigma_y dx$$

$$+\frac{1}{|\Gamma|}\int_\Omega\int_\Gamma |h_0|^2\,d\sigma_y dx = \int_\Omega |h_0|^2\,dx,$$

which yields

$$\frac{1}{|\Gamma|}\int_\Omega\int_\Gamma |\widetilde{h}_0-h_0|^2\,d\sigma_y dx = 0 \quad\Rightarrow\quad \widetilde{h}_0 = h_0(t,x).$$

Now, dividing (4.29) by $\delta \neq 0$ and passing to the limit as $\delta \to +0$ and $\delta \to -0$, we derive

$$
\frac{|\Gamma|}{|Y|} \int_0^t \int_\Omega \partial_\tau w_0[\psi] \, dxd\tau + \frac{|\Gamma|}{|Y|} \int_0^t \int_\Omega \partial_\tau h_0 \, \varphi \, dxd\tau
$$

$$
+ \frac{1}{c_m|Y|} \int_0^t \int_\Omega \int_{Y_i} a_i(\partial_{x_1} z_0^i \mathbf{e}_1 + \nabla_y z_1^i) \cdot (\partial_{x_1} \psi^i \mathbf{e}_1 + \nabla_y \Psi^i) dydxd\tau
$$

$$
+ \frac{1}{c_m|Y|} \int_0^t \int_\Omega \int_{Y_e} a_e(\nabla z_0^e + \nabla_y z_1^e) \cdot (\nabla \psi^e + \nabla_y \Psi^e) \, dydxd\tau
$$

$$
+ (\lambda - \frac{1}{c_m})\frac{|\Gamma|}{|Y|} \int_0^t \int_\Omega w_0[\psi] \, dxd\tau - \frac{|\Gamma|}{|Y|c_m} \int_0^t \int_\Omega h_0[\psi] \, dxd\tau
$$

$$
+ (b + \lambda)\frac{|\Gamma|}{|Y|} \int_0^t \int_\Omega h_0\varphi \, dxd\tau - \theta\frac{|\Gamma|}{|Y|} \int_0^t \int_\Omega w_0\varphi \, dxd\tau
$$

$$
+ \frac{|\Gamma|}{3c_m|Y|} \int_0^t \int_\Omega e^{2\lambda\tau} w_0^3[\psi] \, dxd\tau - \int_0^t \int_\Sigma \frac{e^{-\lambda\tau}}{c_m} J^e \psi^e \, d\sigma d\tau
$$

$$
- a\frac{|\Gamma|}{|Y|} \int_0^t \int_\Omega e^{-\lambda\tau} \varphi \, dxd\tau = 0.
$$

Taking $\psi^i = \psi^e = \varphi = 0$, we obtain $z_1^e(t,x,y) = N^e(y) \cdot \nabla z_0^e(t,x)$, $z_1^i(t,x,y) = N_1^i(y)\partial_{x_1} z_0^i(t,x)$, where N_k^e, N_1^i solve the cell problems (4.39) and (4.40), respectively. Note that in the case when Y_i is a cylinder—constant cross-section—, $N_1^i(y)$ is constant. Recalling the definition of the effective coefficients $(a_e^{\mathrm{eff}})_{kl}$ (4.4), and taking $\Psi^l = 0$, we obtain

$$
\int_0^t \int_\Omega \partial_\tau w_0[\psi] \, dxd\tau + \int_0^t \int_\Omega \partial_\tau h_0 \, \varphi \, dxd\tau
$$

$$
+ \frac{1}{c_m} \int_0^t \int_\Omega a_i^{\mathrm{eff}} \partial_{x_1} z_0^i \, \partial_{x_1} \psi^i dxd\tau + \frac{1}{c_m} \int_0^t \int_\Omega a_e^{\mathrm{eff}} \nabla z_0^e \cdot \nabla \psi^e \, dxd\tau
$$

$$
+ (\lambda - \frac{1}{c_m}) \int_0^t \int_\Omega w_0[\psi] \, dxd\tau - \frac{1}{c_m} \int_0^t \int_\Omega h_0[\psi] \, dxd\tau \tag{4.30}
$$

$$
+ (b + \lambda) \int_0^t \int_\Omega h_0\varphi \, dxd\tau - \theta \int_0^t \int_\Omega w_0\varphi \, dxd\tau
$$

$$
+ \frac{1}{3c_m} \int_0^t \int_\Omega e^{2\lambda\tau} w_0^3[\psi] \, dxd\tau
$$

$$= \frac{|Y|}{c_m|\Gamma|} \int_0^t \int_\Sigma e^{-\lambda\tau} J^e \psi^e \, d\sigma d\tau + a \int_0^t \int_\Omega e^{-\lambda\tau} \varphi \, d\sigma d\tau.$$

Performing the change of unknowns $u_0^l = e^{\lambda\tau} z_0^l$, $v_0 = e^{\lambda\tau} w_0$, $g_0 = e^{\lambda\tau} h_0$, and taking the test functions $e^{-\lambda\tau}\varphi$ and $e^{-\lambda\tau}\psi$ in place of φ and ψ in (4.30), we obtain a weak formulation of (4.2):

$$\int_0^t \int_\Omega \partial_\tau v_0[\psi] \, dxd\tau$$

$$+ \frac{1}{c_m} \int_0^t \int_\Omega a_i^{\text{eff}} \partial_{x_1} u_0^i \, \partial_{x_1} \psi^i dxd\tau + \frac{1}{c_m} \int_0^t \int_\Omega a_e^{\text{eff}} \nabla u_0^e \cdot \nabla \psi^e \, dxd\tau$$

$$+ \frac{1}{c_m} \int_0^t \int_\Omega \left(\frac{1}{3} v_0^3 - v_0 - g_0\right)[\psi] \, dxd\tau$$

$$+ \int_0^t \int_\Omega \left(\partial_\tau g_0 + bg_0 - \theta v_0 - a\right) \varphi \, dxd\tau$$

$$= \frac{|Y|}{c_m|\Gamma|} \int_0^t \int_\Sigma J^e \psi^e \, d\sigma d\tau.$$

Note that in view of the well-posedness of the limit problem proved in the next section, the convergence takes place for the whole sequence. The proof of Theorem 4.1 is completed.

4.5. Well-posedness of the macroscopic problem

In order to prove the well-posedness of the homogenized problem given by its weak formulation (4.30), we rewrite it in matrix form as an abstract parabolic equation. We introduce q_0 solving the auxiliary problem in Ω:

$$-\text{div}(a_e^{\text{eff}} \nabla q_0) - a_i^{\text{eff}} \partial_{x_1 x_1}^2 q_0 = 0, \qquad\qquad x \in \Omega,$$

$$a_e^{\text{eff}} \nabla q_0 \cdot \nu = \frac{|Y|}{|\Gamma|} J^e, \qquad\qquad x \in \Sigma, \qquad\qquad (4.31)$$

$$q_0 = 0, \qquad\qquad x \in S_0 \cup S_L.$$

Here, the effective coefficient $a_i^{\text{eff}} = |Y_i| a_i / |\Gamma|$. Multiplication (4.31) by a smooth test function ψ^e such that $\psi^e = 0$ on $S_0 \cup S_L$ leads to

$$\frac{|Y|}{|\Gamma|} \int_{\Sigma} J^e \psi^e \, d\sigma = \int_{\Omega} a_e^{\text{eff}} \nabla q_0 \cdot \nabla \psi^e \, dx + \int_{\Omega} a_i^{\text{eff}} \partial_{x_1} q_0 \partial_{x_1} \psi^e \, dx. \tag{4.32}$$

Substituting (4.32) into (4.30), and introducing $\widetilde{z}_0^l = z_0^l - q_0 e^{-\lambda t}$, $l = i, e$, we have the following weak formulation:

$$
\begin{aligned}
&\int_0^t \int_{\Omega} \partial_\tau w_0 [\psi] \, dx d\tau + \int_0^t \int_{\Omega} \partial_\tau h_0 \, \varphi \, dx d\tau \\
&+ \frac{1}{c_m} \int_0^t \int_{\Omega} a_i^{\text{eff}} \partial_{x_1} \widetilde{z}_0^i \, \partial_{x_1} \psi^i dx d\tau + \frac{1}{c_m} \int_0^t \int_{\Omega} a_e^{\text{eff}} \nabla \widetilde{z}_0^e \cdot \nabla \psi^e \, dx d\tau \\
&+ \left(\lambda - \frac{1}{c_m} \right) \int_0^t \int_{\Omega} w_0 [\psi] \, dx d\tau - \frac{1}{c_m} \int_0^t \int_{\Omega} h_0 [\psi] \, dx d\tau \\
&+ (b + \lambda) \int_0^t \int_{\Omega} h_0 \varphi \, dx d\tau - \theta \int_0^t \int_{\Omega} w_0 \varphi \, dx d\tau \\
&+ \frac{1}{3 c_m} \int_0^t \int_{\Omega} e^{2\lambda \tau} w_0^3 [\psi] \, dx d\tau \\
&= a \int_0^t \int_{\Omega} e^{-\lambda \tau} \varphi \, d\sigma d\tau + \int_0^t \int_{\Omega} e^{-\lambda \tau} a_i^{\text{eff}} \partial_{x_1 x_1}^2 q_0 \, [\psi] \, dx d\tau.
\end{aligned}
\tag{4.33}
$$

We seek to rewrite the weak formulation (4.33) in matrix form as an abstract parabolic equation. To this end, we first introduce the following functional spaces:

$$H_0 = L^2(\Omega) \times L^2(\Omega),$$

$$H_i = \{ z^i \in L^2(\Omega) : \ \partial_{x_1} z^i \in L^2(\Omega), \ z^i = 0 \text{ on } S_0 \cup S_L \},$$

$$H_e = \{ z^e \in L^2(\Omega) : \ \nabla z^e \in L^2(\Omega)^3, \ z^e = 0 \text{ on } S_0 \cup S_L \},$$

$$X_0 = \{ w = z^i - z^e : \ z^i \in H_i, \ z^e \in H_e \}.$$

The norm in H_i is given by

$$\|z\|_{H_i}^2 = \int_{\Omega} |z|^2 \, dx + \int_{\Omega} |\partial_{x_1} z|^2 \, dx.$$

For the one associated to H_e, we adopt the standard H^1-norm. For each element $w_0 \in X_0$, we associate a unique pair $(\widetilde{z}_0^i, \widetilde{z}_0^e) \in H_i \times H_e$ solving the following problem

$$
\begin{aligned}
-a_i^{\text{eff}} \partial_{x_1 x_1}^2 \widetilde{z}_0^i &= \text{div}(a_e^{\text{eff}} \nabla \widetilde{z}_0^e), & x \in \Omega, \\
\widetilde{z}_0^i - \widetilde{z}_0^e &= w_0, & x \in \Omega, \\
a_e^{\text{eff}} \nabla \widetilde{z}_0^e \cdot \nu &= 0, & x \in \Sigma, \\
\widetilde{z}_0^i = \widetilde{z}_0^e &= 0, & x \in S_0 \cup S_L.
\end{aligned}
\tag{4.34}
$$

The pair $(\widetilde{z}_0^i, \widetilde{z}_0^e)$ can be determined by solving the minimization problem

$$
\|w_0\|_{W_0}^2 := \inf \left\{ \int_\Omega a_i^{\text{eff}} |\partial_{x_1} \widetilde{z}_0^i|^2 \, dx + \int_\Omega a_e^{\text{eff}} \nabla \widetilde{z}_0^e \cdot \nabla \widetilde{z}_0^e \, dx \mid \widetilde{z}_0^i \in W_i, \ \widetilde{z}_0^e \in W_e \right\}.
$$

Note that W_0 is a Hilbert space with a scalar product given by

$$
(w_1, w_2)_{W_0} = \int_\Omega a_i^{\text{eff}} \partial_{x_1} z_1^i \, \partial_{x_1} z_2^i \, dx + \int_\Omega a_e^{\text{eff}} \nabla z_1^e \cdot \nabla z_2^e \, dx,
$$

where (z_1^i, z_1^e) and (z_2^i, z_2^e) solve (4.34) for w_1, w_2 given. Now (4.33) is written in the form

$$
\partial_t \begin{pmatrix} w_0 \\ \\ h_0 \end{pmatrix} + \begin{pmatrix} \dfrac{1}{c_m} A_{\text{eff}} w_0 + \dfrac{1}{c_m} \left(\dfrac{e^{2\lambda t}}{3} w_0^3 - w_0 - h_0 \right) + \lambda w_0 \\ \\ (b + \lambda) h_0 - \theta w_0 \end{pmatrix} = e^{-\lambda t} \begin{pmatrix} a_i^{\text{eff}} \partial_{x_1 x_1}^2 q_0 \\ \\ a \end{pmatrix},
$$

where the operator A_{eff} defined on smooth functions w_0 by

$$
(A_{\text{eff}} w_0, [\psi])_{L^2(\Omega)} := \frac{1}{c_m} \int_\Omega a_i^{\text{eff}} \partial_{x_1} \widetilde{z}_0^i \, \partial_{x_1} \psi^i dx + \frac{1}{c_m} \int_\Omega a_e^{\text{eff}} \nabla \widetilde{z}_0^e \cdot \nabla \psi^e \, dx,
$$

and $(\widetilde{z}_0^i, \widetilde{z}_0^e)$ solve (4.34). In operator form one writes

$$
\begin{aligned}
\partial_t W_0 + \mathbb{A}_0(t, W_0) &= F_0(t), \quad (t, x) \in (0, T) \times \Omega, \\
W_0(0, x) &= W_0^0(x), \quad x \in \Omega.
\end{aligned}
\tag{4.35}
$$

Therein, we have the following operators

$$
\mathbb{A}_0(t, W_0) := B_0^{(1)}(t, W_0) + B_0^{(2)}(t, W_0),
$$

$$B_0^{(1)}(t, W_0) := \begin{pmatrix} \dfrac{1}{c_m} A_{\text{eff}} w_0 + (\lambda - \dfrac{1}{c_m}) w_0 - \dfrac{1}{c_m} h_0 \\ \\ (b + \lambda) h_0 - \theta w_0 \end{pmatrix},$$

$$B_0^{(2)}(t, W_0) := \begin{pmatrix} \dfrac{e^{2\lambda t}}{3c_m} w_0^3 \\ \\ 0 \end{pmatrix},$$

$$F_0(t) := e^{-\lambda t} \begin{pmatrix} a_i^{\text{eff}} \partial_{x_1 x_1}^2 q_0 \\ \\ a \end{pmatrix}.$$

Introducing the spaces

$$H_0 = L^2(\Omega) \times L^2(\Omega),$$

$$V_1 = X_0 \times L^2(\Omega), \quad V_1' = X_0' \times L^2(\Omega),$$

$$V_2 = L^4(\Omega) \times L^2(\Omega), \quad V_2' = L^{4/3}(\Omega) \times L^2(\Omega),$$

we can prove the existence of a unique solution $W_0 \in L^\infty((0, T); H_0) \cap L^2((0, T); V_1) \cap L^4((0, T); V_2)$ to problem (4.35). It follows, as in Section 4.3.2, from Theorem 1.4 in (Lions, 1969) and Remark 1.8 in Chapter 2.

4.6. Formal asymptotic expansions

So as to provide an insight on how the effective coefficients and the corresponding cell problems in (4.2) appear, we apply the formal asymptotic expansion method to the stationary problem $A_\varepsilon v_\varepsilon = \varepsilon f$ for some smooth function $f = f(x)$. Specifically, we write

$$
\begin{aligned}
-\text{div}(a_\varepsilon \nabla u_\varepsilon) &= 0, & x &\in \Omega_\varepsilon^i \cup \Omega_\varepsilon^e, \\
a_e \nabla u_\varepsilon^e \cdot \nu = a_i \nabla u_\varepsilon^i \cdot \nu &= \varepsilon f(x), & x &\in \Gamma_\varepsilon, \\
u_\varepsilon^i - u_\varepsilon^e &= v_\varepsilon, & x &\in \Gamma_\varepsilon, \\
a_e \nabla u_\varepsilon \cdot \nu &= 0, & x &\in \Gamma_\varepsilon^m \cup \Sigma, \\
u_\varepsilon &= 0, & x &\in (S_0 \cup S_L).
\end{aligned}
\tag{4.36}
$$

Take

$$u_\varepsilon^l(x) \sim u_0^l(x, y) + \varepsilon u_1^l(x, y) + \varepsilon^2 u_2^l(x, y) + \dots, \quad y = \frac{x}{\varepsilon},$$

where $x \in \Omega_\varepsilon^l$ and $y \in Y_l$, $l \in \{i, e\}$. Then we get

$$
\begin{aligned}
\operatorname{div}(a_l \nabla u_\varepsilon^l) \sim{} & \frac{1}{\varepsilon^2} \operatorname{div}_y(a_l \nabla_y u_0^l) \\
&+ \frac{1}{\varepsilon} \left(\operatorname{div}_y(a_l \nabla_x u_0^l) + \operatorname{div}_y(a_l \nabla_y u_1^l) + \operatorname{div}_x(a_l \nabla_y u_0^l) \right) \\
&+ \operatorname{div}_x(a_l \nabla_x u_0^l) + \operatorname{div}_x(a_l \nabla_y u_1^l) + \operatorname{div}_y(a_l \nabla_x u_1^l) + \operatorname{div}_y(a_l \nabla_y u_2^l) \\
&+ \varepsilon \left(\operatorname{div}_x(a_l \nabla_x u_1^l)) + \operatorname{div}_x(a_l \nabla_y u_2^l)) + \operatorname{div}_y(a_l \nabla_x u_2^l)) \right) \\
&+ \varepsilon^2 \operatorname{div}_x(a_l \nabla_x u_2^l).
\end{aligned}
$$

Taking the terms of order ε^{-2} in the volume and the ones of order ε^{-1} on the boundary, we obtain the following problem for u_0^l:

$$
\begin{aligned}
-\operatorname{div}_y(a_l \nabla_y u_0^l) &= 0, & y &\in Y_l, \\
a_l \nabla_y u_0^l &= 0 & y &\in \Gamma \cup \Gamma^m, \\
u_0^i \text{ is 1-periodic in } y_1, & \\
\text{and } u_0^e \text{ is } Y\text{-periodic.} &
\end{aligned}
$$

The solution (defined up to an additive constant) does not depend on the fast variable y:

$$u_0^l(x, y) = u_0^l(x), \quad l = i, e. \tag{4.37}$$

For the next step, we take the terms of order ε^{-1} in the volume and those of order 1 on the boundary:

$$
\begin{aligned}
-\operatorname{div}_y(a_l \nabla_y u_1^l) &= 0, & y &\in Y_l, \\
a_l \nabla_y u_1^l \cdot \nu &= -a_l \nabla_x u_0^l \cdot \nu, & y &\in \Gamma \cup \Gamma_m, \tag{4.38}
\end{aligned}
$$

$$u_1^i \text{ is 1-periodic in } y_1$$

$$\text{and } u_1^e \text{ is } Y\text{-periodic.}$$

The solvability condition reads $-\int_\Gamma a_l \nabla_x u_0^l \cdot \nu = 0$, which is fulfilled thanks to (4.37). By seeking a solution of (4.38) in the form $u_1^l(x,y) = \mathbf{N}^l(y) \cdot \nabla_x u_0^l(x)$, we obtain

$$a^l \nabla_y u_1^l(x,y) \cdot \nu = a^l \partial_{y_j} N_i^l(y) \nu_j \partial_{x_i} u_0^l(x),$$

where we assume summation over the repeated indexes. The boundary condition in (4.38) yields a boundary condition for N_i on $\Gamma \cup \Gamma_m$:

$$\left(\partial_{y_j} N_i^l(y) + \delta_{i,j} \right) \nu_j = 0.$$

Then, the functions N_k^e, $k = 1, 2, 3$, solve the cell problems:

$$\begin{aligned}
-\Delta N_k^e &= 0, & y &\in Y_e, \\
\nabla N_k^e \cdot \nu &= -\nu_k, & y &\in \Gamma \cup \Gamma_m, \\
y &\mapsto N_k^e(y) \text{ is } Y - \text{periodic;}
\end{aligned}$$
(4.39)

For the functions N_k^i, due to the periodicity in only one variable y_1, one can see that $N_k^i(y) = -y_k$ for $k \neq 1$, that yields $\partial_{l \neq k} N_k^i = 0$. The first component N_1^i solves the problem

$$\begin{aligned}
-\Delta N_1^i &= 0, & y &\in Y_i, \\
\nabla N_1^i \cdot \nu &= -\nu_1, & y &\in \Gamma \cup \Gamma_m, \\
y &\mapsto N_1^i(y) \text{ is } 1 - \text{periodic;}
\end{aligned}$$
(4.40)

Finally, taking the terms of order 1 in the volume and the ones of order ϵ^1 on the boundary, we obtain the following problem for u_2^l:

$$-\text{div}_y(a^l \nabla_y u_2^l) = \text{div}_x(a^l \nabla_x u_0^l) + \text{div}_x(a^l \nabla_y u_1^l) + \text{div}_y(a^l \nabla_x u_1^l), \qquad y \in Y_l,$$

$$a^l \nabla_y u_2^l \cdot \nu^l = -a^l \nabla_x u_1^l \cdot \nu^l + f(x), \qquad\qquad\qquad y \in \Gamma,$$

$$a^l \nabla_y u_2^l \cdot \nu = 0, \qquad\qquad\qquad\qquad y \in \Gamma_m,$$

u_2^i is 1-periodic in y_1

and u_2^e is Y-periodic.

Here ν^l is the exterior unit normal, and $\nu^e = -\nu^i$ on Γ. The solvability condition reads

$$\int_{Y_l} \left(\mathrm{div}_x(a^l \nabla_x u_0^l) + \mathrm{div}_x(a^l \nabla_y u_1^l) + \mathrm{div}_y(a^l \nabla_x u_1^l) \right) dY - \int_{\Gamma} a^l \nabla_x u_2^l \cdot \nu^l d\sigma = 0.$$

Integrating by parts in the third term of the volume integral, substituting the expression $u_1^l(x, y) = N_i^l(y) \partial_{x_i} u_0^l(x)$, and taking into account that $N_k^i(y) = -y_k$ and $\int_{Y_i} \partial_{l \neq 1} N_1^i dy = 0$, we obtain

$$-\partial_{kj} u_0^e(x) \int_{Y_e} a^e \left(\partial_j N_k^e(y) + \delta_{kj} \right) dy = |\Gamma| f(x),$$

$$|Y_i| a_i \partial_{11} u_0^i(x) = |\Gamma| f(x).$$

Introducing the effective coefficient

$$(a_e^{\mathrm{eff}})_{kl} = \frac{1}{|\Gamma|} \int_{Y_e} a_e(\partial_l N_k^e(y) + \delta_{kl}) dy, \quad k, l = 1, 2, 3,$$

and adding the boundary conditions on $S_0 \cup S_L$ and Σ, we arrive at

$$\frac{|Y_i|}{|\Gamma|} a_i \partial_{11} u_0^i = -a_e^{\mathrm{eff}} \Delta u_0^e = f(x), \qquad\qquad x \in \Omega,$$

$$u_0^{i,e} = 0, \qquad\qquad\qquad\qquad x \in S_0 \cup S_L,$$

$$a_e^{\mathrm{eff}} \nabla u^e \cdot \nu = 0, \qquad\qquad\qquad x \in \Sigma.$$

Acknowledgments

5. CELL ELECTROPERMEABILIZATION MODELING VIA MULTIPLE TRACES FORMULATION AND TIME SEMI-IMPLICIT COUPLING

In the present chapter we simulate the response of biological cells to electrical stimulation in the electropermeabilization process.

The chapter is based on the submitted article: Martínez, I. A., Jerez-Hanckes, C. and Pettersson, I., Cell Electropermeabilization Modeling via Multiple Traces Formulation and Time Semi-Implicit Coupling.

5.1. Introduction

Electropermeabilization designates the use of short high-voltage or electric field pulses to increase the permeability of the cell membrane (Kotnik et al., 2019; Rols, 2006). This process is used to deliver therapeutic molecules, such as drugs and genes, into cells to treat cancer, perform genetic engineering, screen drugs, among others applications (Kim & Lee, 2017), (Choi et al., 2022, Section 4).

Theoretically, several models have been proposed to explain the reversible membrane electropermeabilization mechanism and its potential to allow the access of non-permeant molecules into the cell. However, none of these models has rigorously proven the phenomenon. For instance, during electropermeabilization it is thought that aqueous pores are formed along the cell membrane—a process known as electroporation—thereby increasing the permeability of the membrane. Yet, this has not been experimentally observed to occur for the commonly employed voltages. The pores are either too small to be seen by optical microscopy and too fragile for electron imaging. Only molecular dynamics simulations have been able to provide a corroboration of pore formation (Kotnik et al., 2019, Section 3), (Choi et al., 2022, Section 2.1). Moreover, the application of external electric pulses triggers other physical and chemical cell mechanisms, many of them not fully understood, with complex interactions at multiple length scales, from nanometers at the cell membrane to centimeters in tissues (Kotnik et al., 2019). "Therefore, while the term electroporation

is commonly used among biologists, the term electropermeabilization should be preferred in order to prevent any molecular description of the phenomenon" (Rols, 2006).

Still, mathematical models and numerical methods have been used to gain a better understanding of the different underlying phenomena. For instance, Neu and Krassowska (J. C. Neu & Krassowska, 1999) consider a pure electroporation process by modeling the nanoscale phenomena involved in the creation and resealing of the cell membrane pores, and apply homogenization theory to derive nonlinear time dynamics occurring at the membrane. Well-posedness of the Neu-Krassowska model and a new model including anisotropies are derived in (Ammari et al., 2016). Alternatively, in (Kavian et al., 2014) the authors propose a phenomenological model that forgoes the ab initio understanding of the mechanisms involved. A more complete phenomenological model considers two different stages in the electroporation process: conducting and permeable (Leguèbe et al., 2014). This model also takes into account the diffusion and electric transport of non-permeable molecules. In (Guittet et al., 2017; Mistani et al., 2019), the authors discard particle diffusion and transport in (Leguèbe et al., 2014) to then apply the Voronoi Interface Method (Guittet et al., 2015) for its numerical approximation. Specifically, they construct a Voronoi mesh of the volume which when coupled to a ghost fluid method (Liu et al., 2000) is able to capture discontinuous boundary conditions. Further computational enhancements via parallelization are given in (Mistani et al., 2019).

Instead of solving the volume boundary value problem, we reduce the problem to solving boundary integral equations onto cell membranes via the local Multiple Traces Formulation (MTF) (Hiptmair & Jerez-Hanckes, 2012; Claeys, Hiptmair, & Jerez-Hanckes, 2013; Hiptmair, Jerez-Hanckes, Lee, & Peng, 2014; Claeys, Hiptmair, Jerez-Hanckes, & Pintarelli, 2015; Jerez-Hanckes, Pinto, & Tournier, 2015). Originally introduced to solve acoustic wave transmission problems in heterogeneous scatterers, the local MTF considers independent trace unknowns at either side of the subdomains' boundaries to then enforce continuity conditions weakly via Calderón identities. In (Henríquez et al., 2017; Henríquez & Jerez-Hanckes, 2018) the method was successfully applied to model the electrical behavior of neurons by coupling the Laplace boundary integral operators with Hodgkin-Huxley

nonlinear dynamics. The volume Laplace equations in intra- and extracellular media arises when assuming a quasi-static electromagnetic regime and one can show that for 2D and 3D the model is well posed. Numerically, the authors prove stability and convergence of time semi-implicit discretizations with low- and high (spectral) order spatial boundary unknown representations. Furthermore, the numerical method proposed can be extended to model other nonlinear dynamics.

Following (Henríquez et al., 2017; Henríquez & Jerez-Hanckes, 2018), we employ the MTF to simulate the electric potential response of a fixed number of disjoint cells in three dimensions when they are subject to electric pulses. Spatially, the boundary unknowns will be approximated by spherical harmonics, thereby allowing for spectral convergence rates. The nonlinear dynamics of the cell membrane follow (Kavian et al., 2014).

The rest of the paper is organized as follows. In Section 5.2 we introduce necessary functional spaces. In Section 5.3 we formulate the problem and the corresponding non-linear dynamic model, and derive its boundary integral MTF. In Section 5.4, we present a numerical scheme for spatial and time-domain discretizations, as well as discuss advantages and limitations of the proposed method. Computational results are provided in Section 5.5. Code validation experiments with analytic and overkill solutions confirm our theoretical results and open new avenues of research.

5.2. Functional spaces

The scalar product of two vectors $\mathbf{x} = (x_1, \ldots, x_d), \mathbf{y} = (y_1, \ldots, y_d) \in \mathbb{R}^d, d = 2, 3$, is denoted by $\mathbf{x} \cdot \mathbf{y}$, and $\|\cdot\|_2$ denotes the Euclidean norm. We denote also by $\mathbf{x}^t$ the transpose of $\mathbf{x}$. We write $\delta_{m,l}$ for the Kronecker delta.

Let $\Omega \subset \mathbb{R}^d, d = 1, 2, 3$, be an open non-empty domain with a Lipschitz boundary Γ. In general, we will consider real-valued functional spaces. $C^0(\Omega)$ is the space of continuous functions, and $C^\infty(\Omega)$ is its subspace of infinitely differentiable functions in Ω. The support of a function $u \in C(\Omega)^0$ is defined as $\operatorname{supp}(u) := \overline{\{\mathbf{x} \in \Omega : u(\mathbf{x}) \neq 0\}}$. Then, $C_0^\infty(\Omega) := \{u \in C^\infty(\Omega) : \operatorname{supp}(u) \Subset \Omega\}$, and $C_{comp}^\infty(\Omega) := C_0^\infty(\mathbb{R}^d)|_\Omega$ (Sauter & Schwab,

2010, Section 2.3). The dual of $C_0^\infty(\Omega)$ is the space of distributions or linear functionals on Ω, denoted $\mathcal{D}'(\Omega)$.

Let $\varphi \in C_0^\infty(\Omega)$ and $\alpha = (\alpha_1, \alpha_2..., \alpha_d)$ a multi-index with $\alpha_i \geq 0$ integer numbers, such that $|\alpha| = \sum_{i=1}^d \alpha_i$. With multi-index notation, we write the derivative as

$$D^\alpha \varphi = \frac{\partial^{|\alpha|}\varphi}{\partial x_1^{\alpha_1}\partial x_2^{\alpha_2}...\partial x_d^{\alpha_d}}.$$

We denote by $L^p(\Omega)$ the class of measurable functions with a finite L^p-norm $\|u\|_{L^p(\Omega)} = \left(\int_\Omega |u|^p\, dx\right)^{\frac{1}{p}}$. We say that $g_\alpha \in L^p(\Omega)$ is a generalized derivative of $u \in L^p(\Omega)$ if

$$\int_\Omega u D^\alpha \varphi\, d\mathbf{x} = (-1)^{|\alpha|} \int_\Omega g_\alpha \varphi\, d\mathbf{x}, \quad \forall \varphi \in C_0^\infty(\Omega),$$

and we write $D^\alpha u := g_\alpha$. For $m \in \mathbb{Z}$, $m \geq 1$, and $1 \leq p < \infty$, the Sobolev spaces $W^{m,p}(\Omega)$ can be defined as (Brezis, 2011, Section 9.1)

$$W^{m,p}(\Omega) = \left\{u \in L^p(\Omega) \;:\; D^\alpha u \in L^p(\Omega), |\alpha| \leq m\right\}.$$

The norm for $p = \infty$ is defined by

$$\|f\|_{L^\infty(\Omega)} := \inf\{M \geq 0 : |f| \leq M \text{ almost everywhere in } \Omega\}.$$

Notice that $L^2(\Omega)$ corresponds to $W^{0,2}(\Omega)$. For $s \in \mathbb{R}$, we recall the standard Sobolev spaces $H^s(\Omega)$, with $H^0(\Omega) = L^2(\Omega)$ (Sauter & Schwab, 2010, Section 2.3). For $s \geq 0$, the space $H^s_{loc}(\Omega)$ consists of continuous linear functionals (distributions) on $C^\infty_{comp}(\Omega)$ whose restriction to every compact set $K \subset \Omega$ lies in $H^s(K)$ (Sauter & Schwab, 2010, Section 2.6). Also, we recall the following space (Hiptmair & Jerez-Hanckes, 2012, Section 2.2)

$$H^s_{loc}(\Delta, \Omega) := \{u \in H^s_{loc}(\Omega) : \Delta u \in L^2_{loc}(\Omega)\}.$$

The duality product between a Banach space X and its dual X' is denoted by $\langle \cdot, \cdot \rangle_{X \times X'}$. The inner product in a Hilbert space H is written $(\cdot, \cdot)_H$. We will also write I for the identity operator mapping.

For $T > 0$ and a Hilbert space H, $C^k([0, T]; H)$, $k \in \mathbb{N}_0$, denotes the space of k-times differentiable continuous functions in t with a bounded H-norm for all $t \in [0, T]$. $L^p([0, T]; H)$ is the space of Lebesgue measurable functions with

$$\|f\|^p_{L^p([0,T];H)} = \int_0^T \|f(t)\|^p_H dt < \infty, \quad p \in [1, \infty).$$

These spaces are also referred to as a *Bochner spaces*.

For $u \in C^\infty(\overline{\Omega})$, Dirichlet and Neumann traces operators are defined as

$$\gamma_D u := u|_\Gamma, \qquad \gamma_N u := \nabla u|_\Gamma \cdot \widehat{\mathbf{n}},$$

where $\widehat{\mathbf{n}}$ is the exterior unit normal. For a Lipschitz Γ, the Dirichlet trace has a unique extension to a linear and continuous operator $\gamma_D : H^1_{loc}(\Omega) \to L^2(\Gamma)$. The image of this operator is dense and is denoted by $H^{\frac{1}{2}}(\Gamma)$. The norm is given by

$$\|v\|_{H^{\frac{1}{2}}(\Gamma)} := \{\|u\|_{H^1(\Omega)} : \gamma_D u = v\}.$$

The space of bounded linear functionals on $H^{\frac{1}{2}}(\Gamma)$ is denoted by $H^{-\frac{1}{2}}(\Gamma)$. One can also show that the Neumann trace operator $\gamma_N : H^1_{loc}(\Delta, \Omega) \to H^{-\frac{1}{2}}(\Gamma)$ is continuous (see (Sauter & Schwab, 2010, Section 2.6 to 2.8)). $H^{\frac{1}{2}}(\Gamma)$ and $H^{-\frac{1}{2}}(\Gamma)$ are referred to as Dirichlet and Neumann trace spaces, respectively (Sauter & Schwab, 2010, Sections 2.4, 2.6 and 2.7). The proof of the proposition below can be found in (Sauter & Schwab, 2010, Proposition 2.5.2).

PROPOSITION 5.1. *The triple*

$$H^{\frac{1}{2}}(\Gamma) \subset L^2(\Gamma) \subset H^{-\frac{1}{2}}(\Gamma)$$

is a Gelfand triple, i.e. the spaces are continuously and densely embedded. Therefore, the inner product $(\cdot, \cdot)_{L^2(\Gamma)}$ can be continuously extended to dual pairings on $H^{\frac{1}{2}}(\Gamma) \times H^{-\frac{1}{2}}(\Gamma)$ and $H^{-\frac{1}{2}}(\Gamma) \times H^{\frac{1}{2}}(\Gamma)$.

5.3. Problem Statement and Boundary Integral Formulation

We now present a continuous model used for the electropermeabilization process. The main reference for the nonlinear dynamics is (Kavian et al., 2014), while for the boundary integral formulation used we follow (Hiptmair & Jerez-Hanckes, 2012; Henríquez & Jerez-Hanckes, 2018; Henríquez et al., 2017).

We consider the electric interaction of $\mathcal{N} \in \mathbb{N}$ disjoint spherical cells located at $\mathbf{p_j} \in \mathbb{R}^3$ with radii $R_j \in \mathbb{R}^+$, $j \in \{1, ..., \mathcal{N}\}$. We define the interior space of the jth cell by $\Omega_j := \{\mathbf{x} \in \mathbb{R}^3 : \|\mathbf{x} - \mathbf{p_j}\|_2 < R_j\}$, with its membrane being the boundary $\Gamma_j := \partial\Omega_j = \{\mathbf{x} \in \mathbb{R}^3 : \|\mathbf{x} - \mathbf{p_j}\|_2 = R_j\}$. The extracellular medium is defined as the complement to the intracellular domain:

$$\Omega_0 := \mathbb{R}^3 \setminus \bigcup_{j=1}^{\mathcal{N}} \overline{\Omega}_j.$$

An illustration of the geometry for three cells is presented in Figure 5-1.

5.3.1. Cell Electropermeabilization Model

We now describe a quasi-static electromagnetic problem in intra- and extracellular domains coupled with non-linear dynamics at the cells' membranes described below. This coupling relies on enforcing adequate transmission conditions for potentials and currents across the cells.

For $j \in \{0, ..., N\}$, each cell Ω_j is assumed to have constant conductivity $\sigma_j \in \mathbb{R}^+$. We consider a quasi-static electromagnetic regime, i.e. the frequency of the electric fields is low enough to discard any time delay in electromagnetic wave propagation (cf. (Plonsey & Heppner, 1967) and references therein). Thus, the Maxwell equations can be simplified in the intra- and extracellular media, and the problem is reduced to a boundary-value problem for electric potentials.

For $T \in \mathbb{R}^+$, let $\phi_e : [0, T] \times \Omega_0 \to \mathbb{R}$ be a given external potential, which represents an external electric stimulation. Let $u_0 : [0, T] \times \Omega_0 \to \mathbb{R}$ be the electric potential without excitation in the extracellular medium, so that total external potential is $u_0^{tot} := u_0 + \phi_e$.
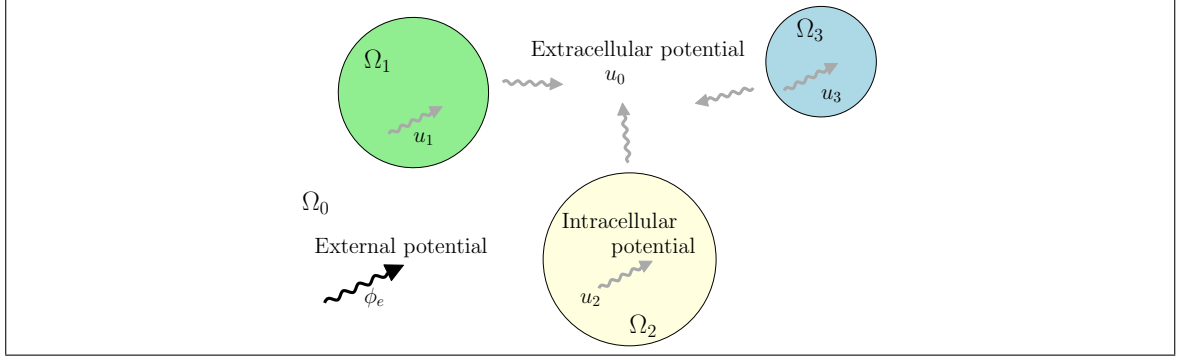
FIGURE 5-1. A system of three cells $\mathcal{N} = 3$.

We denote $u_j : [0, T] \times \Omega_j \to \mathbb{R}$, $j \in \{1, ..., \mathcal{N}\}$, the electric potential inside the j:th cell, as illustrated in Figure 5-1. On the cell membranes Γ_j, the potential is discontinuous, and the difference $v_j := u_j - u_0$ is called the *membrane or transmembrane* potential. At the same time, the flux is assumed to be continuous. These assumptions are well known in electrophysiological models (see (J. C. Neu & Krassowska, 1999; Ammari et al., 2016; Henríquez & Jerez-Hanckes, 2018; Henríquez et al., 2017; Guittet et al., 2017; Mistani et al., 2019; Leguèbe et al., 2014; Kavian et al., 2014). The assumption of the quasi-static regime and the aforementioned transmission conditions yield

$$\text{div}\,(\sigma_j \nabla u_j) = 0, \qquad (t, \mathbf{x}) \in [0, T] \times \Omega_j,\ j \in \{0, ..., \mathcal{N}\},$$

$$-\gamma_D^{0j} u_0 + \gamma_D^j u_j = v_j + \gamma_D^{0j} \phi_e, \qquad (t, \mathbf{x}) \in [0, T] \times \Gamma_j,\ j \in \{1, ..., \mathcal{N}\},$$

$$\sigma_0 \gamma_N^{0j} u_0 + \sigma_j \gamma_N^j u_j = -\sigma_0 \gamma_N^{0j} \phi_e, \qquad (t, \mathbf{x}) \in [0, T] \times \Gamma_j,\ j \in \{1, ..., \mathcal{N}\}.$$

The Dirichlet and Neumann operators used in the last two equations are defined in Section 5.2 for a general domain Ω with boundary Γ. One should keep in mind that they only act in the spatial variable $\mathbf{x}$. For a collection of spheres, we have added super-indices to emphasize where the traces are taken from: $0j$ for the trace arising from Ω_0 to Γ_j, and j for the one from Ω_j to Γ_j.

As mentioned in the introduction, there are different models of the nonlinear dynamics for the electro-permeabilization process. We adopt the phenomenological model presented

in (Kavian et al., 2014) at each cell $j \in \{1, ..., \mathcal{N}\}$, which takes the form:

$$c_{m,j}\partial_t v_j + I_j^{ep}(v_j, Z_j) = -\sigma_j \gamma_N^j u_j \qquad \qquad \text{on } [0, T] \times \Gamma_j,$$

$$I_j^{ep}(v_j, Z_j) = v_j(S_{L,j} + Z_j(t, v_j(t, \mathbf{x}))(S_{ir,j} - S_{L,j})) \qquad \text{on } [0, T] \times \Gamma_j,$$

with $c_{m,j}$ denoting the membrane capacitance per unit area, and I_j^{ep} being the electroper-meabilization current. This last quantity depends on the transmembrane potential v_j and a C^1-function $Z_j : [0, T] \times \Gamma_j \to [0, 1]$ (cf. (Kavian et al., 2014, Lemma 7)). For brevity, and slightly abusing the notations, we write $Z_j(t, \mathbf{x})$ instead of $Z_j(t, v_j(t, \mathbf{x}))$. The variable $Z_j(t, \mathbf{x})$ "measures in some way the likelihood that a given infinitesimal portion of the membrane is going to be electropermeabilized" (Kavian et al., 2014, p 247). Specifically, Z_j enforces the surface membrane conductivity to take values between two parameters: the surface conductivity $S_{ir,j}$ for which the electropermeabilization process becomes irreversible, and the lipid surface conductivity $S_{L,j}$. Indeed, when $Z_j = 0$, the membrane conductivity equals the lipid conductivity, and there is no electropermeabilization; if $Z_j = 1$, the membrane conductivity takes the maximal value above which electropermeabilization is irreversible. Following (Kavian et al., 2014), Z_j satisfies the ordinary differential equation:

$$\frac{\partial}{\partial t} Z_j(t, \lambda) = \max\left(\frac{\beta_j(\lambda) - Z_j(t, \lambda)}{\tau_{ep,j}}, \frac{\beta_j(\lambda) - Z_j(t, \lambda)}{\tau_{res,j}} \right).$$

Here, $\beta_j \in W^{1,\infty}(\mathbb{R}; [0, 1])$. If $\beta_j(v_j) - Z_j(t, v_j)$ is positive, the electric pulse is sufficiently high to enlarge the electropermeabilized region with a characteristic time $\tau_{ep,j}$. Contrarily, if $\beta_j(v_j) - Z_j(t, v_j)$ is negative, the pulse is not high enough to increase the electropermeabilization and the membrane tries to return to its resting state, with a characteristic resealing time $\tau_{res,j}$. Experimental observations suggest that $\tau_{res,j} > \tau_{ep,j}$.

REMARK 5.1. *The model for the dynamics of Z_j is similar to a sliding door model as, instead of being either one or zero, the function can take any value in the interval $[0, 1]$, as well as the function β_j.*

The function β_j is defined by

$$\beta_j(v) := \frac{1 + \tanh(k_{ep,j}(|v| - V_{rev,j}))}{2},\tag{5.1}$$

wherein two additional parameters are introduced: the electropermeabilization switch speed $k_{ep,j}$ between $S_{ir,j}$ and $S_{L,j}$, and $V_{rev,j}$, the transmembrane potential threshold for electropermeabilization to occur. More generally, any function β_j satisfying the following conditions (Kavian et al., 2014) could be used in this model:

$$\beta_j \in W^{1,\infty}(\mathbb{R}),\tag{5.2a}$$

$$v\beta_j'(v) \in L^\infty(\mathbb{R}),\tag{5.2b}$$

$$0 \le \beta_j(v) \le 1,\tag{5.2c}$$

$$\beta_j \text{ is non decreasing in } (0, \infty),\tag{5.2d}$$

$$\lim_{v \to \infty} \beta_j(v) = 1.\tag{5.2e}$$

The chosen β_j (5.1) satisfies the above conditions. This can be checked by recalling the properties of the hyperbolic functions $\tanh : \mathbb{R} \to [-1, 1]$ and $\operatorname{sech} : \mathbb{R} \to [0, 1]$ (Olver, Lozier, Boisvert, Clark, & National Institute of Standards and Technology (U.S.), 2010, Chapter 4):

$$\tanh(x) = \frac{e^x - e^{-x}}{e^x + e^{-x}},$$

$$\frac{d}{dx}\tanh(x) = \operatorname{sech}^2(x) = \frac{4}{(e^x + e^{-x})^2} > 0,$$

$$\lim_{x \to \infty} \tanh(x) = 1, \quad \lim_{x \to -\infty} \tanh(x) = -1.$$

In Figure 5-2, β_j is illustrated for two pairs of parameters.

REMARK 5.2. *This model assumes that the threshold potential V_{rev} is constant throughout the electropermeabilization process.*

In summary, the electropermeabilization dynamic problem reads:

(A) $k_{ep,j} = 40V^{-1}$ and $V_{rev,j} = 1.5V$. (B) $k_{ep,j} = 1V^{-1}$ and $V_{rev,j} = 1.5V$.
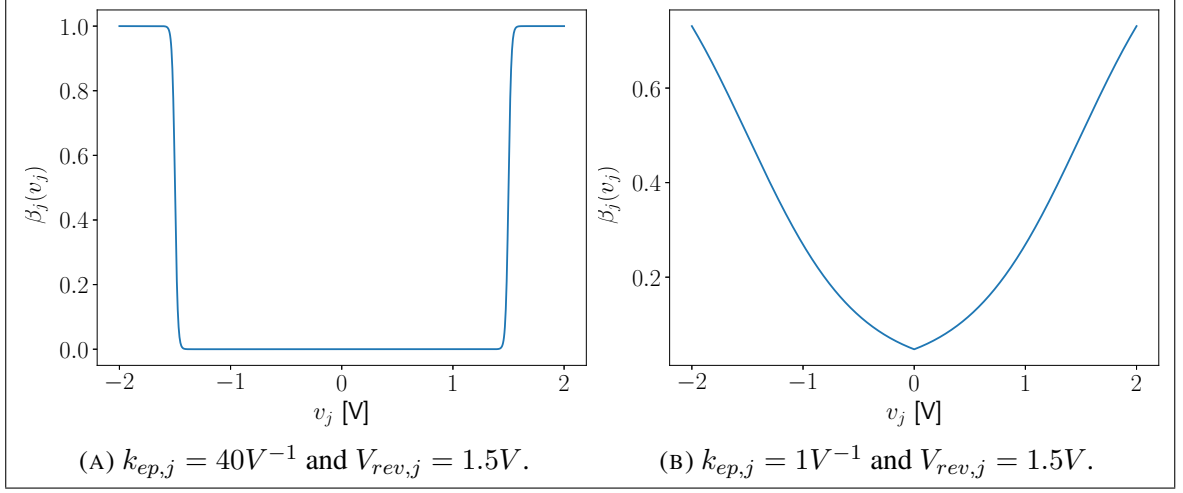
FIGURE 5-2. Values of $\beta_j(v_j)$ for two pairs of parameters. The parameters used in (a) are from (Kavian et al., 2014, Table 1), while the parameters used in (b) are chosen to show what happens with a smaller value of $k_{ep,j}$.

PROBLEM 5.1. *Given $T \in \mathbb{R}^+$, an external potential $\phi_e \in C([0,T], H^1_{loc}(\Omega_0))$, and the initial conditions $u_j^0 \in H^1(\Omega_j)$, and $Z_j^0 \in H^{\frac{1}{2}}(\Gamma_j)$, for $j = 1, \ldots, \mathcal{N}$, we seek $u_j \in C([0,T], H^1(\Omega_j))$, $v_j \in C([0,T], H^{\frac{1}{2}}(\Gamma_j))$, and $Z_j \in C([0,T], H^{\frac{1}{2}}(\Gamma_j))$ for $j \in \{1, ..., \mathcal{N}\}$ such that for $t \in [0,T]$,*

$$\mathrm{div}\,(\sigma_0 \nabla u_0) = 0 \qquad\qquad in\ \Omega_0, \qquad (5.3a)$$

$$\mathrm{div}\,(\sigma_j \nabla u_j) = 0 \qquad\qquad in\ \Omega_j, \qquad (5.3b)$$

$$-\gamma_D^{0j} u_0 + \gamma_D^j u_j = v_j + \gamma_D^{0j} \phi_e \qquad\qquad on\ \Gamma_j, \qquad (5.3c)$$

$$\sigma_0 \gamma_N^{0j} u_0 + \sigma_j \gamma_N^j u_j = -\sigma_0 \gamma_N^{0j} \phi_e \qquad\qquad on\ \Gamma_j, \qquad (5.3d)$$

$$c_{m,j} \partial_t v_j + I_j^{ep}(v_j, Z_j) = -\sigma_j \gamma_N^j u_j \qquad\qquad on\ \Gamma_j, \qquad (5.3e)$$

$$u_j(0, \mathbf{x}) = u_j^0,\ Z_j(0, \mathbf{x}) = Z_j^0 \qquad\qquad in\ \Omega_j \qquad (5.3f)$$

$$u_0(0, \mathbf{x}) = u_0^0 \qquad\qquad in\ \Omega_0, \qquad (5.3g)$$

$$u_0 \to \mathcal{O}(\|\mathbf{x}\|_2^{-1}) \qquad\qquad as\ \|\mathbf{x}\|_2 \to \infty, \qquad (5.3h)$$

with I_j^{ep} defined as:

$$I_j^{ep}(v_j, Z_j) = v_j \left(S_{L,j} + Z_j(t, v_j)(S_{ir,j} - S_{L,j}) \right), \qquad (5.4)$$

where the $Z_j(t, \lambda)$ satisfy:

$$\frac{\partial}{\partial t} Z_j(t, \lambda) = \max \left(\frac{\beta_j(\lambda) - Z_j(t, \lambda)}{\tau_{ep,j}}, \frac{\beta_j(\lambda) - Z_j(t, \lambda)}{\tau_{res,j}} \right) \qquad (5.5)$$

with β_j given by (5.1), and parameters $\tau_{ep,j}, \tau_{res,j}$ described above.

As above, we write $Z_j(x, \mathbf{x}) = Z_j(t, v_j(t, \mathbf{x}))$.

Observe that (5.3h) is the standard decay condition for the Laplace problem in three dimensions that guarantees that the problem is well posed.

REMARK 5.3. *The parameters of each cell, $c_{m,j}$, $V_{ep,j}$, $\tau_{ep,j}$ and $\tau_{res,j}$ might differ from cell to cell. In practical applications, these parameters depend on the cell type, e.g., cancer cells possess material properties different from healthy cells in the same tissue (Fernandez-Aranzamendi et al., 2022; Onemli et al., 2022).*

5.3.2. Boundary integral formulation

Due to the unboundedness of the domain as well as the constant conductivity values inside intra- and extracellular domains, one can write Problem 5.1 using boundary integral operators, thereby reducing the volume problem to a boundary one as in (Hiptmair & Jerez-Hanckes, 2012; Henríquez et al., 2017; Henríquez & Jerez-Hanckes, 2018). To accomplish this, we introduce boundary integral potentials and operators.

5.3.2.1. Boundary integral potential and operators

The free space fundamental solution of the Laplace equation for a source located at $\mathbf{r}'$ ((Jackson, 2013, Section 1.7)), satisfying the decay condition (5.3h) is

$$g(\mathbf{r}, \mathbf{r}') := \frac{1}{4\pi \|\mathbf{r} - \mathbf{r}'\|_2}, \qquad \mathbf{r} \neq \mathbf{r}'.$$

We recall the standard single and double layer operators defined for smooth densities:

$$DL_{0j}\left(\psi\right)\left(\mathbf{r}\right) := \int_{\Gamma_j} \psi\left(\mathbf{r}'\right) \nabla g\left(\mathbf{r},\mathbf{r}'\right) \cdot \widehat{\mathbf{n}}_{0j}\, dS', \quad SL_{0j}\left(\psi\right)\left(\mathbf{r}\right) := \int_{\Gamma_j} \psi\left(\mathbf{r}'\right) g\left(\mathbf{r},\mathbf{r}'\right) dS',$$

$$DL_j\left(\psi\right)\left(\mathbf{r}\right) := \int_{\Gamma_j} \psi\left(\mathbf{r}'\right) \nabla g\left(\mathbf{r},\mathbf{r}'\right) \cdot \widehat{\mathbf{n}}_j\, dS', \quad SL_j\left(\psi\right)\left(\mathbf{r}\right) := \int_{\Gamma_j} \psi\left(\mathbf{r}'\right) g\left(\mathbf{r},\mathbf{r}'\right) dS',$$

with the gradient being taken with respect to $\mathbf{r}'$, $\widehat{\mathbf{n}}_j$ being the exterior normal vector of Ω_j, and $\widehat{\mathbf{n}}_j = -\widehat{\mathbf{n}}_{0j}$. It can be shown that these operators are linear and continuous (cf. (Sauter & Schwab, 2010, Section 3.1), (Henríquez & Jerez-Hanckes, 2018, Section 3.1)), in the following Sobolev spaces:

$$DL_{0j} : H^{\frac{1}{2}}(\Gamma_j) \to H^1_{loc}\left(\mathbb{R}^3 \setminus \cup_{j=1}^{\mathcal{N}}\Gamma_j\right), \quad SL_{0j} : H^{-\frac{1}{2}}(\Gamma_j) \to H^1_{loc}\left(\mathbb{R}^3 \setminus \cup_{j=1}^{\mathcal{N}}\Gamma_j\right),$$

$$DL_j : H^{\frac{1}{2}}(\Gamma_j) \to H^1_{loc}\left(\mathbb{R}^3 \setminus \cup_{j=1}^{\mathcal{N}}\Gamma_j\right), \quad SL_j : H^{-\frac{1}{2}}(\Gamma_j) \to H^1_{loc}\left(\mathbb{R}^3 \setminus \cup_{j=1}^{\mathcal{N}}\Gamma_j\right).$$

We will write u_j in terms of these boundary potentials, and since we aim at rendering Problem 5.1 onto the cells' boundaries, we will take traces of these potentials. This leads to boundary integral operators (BIOs), which are defined by taking the following averages (Sauter & Schwab, 2010, Section 3.1.2):

$$V^0_{i,j} := \frac{1}{2}\left(\gamma^i_D SL_{0j} + \gamma^{0i}_D SL_{0j}\right), \qquad V_j := \frac{1}{2}\left(\gamma^{0j}_D SL_j + \gamma^j_D SL_j\right),$$

$$K^0_{i,j} := \frac{1}{2}\left(\gamma^i_D DL_{0j} + \gamma^{0i}_D DL_{0j}\right), \qquad K_j := \frac{1}{2}\left(\gamma^{0j}_D DL_j + \gamma^j_D DL_j\right), \qquad (5.6)$$

$$K^{*0}_{i,j} := \frac{1}{2}\left(-\gamma^i_N SL_{0j} + \gamma^{0i}_N SL_{0j}\right), \qquad K^*_j := \frac{1}{2}\left(-\gamma^{0j}_N SL_j + \gamma^j_N SL_j\right),$$

$$W^0_{i,j} := -\frac{1}{2}\left(-\gamma^i_N DL_{0j} + \gamma^{0i}_N DL_{0j}\right), \qquad W_j := -\frac{1}{2}\left(-\gamma^{0j}_N DL_j + \gamma^j_N DL_j\right).$$

One can show that these operators are linear and continuous (Sauter & Schwab, 2010, Theorem 3.1.16) in the following Sobolev spaces:

$$V^0_{i,j} : H^{-\frac{1}{2}}(\Gamma_j) \to H^{\frac{1}{2}}(\Gamma_i), \qquad V_j : H^{-\frac{1}{2}}(\Gamma_j) \to H^{\frac{1}{2}}(\Gamma_j),$$

$$W^0_{i,j} : H^{\frac{1}{2}}(\Gamma_j) \to H^{-\frac{1}{2}}(\Gamma_i), \qquad W_j : H^{\frac{1}{2}}(\Gamma_j) \to H^{-\frac{1}{2}}(\Gamma_j),$$

$$K^0_{i,j} : H^{\frac{1}{2}}(\Gamma_j) \to H^{\frac{1}{2}}(\Gamma_i), \qquad K_j : H^{\frac{1}{2}}(\Gamma_j) \to H^{\frac{1}{2}}(\Gamma_j),$$

$$K_{i,j}^{*0} : H^{-\frac{1}{2}}(\Gamma_j) \to H^{-\frac{1}{2}}(\Gamma_i), \qquad\qquad K_j^* : H^{-\frac{1}{2}}(\Gamma_j) \to H^{-\frac{1}{2}}(\Gamma_j).$$

Since the domains are smooth, the jump relations for the potentials across a closed boundary (Sauter & Schwab, 2010, Theorem 3.3.1) yield

$$V_{i,j}^0 = \gamma_D^{0i} SL_{0j}, \qquad\qquad V_j = \gamma_D^j SL_j,$$

$$W_{i,j}^0 = -\gamma_N^{0i} DL_{0j}, \qquad\qquad W_j = -\gamma_N^j DL_j,$$

$$K_{i,j}^0 = \gamma_D^{0i} DL_{0j} \text{ with } i \neq j, \qquad\qquad K_{i,j}^{*0} = \gamma_N^{0i} SL_{0j} \text{ with } i \neq j,$$

and

$$K_{j,j}^0(\psi) = \frac{1}{2}\psi + \gamma_D^{0j} DL_{0j}(\psi), \qquad\qquad K_j(\psi) = \frac{1}{2}\psi + \gamma_D^j DL_j(\psi),$$

$$K_{j,j}^{*0}(\psi) = -\frac{1}{2}\psi + \gamma_N^{0j} SL_{0j}(\psi), \qquad\qquad K_j^*(\psi) = -\frac{1}{2}\psi + \gamma_N^j SL_j(\psi).$$

In the next theorem, we present the integral representation formulas for the electric potentials u_j and u_0.

Theorem 5.2. *((Sauter & Schwab, 2010, Section 3)) The integral representation formulas for $u_j \in H^1(\Omega_j)$, $u_0 \in H^1_{loc}(\Omega_0)$ with the single and double layer operators read*

$$u_0 = -\sum_{i=1}^{\mathcal{N}} DL_{0i}\left(\gamma_D^{0i} u_0\right) + \sum_{i=1}^{\mathcal{N}} SL_{0i}\left(\gamma_N^{0i} u_0\right), \tag{5.7a}$$

$$u_j = -DL_j\left(\gamma_D^j u_j\right) + SL_j\left(\gamma_N^j u_j\right), \quad \forall j \in \{1, ..., \mathcal{N}\}. \tag{5.7b}$$

where we extend u_j by zero to the complement of Ω_j.

The next step is to use the operators introduced in this section and the integral representation formula to write the MTF of Problem 5.1 (cf. (Hiptmair & Jerez-Hanckes, 2012) and later references).

5.3.2.2. Multiple traces formulation for Problem 5.1

For $j \in \{1, ..., \mathcal{N}\}$, we introduce the Cartesian product of Hilbert spaces $\boldsymbol{H}_j :=$ $H^{\frac{1}{2}}(\Gamma_j) \times H^{-\frac{1}{2}}(\Gamma_j)$, with norm

$$\| \cdot \|_{\boldsymbol{H}_j} = \| \cdot \|_{H^{\frac{1}{2}}(\Gamma_j)} + \| \cdot \|_{H^{-\frac{1}{2}}(\Gamma_j)}. \tag{5.8}$$

Let be $\boldsymbol{\phi}, \boldsymbol{\xi} \in \boldsymbol{H}_j$, such that $\boldsymbol{\phi} = (\phi_D, \phi_N)$ and $\boldsymbol{\xi} = (\xi_D, \xi_N)$. We introduce the cross-product over Γ_j (Hiptmair & Jerez-Hanckes, 2012, Section 2.2.1) by

$$\langle \boldsymbol{\phi}, \boldsymbol{\xi} \rangle_{\times, j} := \langle \phi_D, \xi_N \rangle_j + \langle \xi_D, \phi_N \rangle_j,$$

where for brevity we denote $\langle \xi_D, \phi_N \rangle_j := \langle \xi_D, \phi_N \rangle_{H^{\frac{1}{2}}(\Gamma_j) \times H^{-\frac{1}{2}}(\Gamma_j)}$.

We define also the flip-sign operator $\mathsf{X}_j : \boldsymbol{H}_j \to \boldsymbol{H}_j$, $\boldsymbol{\gamma}^{0j} : H_{loc}^1(\Delta, \Omega_0) \to \boldsymbol{H}_j$ and $\boldsymbol{\gamma}^j : H^1(\Delta, \Omega_j) \to \boldsymbol{H}_j$ as:

$$\mathsf{X}_j := \begin{bmatrix} I & 0 \\ 0 & -\frac{\sigma_0}{\sigma_j} I \end{bmatrix}, \quad \boldsymbol{\gamma}^{0j} := \begin{pmatrix} \gamma_D^{0j} \\ \gamma_N^{0j} \end{pmatrix} \quad \text{and} \quad \boldsymbol{\gamma}^j := \begin{pmatrix} \gamma_D^j \\ \gamma_N^j \end{pmatrix}, \quad j \in \{1, ..., \mathcal{N}\}, \tag{5.9}$$

with I being the identity operator in the corresponding functional space, and for simplicity, we adopt the same notation for I in different spaces. Then, we write Dirichlet and Neumamn boundary conditions, (5.3c) and (5.3d), respectively, succinctly as

$$-\mathsf{X}_j \boldsymbol{\gamma}^{0j} u_0 + \boldsymbol{\gamma}^j u_j = \mathsf{X}_j (v_j, \ 0)^t + \mathsf{X}_j \boldsymbol{\gamma}^{0j} \phi_e, \tag{5.10a}$$

$$\boldsymbol{\gamma}^{0j} u_0 - \mathsf{X}_j^{-1} \boldsymbol{\gamma}^j u_j = -(v_j, \ 0)^t - \boldsymbol{\gamma}^{0j} \phi_e. \tag{5.10b}$$

Note that the two equations are equivalent.

Taking Dirichlet and Neumann traces of both (5.7a) and (5.7b), and rewriting the resulting expressions in terms of BIOs, we obtain

$$\gamma_D^{0j} u_0 = -\left(-\frac{1}{2} I \left(\gamma_D^{0j} u_0 \right) + \sum_{i=1}^n K_{j,i}^0 \left(\gamma_D^{0i} u_0 \right) \right) + \sum_{i=1}^n V_{j,i}^0 \left(\gamma_N^{0i} u_0 \right),$$

$$\gamma_N^{0j} u_0 = \sum_{i=1}^{n} W_{j,i}^0 \left(\gamma_D^{0i} u_0 \right) + \left(\frac{1}{2} I \left(\gamma_N^{0j} u_0 \right) + \sum_{i=1}^{n} K_{j,i}^{*0} \left(\gamma_N^{0i} u_0 \right) \right),$$

$$\gamma_D^j u_j = - \left(-\frac{1}{2} I \left(\gamma_D^j u_j \right) + K_j \left(\gamma_D^j u_j \right) \right) + V_j \left(\gamma_N^j u_j \right),$$

$$\gamma_N^j u_j = W_j \left(\gamma_D^j u_j \right) + \left(\frac{1}{2} I \left(\gamma_N^j u_j \right) + K_j^* \left(\gamma_N^j u_j \right) \right).$$

After some algebra, one can write

$$\gamma_D^{0j} u_0 = 2 \left(\sum_{i=1}^{n} -K_{j,i}^0 \left(\gamma_D^{0i} u_0 \right) + \sum_{i=1}^{n} V_{j,i}^0 \left(\gamma_N^{0i} u_0 \right) \right),$$

$$\gamma_N^{0j} u_0 = 2 \left(\sum_{i=1}^{n} W_{j,i}^0 \left(\gamma_D^{0i} u_0 \right) + \sum_{i=1}^{n} K_{j,i}^{*0} \left(\gamma_N^{0i} u_0 \right) \right),$$

$$\gamma_D^j u_j = 2 \left(-K_j \left(\gamma_D^j u_j \right) + V_j \left(\gamma_N^j u_j \right) \right),$$

$$\gamma_N^j u_j = 2 \left(W_j \left(\gamma_D^j u_j \right) + K_j^* \left(\gamma_N^j u_j \right) \right).$$

These expressions can be written in a simpler form:

$$\boldsymbol{\gamma}^{0j} u_0 = 2 \sum_{i=1}^{\mathcal{N}} \mathsf{A}_{j,i}^0 \, \boldsymbol{\gamma}^{0i} u_0, \quad \boldsymbol{\gamma}^j u_j = 2 \, \mathsf{A}_j \, \boldsymbol{\gamma}^j u_j, \quad j \in \{1, ..., \mathcal{N}\},$$

with

$$\mathsf{A}_{j,i}^0 := \begin{bmatrix} -K_{j,i}^0 & V_{j,i}^0 \\ W_{j,i}^0 & K_{j,i}^{*0} \end{bmatrix}, \quad \mathsf{A}_j := \begin{bmatrix} -K_j & V_j \\ W_j & K_j^* \end{bmatrix}.$$

By replacing $\boldsymbol{\gamma}^{0j} u_0$, $\boldsymbol{\gamma}^j u_j$ into (5.10b) and (5.10a), we obtain

$$2 \sum_{i=1}^{n} \mathsf{A}_{j,i}^0 \, \boldsymbol{\gamma}^{0i} u_0 - \mathsf{X}_j^{-1} \boldsymbol{\gamma}^j u_j = -(v_j, \, 0)^t - \boldsymbol{\gamma}^{0j} \phi_e,$$

$$-\mathsf{X}_j \boldsymbol{\gamma}^{0j} u_0 + 2 \, \mathsf{A}_j \, \boldsymbol{\gamma}^j u_j = \mathsf{X}_j (v_j, \, 0)^t + \mathsf{X}_j \boldsymbol{\gamma}^{0j} \phi_e \quad \text{on } \Gamma_j.$$

We introduce Cartesian product space of multiple traces $\mathbb{H} := \Pi_{j=1}^{\mathcal{N}} \boldsymbol{H}_j$ and $\mathbb{H}^{(2)} := \mathbb{H} \times \mathbb{H} = \Pi_{j=1}^{\mathcal{N}} \boldsymbol{H}_j \times \Pi_{j=1}^{\mathcal{N}} \boldsymbol{H}_j$. For $\boldsymbol{\phi}, \boldsymbol{\xi} \in \mathbb{H}^{(2)}$, such that $\boldsymbol{\phi} = (\boldsymbol{\phi}^{01}, ..., \boldsymbol{\phi}^{0\mathcal{N}}, \boldsymbol{\phi}^1, ..., \boldsymbol{\phi}^{\mathcal{N}})$

and $\boldsymbol{\xi} = (\boldsymbol{\xi}^{01}, ..., \boldsymbol{\xi}^{0\mathcal{N}}, \boldsymbol{\xi}^{1}, ..., \boldsymbol{\xi}^{\mathcal{N}})$, we define the cross-product of $\mathbb{H}^{(2)}$ as

$$\langle \boldsymbol{\phi}, \boldsymbol{\xi} \rangle_\times = \sum_{j=1}^{\mathcal{N}} \langle \boldsymbol{\phi}^{0j}, \boldsymbol{\xi}^{0j} \rangle_{\times,j} + \sum_{j=1}^{\mathcal{N}} \langle \boldsymbol{\phi}^{j}, \boldsymbol{\xi}^{j} \rangle_{\times,j}.$$

We will also use the following multiple trace spaces reordering $\mathbb{H}_D := \Pi_{j=1}^{\mathcal{N}} H^{\frac{1}{2}}(\Gamma_j)$, $\mathbb{H}_N := \Pi_{j=1}^{\mathcal{N}} H^{-\frac{1}{2}}(\Gamma_j)$. Now, we can introduce the local Multiple Trace formulation (MTF) operator (Hiptmair & Jerez-Hanckes, 2012, Section 3.2.3), $\mathbf{M}_{\mathcal{N}} : \mathbb{H}^{(2)} \to \mathbb{H}^{(2)}$, for the geometry presented in Section 5.3:

$$\mathbf{M}_{\mathcal{N}} := \begin{bmatrix} 2\mathbf{A}_{0,\mathcal{N}} & -\mathbf{X}_{\mathcal{N}}^{-1} \\ -\mathbf{X}_{\mathcal{N}} & 2\mathbf{A}_{1,\mathcal{N}} \end{bmatrix}, \text{ with } \mathbf{A}_{0,\mathcal{N}} := \begin{bmatrix} \mathsf{A}^0_{1,1} & \mathsf{A}^0_{1,2} & ... & \mathsf{A}^0_{1,\mathcal{N}} \\ \mathsf{A}^0_{2,1} & \mathsf{A}^0_{2,2} & ... & \mathsf{A}^0_{2,\mathcal{N}} \\ \vdots & & \ddots & \vdots \\ \mathsf{A}^0_{\mathcal{N},1} & \mathsf{A}^0_{\mathcal{N},2} & ... & \mathsf{A}^0_{\mathcal{N},\mathcal{N}} \end{bmatrix}, \tag{5.11}$$

$$\mathbf{A}_{1,\mathcal{N}} := \begin{bmatrix} \mathsf{A}_1 & 0 & ... & 0 \\ 0 & \mathsf{A}_2 & ... & 0 \\ \vdots & & \ddots & \vdots \\ 0 & ... & 0 & \mathsf{A}_{\mathcal{N}} \end{bmatrix} \text{ and } \mathbf{X}_{\mathcal{N}} := \begin{bmatrix} \mathsf{X}_1 & 0 & ... & 0 \\ 0 & \mathsf{X}_2 & ... & 0 \\ \vdots & & \ddots & \vdots \\ 0 & ... & 0 & \mathsf{X}_{\mathcal{N}} \end{bmatrix}.$$

With the MTF operator, the interface conditions (5.3b), (5.3c) and (5.3d) (Problem 5.1) can be written as:

$$\mathbf{M}_{\mathcal{N}} \begin{pmatrix} \boldsymbol{\gamma}_u^0 \\ \boldsymbol{\gamma}_u \end{pmatrix} = \begin{pmatrix} -\mathbf{I}_{2\mathcal{N} \times \mathcal{N}} \mathbf{v} \\ \mathbf{X}_{\mathcal{N}} \mathbf{I}_{2\mathcal{N} \times \mathcal{N}} \mathbf{v} \end{pmatrix} + \begin{pmatrix} -\boldsymbol{\gamma}_{\phi_e}^0 \\ \mathbf{X}_{\mathcal{N}} \boldsymbol{\gamma}_{\phi_e}^0 \end{pmatrix}, \tag{5.12}$$

where we use the notation:

$$\boldsymbol{\gamma}_u^0 := \left(\boldsymbol{\gamma}^{01} u_0, \boldsymbol{\gamma}^{02} u_0, \ldots, \boldsymbol{\gamma}^{0\mathcal{N}} u_0 \right)^t,$$

$$\boldsymbol{\gamma}_{\phi_e}^0 := \left(\boldsymbol{\gamma}^{01} \phi_e, \boldsymbol{\gamma}^{02} \phi_e, \ldots, \boldsymbol{\gamma}^{0\mathcal{N}} \phi_e \right)^t,$$

$$\boldsymbol{\gamma}_u := \left(\boldsymbol{\gamma}^{1} u_1, \boldsymbol{\gamma}^{2} u_2, ..., \boldsymbol{\gamma}^{\mathcal{N}} u_{\mathcal{N}} \right)^t, \text{ and}$$

$$\mathbf{v} := \Big(v_1, v_2, v_3, \ldots, v_{\mathcal{N}}\Big)^t,$$

with superscript t denoting the transposition, and the operator $\mathbf{I}_{2\mathcal{N}\times\mathcal{N}} : \mathbb{H}_D \to \mathbb{H}$ is defined as:

$$\mathbf{I}_{2\mathcal{N}\times\mathcal{N}} := \begin{pmatrix} I & 0 & \ldots & 0 \\ 0 & 0 & \ldots & 0 \\ 0 & I & \ldots & 0 \\ 0 & 0 & \ldots & 0 \\ \vdots & \vdots & & \vdots \\ 0 & 0 & \ldots & I \\ 0 & 0 & \ldots & 0 \end{pmatrix}.$$

Notice that the identity operators act on the corresponding Dirichlet traces. The following result is a consequence of (Henríquez & Jerez-Hanckes, 2018, Proposition 3.9, Proposition 3.10) along with the Fredholm alternative.

Theorem 5.3 (Existence, uniqueness and stability)**.** *The operator* $\mathbf{M}_{\mathcal{N}}$ *is a linear, injective and coercive operator in* $\mathbb{H}^{(2)}$*. For all* $\boldsymbol{\xi} \in \mathbb{H}^{(2)}$*, there exists a unique weak solution* $\boldsymbol{\lambda} \in \mathbb{H}^{(2)}$ *of*

$$(\mathbf{M}_{\mathcal{N}}\boldsymbol{\lambda}, \boldsymbol{\phi})_{\times} = (\boldsymbol{\xi}, \boldsymbol{\phi})_{\times}, \quad \forall \boldsymbol{\phi} \in \mathbb{H}^{(2)},$$

that satisfies the following stability estimate:

$$\|\boldsymbol{\lambda}\|_{\mathbb{H}^{(2)}} \le c\|\boldsymbol{\xi}\|_{\mathbb{H}^{(2)}},$$

for a constant $c > 0$.

5.3.2.3. Boundary integral formulation of Problem 5.1

Until this point, we have not introduced the membrane dynamics of Problem 5.1. In the following, we will use the theory presented in (Henríquez et al., 2017; Henríquez & Jerez-Hanckes, 2018) to combine the MTF with the nonlinear dynamics.

Thanks to Theorem 5.3 we can take the inverse of the MTF operator, and (5.12) becomes

$$
\begin{pmatrix} \boldsymbol{\gamma}_u^0 \\ \boldsymbol{\gamma}_u \end{pmatrix} = \mathbf{M}_{\mathcal{N}}^{-1} \begin{pmatrix} -\mathbf{I}_{2\mathcal{N}\times\mathcal{N}}\,\mathbf{v} \\ \mathbf{X}_{\mathcal{N}}\,\mathbf{I}_{2\mathcal{N}\times\mathcal{N}}\,\mathbf{v} \end{pmatrix} + \mathbf{M}_{\mathcal{N}}^{-1} \begin{pmatrix} -\boldsymbol{\gamma}_{\phi_e}^0 \\ \mathbf{X}_{\mathcal{N}}\,\boldsymbol{\gamma}_{\phi_e}^0 \end{pmatrix}.
$$

The even components of the vector γ_u (the interior Neumann traces), related to the nonlinear dynamics of the problem by (5.3e), can be retrieved as follows:

$$
\begin{pmatrix} \sigma_1\gamma_N^1(u_1) \\ \sigma_2\gamma_N^2(u_2) \\ \vdots \\ \sigma_{\mathcal{N}}\gamma_N^{\mathcal{N}}(u_{\mathcal{N}}) \end{pmatrix} = \boldsymbol{\sigma}_{\mathcal{N}\times 4\mathcal{N}}\mathbf{M}_{\mathcal{N}}^{-1}\left(\begin{pmatrix} -\mathbf{I}_{2\mathcal{N}\times\mathcal{N}}\,\mathbf{v} \\ \mathbf{X}_{\mathcal{N}}\,\mathbf{I}_{2\mathcal{N}\times\mathcal{N}}\,\mathbf{v} \end{pmatrix} + \begin{pmatrix} -\boldsymbol{\gamma}_{\phi_e}^0 \\ \mathbf{X}_{\mathcal{N}}\,\boldsymbol{\gamma}_{\phi_e}^0 \end{pmatrix} \right),
$$

where the dimensions of $\boldsymbol{\sigma}_{\mathcal{N}\times 4\mathcal{N}}$ are $\mathcal{N}\times 4\mathcal{N}$, the first half containing only zeros:

$$
\boldsymbol{\sigma}_{\mathcal{N}\times 4\mathcal{N}} := \begin{pmatrix} 0 & \dots & 0 & \sigma_1 I & 0 & 0 & \dots & 0 \\ 0 & \dots & 0 & 0 & 0 & \sigma_2 I & \dots & 0 \\ \vdots & & \vdots & \vdots & \vdots & \vdots & & \vdots \\ 0 & \dots & 0 & 0 & 0 & 0 & \dots & \sigma_{\mathcal{N}} I \end{pmatrix}.
$$

Now, we define the Dirichlet-to-Neumann operators $\mathcal{J}_{\mathcal{N}} : \mathbb{H}_D \to \mathbb{H}_N$, and $\Phi : H_{loc}^1(\Omega_0) \to \mathbb{H}_N$ as

$$
\mathcal{J}_{\mathcal{N}}(\mathbf{v}) := \boldsymbol{\sigma}_{\mathcal{N}\times 4\mathcal{N}}\mathbf{M}_{\mathcal{N}}^{-1} \begin{pmatrix} -\mathbf{I}_{2\mathcal{N}\times\mathcal{N}}\,\mathbf{v} \\ \mathbf{X}_{\mathcal{N}}\,\mathbf{I}_{2\mathcal{N}\times\mathcal{N}}\,\mathbf{v} \end{pmatrix}, \text{ and } \Phi(\phi_e) := \boldsymbol{\sigma}_{\mathcal{N}\times 4\mathcal{N}}\mathbf{M}_{\mathcal{N}} \begin{pmatrix} -\boldsymbol{\gamma}_{\phi_e}^0 \\ \mathbf{X}_{\mathcal{N}}\,\boldsymbol{\gamma}_{\phi_e}^0 \end{pmatrix}.
$$

$$(5.13)$$

Theorem 5.4. *The operator $\mathcal{J}_{\mathcal{N}} : \mathbb{H}_D \to \mathbb{H}_N$ is continuous and coercive.*

This theorem is proved as in (Henríquez & Jerez-Hanckes, 2018, Lemma 4.3).

REMARK 5.4. *The MTF (5.11) is similar to one in (Henríquez & Jerez-Hanckes, 2018) and (Henríquez et al., 2017). Specifically, (5.11) is multiplied by two, and the first row does not have a factor σ_j as in (Henríquez et al., 2017) and (Henríquez & Jerez-Hanckes, 2018).*

Now we can finally rewrite Problem 5.1 as an abstract parabolic equation on Γ_j.

PROBLEM 5.5. *Given a final time $T \in \mathbb{R}^+$, the external potential $\phi_e \in C([0,T], H^1_{loc}(\Omega_0))$ and the initial conditions $v_j(0) = v_0 \in H^{\frac{1}{2}}(\Gamma_j)$, $Z_j(0) = Z_j^0 \in H^{\frac{1}{2}}(\Gamma_j)$, for $j \in \{1,...,\mathcal{N}\}$. We seek $\mathbf{v} = (v_1,\ldots,v_\mathcal{N})^t$, with $v_j \in C([0,T], H^{\frac{1}{2}}(\Gamma_j))$, and $\mathbf{Z} = (Z_1,\ldots,Z_\mathcal{N})^t$, $Z_j \in C([0,T], H^{\frac{1}{2}}(\Gamma_j))$, for $j \in \{1,...,\mathcal{N}\}$, such that*

$$\mathbf{C_m}\partial_t\mathbf{v} = -\mathbf{I}^{ep}(\mathbf{v},\mathbf{Z}) - \mathcal{J}_\mathcal{N}(\mathbf{v}) - \Phi(\phi_e) \text{ on } [0,T] \times \Gamma_j, \qquad (5.14)$$

where $\mathbf{C_m}$ is a diagonal matrix $\mathrm{diag}(c_{m,1},\ldots,c_{m,\mathcal{N}})$; the operators $\mathcal{J}_\mathcal{N}(\mathbf{v})$ and $\Phi(\phi_e)$ are defined in (5.13). The vector $\mathbf{I}^{ep}(\mathbf{v},\mathbf{Z}) = (I_1^{ep}(v_1,Z_1),\ldots,I_\mathcal{N}^{ep}(v_\mathcal{N},Z_\mathcal{N}))^t$ satisfy (5.4), (5.5) and (5.1).

5.4. Numerical Approximation

In this section we propose a numerical solution of Problem 5.5. We use a semi-implicit time stepping scheme, similar to one used in (Henríquez et al., 2017; Henríquez & Jerez-Hanckes, 2018) (see Section 5.4.1). For the space discretization, we follow an analogous approach in the two-dimensional case employed in (Henríquez & Jerez-Hanckes, 2018), using spherical harmonics as a spacial basis. Since we consider a three-dimensional case, and do not work with complex valued functions, we employ real spherical harmonics to approximate boundary unknowns.

5.4.1. Semi-implicit time stepping scheme

Let $\mathcal{T}_S := \{t_s\}_{s=0}^S$ denote the uniform partition of the time interval $[0,T]$, with $T \in \mathbb{R}^+$, and $S \in \mathbb{N}$, where the time step is $\tau = T/S$, and $t_s = s\tau$. Write

$$t_{s+\frac{1}{2}} := t_s + \frac{\tau}{2}, \quad s \in \{0,\ldots,S-1\},$$

for the midstep between t_s and t_{s+1}. For a time dependent quantity $\phi(t)$, we write $\phi^{(s)} = \phi(t_s)$, and we define the following quantities:

$$\phi^{(s+\frac{1}{2})} := \phi(t_{s+\frac{1}{2}}), \qquad \overline{\phi}^{(s+\frac{1}{2})} := \frac{\phi^{(s+1)} + \phi^{(s)}}{2},$$

$$\hat{\phi}^{(s+\frac{1}{2})} := \frac{3\phi^{(s)} - \phi^{(s-1)}}{2}, \qquad \overline{\partial}\phi^{(s)} := \frac{\phi^{(s+1)} - \phi^{(s)}}{\tau}.$$

With these, we approximate in time (5.5) and (5.5) as follows:

$$\mathbf{C_m}\overline{\partial}\mathbf{v}^{(s)} = -\mathbf{I}^{ep}\left(\widehat{\mathbf{v}}^{(s+\frac{1}{2})}, \widehat{\mathbf{Z}}^{(s+\frac{1}{2})}\right) - \mathcal{J}_{\mathcal{N}}\left(\overline{\mathbf{v}}^{(s+\frac{1}{2})}\right) - \Phi(\phi_e^{(s+\frac{1}{2})}),$$

$$\overline{\partial}^{(s)}Z_j = \max\left(\frac{\beta_j(\widehat{v}_j^{(s+\frac{1}{2})}) - \widehat{Z}_j^{(s+\frac{1}{2})}}{\tau_{ep,j}}, \frac{\beta_j(\widehat{v}_j^{(s+\frac{1}{2})}) - \widehat{Z}_j^{(s+\frac{1}{2})}}{\tau_{res,j}}\right).$$

From these expressions, we can notice that

(i) At each iteration, the approximation at t_{s+1} requires two previous steps, t_s and t_{s-1}, but we only have information about the time t_0. Thus, we will estimate the values for the time t_1 with a predictor-corrector algorithm introduced later in this Section.

(ii) Provided with values for the two previous time steps, unknowns for the next time are obtained in terms of $\overline{\partial}\mathbf{v}^{(s)}$, $\overline{\mathbf{v}}^{(s+\frac{1}{2})}$ and $\overline{\partial}^{(s)}$, which are linear. Nonlinear terms are evaluated with values already known, i.e. they are explicit terms, unlike the others. For this reason, the time scheme is called semi-implicit.

(iii) At each time step, the discrete problem to be solved is linear. One could choose time-domain schemes with implicit non-linear parts. Consequently, more information about $\mathbf{I}^{ep}$ may be needed. In contrast, our semi-implicit time only requires us to evaluate the function $\mathbf{I}^{ep}$.

(iv) The method is not fully implicit, and the time step τ needs to be small enough for the scheme to converge.

The predictor-corrector algorithm can be found in detail in (Thomée, 2006, Chapter 13), (Ganesh & Mustapha, 2007), (Henríquez & Jerez-Hanckes, 2018, Section 6.3) or

(Henríquez et al., 2017, Algorithm 1). Set $\mathbf{w}^{(0)} = \mathbf{v}^{(0)}$ and $\mathbf{Q}^{(0)} = \mathbf{Z}(0)$. Then, proceed as follows:

(I) *Predictor.* First, construct predictions $\mathbf{w}^{(1)}$ and $\mathbf{Q}^{(1)}$ by solving the linear system:

$$\mathbf{C_m}\overline{\partial}\mathbf{w}^{(0)} = -\mathbf{I}^{ep}\left(\mathbf{w}^{(0)}, \mathbf{Q}^{(0)}\right) - \mathcal{J}_{\mathcal{N}}\left(\overline{\mathbf{w}}^{(\frac{1}{2})}\right) - \Phi\left(\phi_e^{(\frac{1}{2})}\right),$$

$$\overline{\partial}Q_j^{(0)} = \max\left(\frac{\beta_j(w_j^{(0)}) - Q_j^{(0)}}{\tau_{ep,j}}, \frac{\beta_j(w_j^{(0)}) - Q_j^{(0)}}{\tau_{res,j}}\right) \quad \forall j \in \{1, ..., \mathcal{N}\}.$$

(II) *Corrector.* Then, correct $\mathbf{w}^{(1)}$ and $\mathbf{Q}^{(1)}$ to obtain final values for $\mathbf{v}^{(1)}$ and $\mathbf{Z}^{(1)}$ through:

$$\mathbf{C_m}\overline{\partial}\mathbf{v}^{(0)} = -\mathbf{I}^{ep}\left(\widehat{\mathbf{w}}^{(\frac{1}{2})}, \widehat{\mathbf{Q}}^{(\frac{1}{2})}\right) - \mathcal{J}_{\mathcal{N}}\left(\overline{\mathbf{v}}^{(\frac{1}{2})}\right) - \Phi\left(\phi_e^{(\frac{1}{2})}\right),$$

$$\overline{\partial}^{(0)}Z_j = \max\left(\frac{\beta_j(\widehat{w}_j^{(\frac{1}{2})}) - \widehat{Q}_j^{(\frac{1}{2})}}{\tau_{ep,j}}, \frac{\beta_j(\widehat{w}_j^{(\frac{1}{2})}) - \widehat{Q}_j^{(\frac{1}{2})}}{\tau_{res,j}}\right) \quad \forall j \in \{1, ..., \mathcal{N}\}.$$

From the corrector equations, $\mathbf{v}^{(1)}$ and $\mathbf{Z}^{(1)}$ are obtained implicitly. Finally, before going to the spatial discretization, we recall the following result:

Theorem 5.6. *(Henríquez et al., 2017, Lemma 7). Let $\phi \in C^2([0,T]; L^2(\Gamma_j))$, $j \in \{1, \ldots, \mathcal{N}\}$ then it holds that*

$$\left\|\overline{\phi}^{(s+\frac{1}{2})} - \phi^{(s+\frac{1}{2})}\right\|_{L^2(\Gamma_j)} \le \frac{\tau^2}{4} \max_{t \in [t_s, t_{s+1}]} \left\|\partial_t^2 \phi(t)\right\|_{L^2(\Gamma_j)},$$

$$\left\|\widehat{\phi}^{(s+\frac{1}{2})} - \phi^{(s+\frac{1}{2})}\right\|_{L^2(\Gamma_j)} \le \frac{5\tau^2}{16} \max_{t \in [t_{s-1}, t_{s+1}]} \left\|\partial_t^2 \phi(t)\right\|_{L^2(\Gamma_j)},$$

furthermore, if $\phi \in C^3([0,T]; L^2(\Gamma_j))$,

$$\left\|\overline{\partial}\phi^{(s)} - \partial_t \phi^{(s+\frac{1}{2})}\right\|_{L^2(\Gamma_j)} \le \frac{\tau^2}{48} \max_{t \in [t_s, t_{s+1}]} \left\|\partial_t^3 \phi(t)\right\|_{L^2(\Gamma_j)}.$$

5.4.2. Spatial discretization

We now spatially discretize Problem 5.5. We start by introducing the real spherical harmonics used as spatial basis for the Dirichlet and Neumann traces (5.20). Then, we proceed with the BIOs discretization (see Theorem 5.10). Finally, the semi-explicit time
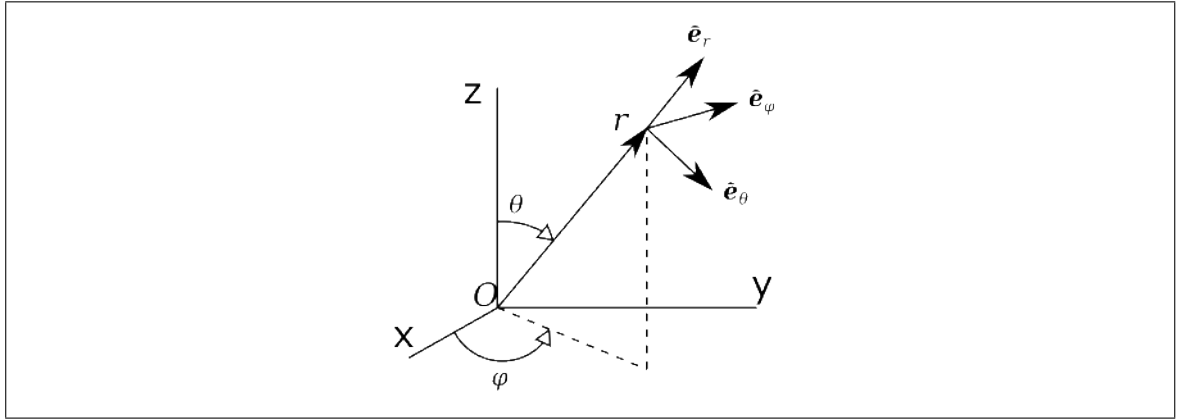
FIGURE 5-3. Illustration of spherical coordinates. Adapted from (Siriudie, n.d.).

method and the spatial discretization are combined into a fully discrete scheme (see Problem (5.11)).

5.4.2.1. Spherical coordinates and spherical harmonics

A vector is written as $\mathbf{r} = (r, \varphi, \theta)^t$, with $r \in [0, \infty)$, $\varphi \in [0, 2\pi)$ and $\theta \in [0, \pi]$, which in Cartesian coordinates is equivalent to $\mathbf{r} = r (\sin \theta \cos \varphi, \sin \theta \sin \varphi, \cos \theta)^t$ (Vollmer & Yu, 2020, Appendix B). This is illustrated in Figure 5-3. Angles φ and θ are shown explicitly to avoid confusion, and the unitary vectors of the system are also sketched, which can be written in Cartesian coordinates as

$$\widehat{\mathbf{e}}_r = (\sin \theta \cos \varphi, \sin \theta \sin \varphi, \cos \theta)^t,$$

$$\widehat{\mathbf{e}}_\theta = (\cos \theta \cos \varphi, \cos \theta \sin \varphi, -\sin \theta)^t,$$

$$\widehat{\mathbf{e}}_\varphi = (-\sin \varphi, \cos \varphi, 0)^t.$$

Lastly, we recall the form of the gradient operator in spherical coordinates:

$$\nabla f = \frac{\partial f}{\partial r} \widehat{\mathbf{e}}_r + \frac{1}{r} \frac{\partial f}{\partial \theta} \widehat{\mathbf{e}}_\theta + \frac{1}{r \sin \theta} \frac{\partial f}{\partial \varphi} \widehat{\mathbf{e}}_\varphi \qquad (5.15)$$

Spherical harmonics of degree l and order m are defined using spherical coordinates as (Wieczorek & Meschede, 2018, Section 2), (Freeden & Gutting, 2013, Example 4.3.33):

$$Y_{l,m}(\theta, \varphi) := \sqrt{(2 - \delta_{m,0}) \frac{(2l+1)(l-m)!}{4\pi(l+m)!}} P_l^m(\cos\theta) \cos m\varphi, \text{ and} \qquad (5.16a)$$

$$Y_{l,-m}(\theta, \varphi) := \sqrt{(2 - \delta_{m,0}) \frac{(2l+1)(l-m)!}{4\pi(l+m)!}} P_l^m(\cos\theta) \sin m\varphi, \qquad (5.16b)$$

with $l \in \mathbb{N}_0$, $m \in \mathbb{Z}$ such that $0 \leq m \leq l$. If $m = 0$, then $\delta_{m,0} = 1$, and it is zero otherwise. P_l^m are the associated Legendre functions of degree l and order m defined as:

$$P_l^m(x) := (-1)^m (1-x^2)^{\frac{m}{2}} \frac{d^m}{dx^m} P_l(x), \quad \text{with} \quad P_l(x) := \frac{1}{2^l l!} \frac{d^l}{dx^l}(x^2-1)^l. \quad (5.17)$$

Here, the term $(-1)^m$ is the Condon-Shortley phase factor. The next result can be found proven in (Gallier & Quaintance, 2020, Section 7.3 and 7.5), (Atkinson & Han, 2012, Section 2.8), (Nédélec, 2001, Theorem 2.4.4), (Colton & Kress, 2013, Section 2.3).

Theorem 5.7. *Spherical harmonics are dense in $C(\mathbb{S}^2)$, with $\mathbb{S}^2$ the surface of the unit sphere, and form a complete orthonormal system in $L^2(\mathbb{S}^2)$ with respect to the internal product defined by:*

$$(\psi, \xi)_{L^2(\mathbb{S}^2)} = \int_0^{2\pi} \int_0^{\pi} \psi(\theta, \varphi) \xi(\theta, \varphi) \sin(\theta) \, d\theta d\varphi, \qquad (5.18)$$

They also are orthogonal in $H^1(\mathbb{S}^2)$.

Let be $j \in \{1, ..., \mathcal{N}\}$. We define the reference system j as the one centered at $\mathbf{p_j}$ with the same orientation that the reference system centered in the origin (see Figure 5-4 for an example with two spheres). Furthermore, we denote by $Y_{l,m,j}$ the spherical harmonic $Y_{l,m}$ centered in the origin of the reference system j. Thus, if $(r_j, \varphi_j, \theta_j)$ are the vector spherical coordinates of $\mathbf{r_j}$ in the reference system j, we have that $Y_{l,m,j}(\mathbf{r}_j) = Y_{l,m}(\theta_j, \varphi_j)$.

For $L \in \mathbb{N}_0$ and $j \in \{1, ..., \mathcal{N}\}$, we define subspaces

$$\mathcal{Y}_L(\Gamma_j) := \text{span}\left\{ Y_{l,m,j} : l \in \mathbb{N}_0, m \in \mathbb{Z}, l \leq L, |m| \leq l \right\}, \qquad (5.19)$$
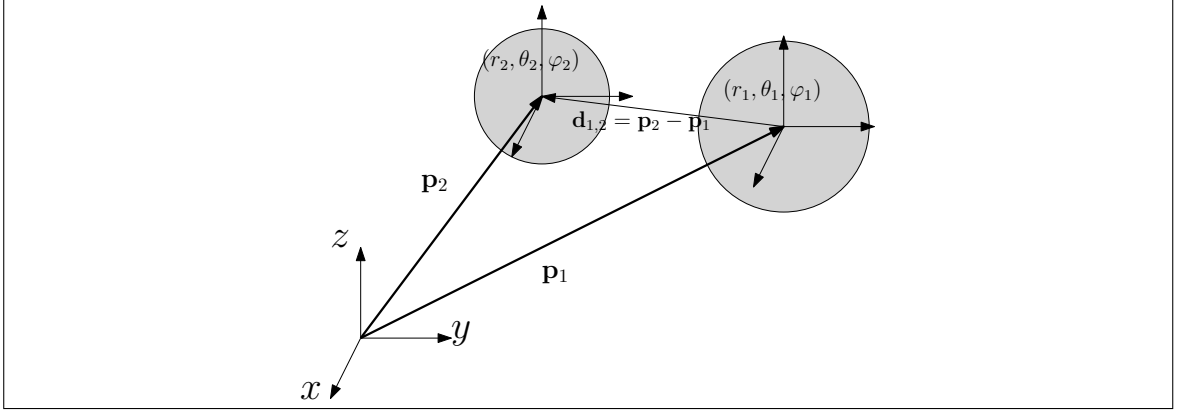
FIGURE 5-4. Illustration of the reference systems 1 and 2, for $\mathcal{N}$ spheres.

equipped with the $L^2(\Gamma_j)-$norm. Notice that the dimension of each subspace is $(L+1)^2$.

PROPOSITION 5.2 (Density). *The sequence of subspaces $\{\mathcal{Y}_L(\Gamma_j)\}_{L\in\mathbb{N}_0}$ is dense in $H^{\frac{1}{2}}(\Gamma_j)$ and in $H^{-\frac{1}{2}}(\Gamma_j)$.*

PROOF. The result follows from the density of spherical harmonics in the spaces of continuous functions (Atkinson & Han, 2012, Section 2.8) and Proposition 5.1. $\square$

This last result justifies the discretization of all boundary Dirichlet and Neumann unknowns with spherical harmonics. At a given time t, for $j \in \{1, ..., \mathcal{N}\}$, we write $u_{D,0j}^L$, $u_{N,0j}^L$, $u_{D,j}^L$, $u_{N,j}^L$, v_j^L and z_j^L in $\mathcal{Y}_L(\Gamma_j)$ for the approximations of $\gamma_D^{0j}u_0$, $\gamma_N^{0j}u_0$, $\gamma_D^j u_j$, $\gamma_N^j u_j$, v_j and Z_j, respectively. They can be written as the following series expansions:

$$u_{D,0j}^L = \sum_{l=0}^L \sum_{m=-l}^l u_{D,0j}^{l,m} Y_{l,m,j}, \qquad u_{N,0j}^L = \sum_{l=0}^L \sum_{m=-l}^l u_{N,0j}^{l,m} Y_{l,m,j}, \tag{5.20a}$$

$$u_{D,j}^L = \sum_{l=0}^L \sum_{m=-l}^l u_{D,j}^{l,m} Y_{l,m,j}, \qquad u_{N,j}^L = \sum_{l=0}^L \sum_{m=-l}^l u_{N,j}^{l,m} Y_{l,m,j}, \tag{5.20b}$$

$$v_j^L = \sum_{l=0}^L \sum_{m=-l}^l v_j^{l,m} Y_{l,m,j}, \qquad z_j^L = \sum_{l=0}^L \sum_{m=-l}^l z_j^{l,m} Y_{l,m,j}, \tag{5.20c}$$

with $u_{D,0j}^{l,m}$, $u_{N,0j}^{l,m}$, $u_{D,j}^{l,m}$, $u_{N,j}^{l,m}$, $v_j^{l,m}$, and $z_j^{l,m}$ being constants in the space but varying in time. Notice that the norm in $\mathcal{Y}_L(\Gamma_j)$ of any of these functions is the square root of the sum of

squared coefficients times the radius of Γ_j, i.e.

$$\left\|v_j^L\right\|_{\mathcal{Y}_L(\Gamma_j)} = R_j \sqrt{\sum_{l=0}^{L} \sum_{m=-l}^{l} (v_j^{l,m})^2}. \tag{5.21}$$

Finally, let $\mathbb{Y}_L := \Pi_{j=1}^{\mathcal{N}} \mathcal{Y}_{\mathcal{L}}(\Gamma_j)$, and define the following vectors in $\mathbb{Y}_L$:

$$\mathbf{v}^L := \left(v_1^L, \ldots, v_j^L, \ldots, v_{\mathcal{N}}^L\right)^t, \qquad \mathbf{Z}^L := \left(z_1^L, \ldots, z_j^L, \ldots, z_{\mathcal{N}}^L\right)^t, \tag{5.22a}$$

$$\mathbf{u}_{D,0}^L := \left(u_{D,01}^L, \ldots, u_{D,0j}^L, \ldots, u_{D,0\mathcal{N}}^L\right)^t, \quad \mathbf{u}_D^L := \left(u_{D,1}^L, \ldots, u_{D,j}^L, \ldots, u_{D,\mathcal{N}}^L\right)^t, \tag{5.22b}$$

$$\mathbf{u}_{N,0}^L := \left(u_{N,01}^L, \ldots, u_{N,0j}^L, \ldots, u_{N,0\mathcal{N}}^L\right)^t, \quad \mathbf{u}_D^L := \left(u_{N,1}^L, \ldots, u_{N,j}^L, \ldots, u_{N,\mathcal{N}}^L\right)^t. \tag{5.22c}$$

The norm for a function in $\mathbb{Y}_L$, for example, $\mathbf{v}^L$, is

$$\left\|\mathbf{v}^L\right\|_{\mathbb{Y}_L} = \sqrt{\sum_{j=1}^{\mathcal{N}} \|v_j^L\|_{\mathcal{Y}_L(\Gamma_j)}^2}.$$

5.4.2.2. BIOs discretization

The fundamental solution can be expanded using spherical harmonics (Freeden & Gutting, 2013, Theorem 4.3.29, Lemma 4.4.1 and Remark 4.4.2) as the following result shows.

Theorem 5.8. *Let* $\mathbf{r}$, $\mathbf{r}'$ *be vectors, whose spherical coordinates in the reference system* j *are* $(r_j, \theta_j, \varphi_j)$ *and* $(r_j', \theta_j', \varphi_j')$, *respectively. For* $r_j > r_j'$ *we have that*

$$g\left(\mathbf{r}, \mathbf{r}'\right) = \sum_{l=0}^{\infty} \frac{1}{2l+1} \frac{r_j'^l}{r_j^{l+1}} \sum_{m=-l}^{l} Y_{l,m,j}\left(\mathbf{r}\right) Y_{l,m,j}\left(\mathbf{r}'\right). \tag{5.23}$$

Moreover, the series (5.23) and its term by term first derivatives with respect to r_j *or* r_j' *are absolutely and uniformly convergent on compact subsets with* $r_j > r_j'$ *(Colton & Kress, 2013, Section 2.3, p.23 and p.24).*

Theorem 5.9. *Let be* $j \in \{1, \ldots, \mathcal{N}\}$, *and* R_j *the radius of* Ω_j.

(i) *Let* $\mathbf{r} \in \Omega_0$ *and* $\mathbf{r} = (r, \theta, \varphi)$ *be expressed in the jth spherical coordinate system, then*

$$DL_{0j}(Y_{l,m,j})(\mathbf{r}) = -\frac{l}{2l+1}\left(\frac{R_j}{r}\right)^{l+1}Y_{l,m}(\theta, \varphi),$$

$$SL_{0j}(Y_{l,m,j})(\mathbf{r}) = \frac{R_j}{2l+1}\left(\frac{R_j}{r}\right)^{l+1}Y_{l,m}(\theta, \varphi).$$

(ii) *Let* $\mathbf{r} \in \Omega_j$ *and* $\mathbf{r} = (r, \theta, \varphi)$ *expressed in the jth spherical coordinate system, then*

$$DL_j(Y_{l,m,j})(\mathbf{r}) = -\frac{l+1}{2l+1}\left(\frac{r}{R_j}\right)^{l}Y_{l,m}(\theta, \varphi),$$

$$SL_j(Y_{l,m,j})(\mathbf{r}) = \frac{R_j}{2l+1}\left(\frac{r}{R_j}\right)^{l}Y_{l,m}(\theta, \varphi).$$

PROOF. The result follows from Theorem 5.8 and the orthonormality of spherical harmonics. $\square$

Theorem 5.10. *The diagonal forms of the BIOs* (5.6) *are:*

$$V_{j,j}^0\left(Y_{l,m,j}\right) = \frac{1}{2l+1}R_jY_{l,m,j}, \qquad V_j\left(Y_{l,m,j}\right) = \frac{1}{2l+1}R_jY_{l,m,j},$$

$$K_{j,j}^0\left(Y_{l,m,j}\right) = \frac{1}{2(2l+1)}Y_{l,m,j}, \qquad K_j\left(Y_{l,m,j}\right) = -\frac{1}{2(2l+1)}Y_{l,m,j},$$

$$K_{j,j}^{*0}\left(Y_{l,m,j}\right) = \frac{1}{2l+1}Y_{l,m,j}, \qquad K_j^*\left(Y_{l,m,j}\right) = -\frac{1}{2(2l+1)}Y_{l,m,j},$$

$$W_{j,j}^0\left(Y_{l,m,j}\right) = \frac{l(l+1)}{2l+1}\frac{1}{R_j}Y_{l,m,j}, \qquad W_j\left(Y_{l,m,j}\right) = \frac{l(l+1)}{2l+1}\frac{1}{R_j}Y_{l,m,j}.$$

PROOF. The result follows from Theorem 5.9 and the definitions of the BIOs presented in (5.6). Similar diagonal forms can also be found in (Vico, Greengard, & Gimbutas, 2014, Section 3 and Table 2), where the result is stated for complex spherical harmonics on the unit sphere. $\square$

Corollary 5.1. *The following holds*

$$\left(V_{j,j}^0\left(Y_{l,m,j}\right), Y_{p,q,j}\right)_{L^2(\Gamma_j)} = \left(V_j\left(Y_{l,m,j}\right), Y_{p,q,j}\right)_{L^2(\Gamma_j)} = \frac{R_j^3}{2l+1}\delta_{l,p}\delta_{m,q},$$

$$\left(K_{j,j}^0\left(Y_{l,m,j}\right),Y_{p,q,j}\right)_{L^2(\Gamma_j)} = -\left(K_j\left(Y_{l,m,j}\right),Y_{p,q,j}\right)_{L^2(\Gamma_j)} = \frac{R_j^2}{2(2l+1)}\delta_{l,p}\delta_{m,q},$$

$$\left(K_{j,j}^{*0}\left(Y_{l,m,j}\right),Y_{p,q,j}\right)_{L^2(\Gamma_j)} = -\left(K_j^*\left(Y_{l,m,j}\right),Y_{p,q,j}\right)_{L^2(\Gamma_j)} = \frac{R_j^2}{2(2l+1)}\delta_{l,p}\delta_{m,q},$$

$$\left(W_{j,j}^0\left(Y_{l,m,j}\right),Y_{p,q,j}\right)_{L^2(\Gamma_j)} = \left(W_j\left(Y_{l,m,j}\right),Y_{p,q,j}\right)_{L^2(\Gamma_s)} = \frac{l(l+1)}{2l+1}R_j\delta_{l,p}\delta_{m,q},$$

with $\delta_{l,p}$, $\delta_{m,q}$ denoting the standard Kronecker deltas. Also, for the scalar identity operators presented in Section 5.3.2, it holds that

$$\left(I\left(Y_{l,m,j}\right),Y_{p,q,j}\right)_{L^2(\Gamma_j)} = R_j^2\delta_{l,p}\delta_{m,q}.$$

Cross-interaction operators, e.g. $V_{i,j}^0$ for $i \neq j$, are non-singular and generally non diagonalizable. The double and single layer operators analytic expressions presented in Theorem 5.9 can be used to compute the non-singular integrals for $i \neq j$:

$$\left(V_{i,j}^0\left(Y_{l,m,j}\right);Y_{p,q,i}\right)_{L^2(\Gamma_i)} = \int_{\Gamma_i} SL_{0j}(Y_{l,m,j})Y_{p,q,i}\,d\Gamma_i, \tag{5.24a}$$

$$\left(K_{i,j}^0\left(Y_{l,m,j}\right);Y_{p,q,i}\right)_{L^2(\Gamma_i)} = \int_{\Gamma_i} DL_{0j}(Y_{l,m,j})Y_{p,q,i}\,d\Gamma_i, \tag{5.24b}$$

$$\left(K_{i,j}^{*0}\left(Y_{l,m,j}\right);Y_{p,q,i}\right)_{L^2(\Gamma_i)} = \int_{\Gamma_i} \widehat{\mathbf{n}}_{0i}\cdot\nabla SL_{0j}(Y_{l,m,j})Y_{p,q,i}\,d\Gamma_i, \tag{5.24c}$$

$$\left(W_{i,j}^0\left(Y_{l,m,j}\right);Y_{p,q,i}\right)_{L^2(\Gamma_i)} = -\int_{\Gamma_i} \widehat{\mathbf{n}}_{0i}\cdot\nabla DL_{0j}(Y_{l,m,j})Y_{p,q,i}\,d\Gamma_i. \tag{5.24d}$$

The gradients therein are expressed using (5.15). Approximations of the integrals (5.24) are provided via Gauss-Legendre quadratures. Specifically, along θ, we use the change of variable $u = cos(\theta)$. Then, variable functions are sampled at the zeros of the Legendre Polynomial of degree $L_c + 1$, whereas the trapezoidal rule is applied to equally spaced nodes in φ, with $2L_c + 1$ points. If the function being integrated has a spherical harmonic expansion with coefficients equal to zero for degrees higher than L_c, then the quadrature yields the exact result, assuming that there are not other sources of error (Wieczorek & Meschede, 2018). Moreover, quadrature in φ can be computed using the Fast Fourier Transform.

REMARK 5.5. *One would expect L_c to be greater than p and l in (5.24). Yet, without further analysis, it is not known if a polynomial of degree L_c is a good approximation for $SL_{0j}(Y_{l,m,j})Y_{p,q,i}$, $DL_{0j}(Y_{l,m,j})Y_{p,q,i}$, $\nabla SL_{0j}(Y_{l,m,j})\cdot\widehat{\mathbf{n}}_{0i}\,Y_{p,q,i}$ and $\nabla SL_{0j}(Y_{l,m,j})\cdot\widehat{\mathbf{n}}_{0i}\,Y_{p,q,i}$, since, as the translation theorems for spherical harmonics highlight, the translation of only one spherical harmonic is expressed as another infinite series of spherical harmonics.*

REMARK 5.6. *Notice that (5.24) can also be computed using a translation theorem for real spherical harmonics as in (Rico, López, Ema, & Ramírez, 2013; Aganin & Davletshin, 2018). In this case, the integral has an explicit expression and does not need to be computed numerically. Instead, the computing efforts focus on calculating the coefficients given by the translation theorem.*

Corollary 5.2. *The following holds*

$$\left(V_{i,j}^0\left(Y_{l,m,j}\right);Y_{p,q,i}\right)_{L^2(\Gamma_i)} = \left(V_{j,i}^0\left(Y_{p,q,i}\right);Y_{l,m,j}\right)_{L^2(\Gamma_j)},$$

$$\left(K_{i,j}^0\left(Y_{l,m,j}\right);Y_{p,q,i}\right)_{L^2(\Gamma_i)} = -\frac{l}{R_j}\left(V_{i,j}^0\left(Y_{l,m,j}\right);Y_{p,q,i}\right)_{L^2(\Gamma_i)},$$

$$\left(K_{j,i}^{*0}\left(Y_{p,q,i}\right);Y_{l,m,j}\right)_{L^2(\Gamma_j)} = \left(K_{i,j}^0\left(Y_{l,m,j}\right);Y_{p,q,i}\right)_{L^2(\Gamma_i)},$$

$$\left(W_{i,j}^0\left(Y_{l,m,j}\right);Y_{p,q,i}\right)_{L^2(\Gamma_i)} = \frac{l}{R_j}\left(K_{i,j}^{*0}\left(Y_{l,m,j}\right);Y_{p,q,i}\right)_{L^2(\Gamma_i)}.$$

PROOF. The result follows from Theorem 5.9 along with the definition of the BIOs. □

From this last corollary, it can be deduced that the integrals of all the cross-interactions of a couple of spheres i and j (5.24) can be derived having the results of the expression (5.24a) for all of the l, m, p and q needed, which avoids the need of computing numerically the other integral expressions.

5.4.3. Fully discrete scheme.

Following the conventions introduced in Section 5.4.1, we state the semi-implicit in time and space numerical discretization of Problem 5.5:

PROBLEM 5.11. *Let* $\mathbf{v}^{L,(0)}$ *and* $\mathbf{Z}^{L,(0)}$ *in* $\mathbb{Y}_L$ *be given. Then, for* $s \in \{2, ..., S-1\}$, *we seek* $\mathbf{v}^{L,(s)}$, $\mathbf{Z}^{L,(s)}$ *in* $\mathbb{Y}_L$ *solution of:*

$$\left(\mathbf{C_m} \overline{\partial} \mathbf{v}^{L,(s)} + \mathcal{J}_{\mathcal{N}}\left(\overline{\mathbf{v}}^{L,(s+\frac{1}{2})} \right) + \mathbf{I}^{ep}\left(\hat{\mathbf{v}}^{L,(s+\frac{1}{2})}, \hat{\mathbf{Z}}^{L,(s+\frac{1}{2})} \right) + \Phi\left(\phi_e^{(s+\frac{1}{2})} \right), \mathbf{y} \right)_{\mathbb{Y}_L} = 0$$
(5.25)

and

$$\overline{\partial}^{(s)} Z_j^L = \max\left(\frac{\beta_j(\widehat{v}_j^{L,(s+\frac{1}{2})}) - \widehat{Z}_j^{L,(s+\frac{1}{2})}}{\tau_{ep,j}}, \frac{\beta_j(\widehat{v}_j^{L,(s+\frac{1}{2})}) - \widehat{Z}_j^{L,(s+\frac{1}{2})}}{\tau_{res,j}} \right),$$
(5.26)

for all $\mathbf{y} \in \mathbb{Y}_L$. *For* $s = 1$ *we use the equivalent weak formulation of the corrector-predictor algorithm presented in 5.4.1.*

In order to solve Problem 5.11, at each time step, with the exception of the predictor-corrector algorithm, we solve the weak linear system equivalent to

$$\begin{bmatrix} 4\mathbf{A}_{0,\mathcal{N}} & -2\mathbf{X}_{\mathcal{N}}^{-1} & \mathbf{I}_{2\mathcal{N}\times\mathcal{N}} \\ -2\mathbf{X}_{\mathcal{N}} & 4\mathbf{A}_{1,\mathcal{N}} & -\mathbf{X}_{\mathcal{N}}\mathbf{I}_{2\mathcal{N}\times\mathcal{N}} \\ & \boldsymbol{\sigma}_{\mathcal{N}\times4\mathcal{N}} & \frac{1}{\tau}\mathbf{C_m} \end{bmatrix} \begin{pmatrix} \overline{\mathbf{u}}_{D,0}^{L,(s+1/2)} \\ \overline{\mathbf{u}}_{N,0}^{L,(s+1/2)} \\ \overline{\mathbf{u}}_{D}^{L,(s+1/2)} \\ \overline{\mathbf{u}}_{N}^{L,(s+1/2)} \\ \mathbf{v}^{L,(s+1)} \end{pmatrix} = \begin{pmatrix} -\left(2\gamma^0_{\phi_e^{L,(s+\frac{1}{2})}} +\mathbf{I}_{2\mathcal{N}\times\mathcal{N}}\mathbf{v}^{L,(s)} \right) \\ \mathbf{X}_{\mathcal{N}}\left(2\gamma^0_{\phi_e^{L,(s+\frac{1}{2})}} +\mathbf{I}_{2\mathcal{N}\times\mathcal{N}}\mathbf{v}^{L,(s)} \right) \\ \frac{1}{\tau}\mathbf{C_m}\mathbf{v}^{L,(s)} -\mathbf{I}^{ep}\left(\hat{\mathbf{v}}^{L,(s+\frac{1}{2})}, \hat{\mathbf{Z}}^{L,(s+\frac{1}{2})} \right) \end{pmatrix}, \quad (5.27)$$

where the test function is in $\mathbb{Y}_L \times \mathbb{Y}_L \times \mathbb{Y}_L \times \mathbb{Y}_L \times \mathbb{Y}_L$. Notice that we obtain mid-steps $(s + 1/2)$ for traces of extra- and intracellular potentials, whereas only the transmembrane potential is obtained at time steps s.

To retrieve the values of $\mathbf{u}_{D,0}^{L,(s)}$, $\mathbf{u}_{N,0}^{L,(s)}$, $\mathbf{u}_{D}^{L,(s)}$ and $\mathbf{u}_{N}^{L,(s)}$ (5.22) at the time step s, the following weak system can be used:

$$\left(\mathbf{M}_{\mathcal{N}}\begin{pmatrix} \mathbf{u}_{D,0}^{L,(s)} \\ \mathbf{u}_{N,0}^{L,(s)} \\ \mathbf{u}_{D}^{L,(s)} \\ \mathbf{u}_{N}^{L,(s)} \end{pmatrix}, \begin{pmatrix} \mathbf{y}_{D,0} \\ \mathbf{y}_{N,0} \\ \mathbf{y}_{D} \\ \mathbf{y}_{N} \end{pmatrix} \right)_{\times} = \left(\begin{pmatrix} -\mathbf{I}_{2\mathcal{N}\times\mathcal{N}}\,\mathbf{v}^{L,(s)} \\ \mathbf{X}_{\mathcal{N}}\mathbf{I}_{2\mathcal{N}\times\mathcal{N}}\,\mathbf{v}^{L,(s)} \end{pmatrix} + \begin{pmatrix} -\gamma^0_{\phi_e^{(s)}} \\ \mathbf{X}_{\mathcal{N}}\gamma^0_{\phi_e^{(s)}} \end{pmatrix}, \begin{pmatrix} \mathbf{y}_{D,0} \\ \mathbf{y}_{N,0} \\ \mathbf{y}_{D} \\ \mathbf{y}_{N} \end{pmatrix} \right)_{\times},$$

for all $\mathbf{y}_{D,0}$, $\mathbf{y}_{N,0}$, $\mathbf{y}_D$ and $\mathbf{y}_N$ in $\mathbb{Y}_L$.

REMARK 5.7. *With the exception of the scalar operators inside of $\mathbf{A}_{0,\mathcal{N}}$ and $\mathbf{I}^{ep}$, which are computed numerically, all other matrices are diagonalizable and analytic for the geometry here considered (Theorem 5.1). Thus, the discrete matrix used to solve at each time step is almost entirely block diagonal.*

REMARK 5.8. *Note that if changing $\mathbf{I}^{ep}$ without modifying the dynamics for the transmembrane potentials, leads to a modified right-hand side in the linear system of equation (5.27).*

5.5. Numerical Results

In this section, we verify and test the proposed computational scheme. To this end, we first check the MTF implementation for single and multiple cells to then combine it with the semi-implicit time-domain method. Next, we perform tests for linear and nonlinear dynamics. Physical parameters used thorough the Section are given in (Mistani et al., 2019, Table 1) and (Kavian et al., 2014, Table 1).

5.5.1. Hardware and Code Implementation

Numerical results were obtained in a machine with Quad Core Intel Core i7-4770 (-MT MCP-), 1498 MHz, 31982.1 MiB RAM (90% available for computations), with operating system Linux Mint 20.3 Una and Kernel: 5.4.0-131- generic x86_64. Simulation codes were programmed on Python 3.10. Its installation was via the open-source platform Anaconda[1], Conda[2] 4.13.0, and using the conda-forge repository (conda-forge community, 2015).[3] With the `numpy` library, we take advantage of vectorized computations (Harris et al., 2020). Moreover, we only use direct solvers. The linear solvers and LU decomposition in `numpy` and `scipy` are routines from LAPACK (Anderson et al., 1999). The code is implemented sequentially, which gives space to parallelization and optimization. Lastly, in the following experiments we do not implement any form of matrix compression.

---

[1] `https://www.anaconda.com/products/distribution`
[2] `https://docs.conda.io/projects/conda/en/stable/`
[3] The following packages were installed explicitly: `pyshtools` 4.10 (Wieczorek & Meschede, 2018), (conda install pyshtools=4.10), `numpy` 1.23.1 (Harris et al., 2020), `scipy` 1.9.0 (Virtanen et al., 2020), and `matplotlib-base` 3.5.2 (Hunter, 2007).

5.5.2. Code validation

In order to validate our code, we recall the properties which should be satisfied by a solution at each time. Specifically, the numerical solution is required to fulfill discrete Calderón identities at the boundaries, as well as discrete jump conditions. As the computed results are per se approximations this properties do not hold exactly, thus we define the following errors:

- Discrete Calderón exterior and interior errors respectively:

$$\left\| (2\mathbf{A}_{0,\mathcal{N}} - \mathbf{I}) \begin{pmatrix} \mathbf{u}_{D,0}^{L,(s+1)} \\ \mathbf{u}_{N,0}^{L,(s+1)} \end{pmatrix} \right\|_{\mathbb{Y}_L \times \mathbb{Y}_L}, \quad \left\| (2\mathbf{A}_{1,\mathcal{N}} - \mathbf{I}) \begin{pmatrix} \mathbf{u}_{D}^{L,(s+1)} \\ \mathbf{u}_{N}^{L,(s+1)} \end{pmatrix} \right\|_{\mathbb{Y}_L \times \mathbb{Y}_L}. \tag{5.28}$$

- Jump error:

$$\left\| \begin{pmatrix} \mathbf{u}_{D,0}^{L,(s+1)} \\ \mathbf{u}_{N,0}^{L,(s+1)} \end{pmatrix} - \mathbf{X}_{\mathcal{N}}^{-1} \begin{pmatrix} \mathbf{u}_{D}^{L,(s+1)} \\ \mathbf{u}_{N}^{L,(s+1)} \end{pmatrix} + \mathbf{I}_{2\mathcal{N} \times \mathcal{N}} \mathbf{v}^L + \boldsymbol{\gamma}^{0j} \phi_e^L \right\|_{\mathbb{Y}_L \times \mathbb{Y}_L} \approx 0. \tag{5.29}$$

Here the norm $\| \cdot \|_{\mathbb{Y}_L \times \mathbb{Y}_L}$ is computed as

$$\left\| \begin{pmatrix} \mathbf{u}_{D}^{L,(s+1)} \\ \mathbf{u}_{N}^{L,(s+1)} \end{pmatrix} \right\|_{\mathbb{Y}_L \times \mathbb{Y}_L}^2 = \left\| \mathbf{u}_{D}^{L,(s+1)} \right\|_{\mathbb{Y}_L}^2 + \left\| \mathbf{u}_{N}^{L,(s+1)} \right\|_{\mathbb{Y}_L}^2.$$

In what follows, we will use the following notations:

- Relative error in $L^2(\Gamma_j)$:

$$re_2(\phi_1, \phi_2)_j := \frac{\|\phi_1 - \phi_2\|_{L^2(\Gamma_j)}}{\|\phi_1\|_{L^2(\Gamma_j)}}. \tag{5.30}$$

  This error is computed for spherical harmonics expansions when possible (5.21) or using the numerical quadrature presented at the end of Section 5.4.2.2.

- Relative error in $C^0\left((0,T), L^2(\Gamma_1)\right)$:

$$re_{\infty,2}(\phi_1, \phi_2)_j := \frac{\max_{t_s \in T_s} \|\phi_1(t_s + \tau/2) - \phi_2(t_s + \tau/2)\|_{L^2(\Gamma_j)}}{\max_{t_s \in T_s} \|\phi_1(t_s + \tau/2)\|_{L^2(\Gamma_j)}}. \tag{5.31}$$

- Relative error in $L^2\left((0,T), L^2(\Gamma_1)\right)$:

$$re_{2,2}(\phi_1, \phi_2)_j := \frac{\|\phi_1 - \phi_2\|_{L^2((0,T),L^2(\Gamma_1))}}{\|\phi_1\|_{L^2((0,T),L^2(\Gamma_1))}}. \tag{5.32}$$

The approximation of the time integral is done by a composite trapezoidal rule using the points of the computed time mid-steps.

5.5.2.1. Spectral Spatial Discretization

In what follows, we seek a minimum number of spherical harmonics (L) required to yield a good approximation of ϕ_e on the surface of each sphere. As we will show, this depends on ϕ_e, the geometric configuration, and in particular, on the distance between cells.

Let be ϕ_e^L the projection of ϕ_e onto $\mathcal{Y}_L(\Gamma_1)$ (5.19) at a given time. As a first approximation, we compute the relative error in $L^2(\Gamma_1)$ numerically, i.e. $re_2(\phi_e, \phi_e^L)_1$ (5.30), where Ω_1 is centered at the origin of the coordinate system. Both functions can not be evaluated exactly due to machine precision. Thus, the function ϕ_e used is the default approximation of the original and not its spherical harmonics approximation. The evaluation of ϕ_e^L also depends on the evaluation of the spherical harmonics, with an increasing error as a function of L (Wieczorek & Meschede, 2018).

Approximation errors for the following three functions are computed

$$\phi_{e_1}(\mathbf{r}) := 3.1, \tag{5.33a}$$

$$\phi_{e_2}(x, y, z) := -3.1z, \tag{5.33b}$$

$$\phi_{e_3}(\mathbf{r}) := \frac{a}{4\pi\sigma_0 \left\| \mathbf{r} - \mathbf{p_0} \right\|_2}, \tag{5.33c}$$

with parameters for ϕ_{e_3} in Table 5.1. The function ϕ_{e_1} is constant, ϕ_{e_2} is linear and ϕ_{e_3} is a point source at $\mathbf{p_0}$. The results obtained are presented in Figure 5-5. For the constant ϕ_{e_1} and linear ϕ_{e_2} one requires spherical harmonics of degree $L = 0$ or $L = 1$, respectively. This is expected as any other coefficient is equal to zero.

For the point source ϕ_{e_3}, the spherical harmonic expansion is known and has infinite number of non-zero terms (cf. Theorem 5.8). We perform computations for four different distances from the point source. One can observe that the values of L needed to obtain a small error depend on how close the source point $\mathbf{p_0}$ is to the surface of the sphere. This

TABLE 5.1. Parameters used in Section 5.5.2.1 for studying the convergence of the spherical harmonics approximation of ϕ_{e_3} (5.33c). Values for σ_0 comes from (Kavian et al., 2014, Table 1) and for R_1 from (Mistani et al., 2019, Table 1).

Parameter	Symbol	Value	Unit
Intensity	a	1	μA
Source position	$\mathbf{p_0}$	(0, 0, d)	μm
Extracellular conductivity	σ_0	5	$\mu S/\mu m$
Cell radius	R_1	10	μm
External stimuli	ϕ_{e_3}	$a/(4\pi\sigma_0 \|\mathbf{r} - \mathbf{p_0}\|_2)$	V

(A) Relative errors for constant ϕ_{e_1} and linear ϕ_{e_2}. $L = 0$ and $L = 1$ are enough to obtain a good approximation of the functions.

(B) Relative errors for ϕ_{e_3} (5.33c) for four different distances, d, from the point source to the origin, the distance to the sphere is $d - R_1$. At close distance L needs to be high so as to maintain a given error. Parameter values are given in Table 5.1.

FIGURE 5-5. Relative errors (5.30) computed in Section 5.5.2.1, between ϕ_e (5.33) and its approximations in spherical harmonics ϕ_e^L in a sphere of radius 10 μm.

is shown by decreasing the distance d—the distance to the sphere being $d - R_1$ from the point source to the origin—and computing the relative error.

In general, if the discretization does not lead to a finite expansion, with zero coefficients after from some index, ϕ_e is not represented exactly, and the accuracy might depend on the geometry, as it is the case for ϕ_{e_3}.

5.5.2.2. MTF Validation

As mentioned above, we verify first the MTF method without time evolution, by solving Problem 5.12 for four different geometrical configurations and sources. In all four experiments, we set $\mathbf{v} = \mathbf{0}$ and use the point source ϕ_{e_3} given in (5.33c).

- **Example 1**: One sphere centered at the origin with intracellular conductivity $\sigma_1 = \sigma_0$ (phantom sphere).
- **Example 2**: One sphere centered at the origin with intracellular conductivity σ_1 different from σ_0.
- **Example 3**: Three (aligned) spheres. The first and the third one have conductivity σ_0 (phantom sphere), while the one in the middle has a different conductivity σ_1.
- **Example 4**: 27 spheres arranged in a 3×3 lattice in three-dimensional space. One of the spheres, the cell attached to the origin, has conductivity σ_1, the rest of the spheres have conductivity σ_0 (phantom spheres).

The parameters used for validation for Examples 1 and 2 for a single sphere are presented in Table 5.2, for Example 3 in Table 5.4, and for Example 4 in Table 5.5. Due to the results of the previous section (see Figure 5-5b), we choose $L = 50$, which we consider sufficient for the case $d = 20$ in the first three Examples, while in Example 4 we use $L = 23$ as the point source is farther away. Discrete Calderón and jump errors (5.28), (5.29) are presented in Table 5.3 for these four Examples.

In Example 1, the sphere has the same properties as the exterior medium, and we expect the external traces to be zero, while the interior traces are equal to the traces of ϕ_{e_3}. To check this, the following norms were computed:

$$\left\| \begin{pmatrix} \mathbf{u}_{D,01}^{50} \\ \mathbf{u}_{N,01}^{50} \end{pmatrix} \right\|_{\mathbb{Y}_{50} \times \mathbb{Y}_{50}} = 3.30 \cdot 10^{-19} \text{ and } \left\| \begin{pmatrix} \mathbf{u}_{D,1}^{50} - \gamma_D^{01} \phi_e^{50} \\ \mathbf{u}_{N,1}^{50} + \gamma_N^{01} \phi_e^{50} \end{pmatrix} \right\|_{\mathbb{Y}_{50} \times \mathbb{Y}_{50}} = 7.32 \cdot 10^{-20},$$

where the quantities are approximated to three significant digits. The Calderón and jump errors (5.28), (5.29) are of order of 10^{-19}, and are presented in Table 5.3. We display four

TABLE 5.2. Parameters used in Section 5.5.2.2 for Examples 1 and 2 for the MTF validation. The point source potential ϕ_{e_3} is found in (5.33c). Conductivity values are from (Kavian et al., 2014, Table 1), cell radius from (Mistani et al., 2019, Table 1).

Parameter	Symbol	Example 1	Example 2	Unit
Intensity	a	1	1	μA
Source position	$\mathbf{p_0}$	(0, 0, 20)	(0, 0, 20)	μm
Extracellular conductivity	σ_0	5	5	μS/μm
Intracellular conductivity	σ_1	5	0.455	μS/μm
Cell radius	R_1	10	10	μm
Maximum degree of spherical harmonics	L	50	50	

TABLE 5.3. Discrete Calderón errors and jump errors for Examples 1-4 from Section 5.5.2.2. The first two Examaples cosider a only one sphere, Example 3 three spheres and 27 spheres for Example 4. The values are approximated to three significant digits.

Error	Example 1	Example 2	Example 3	Example 4
Discrete Calderón exterior	$3.59 \cdot 10^{-19}$	$2.61 \cdot 10^{-17}$	$2.38 \cdot 10^{-16}$	$6.28 \cdot 10^{-17}$
Discrete Calderón interior	$1.06 \cdot 10^{-19}$	$2.61 \cdot 10^{-17}$	$2.31 \cdot 10^{-16}$	$6.41 \cdot 10^{-17}$
Jump error	$4.20 \cdot 10^{-19}$	$2.61 \cdot 10^{-17}$	$2.38 \cdot 10^{-16}$	$3.41 \cdot 10^{-17}$

plots of the volume potentials reconstructed from the traces (cf. Theorem 5.2) in Figures 5-6 and 5-7. For the field generated by ϕ_{e_3}, the intra- and extracellular potentials are practically the same and cell the becomes invisible.

In Example 2, the sphere has a different conductivity than the extracellular space, and an analytic solution can be obtained. In Figure 5-8 the relative errors in $L^2(\Gamma_1)$ (5.30) of the computed solutions for different L against the analytic solution are presented. The image shows the expected exponential convergence with respect to the maximum degree of the spectral basis L. The discrete Calderón and jump errors are given in Table 5.3. The external field generated by the sphere is shown in Figure 5-9, where u_0^{50} is of order at most 10^{-4} near the sphere, which was not the case in Example 1 (see Figure 5-7).

Example 3 involves three spheres, two of those having the same properties as the external medium, while the one in the middle is different (see Figure 5-10). Therefore, the traces of the latter should be equal to the ones computed without the first two, i.e. the same

(A) Electric fields u_0^{50} and u_1^{50} plotted in the plane $y = 0$. The field u_1^{50} is the same as ϕ_{e_3} in that domain. Recall that ϕ_{e_3} is only defined on the exterior of the sphere, so this is the expected behaviour.

(B) Electric fields u_0^{50} plus ϕ_{e_3} in the exterior of the sphere, and u_1^{50} in the interior plotted in the plane $y = 0$. It can be observed that it is like there is no sphere, which is the expected behaviour.

(C) Electric fields u_0^{50} and u_1^{50} plotted in the plane $z = 0$. Note that ϕ_{e_3} is only defined on the exterior of the sphere, so this is the expected behaviour.

(D) Electric fields u_0^{50} plus ϕ_{e_3} in the exterior of the sphere, and u_1^{50} in the interior, plotted in the plane $z = 0$. It can be observed that it is like there is no sphere, which is the expected behaviour.

FIGURE 5-6. Electric field plots in Example 1 of Section 5.5.2.2. Parameters used are in Table 5.2.

as in Example 2. The relative $L^2(\Gamma_1)$ error of the difference between the analytic solution for the four traces and the numerical one corresponding to the sphere with different conductivity, is $6.06 \cdot 10^{-15}$. In Figure 5-10, u_0^{50} is plotted where the only sphere showing a response to ϕ_{e_3} is the sphere in the middle that has different properties compared to the

(A) Cut $y = 0$.

(B) Cut $z = 0$.
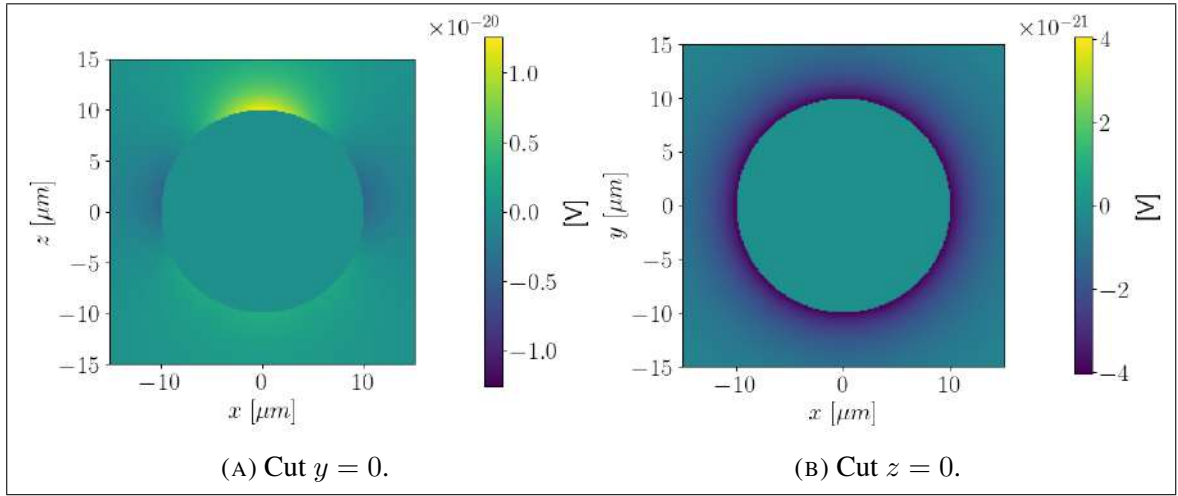
FIGURE 5-7. External field u_0^{50} in Example 1, Section 5.5.2.2. Notice that the values are of order 10^{-20}, which we consider to be approximately zero. This is showed for later comparison with Example 2, Figure 5-9. Parameters used are in Table 5.2.
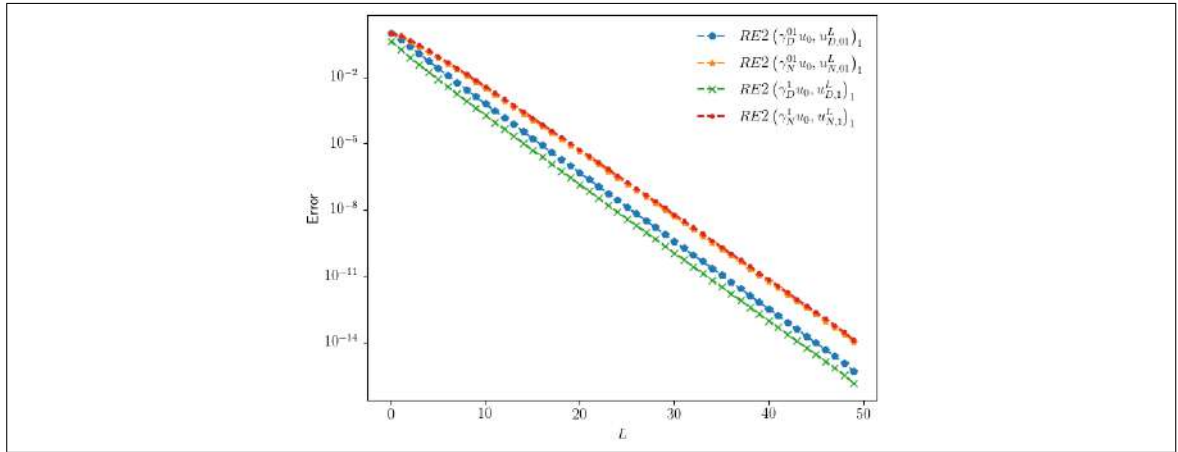
FIGURE 5-8. Error convergence for the traces in Example 2 (Section 5.5.2.2). The relative error $L^2(\Gamma_1)$ (5.30) is computed against the analytic solution, with exponential convergence as L increases. Parameter values are given in Table 5.2.

external medium. Discrete Calderón and jump errors are given in Table 5.3, with errors of order 10^{-16}.

Lastly, we run Example 4, a simulation with 27 spheres with only one of them having a conductivity different from the external one σ_0. The cells are arranged in corners of a cubic

(A) Plane $y = 0$.   (B) Plane $z = 0$.
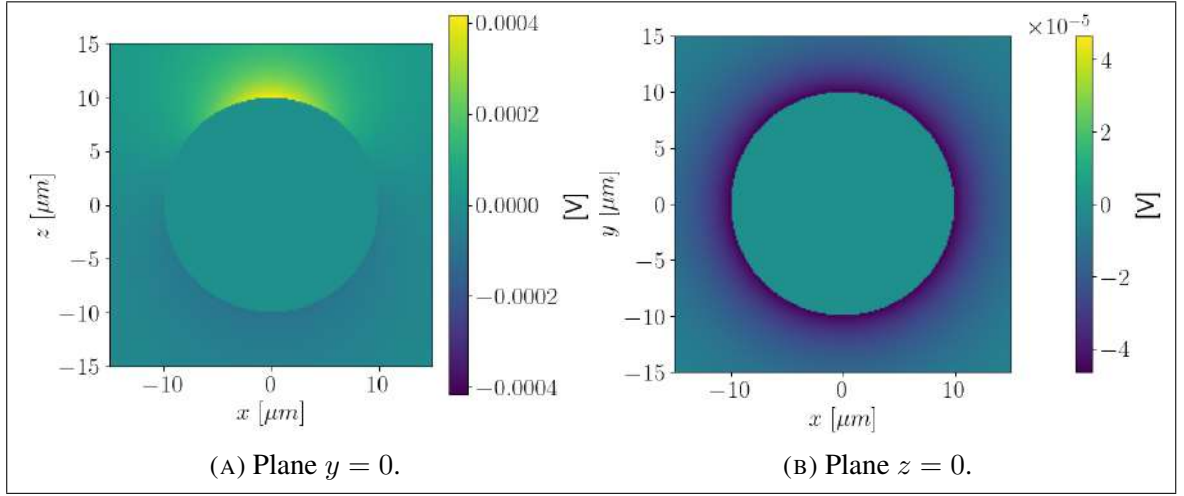
FIGURE 5-9. Field u_0^{50} in Example 2, Section 5.5.2.2 with parameters in Table 5.2. Here, u_0^{50} is much larger compared with Example 1 (see Figure 5-7) and cannot be considered to be zero. Note that in Example 3, with two phantom spheres, u_0^{50} in Figure 5-10 in similar to the present case.

TABLE 5.4. Parameters used for the MTF verification with $\phi_{e_3} = 1/(4\pi\sigma_0 \|\mathbf{r} - \mathbf{p_0}\|_2)$ in Example 3, Section 5.5.2.2. Conductivities are given in (Kavian et al., 2014, Table 1) and radii are in (Mistani et al., 2019, Table 1).

Parameter	Symbol	Value	Unit
Source position	$\mathbf{p_0}$	(0, 0, 20)	μm
Extracellular conductivity	σ_0	5	μS/μm
Cell 1 intracellular conductivity	σ_1	0.455	μS/μm
Cell 2 and 3 intracellular conductivity	σ_2, σ_3	5	μS/μm
Cell 1 radius	R_1	10	μm
Cell 2 radius	R_2	8	μm
Cell 3 radius	R_3	9	μm
Cell 1 center position	$\mathbf{p_1}$	(0, 0, 0)	μm
Cell 2 center position	$\mathbf{p_2}$	(25, 0, 0)	μm
Cell 3 center position	$\mathbf{p_3}$	(-24, 0, 0)	μm
Maximum degree of spherical harmonics	L	50	
Quadrature degree	L_c	100	

lattice, with parameters presented in Table 5.5. This time, the source position is located at $(0, 0, -50)$, and we choose $L = 23$ which is lower than in the previous examples.

We expect a similar behaviour for the electric potential as in Example 3, though with a smaller response due the point source being further. Computed relative errors between

(A) Plane $y = 0$. (B) Plane $z = 0$.

in Figure 5-9.
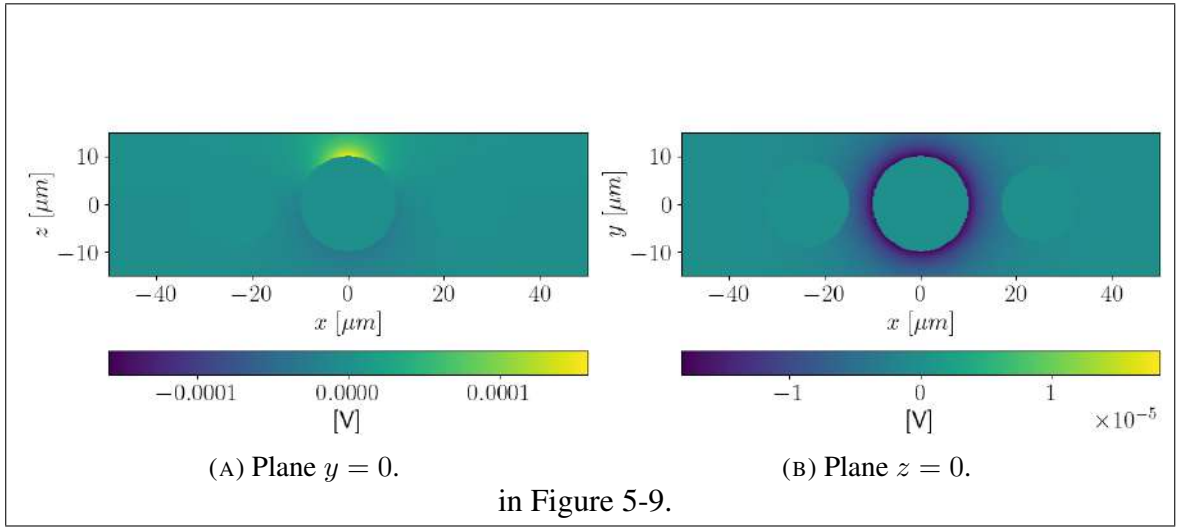
FIGURE 5-10. Field u_0^{50} of Example 3, Section 5.5.2.2 with parameters from Table 5.4. The resulting field is approximately the same as the one in Example 2, as it can be seen

TABLE 5.5. Parameters used for the MTF verification with $\phi_{e_3} = 1/(4\pi\sigma_0 \|\mathbf{r} - \mathbf{p_0}\|_2)$ with 27 spheres in Example 4, Section 5.5.2.2. Parameters for the conductivities are given in (Kavian et al., 2014, Table 1) and radii are in (Mistani et al., 2019, Table 1).

Parameter	Symbol	Value	Unit
Source position	$\mathbf{p_0}$	(0, 0, -50)	μm
Extracellular conductivity	σ_0	5	μS/μm
Cell 1, intracellular conductivity	σ_1	0.455	μS/μm
Cell j ($1 < j \le 27$), intracellular conductivity	σ_j	5	μS/μm
Cell j, radius	R_j	10	μm
Cell 1, center position	$\mathbf{p_1}$	(0, 0, 0)	μm
Minimum distance between spheres		5	μm
Maximum degree of spherical harmonics	L	23	
Quadrature degree	L_c	100	

the four traces obtained and their analytic counterparts in the $L^2(\Gamma_1)$-norm is $3.14 \cdot 10^{-15}$, which we consider to be zero. In Figure 5-11 u_0^{23} is plotted, where it can be observed that only the sphere in the down left corner is showing a response to ϕ_{e_3}. Discrete Calderón and jump errors are of order 10^{-17} and presented in Table 5.3.
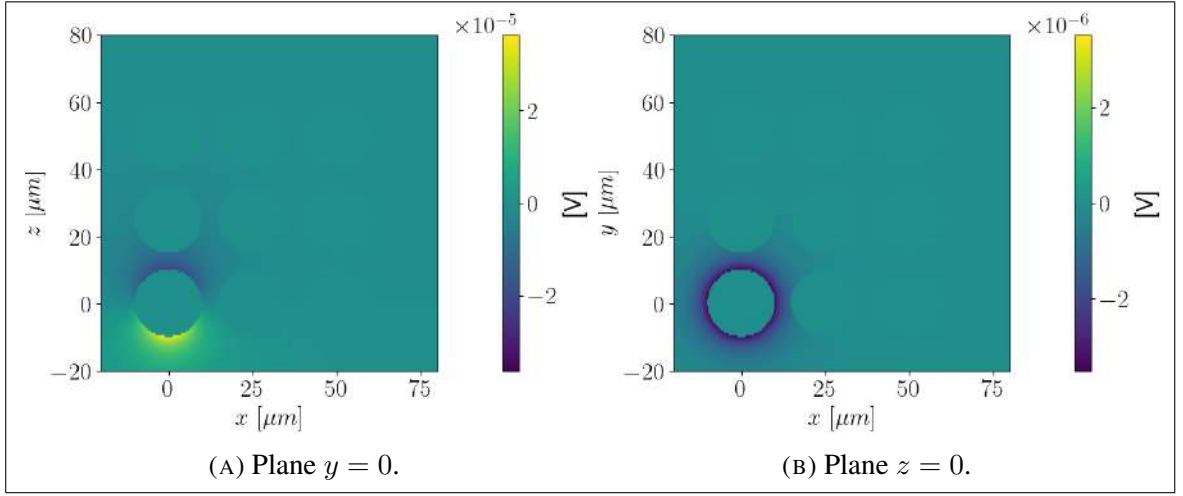
FIGURE 5-11. Field u_0^{23} in Example 3, Section 5.5.2.2 with parameters in Table 5.5. The only sphere showing a response is the one with different conductivity, which is the expected result.

5.5.2.3. Semi-implicit time approximation validation: linear case

To validate the proposed time discretization, we solve problem (5.25) for a linear current with only one cell:

$$c_{m,1}\partial_t v_1 + \frac{1}{r_{m,1}}v_j = -\sigma_1\gamma_N^1 u_1,$$

where instead of $I_1^{ep}(v_1, Z_1)$ we use $\frac{1}{r_{m,1}}v_j$. Additionally, we assume that ϕ_e can be factorized $\phi_e(t, \mathbf{r}) = \phi_{time}(t)\phi_{space}(\mathbf{r})$. If ϕ_{space} is expanded in spherical harmonics, the coefficients for the equivalent expansion of v_1, $v_1^{l,m}$, can be obtained by solving

$$\frac{\partial}{\partial_t}v_1^{l,m} + \alpha_1^{l,m}\,v_1^{l,m} = -\beta_1^{l,m}\,\phi_{time}(t),$$

with

$$\alpha_1^{l,m} := \frac{1}{c_m R_m} + \frac{\sigma_0\sigma_1 l(l+1)}{c_m R_1(\sigma_0(l+1)+\sigma_1 l)},$$

$$\beta_1^{l,m} := \frac{\sigma_0\sigma_1 l(b_{d,l,m}(l+1) - b_{n,l,m}R_1)}{c_m R_1(\sigma_0(l+1)+\sigma_1 l)},$$

where $b_{d,l,m}$ and $b_{n,l,m}$ are the coefficient of degree l and order m of the Dirichlet and Neumann expansion of ϕ_{space} on the cell membrane, respectively. Then, the spherical

harmonic expansion coefficients of v_1 are

$$v_1^{l,m}(t) = -\beta_1^{l,m} e^{-\alpha_1^{l,m}t} \int_0^t \phi_{time}(s) e^{\alpha_1^{l,m}s} ds + v_1^{l,m}(0) e^{-\alpha_1^{l,m}t}.$$

For $\phi_{time-exp}(t) := e^{-t}$ and initial condition $v_1^{(0)} = 0$, the solution is

$$v_1^{l,m}(t) = -\frac{\beta_1^{l,m}}{\alpha_1^{l,m} - 1} \left(e^{-t} - e^{-\alpha_1^{l,m}t} \right),$$

and for $\phi_{time-cte}(t) := 1$ and initial condition $v_1^{(0)} = 0$, one has

$$v_1^{l,m}(t) = -\frac{\beta_1^{l,m}}{\alpha_1^{l,m}} \left(1 - e^{-\alpha_1^{l,m}t} \right).$$

To approximate the first bound in Theorem 5.6, we compute the second derivative in time of the analytic solution obtained. Specifically, for $\phi_{time-exp}$, the second derivative is

$$\partial_t^2 v_1^{l,m}(t) = -\frac{\beta_1^{l,m}}{\alpha_1^{l,m} - 1} \left(e^{-t} - (\alpha_1^{l,m})^2 e^{-\alpha_1^{l,m}t} \right),$$

whereas for $\phi_{time-cte}$, one has

$$\partial_t^2 v_1^{l,m}(t) = \beta_1^{l,m} \alpha_1^{l,m} e^{-\alpha_1^{l,m}t}.$$

With these, we compare the approximated solution $\overline{v}_1^{25}$ with its analytic expression v_1 and check if the first bound of Theorem 5.6 holds. We present simulation results for the two different time parts of ϕ_e, $\phi_{time-exp}$ and $\phi_{time-cte}$. We use a point source function for the spatial part of ϕ_e. Parameters are presented in Table 5.6.

Figure 5-12 showcases values of the transmembrane potentials $\overline{v}_1^{25}$ ($\tau = 0.025\ \mu$s) and v_1 at the north pole of the cell ($\theta = 0$). The approximated solutions are very close to the analytic one for the scale presented with errors in Figure 5-13. In Figure 5-13, the absolute error of the difference between $\overline{v}_1^{23}$ ($\tau = 0.025\mu$s) and v_1 in space is presented for each mid-time step. We compute also $\frac{\tau^2}{4} \left\| \partial_t^2 v_1 \right\|_{L^2(\Gamma_j)}$ to validate the first bound in Theorem 5.6. For $\phi_{time-exp}$, the absolute error satisfies the first bound in Theorem 5.6 everywhere except

TABLE 5.6. Parameters used for the time scheme validation in Section 5.5.2.3 where linear dynamics are assumed. The external potential is $\phi_e = I(t)/(4\pi\sigma_0 \|\mathbf{r} - \mathbf{p_0}\|_2)$ and only one cell is considered. Conductivity values are given in (Kavian et al., 2014, Table 1), the cell radius and the specific membrane capacitance are given in (Mistani et al., 2019, Table 1), and the specific membrane resistance is from (Henríquez et al., 2017, Table 1).

Parameter	Symbol	Values	Unit
Intensity	$I(t)$	e^{-t} and 1	μA
Source position	$\mathbf{p_0}$	(0, 0, 50)	μm
Extracellular conductivity	σ_0	5	μS/μm
Intracellular conductivity	σ_1	0.455	μS/μm
Specific membrane capacitance	$c_{m,1}$	$9.5 \cdot 10^{-3}$	pF/$(\mu$m$)^2$ (=F/m^2)
Specific membrane resistance	$r_{m,1}$	$1 \cdot 10^5$	M$\Omega(\mu$m$)^2$
Cell Radius	R_1	7	μm
Length time step	τ	0.025	μs
Final time	T	2.5	μs
Maximum degree of spherical harmonics	L	25	

(A) $\phi_{time-ext}(t) = e^{-t}$.

(B) $\phi_{time-cte}(t) = 1$.
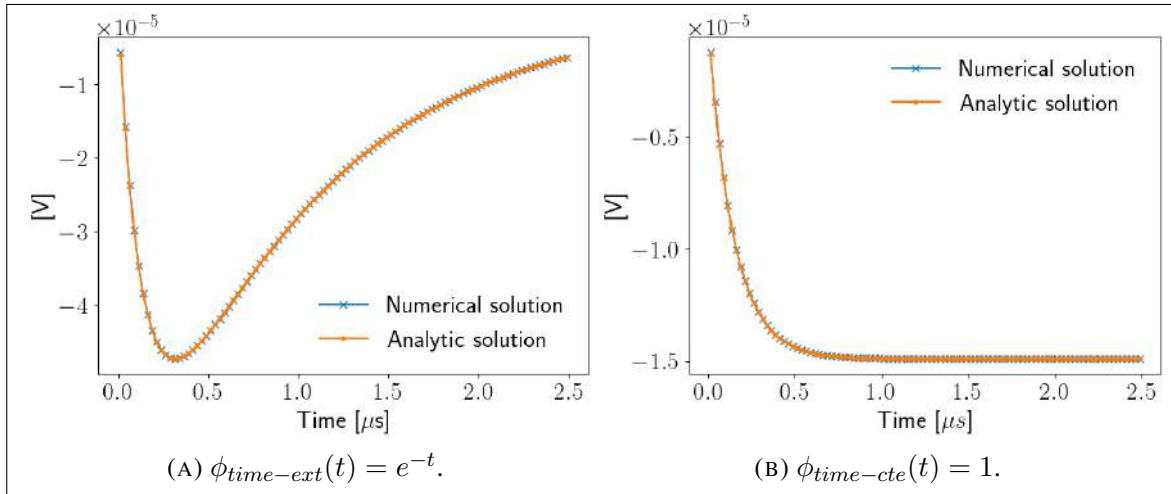
FIGURE 5-12. Evolution of $\overline{v}_1^{25}$ (discrete approximation with $\tau = 0.025\,\mu$s) and v_1 (analytic solution) at the north pole of the cell ($\theta = 0$) for the validation of the time scheme in Section 5.5.2.3 for linear dynamics. Parameters employed are given in Table 5.6.

for the range between $0.4\,\mu$s and $0.7\,\mu$s, caused by a too large τ. For $\phi_{time-cte}$ the bound is fulfilled at all times.

(A) $\phi_{time}(t) = e^{-t}$.　　　　　　　　(B) $\phi_{time}(t) = 1$.
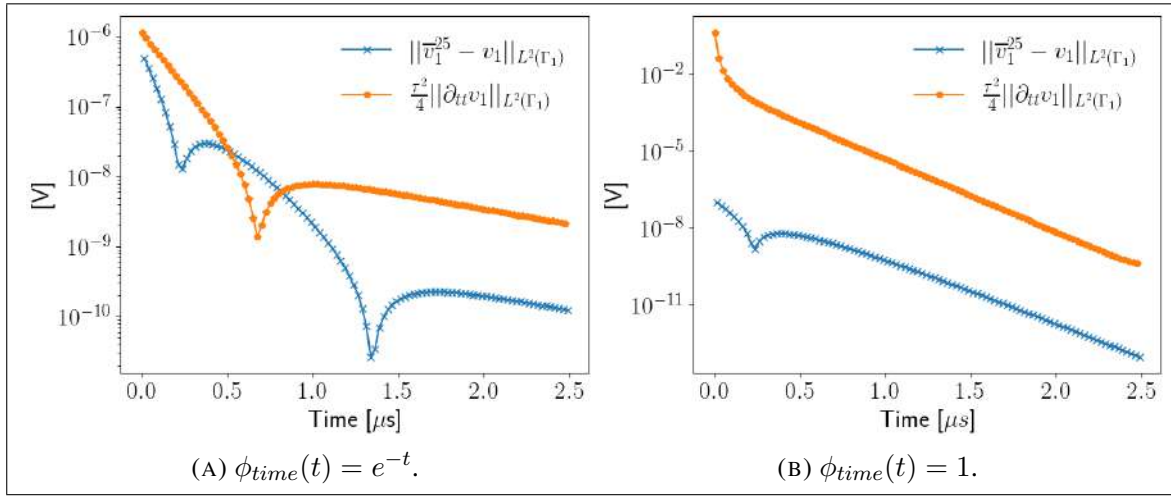
FIGURE 5-13. Absolute error in $L^2(\Gamma_1)$ between $\overline{v}_1^{25}$ (discrete approximation) and v_1 (analytic solution), as well as $\frac{\tau^2}{4}\left\|\partial_t^2 v_1(t_s)\right\|_{L^2(\Gamma_j)}$, plotted to verify the bound given by Theorem 5.6 for the time scheme from Section 5.5.2.3 where linear dynamics are assumed. Note that the plot of $\frac{\tau^2}{4}\left\|\partial_t^2 v_1(t_s)\right\|_{L^2(\Gamma_j)}$ is above the absolute error. The length of the time step τ is 0.025 μs, the rest of the parameters used are in Table 5.6.

(A) $\phi_{time-exp}(t) = e^{-t}$.　　　　　　　　(B) $\phi_{time-cte}(t) = 1$.
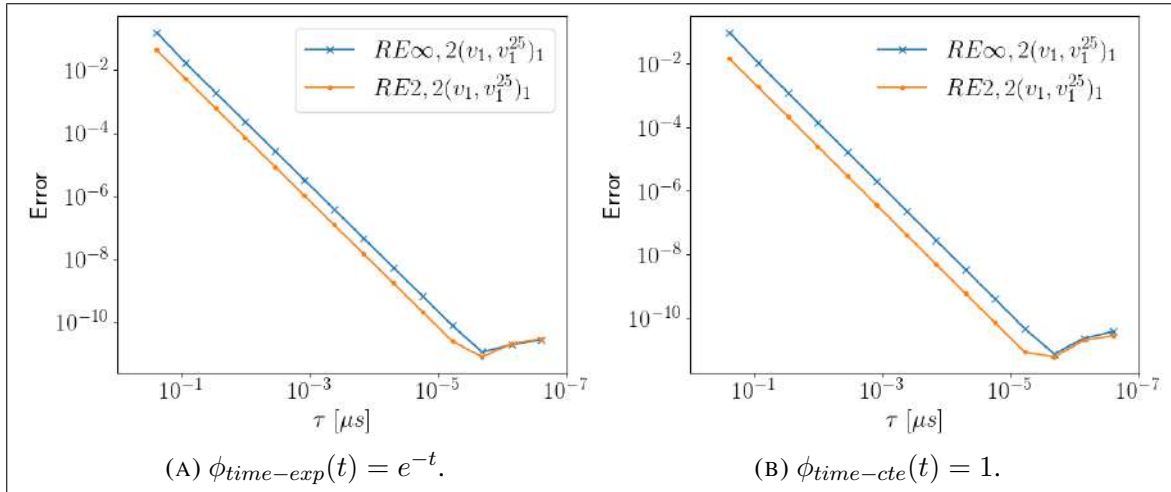
FIGURE 5-14. Error convergence for diminishing time steps τ for the time scheme in Section 5.5.2.3 where linear dynamics are assumed. The slope of the errors on the log-log plot is approximately equal to two, i.e. error converges as τ^2. Relative errors $re_{\infty,2}(v_1, v_1^{25})_1$ and $re_{2,2}(v_1, v_1^{25})_1$ are given in (5.31) and (5.32), respectively. Simulation parameters can be found in Table 5.6.

Finally, Figure 5-14 presents the relative error in time and space for decreasing values of τ. We compute the error using two norms: an approximation of the $C^0\left((0,T), L^2(\Gamma_1)\right)$-norm taking the maximum value at each mid-step computed (5.31), and an approximation of the $L^2\left((0,T), L^2(\Gamma_1)\right)$-norm, using a composite trapezoidal rule with the computed mid-steps (5.32). We observe that the slope of the errors in the log-log plot is close to two, therefore the error decreases as τ^2.

5.5.3. Numerical Results for a Single Cell with Nonlinear Dynamics

After having verified our numerical scheme for the linear dynamics, we now we study the nonlinear model for the electropermeabilization dynamics for a single cell (Problem 5.5). Note that in (Henríquez & Jerez-Hanckes, 2018, Theorem 6.14) the authors provide error estimates by solving the nonlinear dynamical problem in 2D, where they use the Hodgkin-Huxley dynamics to simulate the response of neurons. The estimates depend on four terms: the first two are the norms of the difference between initial conditions and approximated ones used in the computations; the third is related to the spatial discretization, where a spectral basis in 2D is used, and this term is proved to decay exponentially with the total number of functions in the spatial discretization basis; the fourth one is related to the time approximation, and it decays as τ^2. In the present work, we do not derive error estimate, but given this previous result, we expect a similar behavior. In other words, fixing the maximum degree of spherical harmonics L used in the discretization and decreasing the length of the time step τ, we expect to see the error converging to a constant depending on L. Similarly, if we fix τ and increase L, we expect the error to converge to a constant depending on τ.

5.5.3.1. Time convergence for a fixed L

We use the parameters presented in Table 5.7 to solve the non-linear discrete Problem 5.11, with external applied potential $\phi_e = 5z \cdot 10^{-2}$, and initial conditions equal to zero. Since we no longer possess an analytic solution for comparison, we check for convergence as time steps become smaller. We remark that L is fixed.

TABLE 5.7. Parameters used for the simulation of a single cell with non-linear dynamics (5.3e) in Section 5.5.3.1 when studying the time convergence with fixed L. Parameters used are found in (Kavian et al., 2014, Table 1).

Parameter	Symbol	Values	Unit
Cell Radius	R_1	10	μm
Time part of ϕ_e	ϕ_{time}	1	
Spatial part of ϕ_e	$\phi_{spatial}$	$5\,z \cdot 10^{-2}$	V
Extracellular conductivity	σ_0	5	μS/μm
Intracellular conductivity	σ_1	0.455	μS/μm
Lipid surface conductivity	$S_{L,1}$	$1.9 \cdot 10^{-6}$	μS/$(\mu$m$)^2$
Irreversible surface conductivity	$S_{ir,1}$	$2.5 \cdot 10^2$	μS/$(\mu$m$)^2$
Specific membrane capacitance	$c_{m,1}$	$9.5 \cdot 10^{-3}$	pF/$(\mu$m$)^2$
Transmembrane potential threshold	$V_{rev,1}$	1.5	V
Electropermeabilization switch speed	$k_{ep,1}$	40	V^{-1}
Characteristic time of electropermeabilization	$\tau_{ep,1}$	1	μs
Characteristic resealing time	$\tau_{res,1}$	10^3	μs
Final time	T	26	μs
Maximum degree of spherical harmonics	L	1	
Quadrature degree	L_c	2	

Table 5.8 displays the norms of the error between two successively refined solutions for different time steps. These results show a convergence rate of one as the time step decreases, and thus we do not obtain the same as in (Henríquez & Jerez-Hanckes, 2018). This is due to the lesser regularity in time of the functions used in the non-linear electropermeabilization model.

In Figure 5-15, we plot the evolution of the transmembrane potential v_1^1 for three different values of τ. Though the solution shapes are similar, the signals peak at different locations and coincide as the time step decreases. Specifically, between $\tau = 2.6 \cdot 10^{-3} \mu$s and $\tau = 2.6 \cdot 10^{-4} \mu$s, there is a delay of less than $0.16\ \mu$s, while between $\tau = 2.6 \cdot 10^{-4} \mu$s and $\tau = 2.6 \cdot 10^{-5} \mu$s the delay is less than $0.017\ \mu$s.

5.5.3.2. Spatial convergence with nonlinear dynamics

We now present numerical results for different maximum degrees of the spherical harmonics, $L = 51$ and $L \in [1, 2, ..., 36]$. Given that we use a spectral discretization in space,

TABLE 5.8. Error convergence of solutions obtained for the nonlinear problem with one cell from Section 5.5.3.1 for fixed L. Computed norms are the difference between two successive solutions. Parameters used are in Table 5.7.

τ_i	Value [μs]	$\max_{t\in[0,T]} \lvert\lvert v_1^{1,\tau_{i+1}} - v_1^{1,\tau_i}\rvert\rvert_{L^2(\Gamma_1)}$	$\max_{t\in[0,T]} \lvert\lvert Z_1^{1,\tau_{i+1}} - Z_1^{1,\tau_i}\rvert\rvert_{L^2(\Gamma_1)}$
τ_1	$2.6\cdot10^{-3}$	-	-
τ_2	$2.6\cdot10^{-4}$	8.8	$4.64\cdot10^{-3}$
τ_3	$2.6\cdot10^{-5}$	0.9	$3.02\cdot10^{-4}$
τ_4	$2.6\cdot10^{-6}$	0.097	$3.59\cdot10^{-5}$
τ_5	$2.6\cdot10^{-7}$	0.0097	$3.15\cdot10^{-6}$

FIGURE 5-15. Evolution of v_1^1 at the north pole of the cell ($\theta = 0$) for different lengths of time step τ illustrating the time convergence for fixed L, Section 5.5.3.1. The image at the right is zoomed near to the maximum value of v_1^1. Parameters employed are given in Table 5.7.

we expect an exponential decrease in the error when increasing the maximum degree L—recall that the number of spatial discretization functions basis is $((L + 1)^2)^4$. The external applied potential is $\phi_e = 5z\cdot10^{-2}$ until $t = 5$ and equal to zero thereafter. Initial conditions are set to zero.

First, we analyze the error convergence for the coefficients of v_1^L, which are functions only of time. For each result computed with the maximum degree of the spherical harmonics being less than 37, we compare against the result with $L = 51$. For this, we calculate the relative error of the coefficients $v_1^{l,0}$, for odd l, and for the different maximum degrees

---

[4]The parameters used are provided in Table 5.9. Notice that extra- and intracellular conductivities have different values from the previous simulations, and were changed to obtain a response of the impulse sooner.

TABLE 5.9. Parameters used in the numerical simulations with one cell to study the convergence in space in Section 5.5.3.2, with the non-linar dynamics of the electropermeabilization model. The specific choice of extra- and intracellular conductivities, different from the previous simulations, allow us to obtain a response of the impulse sooner in time. The rest of the parameters are from (Kavian et al., 2014, Table 1). The external applied potential used is equal to zero after $t = 5$.

Parameter	Symbol	Values	Unit
Cell Radius	R_1	10	μm
External applied potential	ϕ_e	$5\,z \cdot 10^{-2}$	V
Extracellular conductivity	σ_0	15	μS/μm
Intracellular conductivity	σ_1	1.5	μS/μm
Specific membrane capacitance	$c_{m,1}$	$9.5 \cdot 10^{-3}$	pF/$(\mu$m$)^2$ (=F/m^2)
Lipid surface conductivity	$S_{L,1}$	$1.9 \cdot 10^{-6}$	μS/$(\mu$m$)^2$
Irreversible surface conductivity	$S_{ir,1}$	$2.5 \cdot 10^2$	μS/$(\mu$m$)^2$
Specific membrane capacitance	$c_{m,1}$	$9.5 \cdot 10^{-3}$	pF/$(\mu$m$)^2$
Transmembrane potential threshold	$V_{rev,1}$	1.5	V
Electropermeabilization switch speed	$k_{ep,1}$	40	V^{-1}
Characteristic time of electropermeabilization	$\tau_{ep,1}$	1	μs
Characteristic resealing time	$\tau_{res,1}$	10^3	μs
Final time	T	10	μs
Length time step	τ	≈ 0.0024	μs
Quadrature degree	L_c	150	μs

L, using the $L^2(0,T)$ and $C^0(0,T)$ norms. The results are shown in Figures 5-16 and 5-17, where it can be seen than after $L = 11$ the coefficients start converging. For $m \neq 0$ or l even, the obtained coefficients are close to zero.

Second, we look at the convergence of the coefficients of Z_1^L. For this, we calculate the relative error, using the $L^2(0,T)$ and $C^0(0,T)$ norms of the difference between the coefficients $Z_1^{l,0}$, for l even and for the different maximum degrees L. Results are shown in Figures 5-18 and 5-19, where we observe the norm tends to converge exponentially. For $m \neq 0$ or l odd, coefficients obtained vanish.

Next, we compute the relative error in $C^0\left((0,T), L^2(\Gamma_1)\right)$ and $L^2\left((0,T), L^2(\Gamma_1)\right)$ between v_1^L and v_1^{51}, and between Z_1^L and Z_1^{51}. The results are shown in Figure 5-20. The plots are in a log-linear scale, and the errors tends to form a straight line with the slope of order -10^{-2}, which suggests an exponential rate of convergence. Recall, that β (5.1) in

FIGURE 5-16. For a fixed l, the relative error in $L^2(0,T)$ between coefficients $v_1^{l,0}$ of v_1^L and v_1^{51} is plotted. The time step used is $\tau \approx 0.0024\,\mu$s. The $x-$axis indicates the maximum degree used for the discretization of v_1^L, and the $y-$axis indicates the error. After $L = 11$ the coefficients start to converge. Parameters used are in Table 5.9.
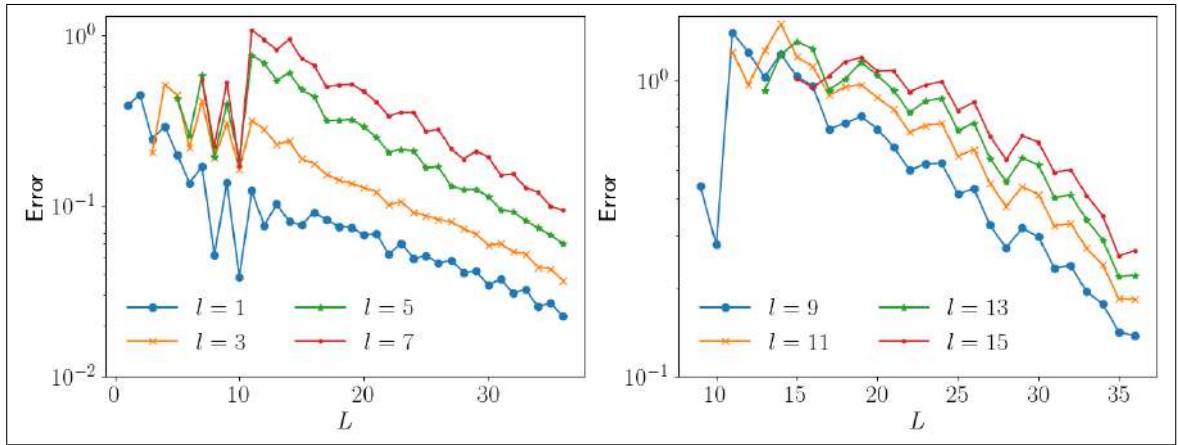
FIGURE 5-17. For a fixed l, the relative error in $\max_{(0,T)}$ between coefficients $v_1^{l,0}$ of v_1^L and v_1^{51} is plotted. The $x-$axis indicates the maximum degree used for the discretization of v_1^L, and the $y-$axis indicates the error. After $L = 11$ the ccoefficients start to converge. Parameters used are in Table 5.9.

our case is only continuous $C^0(\mathbb{R})$ due to the discontinuity of the derivative at the origin worsening the rate of convergence.

While the obtained Z_1 is an even function in space, v_1 is an odd one. Thus, the nonlinear current, is an odd function in space. The external applied potential is an odd function,
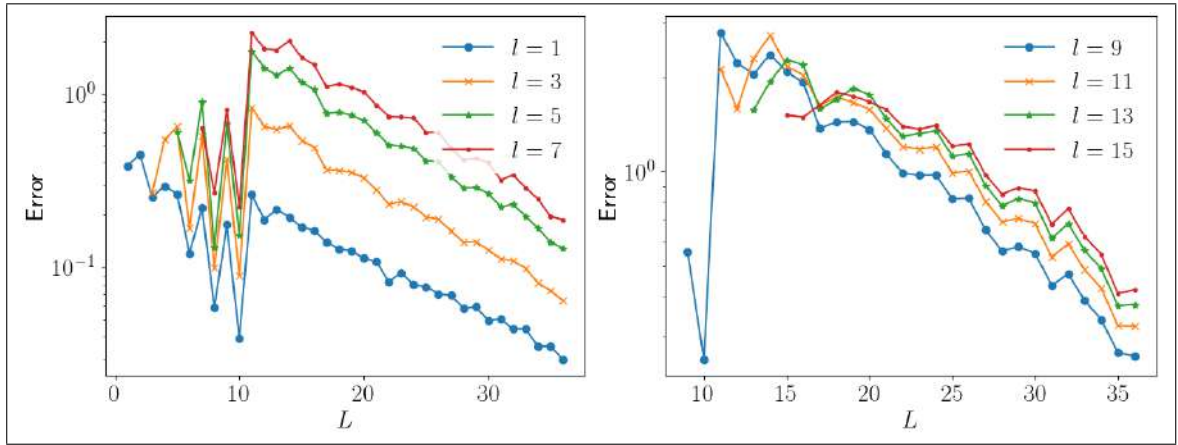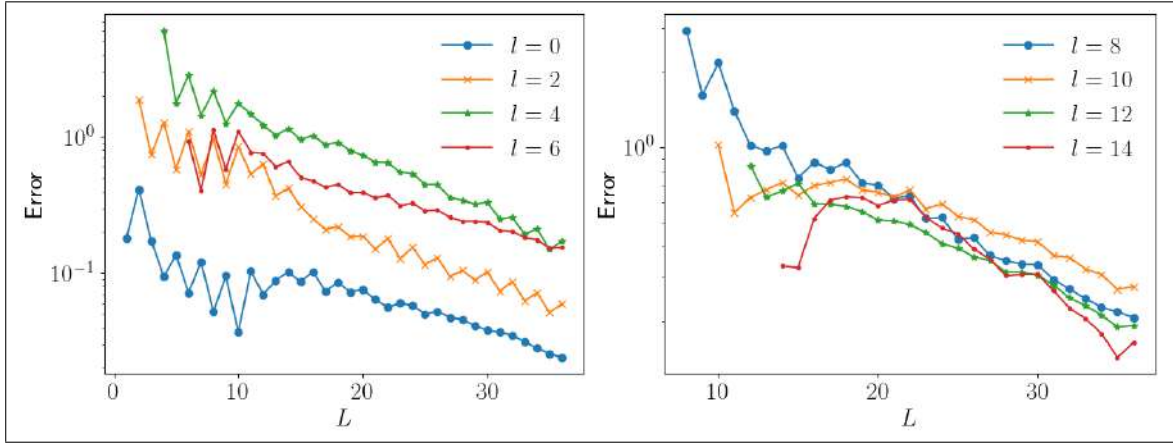
FIGURE 5-18. For a fixed l, the relative error in $L^2((0,T))$ between the co-efficients $Z_1^{l,0}$ of Z_1^L and Z_1^{51} is plotted. The length of the time step used is $\tau \approx 0.0024 \ \mu$s. The $x-$axis indicates the maximum degree used for the discretization o Z_1^L, and the $y-$axis indicates the error. The results show convergence. Parameters used are in Table 5.9.
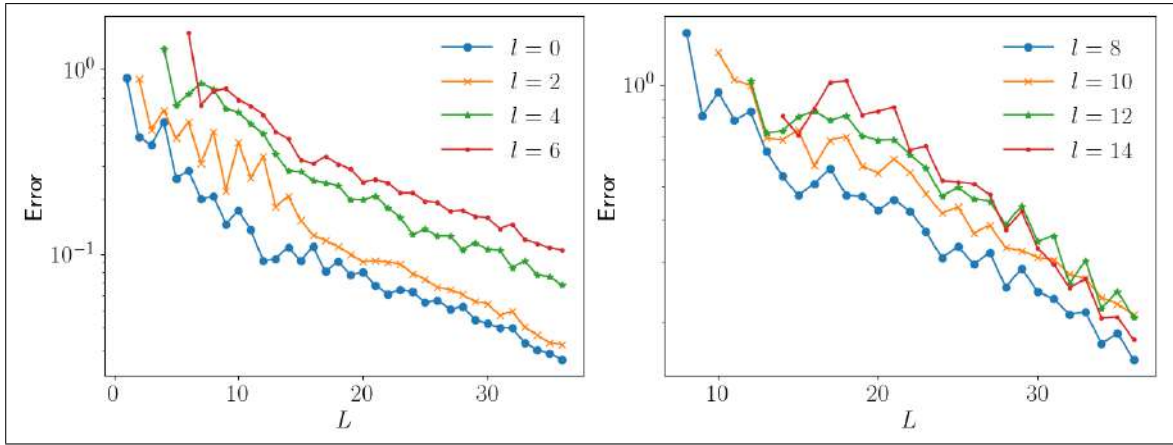
FIGURE 5-19. Spatial convergence in the case of nonlinear dynamics in Section 5.5.3.2: for a fixed l, the relative error in $C(0,T)$ norm between the coefficients $Z_1^{l,0}$ of Z_1^L and Z_1^{51} is plotted. The length of the time step used is $\tau \approx 0.0024 \ \mu$s. The $x-$axis indicates the maximum degree used for the discretization o Z_1^L, and the $y-$axis indicates the error. Parameters used are in Table 5.9.

so we expect that v_1 has an odd component, while Z_1 is defined by an ordinary differential equation that takes v_1 in to an even function.

(A) Relative norms for v_1^L. (B) Relative norms for Z_1^L.

FIGURE 5-20. Spatial convergence for the nonlinear dynamics, Section 5.5.3.2. Relative norms in space and time of computed solutions against an overkill of $L = 51$. On the left, results for v_1^L, while on the right Z_1^L is displayed with time step $\tau \approx 0.0024$ μs. The relative error $re_{\infty,2}(v_1, v_1^{51})_1$ (5.31) 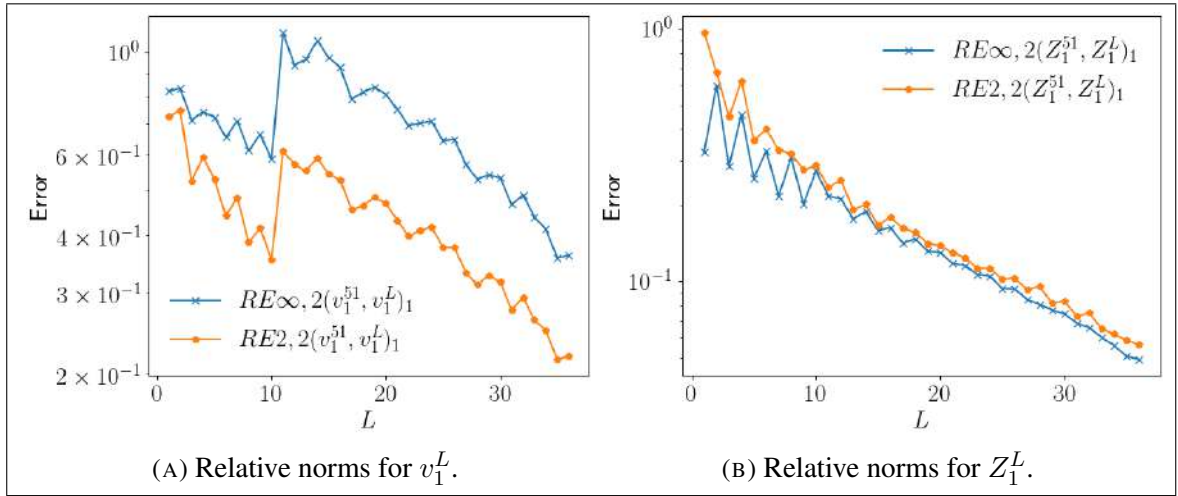is computed in the $C^0\left((0,T), L^2(\Gamma_1)\right)$-norm, and the error for $re_{2,2}(v_1, v_1^{51})_1$ (5.32) is computed in the $L^2\left((0,T), L^2(\Gamma_1)\right)$-norm. The $x-$axis indicates the maximum degree used for the discretization of the solution, and the $y-$axis indicates the error. Convergence starts from $L = 11$. Plots are in log-linear scale, and error tends to form a straight line with slope of approximately -10^{-2}, i.e. exponential rate of convergence. Parameters used are in Table 5.9.

Finally, in Figure 5-21 we plot the evolution in time of v_1^{17}, v_1^{24}, v_1^{35}, and v_1^{51} at the north pole. The differences between the results are more noticeable after the peak of the potential and when the cell tries to stabilize it.

5.5.4. Results with multiple cells

In previous sections, the convergence of the numerical method was studied for a single cell. We proceed now with the case of multiple cells to perform five experiments in the nonlinear case. The examples presented highlight how the distance among cells affects the results as all cell conductivities are set to the same value σ_1.

- Example 5: Three cells aligned along the x-axis and far from each other, with distance between cells $18R_1$.
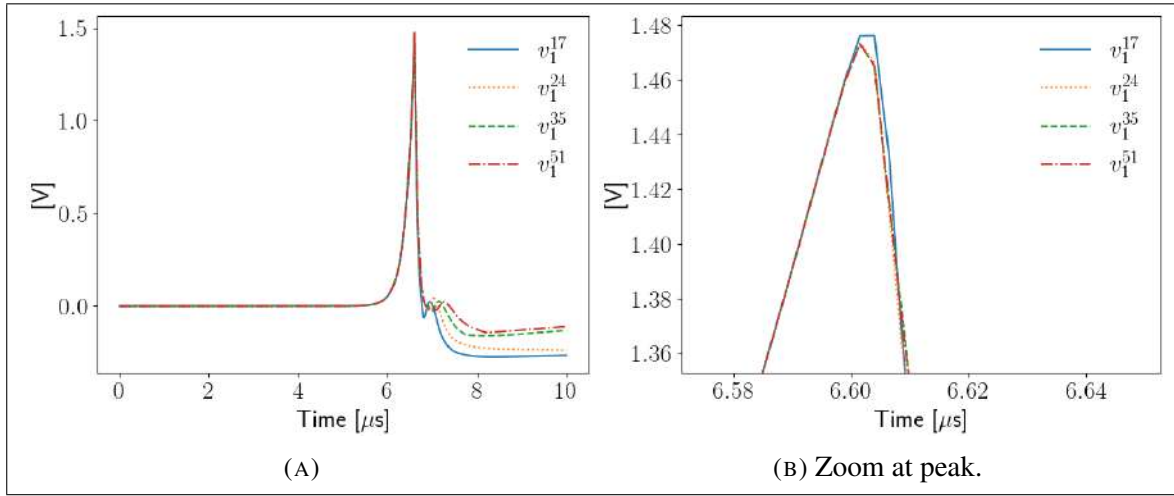
FIGURE 5-21. Evolution of the transmembrane potentials v_1^{17}, v_1^{24}, v_1^{35} and v_1^{51} at the north pole of the cell ($\theta = 0$) obtained in Section 5.5.3.2 where the spatial convergence for one cell in the nonlinear case is studied. The picture on the right is a zoomed image of the transmembrane potential peak. The time step used is $\tau \approx 0.0024 \, \mu$s, with parameters given in Table 5.9.

- Example 6: Three cells aligned along the x-axis, near from each other, with distance between cells $R_1/2$.

- Example 7: Three cells aligned along the z-axis, far from each other, with distance between them $18R_1$.

- Example 8: Three cells aligned along the z-axis, close from to other, with distance between cells $R_1/2$.

- Example 9: Eight cells aligned in a cubic lattice, the nearest distance between two cells is $R_1/2$, the first sphere is at the origin.

Cell radii and physical parameters used for Examples 5–9 are presented in Table 5.10. The extra- and intracellular conductivities have different values from the simulations of other Sections, and were changed so as to obtain a response of the impulse sooner. Coordinates of the cells' center in Examples 5–8 are given in Table 5.11 and sketched in Figure 5-22, while cells' centers in Example 9 are located at the corners of a cube of length 25

TABLE 5.10. Parameters used in Examples 5–9 (multiple cells, nonlinear dynamics) from Section 5.5.4. Parameters for the radii are from (Mistani et al., 2019, Table 1), the electrical parameters are from (Kavian et al., 2014, Table 1), except for extra- and intracellular conductivities that were changed to obtain a response of the impulse sooner.

Parameter	Symbol	Value	Unit
Extracellular conductivity	σ_0	15	μS/μm
Intracellular conductivity	$\sigma_j, j \geq 1$	1.5	μS/μm
Cell j radius	R_1	10	μm
Time part of ϕ_e	$\phi_{time}(t)$	1	
Spatial part of ϕ_e	$\phi_{spatial}$	$5\,z \cdot 10^{-2}$	V
Lipid surface conductivity	$S_{L,1}$	$1.9 \cdot 10^{-6}$	μS/$(\mu$m$)^2$
Irreversible surface conductivity	$S_{ir,1}$	$2.5 \cdot 10^2$	μS/$(\mu$m$)^2$
Specific membrane capacitance	$c_{m,1}$	$9.5 \cdot 10^{-3}$	pF/$(\mu$m$)^2$
Transmembrane potential threshold	$V_{rev,1}$	1.5	V
Electropermeabilization switch speed	$k_{ep,1}$	40	V^{-1}
Characteristic time of electropermeabilization	$\tau_{ep,1}$	1	μs
Characteristic resealing time	$\tau_{res,1}$	10^3	μs
Final time	T	10	μs

TABLE 5.11. Center positions for Examples 5–8 from Section 5.5.4, where nonlinear dynamics with three cells are simulated.

Center position	Symbol	Example 5	Example 6	Example 7	Example 8	Unit
Cell 1	$\mathbf{p_1}$	(0, 0, 0)	(0, 0, 0)	(0, 0, 0)	(0, 0, 0)	μm
Cell 2	$\mathbf{p_2}$	(200, 0, 0)	(25, 0, 0)	(0, 0, 200)	(0, 0, 25)	μm
Cell 3	$\mathbf{p_3}$	(-200, 0, 0)	(-25, 0, 0)	(0, 0, -200)	(0, 0, -25)	μm

TABLE 5.12. Cells' position in Examples 9 from Section 5.5.4, where nonlinear dynamics with eight cells are simulated.

Center position	Symbol	Value in μm	Center position	Symbol	Value in μm
Cell 1	$\mathbf{p_1}$	(0, 0, 0)	Cell 5	$\mathbf{p_5}$	(0, 0, 25)
Cell 2	$\mathbf{p_2}$	(25, 0, 0)	Cell 5	$\mathbf{p_6}$	(25, 0, 25)
Cell 3	$\mathbf{p_3}$	(0, 25, 0)	Cell 7	$\mathbf{p_7}$	(0, 25, 25)
Cell 4	$\mathbf{p_4}$	(25, 25, 0)	Cell 8	$\mathbf{p_8}$	(25, 25, 25)

μm, with one corner at the origin and other one at $(25, 25, 25)$ (cf. Table 5.12). The external applied potential in Examples 5–9 is $\phi_e = 5z \cdot 10^{-2}$ until $t = 5\ \mu$s and equal to zero thereafter. Also, initial conditions are set to be zero.
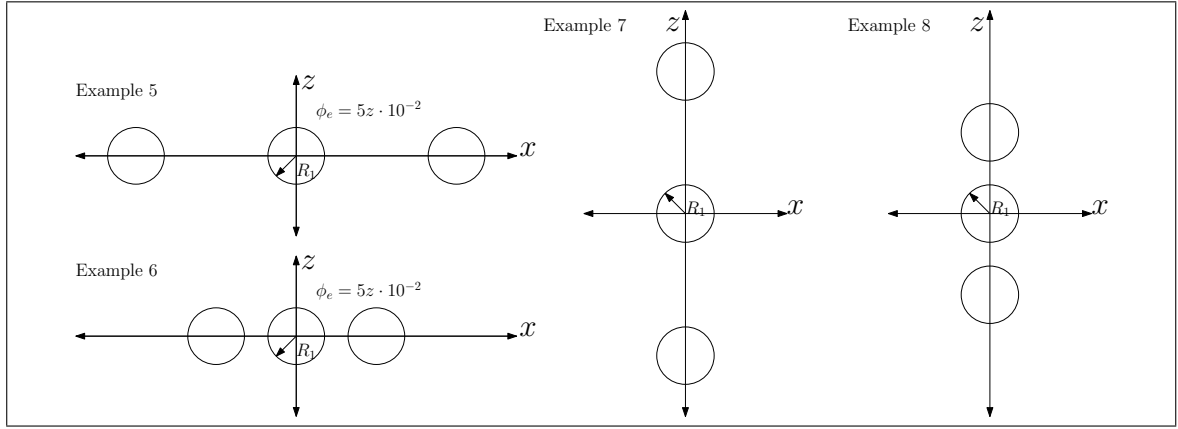
FIGURE 5-22. Illustration for Examples 5–8 in Section 5.5.4.

In what follows, we present results for a time step $\tau \approx 6.1 \cdot 10^{-4}$. The maximum degree of spherical harmonics used for Examples 5–8 is $L = 35$, while for Example 9 $L = 25$. Quadrature degree used in all examples is $L_c = 100$. Figures 5-23, 5-24, 5-25, 5-26 and 5-27 showcase the evolution of the transmembrane potentials v_j^L and the variables Z_j^L for each cell at their north pole.

In Example 5, $\phi_e = 5z \cdot 10^{-2}$ and thus, the perceived excitation for the three cells is the same. Moreover, the cells are relatively far away from each other, therefore, there is almost no interaction among them, and the potentials v_j^{35} and Z_j^{35} look similar, for all j (see Figure 5-21).

In Example 6, we take the same parameters as in Example 5, except for reducing the distance between cells, which is now $R_1/2$. Hence, the interaction between cells is stronger, and the shapes of the potentials v_j^{35} and Z_j^{35} change (see Figure 5-24). One should compare with the previous example in Figure 5-23). Note that, due to the symmetry and the form of the external $\phi_e = 5z \cdot 10^{-2}$, cells 2 and 3 should have the same response at the north pole. They are, however, slightly different, hinting at further refinement.

Examples 7 and 8 are similar to Examples 5 and 6 except that the cells are now aligned along the z-axis. Thus, the excitation $\phi_e = 5z \cdot 10^{-2}$ is perceived differently by the cells. In Example 8, the distance between cells is $R_1/2$, and consequently, the interaction between

(A) Evolution of the transmembrane potentials v_j^{35} at the north pole of each j cell ($\theta = 0$). (B) Evolution of the Z_j^{35} at the north pole of each j cell ($\theta = 0$).
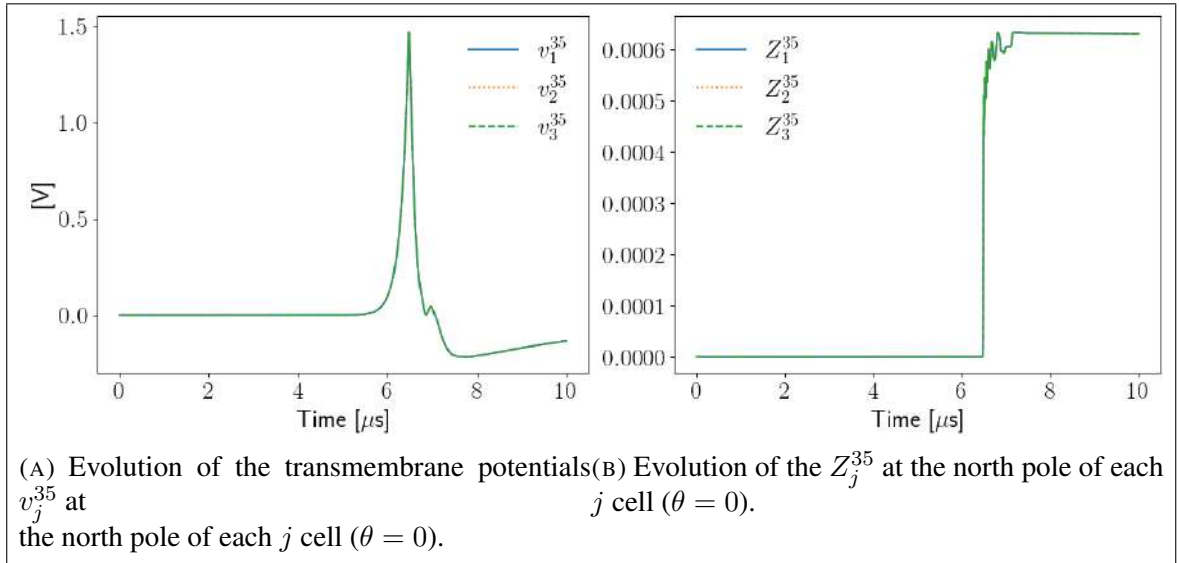
FIGURE 5-23. Example 5 in Section 5.5.4. Since cells are far from each other, they interact weakly among them, and thus the perceived excitation for each of them is the same. Consequently, the transmembrane potentials v_j^{35} and Z_j^{35} are practically equal for all cells. The time step is $\tau \approx 6.1 \cdot 10^{-4}$. Parameters employed are found in Tables 5.10 and 5.11.

(A) Evolution of the transmembrane potentials v_j^{35} at the north pole of each j cell ($\theta = 0$). (B) Evolution of Z_j^{35} at the north pole of each j cell ($\theta = 0$).

FIGURE 5-24. Example 6 from Section 5.5.4. Cells are near each other and the interaction among them influences the transmbembrane potential v_j^{35} and Z_j^{35} (cf. Example 5 in contrast). Notice that the only difference between Example 5 and 6 is the distance between successive cells. The time step is $\tau \approx 6.1 \cdot 10^{-4}$, and the parameters employed are given in Tables 5.10 and 5.11.

138

(A) Evolution of the transmembrane potentials v_j^{35} at the north pole of each j cell ($\theta = 0$). (B) Evolution of Z_j^{35} at the north pole of each j cell ($\theta = 0$).
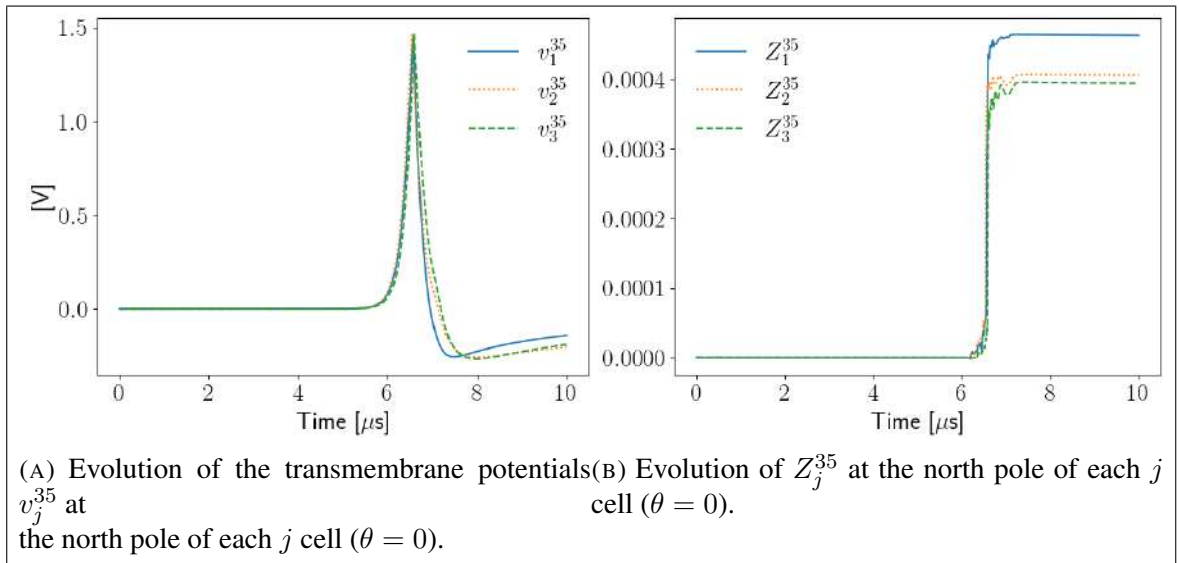
FIGURE 5-25. Example 7 from Section 5.5.4. Cell centers are along the z axis and far from each other while the external applied potential is perceived differently by each cells. The time step is $\tau \approx 6.1 \cdot 10^{-4}$, and the parameters employed are given in Tables 5.10 and 5.11.

(A) Evolution of the transmembrane potentials v_j^{35} at the north pole of each j cell ($\theta = 0$). (B) Evolution of Z_j^{35} at the north pole of each j cell ($\theta = 0$).

FIGURE 5-26. Example 8 from Section 5.5.4. Cell centers are along the z axis and close to each other, and thus the external applied potential is varies over each cell. The time step is $\tau \approx 6.1 \cdot 10^{-4}$, and the parameters employed are given in Tables 5.10 and 5.11.

(A) Evolution of the transmembrane potentials v_j^{25} at the north pole of each j cell with j between 1 and 4.

(B) Evolution of the transmembrane potentials v_j^{25} at the north pole of each j cell with j between 5 and 8.

(C) Evolution of Z_j^{25} at the north pole of each j cell between 1 and 4.

(D) Evolution of Z_j^{25} at the north pole of each j cell between 5 and 8.
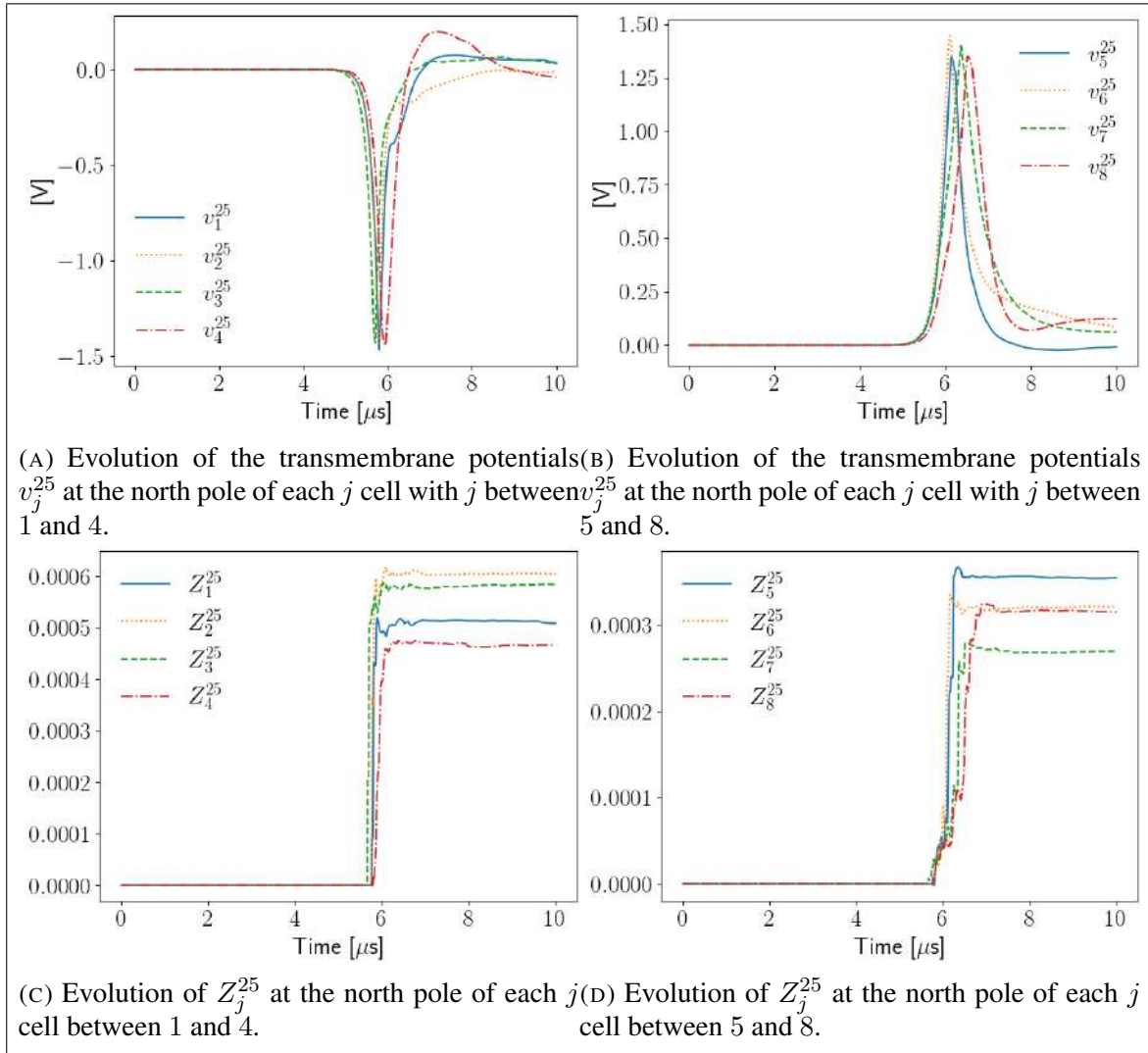
FIGURE 5-27. Example 9 from Section 5.5.4. The first four cells are in the plane $z = 0$, while the others are in the plane $z = 25$. The time step is $\tau \approx 6.1 \cdot 10^{-4}$, and the parameters employed are given in Tables 5.10 and 5.11.
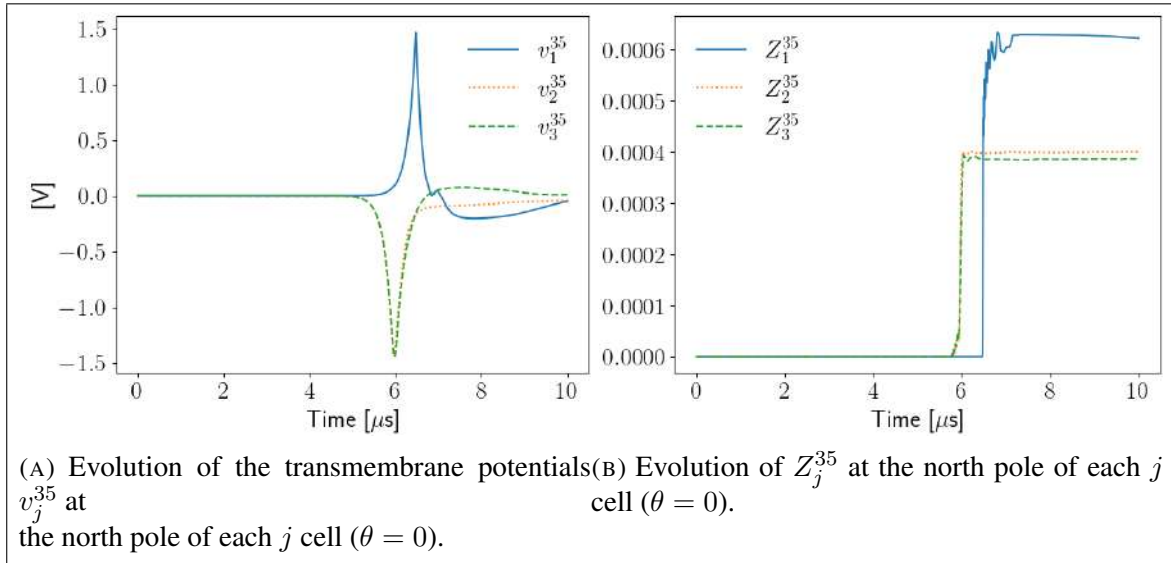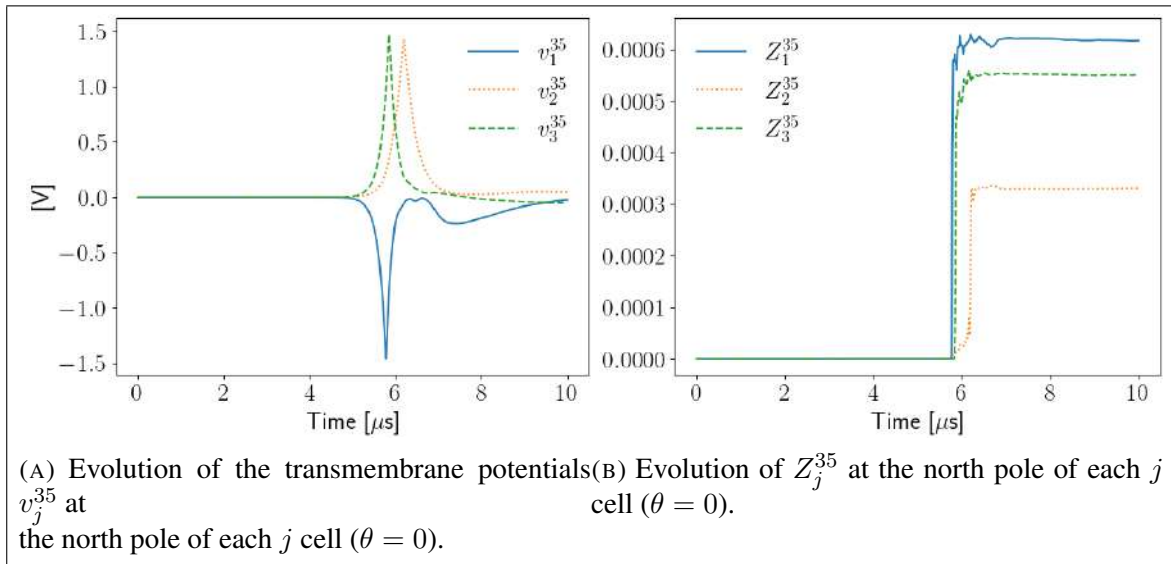
the cells leads to different transmembrane potentials compared to those of Example 7 (see Figures 5-25 and 5-26). Specifically, the transmembrane potential at the cell located at $\mathbf{p}_1$ increases and reaches its maximum around 1.5 in Example 7, while in Example 8 it decreases and reaches a minimum value around -1.5, see Figure 5-25 and 5-26. In addition, the excitation ϕ_e in this case coincides with the one for the middle cell in Examples 7 and

(A) $t = 5\ \mu$s.

(B) $t = 5.75\ \mu$s.

(C) $t = 6\ \mu$s.

(D) $t = 6.25\ \mu$s.

(E) $t = 6.5\ \mu$s.

(F) $t = 7\ \mu$s.

FIGURE 5-28. Transmembrane voltages v_j^{25} obtained in Example 9 of Section 5.5.4 at different times. The length of the time step is $\tau \approx 6.1 \cdot 10^{-4}$. Parameters employed are given in Tables 5.10 and 5.11.
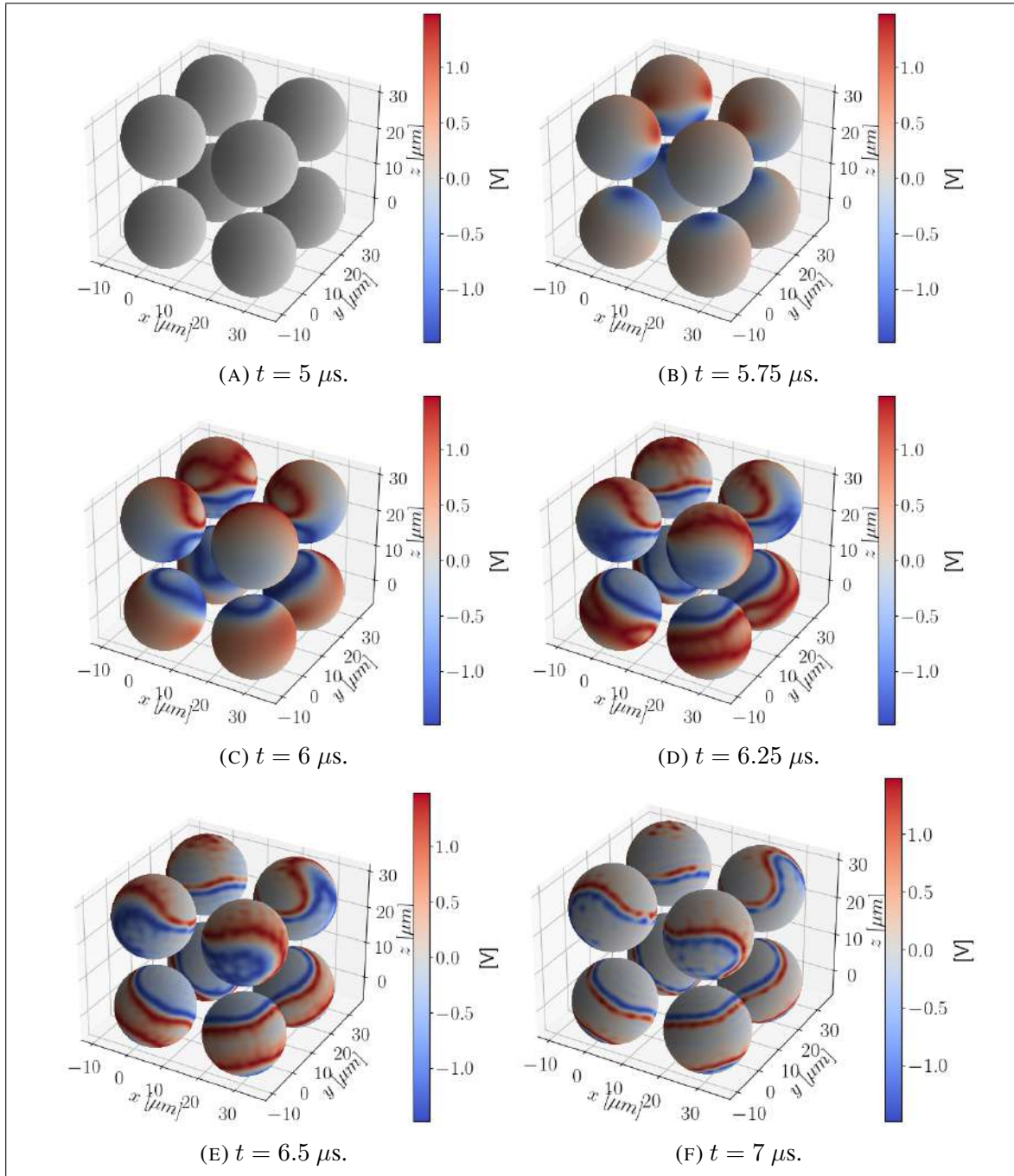
8, so the difference in the behaviour is due to the smaller distance to the other two cells in Example 8 when compared to the situation of Example 7.

Finally, in Example 9 eight cells close to each other are simulated. In Figure 5-27, the corresponding transmembrane voltage v_j^{25} and Z_j^{25} at the north pole are presented. The cells with the centers in the plane $z = 0$ show similar response—see Table 5.12 for the center position of each cell—, while the cells with centers in the plane $z = 25$ have similar response too while differing from cells beneath them. Figure 5-28 shows six snapshots of the transmembrane voltages for the eight cells. It can be seen that the transmembrane voltage starts changing earlier in the parts of the surface close to the rest of the cells, therefore the interaction between them is crucial.

5.6. Conclusions and future work

In this work, we consider the electropermeabilization of disjoint cells following the nonlinear dynamics from (Kavian et al., 2014). Specifically, we recast the volume boundary value problem via a MTF and obtain a parabolic system of boundary integral equations on the cell membrane. This constitutes a significant extension of the numerical method presented in (Henríquez & Jerez-Hanckes, 2018). For simplicity, we assumed that the cells have spherical shape, although the method can be extended to cells with other shapes.

The semi-implicit time stepping scheme presented requires two previous steps, and allows to evaluate explicitly the expression corresponding to the nonlinear dynamics, that results in solving a linear system for each time iteration. A current the scheme only works for relatively small time steps. The proposed method allows one to change the model for the nonlinear dynamics in an amicable way, as long as it is only a change of the nonlinear term and the variables that are not the transmembrane potential. In this case, only the right-hand side of the system to be solved (5.27) and the equations corresponding to the additional variables that are not the transmembrane potential change. This is one of the advantages of the numerical method employed.

Further improvements to the numerical method to be implemented in the future are matrix compression and parallelization techniques, along with an efficient solver for linear systems at each time step.

5.7. Acknowledgements

6. CONCLUSIONS

The thesis concerns the mathematical modeling and numerical simulations of problems arising in electrophysiology. There are two groups of problems addressed in the thesis.

The first one concerns the modeling of signal propagation in myelinated axons and nerve fascicle. Modeling electrical stimulation in tissues faces many difficulties, including the nonlinear dynamics and complex geometries. We use multiscale modeling, and in particular the homogenization technique, to derive macroscopic models for the electric potential. In the case of an individual axon, the behaviour of the potential is governed by a nonlinear cable equation, while in the case of bundles, we obtain a bidomain model. The technique being used combines the two-scale convergence method and the method of monotone operators. The numerical computations are performed to illustrate the dependence of the effective coefficients on the area of the unmyelinated part of the membrane.

In the second part of the thesis, we address the cellular electro-permeabilization, that is changing the permeability of the cell membrane by applying electrical pulses. Using the multiple traces formulation, we develop a mathematical framework for the numerical resolution of cellular electro-permeabilization models in three dimensions. Namely, reducing the problem to boundary integral equations on cell membranes, we simulate the electric potential response for a fixed number of disjoint spherical cells.

In our further work we will compare numerical solutions of the homogenized models for individual axons and axon bundles with the solutions of microscopic three-dimensional models. This allow us to study numerically the rate of convergence, as $\varepsilon \to 0$, from the microscopic models to the macroscopic one. Also, we will make improvements to the numerical method implemented for the problem of electropermeabilization, among them parallelizing and matrix compression techniques, and will continue exploring the modeling issues of the electro-permeabilization phenomena and implementing other nonlinear dynamics for the process.

References

Acerbi, E., ChiadoPiat, V., Dal Maso, G., & Percivale, D. (1992). An extension theorem from connected sets, and homogenization in general periodic domains. *Nonlinear Analysis: Theory, Methods & Applications*, *18*(5), 481–496.

Aganin, A. A., & Davletshin, A. I. (2018, April). Transformation of Irregular Solid Spherical Harmonics with Parallel Translation of the Coordinate System. *Lobachevskii Journal of Mathematics*, *39*(3), 433–438. doi: 10.1134/S1995080218030022

Allaire, G. (1992). Homogenization and two-scale convergence. *SIAM Journal on Mathematical Analysis*, *23*(6), 1482–1518.

Allaire, G., & Damlamian, A. (1995). Two-scale convergence on periodic surfaces and applications. In A. Bourgeat, C. Carasso, L. S, & Mikelić (Eds.), *Mathematical modelling of flow through porous media.* World Scientific.

Amar, M., Andreucci, D., Bisegna, P., & Gianni, R. (2006). On a hierarchy of models for electrical conduction in biological tissues. *Mathematical Methods in the Applied Sciences*, *29*(7), 767–787.

Amar, M., Andreucci, D., Bisegna, P., & Gianni, R. (2013). A hierarchy of models for the electrical conduction in biological tissues via two-scale convergence: the nonlinear case. *Differential and Integral Equations*, *26*(9/10), 885–912.

Amar, M., Andreucci, D., & Timofte, C. (2021). Homogenization of a modified bidomain model involving imperfect transmission. *Communications on Pure and Applied Analysis*, *20*(5), 1755–1782.

Ammari, H., Widlak, T., & Zhang, W. (2016, July). Towards monitoring critical microscopic parameters for electropermeabilization. *Quarterly of Applied Mathematics*, *75*(1), 1–17. doi: 10.1090/qam/1449

Anastassiou, C. A., & Koch, C. (2015). Ephaptic coupling to endogenous electric field activity: why bother? *Current opinion in neurobiology*, *31*, 95–103.

Anastassiou, C. A., Perin, R., Markram, H., & Koch, C. (2011). Ephaptic coupling of cortical neurons. *Nature neuroscience*, *14*(2), 217.

Anderson, E., Bai, Z., Bischof, C., Blackford, S., Demmel, J., Dongarra, J., . . . Sorensen, D. (1999). *LAPACK users' guide* (Third ed.). Philadelphia, PA: Society for Industrial and Applied Mathematics.

Atkinson, K., & Han, W. (2012). *Spherical harmonics and approximations on the unit sphere: an introduction* (Vol. 2044). Springer Science & Business Media.

Bakhvalov, N., & Panasenko, G. (1989). *Homogenisation: Mathematical problems in the mechanics of composite materials*. Springer Netherlands.

Barr, R. C., & Plonsey, R. (1992). Electrophysiological interaction through the interstitial space between adjacent unmyelinated parallel fibers. *Biophysical journal*, *61*(5), 1164–1175.

Basser, P. (1993). Cable equation for a myelinated axon derived from its microstructure. *Medical & biological engineering & computing*, *31*(1), S87–S92.

Basser, P. J., & Roth, B. J. (2000). New currents in electrical stimulation of excitable tissues. *Annual Review of Biomedical Engineering*, *2*(1), 377-397.

Bendahmane, M., Mroue, F., Saad, M., & Talhouk, R. (2019). Unfolding homogenization method applied to physiological and phenomenological bidomain models in electrocardiology. *Nonlinear Analysis: Real World Applications*, *50*, 413–447.

Bensoussan, A., Lions, J.-L., & Papanicolaou, G. (2011). *Asymptotic analysis for periodic structures* (Vol. 374). American Mathematical Soc.

Binczak, S., Eilbeck, J., & Scott, A. C. (2001). Ephaptic coupling of myelinated nerve fibers. *Physica D: Nonlinear Phenomena*, *148*(1-2), 159–174.

Bokil, H., Laaris, N., Blinder, K., Ennis, M., & Keller, A. (2001). Ephaptic interactions in the mammalian olfactory system. *Journal of Neuroscience*, *21*(20), RC173–RC173.

Bourgault, Y., Coudiere, Y., & Pierre, C. (2009). Existence and uniqueness of the solution for the bidomain model used in cardiac electrophysiology. *Nonlinear Analysis: Real World Applications*, *10*(1), 458–482.

Brezis, H. (2011). *Functional Analysis, Sobolev Spaces and Partial Differential Equations* (First ed.). Springer New York, NY. doi: 10.1007/978-0-387-70914-7

Choi, S.-E., Khoo, H., & Hur, S. C. (2022, June). Recent Advances in Microscale Electroporation. *Chemical Reviews*, acs.chemrev.1c00677. doi: 10.1021/acs.chemrev.1c00677

Claeys, X., Hiptmair, R., & Jerez-Hanckes, C. (2013). Multitrace boundary integral equations. In *Direct and inverse problems in wave propagation and applications* (Vol. 14, pp. 51–100). De Gruyter, Berlin.

Claeys, X., Hiptmair, R., Jerez-Hanckes, C., & Pintarelli, S. (2015). Novel multitrace boundary integral equations for transmission boundary value problems. In A. S. Fokas & B. Pelloni (Eds.), *Unified transform for boundary value problems: Applications and advances* (pp. 227–258). Philadelphia, SIAM.

Collin, A., & Imperiale, S. (2018). Mathematical analysis and 2-scale convergence of a heterogeneous microscopic bidomain model. *Mathematical Models and Methods in Applied Sciences*, *28*(05), 979–1035.

Colton, D., & Kress, R. (2013). *Inverse acoustic and electromagnetic scattering theory* (third ed., Vol. 93). Springer Science & Business Media New York.

conda-forge community. (2015, July). *The conda-forge Project: Community-based Software Distribution Built on the conda Package Format and Ecosystem.* Zenodo. Retrieved from `https://doi.org/10.5281/zenodo.4774216` doi: 10.5281/zenodo.4774216

De Giorgi, E., & Spagnolo, S. (1979). Convergence problems for functionals and operators. *Ennio De Giorgi*, *487*.

Fernandez-Aranzamendi, E., San-Román, E., Castillo-Araníbar, P., Luz-Ventura, González-Posadas, V., & Segovia-Vargas, D. (2022, May). Breast tumor classification by age and size based on analysis of dielectric properties performed on in vivo and ex vivo measurements. In *2022 International Workshop on Antenna Technology (iWAT)* (pp. 192–195).

FitzHugh, R. (1955). Mathematical models of threshold phenomena in the nerve membrane. *The Bulletin of Mathematical Biophysics*, *17*(4), 257–278.

Franzone, P. C., & Savaré, G. (2002). Degenerate evolution systems modeling the cardiac electric field at micro-and macroscopic level. In *Evolution equations, semigroups and functional analysis* (pp. 49–78). Springer.

Freeden, W., & Gutting, M. (2013). *Special Functions of Mathematical (Geo-)Physics*. Basel: Springer Basel. doi: 10.1007/978-3-0348-0563-6

Freidlin, M. (1964). Dirichlet's problem for an equation with periodic coefficients depending on a small parameter. *Theory of Probability & Its Applications*, *9*(1), 121–125.

Gallier, J., & Quaintance, J. (2020). Spherical harmonics and linear representations of lie groups. In *Differential geometry and lie groups* (pp. 265–360). Springer.

Ganesh, M., & Mustapha, K. (2007, February). A fully discrete H 1-Galerkin method with quadrature for nonlinear advection–diffusion–reaction equations. *Numerical Algorithms*, *43*(4), 355–383. doi: 10.1007/s11075-007-9066-6

Grandelius, E., & Karlsen, K. H. (2019). The cardiac bidomain model and homogenization. *Networks and Heterogeneous Media*, *14*(1), 173–204.

Guittet, A., Lepilliez, M., Tanguy, S., & Gibou, F. (2015, October). Solving elliptic problems with discontinuities on irregular domains – the Voronoi Interface Method. *Journal of Computational Physics*, *298*, 747–765. doi: 10.1016/j.jcp.2015.06.026

Guittet, A., Poignard, C., & Gibou, F. (2017, March). A Voronoi Interface approach to cell aggregate electropermeabilization. *Journal of Computational Physics*, *332*, 143–159. doi: 10.1016/j.jcp.2016.11.048

Harris, C. R., Millman, K. J., van der Walt, S. J., Gommers, R., Virtanen, P., Cournapeau, D., . . . Oliphant, T. E. (2020, September). Array programming with NumPy. *Nature*, *585*(7825), 357–362. Retrieved from `https://doi.org/10.1038/s41586-020-2649-2` doi: 10.1038/s41586-020-2649-2

Henríquez, F., & Jerez-Hanckes, C. (2018). Multiple traces formulation and semi-implicit scheme for modelling biological cells under electrical stimulation. *ESAIM Mathematical Modelling and Numerical Analysis*, *52*(2), 659–703. Retrieved from `https://doi.org/10.1007/s00211-016-0835-9` doi: 10.1007/s00211-016-0835-9

Henríquez, F., Jerez-Hanckes, C., & Altermatt, F. (2017). Boundary integral formulation and semi-implicit scheme coupling for modeling cells under electrical stimulation. *Numer. Math.*, *136*(1), 101–145. Retrieved from `https://doi.org/10.1007/s00211-016-0835-9` doi: 10.1007/s00211-016-0835-9

Hiptmair, R., & Jerez-Hanckes, C. (2012). Multiple traces boundary integral formulation for helmholtz transmission problems. *Advances in Computational Mathematics*, *37*(1), 39–91.

Hiptmair, R., Jerez-Hanckes, C., Lee, J.-F., & Peng, Z. (2014). Domain decomposition for boundary integral equations via local multi-trace formulations. In *Domain decomposition methods in science and engineering xxi* (p. 43-57). Springer International Publishing.

Hodgkin, A. L., & Huxley, A. F. (1952, August). A quantitative description of membrane current and its application to conduction and excitation in nerve. *The Journal of Physiology*, *117*(4), 500–544.

Hunter, J. D. (2007). Matplotlib: A 2d graphics environment. *Computing in Science & Engineering*, *9*(3), 90–95. doi: 10.1109/MCSE.2007.55

Jackson, J. D. (2013). *Classical electrodynamics* (3. ed., repr. 2013, student ed ed.). Hoboken, NY: Wiley.

Jæger, K. H., & Tveito, A. (2021). Derivation of a cell-based mathematical model of excitable cells. In *Modeling excitable tissue* (pp. 1–13). Springer, Cham.

Jerez-Hanckes, C., Martínez, I. A., Pettersson, I., & Rybalko, V. (2021). Multiscale analysis of myelinated axons. In *Emerging problems in the homogenization of partial differential equations* (pp. 17–35). Springer.

Jerez-Hanckes, C., Pettersson, I., & Rybalko, V. (2020, March). Derivation of cable equation by multiscale analysis for a model of myelinated axons. *Discrete and Continuous Dynamical Systems-Series B*, *25*(3), 815–839.

Jerez-Hanckes, C., Pinto, J., & Tournier, S. (2015). Local multiple traces formulation for high-frequency scattering problems. *J. Comput. Appl. Math.*, *289*, 306–321.

Jikov, V. V., Kozlov, S. M., & Oleinik, O. A. (2012). *Homogenization of differential operators and integral functionals*. Springer Science & Business Media.

Kavian, O., Leguèbe, M., Poignard, C., & Weynans, L. (2014, January). Electropermeabilization Modeling at the Cell Scale. *Journal of Mathematical Biology*, *68*(1-2), 235–265. doi: 10.1007/s00285-012-0629-3

Keller, J. B. (1964). A theorem on the conductivity of a composite medium. *Journal of Mathematical Physics*, *5*(4), 548–549.

Kim, K., & Lee, W. G. (2017). Electroporation for nanomedicine: A review. *Journal of Materials Chemistry B*, *5*(15), 2726–2738. doi: 10.1039/C7TB00038C

Kotnik, T., Rems, L., Tarek, M., & Miklavčič, D. (2019, May). Membrane Electroporation and Electropermeabilization: Mechanisms and Models. *Annual Review of Biophysics*, *48*(1), 63–91. doi: 10.1146/annurev-biophys-052118-115451

Leguèbe, M., Silve, A., Mir, L. M., & Poignard, C. (2014, November). Conducting and permeable states of cell membrane submitted to high voltage pulses: Mathematical and numerical studies validated by the experiments. *Journal of Theoretical Biology*, *360*, 83–94. doi: 10.1016/j.jtbi.2014.06.027

Li, D. C., & Li, Q. (2017). Electrical stimulation of cortical neurons promotes oligodendrocyte development and remyelination in the injured spinal cord. *Neural regeneration research*, *12*(10), 1613.

Lin, J., & Keener, J. P. (2010). Modeling electrical activity of myocardial cells incorporating the effects of ephaptic coupling. *Proceedings of the National Academy of Sciences*, *107*(49), 20935–20940.

Lions, J.-L. (1969). *Quelques méthodes de résolution de problemes aux limites non linéaires*. Dunod.

Liu, X.-D., Fedkiw, R. P., & Kang, M. (2000, May). A Boundary Condition Capturing Method for Poisson's Equation on Irregular Domains. *Journal of Computational Physics*, *160*(1), 151–178. doi: 10.1006/jcph.2000.6444

Mackey, M. C., & Maini, P. K. (2015, May). What Has Mathematics Done for Biology? *Bulletin of Mathematical Biology*, *77*(5), 735–738.

Maini, P. K. (2002). Making Sense of Complex Phenomena in Biology. In G. Bock & J. A. Goode (Eds.), *In silico' simulation of biological processes* (1st ed., Vol. 247, pp. 53–65). John Wiley & Sons, Ltd.

Mandonnet, E., & Pantz, O. (2011). The role of electrode direction during axonal bipolar electrical stimulation: a bidomain computational model study. *Acta Neurochirurgica*, *153*(12), 2351–2355.

Marchenko, V., & Khruslov, E. (2006). *Homogenization of partial differential equations* (Vol. 46). Boston, MA: Birkhäuser Boston Inc. (Translated from the 2005 Russian original by M. Goncharenko and D. Shepelsky)

Marchenko, V. A., & Khruslov, E. Y. (1964). Boundary-value problems with fine-grained boundary. *Matematicheskii Sbornik*, *107*(3), 458–472.

Matano, H., & Mori, Y. (2011). Global existence and uniqueness of a three-dimensional model of cellular electrophysiology. *Discrete Contin. Dyn. Syst*, *29*, 1573–1636.

Maxwell, J. C. (1873). *A treatise on electricity and magnetism* (Vol. 1). Clarendon press.

McIntyre, C. C., Richardson, A. G., & Grill, W. M. (2002). Modeling the excitability of mammalian nerve fibers: influence of afterpotentials on the recovery cycle. *Journal of neurophysiology*, *87*(2), 995–1006.

Meffin, H., Tahayori, B., Sergeev, E. N., Mareels, I. M., Grayden, D. B., & Burkitt, A. N. (2014). Modelling extracellular electrical stimulation: Iii. derivation and interpretation of neural tissue equations. *Journal of neural engineering*, *11*(6), 065004.

Meunier, C., & d'Incamps, B. L. (2008). Extending cable theory to heterogeneous dendrites. *Neural Computation*, *20*(7), 1732-1775.

Minty, G. (1962). Monotone (nonlinear) operators in hilbert space. *Duke Math. J.*, *29*, 341–346.

Mistani, P., Guittet, A., Poignard, C., & Gibou, F. (2019, March). A parallel Voronoi-based approach for mesoscale simulations of cell aggregate electropermeabilization. *Journal of Computational Physics*, *380*, 48–64. doi: 10.1016/j.jcp.2018.12.009

Nagumo, J., Arimoto, S., & Yoshizawa, S. (1962). An active pulse transmission line simulating nerve axon. *Proceedings of the IRE*, *50*(10), 2061–2070.

Nédélec, J.-C. (2001). *Acoustic and electromagnetic equations: integral representations for harmonic problems* (Vol. 144). Springer Science & Business Media.

Neu, J., & Krassowska, W. (1993). Homogenization of syncytial tissues. *Critical reviews in biomedical engineering*, *21*(2), 137—199.

Neu, J. C., & Krassowska, W. (1999, March). Asymptotic model of electroporation. *Physical Review E*, *59*(3), 3471–3482. doi: 10.1103/PhysRevE.59.3471

Nguetseng, G. (1989). A general convergence result for a functional related to the theory of homogenization. *SIAM Journal on Mathematical Analysis*, *20*(3), 608–623.

Olver, F. W. J., Lozier, D. W., Boisvert, R. F., Clark, C. W., & National Institute of Standards and Technology (U.S.) (Eds.). (2010). *NIST handbook of mathematical functions*. Cambridge ; New York: Cambridge University Press : NIST.

Onemli, E., Joof, S., Aydinalp, C., Pastaci Özsobaci, N., Ateş Alkan, F., Kepil, N., ... Yilmaz, T. (2022, December). Classification of rat mammary carcinoma with large scale in vivo microwave measurements. *Scientific Reports*, *12*(1), 349.

Pazy, A. (2012). *Semigroups of linear operators and applications to partial differential equations* (Vol. 44). Springer Science & Business Media.

Pennacchio, M., Savaré, G., & Franzone, P. C. (2005). Multiscale modeling for the bioelectric activity of the heart. *SIAM Journal on Mathematical Analysis*, *37*(4), 1333–1370.

Pettersson, I. (2017). Two-scale convergence in thin domains with locally periodic rapidly oscillating boundary. *Differential Equations* & *Applications*, *9*(3), 393–412. doi: 10.7153/dea-2017-09-28

Plonsey, R., & Heppner, D. B. (1967, December). Considerations of quasi-stationarity in electrophysiological systems. *The Bulletin of Mathematical Biophysics*, *29*(4), 657–664. doi: 10.1007/BF02476917

Poisson, S.-D. (1821). Memoires sur ia theorie du magnetisme. *Memoires le l'Academie Sciences de France*, *5*, 247–338.

Rall, W. (1969). Time constants and electrotonic length of membrane cylinders and neurons. *Biophysical Journal*, *9*(12), 1483 - 1508. Retrieved from `http://www.sciencedirect.com/science/article/pii/S0006349569864672` doi: https://doi.org/10.1016/S0006-3495(69)86467-2

Ramon, F., & Moore, J. W. (1978). Ephaptic transmission in squid giant axons. *American Journal of Physiology-Cell Physiology*, *234*(5), 162–169.

Rattay, F. (1990). *Electrical nerve stimulation*. Springer.

Rico, J. F., López, R., Ema, I., & Ramírez, G. (2013, May). Translation of real solid spherical harmonics. *International Journal of Quantum Chemistry*, *113*(10), 1544–1548. doi: 10.1002/qua.24356

Rols, M.-P. (2006). Electropermeabilization, a physical method for the delivery of therapeutic molecules into cells. *Biochimica et Biophysica Acta (BBA) - Biomembranes*, *1758*(3), 423-428.

Sauter, S. A., & Schwab, C. (2010). *Boundary Element Methods* (Vol. 39). Berlin, Heidelberg: Springer Berlin Heidelberg.

Showalter, R. E. (2013). *Monotone operators in banach space and nonlinear partial differential equations* (Vol. 49). American Mathematical Soc.

Siriudie. (n.d.). `https://commons.wikimedia.org/wiki/File:GB_3102.11_Figure_5.svg`. (Accessed on 10 September 2022)

Standring, S. (2021). *Gray's anatomy e-book: the anatomical basis of clinical practice*. Elsevier Health Sciences.

Thomée, V. (2006). *Galerkin finite element methods for parabolic problems* (2nd ed ed.) (No. v. 25). Berlin ; New York: Springer.

Tveito, A., Jæger, K. H., Lines, G. T., Paszkowski, Ł., Sundnes, J., Edwards, A. G., ... Einevoll, G. T. (2017). An evaluation of the accuracy of classical models for computing the membrane potential and extracellular potential for neurons. *Frontiers in computational neuroscience*, *11*, 27.

Veneroni, M. (2006). Reaction-diffusion systems for the microscopic cellular model of the cardiac electric field. *Math. Methods Appl. Sci.*, *29*(14), 1631–1661.

Vico, F., Greengard, L., & Gimbutas, Z. (2014). Boundary integral equation analysis on the sphere. *Numerische Mathematik*, *128*(3), 463–487.

Virtanen, P., Gommers, R., Oliphant, T. E., Haberland, M., Reddy, T., Cournapeau, D., ... SciPy 1.0 Contributors (2020). SciPy 1.0: Fundamental Algorithms for Scientific Computing in Python. *Nature Methods*, *17*, 261–272. doi: 10.1038/s41592-019-0686-2

Vollmer, F., & Yu, D. (2020). *Optical whispering gallery modes for biosensing: From physical principles to applications*. Cham: Springer.

Wahls, T. L., Reese, D., Kaplan, D., & Darling, W. G. (2010). Rehabilitation with neuromuscular electrical stimulation leads to functional gains in ambulation in patients with secondary progressive and primary progressive multiple sclerosis: A case series report. *The Journal of Alternative and Complementary Medicine*, *16*(12), 1343–1349.

Wieczorek, M. A., & Meschede, M. (2018). SHTools: Tools for Working with Spherical Harmonics. *Geochemistry, Geophysics, Geosystems*, *19*(8), 2574–2592. doi: 10.1029/2018GC007529

Winslow, R. L., Trayanova, N., Geman, D., & Miller, M. I. (2012, October). Computational Medicine: Translating Models to Clinical Care. *Science Translational Medicine*, *4*(158), 1-11.

Zhikov, V. (2000). On an extension and an application of the two-scale convergence method. *Mat. Sb.*, *191*(7), 31–72. Retrieved from http://dx.doi.org/10.1070/SM2000v191n07ABEH000491 doi: 10.1070/SM2000v191n07ABEH000491